Ultracold Lithium-6 Atoms in the BEC-BCS Crossover:Experiments and the Construction of a New Apparatus

Martin Teichmann

École Normale Supérieure
Département de Physique

Laboratoire Kastler Brossel

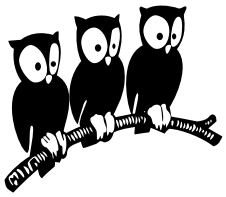

Thèse de Doctorat de l'Université Paris 6

Spécialité : Physique Quantique

présentée par

Martin Teichmann

pour obtenir le grade de Docteur de l'Université Paris 6

Atomes de lithium-6 ultra froids dans la transition BEC-BCS : expériences et construction d'un montage expérimental

Ultracold Lithium-6 Atoms in the BEC-BCS Crossover: Experiments and the Construction of a New Apparatus

---

Soutenue le 27 septembre 2007

devant le jury composé de :

Roland Combescot	Examinateur
Frédédric Chevy	Examinateur
Tilman Pfau	Examinateur
Christian Miniatura	Rapporteur
Christoph Westbrook	Rapporteur
Christophe Salomon	Directeur de thèse

Contents

Chapter 1

Introduction

"The interactions of all other elements, even noble gases, is too large, therefore Helium will stay the only superfluid" writes H. Vogel in "Gerthsen-Physik" [1], a not-so-old introductory physics textbook. Nowadays it is a standard procedure in the laboratory to create superfluid dilute gases of various alkali metals. This shows how unbelievable and groundbreaking the work on cold atoms was over the last years. A superfluid is a liquid of vanishing viscosity, a situation that strange that Richard Feynman quotes John von Neuman of having it called "Dry Water" to underline how unthinkable such a state is [2].

It all started from a rather unconventional root, atomic physics, a field so unfamiliar to the general public that it is often confused with nuclear physics. It was the invention of the laser, which made this field possible. Suddenly, precision spectroscopy improved drastically and found a new use: the cooling of neutral atoms and ions. A masterpiece of this field was the invention of the magneto-optical trap, proposed by Jean Dalibard and first realized by Raab *et al.* [3], which made it possible to take over a hitherto independent field, the struggle to create a quantum gas and especially a Bose-Einstein condensate (BEC), attempted for decades in Hydrogen [4] but finally carried out first in 1995 with laser cooled atomic gases [5,6]. The ado was not about nothing, as the founders of this field, Steven Chu, William D. Phillips and Claude Cohen-Tannoudji, were awarded the 1997 Nobel prize in physics. The first creators of Bose-Einstein condensation in dilute gases, Eric A. Cornell, Carl E. Wieman and Wolfgang Ketterle, followed in 2001.

This enormous success led to an explosion in the field. Cold atoms are nowadays studied in many laboratories around the world. Shortly after the first realization of BEC, physicists started to ask: but what will happen with fermions? Answering this question opened a large field of

research, which is still growing.

Cold atoms are a wonderland for theorists: nowhere more than here can physical principles be reduced to their purest meaning. We can study fermions which are just that, and we can tune their interactions – using a Feshbach resonance – at will. Thus, cold atoms can be seen as a model system, having essentially the same behavior as superconductors, neutron stars or the quark-gluon plasma [7], to name a few, without the downsides of impurities as in solid state systems.

All the mentioned systems can be put under one universal umbrella: a phase transition to *superfluidity* occurs below the *critical temperature* T_c. As mentioned above, superfluidity is a state in which the particles flow completely frictionless. If the particles carry a charge, one speaks of superconductivity.[1] Microscopically, this effect can be described by the particles forming pairs. These pairs are bosonic, and below T_c the pairs start to occupy the ground state in macroscopic numbers, forming a *Bose-Einstein condensate*.

The nature of these pairs is very different in the various types of superfluidity. In the case of superfluid He-4 and the mentioned BEC in cold bosonic gases, the pairs consist of the ion core and the valence electron. The binding is sufficiently strong to treat the atoms as bosonic particles on their own. On the other hand, in superconductors, we have weakly bound *Cooper pairs*, described by a theory by Bardeen, Cooper and Schrieffer [9], which is termed *BCS theory*, after their inventors. The advantage of working with cold atoms is that we can smoothly change between all these behaviors, from very weak to very strong interactions.

A very good illustration of this universality can be found in an article by M. Holland *et al.* [10], shown in figure 1.1. The different kinds of superfluidity span a range of six orders of magnitude in their critical temperature. Nevertheless, they can all be described by the same theory. This theory is based on a binding of fermionic particles to bosonic pairs. The binding energy spreads over 15 orders of magnitude. Our experiments on cold fermionic atomic gases are located in the center of the graph, on the border between the two different extremes. On the left in the graph, the weakly bound particles that can still be seen as single fermionic particles, and on the right the strongly bound compound bosons.

The situation is even richer for cold atoms: We do not only have a

[1] The equivalence of superfluidity and superconductivity was already realized by F. London [8], long before any microscopic description was available.

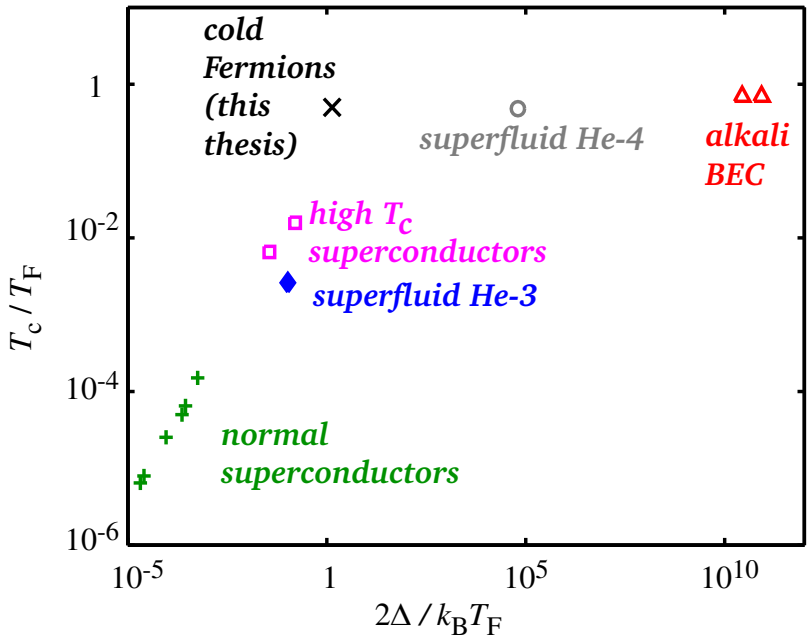

Figure 1.1: The critical temperature and the pair binding energy of various superfluid fermionic systems. The two bosonic systems in the graph (He-4 and alkali BEC) are considered as composite boson consisting of the ionic core and the valence electron for alkali, and of the ionic core and one electrons for He-4. Our experiments are marked as ×. Figure modified from reference [10].

crossover from weak to strong interactions, but instead, looking at it from a mean-field standpoint, we have weak *attractive* interactions in the BCS limit, and weak *repulsive* interactions between the strongly bound pairs, which we call molecules. This is important, because this enables us to condense the molecules into a BEC, it would implode if the interactions were attractive. In between these two weakly interacting limits lies a zone where the interactions are sufficiently strong to form stable pairs, but not yet strongly bound enough to be considered particles on their own. This region has drawn large attention to theorists, because the approximations usually used in many-body theory do not hold anymore, as the parameters around which the approximations are performed are not small.

At the 10$^{\text{th}}$ International Conference on Recent Progress in Many-Body Theories [11], a challenge was posed by George Bertsch:

> What are the ground state properties of the many-body system composed of spin-1/2-fermions interacting via a zero-range, infinite scattering-length contact interaction.

What was thought of as a toy model to describe the behavior of neutron stars, started a large discussion in the field. Furthermore, as a rare exception for neutron star theorists, an experimental realization was possible [12]. In the very center of the crossover that we just described, the fermionic atoms fulfill, at least as a very good approximation, the conditions of this challenge. This means that the crossover forms a link between different parts of physics.

It is this transition, from a bosonic to a fermionic gas, that this thesis is devoted to. As this transition is smooth, it is known in the literature as the *BEC-BCS crossover*.

The pioneering work in the field of fermionic gases started around 1997. The group at JILA had reached quantum degeneracy of ^{40}K [13] in 1998, while the groups at Rice [14] and our group [15] used ^{6}Li and reached quantum degeneracy in 2001, followed by the groups at MIT [16] with ^{6}Li and Florence [17] with ^{40}K. The most important tool to manipulate the atoms, the Feshbach resonance, was found and characterized [18,19]. The next important step was the creation of weakly bound molecules in such a resonance [20]. Our group showed that these molecules are surprisingly long-lived in ^{6}Li [21]. Together with an exact calculation of the scattering length between molecules [22], this laid the foundations for the creation of molecular Bose-Einstein condensate at Innsbruck [23], JILA [24], MIT [25] and our group (see the article in appendix A.1). The condensation of fermion pairs on the BCS side has been shown at

JILA, where they use magnetic field ramps to project these pairs onto molecules on the BEC side [26]. The same group also determined the condensation temperature throughout the resonance region [27].

Various properties of fermionic superfluidity have been studied. In this thesis, we show that the expansion of a cold gas close to zero temperature in the crossover follows the hydrodynamic equations typical of the superfluid phase. The momentum distribution of the particles shows the smoothing predicted by BCS theory. At the same time, the other groups were not lazy: The Innsbruck group reported on the pairing of atoms using a radio frequency spectroscopy technique [28]. In another experiment they showed that collective excitations behave as predicted for a hydrodynamic gas [29]. In precision measurements, they were able to distinguish the basic mean-field BCS theory from more advanced Monte-Carlo simulations [30]. The thermodynamics of a gas in the BEC-BCS crossover was studied by measuring its heat capacity at Duke University [31]. At MIT, the creation of vortices, seen as the first direct proof of superfluidity, was shown [32].

There are other important work carried out besides the BEC-BCS crossover. After the group at JILA localized Feshbach resonances with p-wave symmetry in ^{40}K [33], the group at MIT [34] and our group found them in ^{6}Li as well. This is interesting to compare with superfluid ^{3}He, which also shows p-wave symmetry [35], and not an s symmetry like the Feshbach resonance used in the crossover. This might someday lead to a new BEC-BCS-p-wave-crossover physics. Resonances between different isotopes, described in this thesis, provide a straight forward extension to the field of Feshbach physics, and is nowadays used in many research groups.

A rather different experiment on cold fermionic atoms has been presented by the group at Amsterdam. They performed the Hanbury-Brown and Twiss experiment, which showed photon bunching in light, with metastable, fermionic ^{3}He. In close cooperation with the Orsay group which had performed the same experiment on bosonic metastable ^{4}He [36], they were able to show an anti-bunching effect in fermions [37].

This thesis consists of six chapters: In the current introduction, we gave a general overview of the field. In chapter 2 we present an introduction to the theory of the presented subject, giving a broad overview while focusing on details necessary to understand and interpret the experiments. We will begin with a description of scattering by cold atoms and discuss the Feshbach resonance. Afterwards, we will present a many-body theory of the crossover mostly based on BCS theory. During my thesis, we realized that many experiments were nearly impossible

to perform using our previous experimental setup. We decided to do a major reconstruction of the setup. Chapter 3 will describe these efforts. Chapter 4 is devoted to the techniques needed to interpret our data, which is not always easy as experimental constraints often do not fit to theoretical concepts. The above mentioned reconstruction is still underway, therefore, the results presented in chapter 5 were not performed with the new setup, but still date from the old setup, an exhaustive description of which has been given by my predecessors [38,39]. We will conclude this thesis in chapter 6.

Chapter 2

Theory

Da steh' ich nun ich armer Thor!
Und bin so klug als wie zuvor
– J.W. Goethe, *Faust I*

The theory of cold atomic gases is a very large field, already covered by entire textbooks [40,41]. Here, we want to present the parts that are necessary to understand our experiment. We start with a general introduction into fermionic gases, presenting the most important formulae. We then consider the scattering between atoms as this forms a basis for all the effects we want to study, going more into the details of Feshbach resonances, the main tool used in tuning the scattering properties. Afterwards we will look at the big picture, trying to understand superfluidity using the BCS theory.

2.1 Fermionic gases

In quantum mechanics, all particles can be classified as bosons or fermions, depending on whether their spin is integer or half-integer, respectively. In our experiment we study gases of fermionic ^{6}Li. They can be seen as generic representatives for many kinds of fermions, since, as we will see, their interactions are tunable to match those of other fermionic systems. The choice of Li was not a complicated one: due to their simple electronic structure, alkali atoms are the easiest to cool optically. The only fermionic alkali isotopes with a non-negligible natural abundance are ^{6}Li and ^{40}K (where the latter is already very rare with a natural abundance of around 0,01%). The choice between the two is a matter of preference, both atoms have their specific advantages. We

chose Li because the large abundance of a bosonic and a fermionic Li isotope was appealing, as we can obtain the best of both worlds with only one cooling laser system.

The Li gas we study is very dilute, around 10^{13} atoms/cm^3, and can be described by an ideal fermionic gas whose properties we want to recall in the following. The low density is necessary, since at the temperatures we work, the ground state of our atoms is not gaseous but solid. The gas can relax into this absolute ground state by inelastic collisions. The art of cold atom gases is to stabilize the gas in the metastable state by inhibiting these inelastic collisions. We need at least three atoms in a collision to form a bound pair to conserve energy and momentum. The three-body collision rate increases quadratically with density, this is where the low density comes into play. We can decrease the collision rate further if we bring the atoms into spin states where selection rules forbid collisions.

An ensemble of indistinguishable fermions without interactions follows the Fermi-Dirac statistics, meaning that the probability to occupy a state with energy E is

$$f(E) = \frac{1}{e^{\beta(E-\mu)} + 1} \tag{2.1}$$

where $\beta = 1/k_B T$ is the inverse temperature and μ is the chemical potential needed to fix the number of particles. Looking closely at this distribution, we note that at zero temperature the fermions will occupy all the states below μ and none above. At zero temperature, this μ is called the *Fermi Energy*, $E_F = \mu(T = 0)$. Likewise, we define a Fermi wave vector k_F by $E_F = \hbar^2 k_F^2/2m$, where m is the fermion's mass. In phase space, there is on average one state per volume $(2\pi\hbar)^3$ [42]. If all states below k_F are filled, we can thus calculate the density of the gas as

$$n = \frac{k_F^3}{6\pi^2} \tag{2.2}$$

The simplest way to describe a fermionic gas is the homogeneous case, when there is no potential, and the fermions are just free particles in space. In the experiments, we need to confine the atoms in the minimum of a smooth potential well, which we call a trap. Such traps can, for example, be generated using magnetic fields, or lasers, or both, as we will see in the experimental chapter. In practice, we usually approximate the trap by its Taylor expansion around its minimum up to the quadratic term, leading to a harmonic potential. It is the experimenter's duty to ensure the validity of this approximation.

We normally describe a gas in a harmonic trap using the local density approximation (LDA). In this approximation we assume that the gas locally behaves like a homogeneous gas. We assume the chemical potential μ_0 to be constant over the trap, meaning that

$$\mu_0 = \mu(n(\mathbf{r})) + V(\mathbf{r}) \tag{2.3}$$

where $\mu(n)$ is the equation of state of the homogeneous system. In the case of a noninteracting gas, we can calculate the Fermi energy in the center of the trap as $E_F = \hbar\bar{\omega}(6N)^{1/3}$, where we define $\bar{\omega}^3 = \omega_x\omega_y\omega_z$. Likewise, we can calculate the Fermi wave vector as $k_F = (48N)^{1/6}/a_{ho}$, where a_{ho} is the harmonic oscillator length, $a_{ho} = \sqrt{\hbar/m\bar{\omega}}$. At other points in the trap we can define a local Fermi energy and wave vector, calculated from the density at this point. To avoid confusion, we label them $\tilde{E}_F$ and $\tilde{k}_F$, while we use k_F and E_F always in the sense that we just defined.

We normally use traps where two of the trapping frequencies are nearly the same and higher than the third one. In this case we can assume cylindrical symmetry. We call the radial frequency ω_z and the axial frequency $\omega_\perp$. The cloud will have a cigar-like shape, and we call the ratio between the two frequencies the *ellipticity* $\lambda = \omega_z/\omega_\perp$.

2.2 A reminder on scattering theory

Naively, one would expect that for the low densities we work at, scattering should become negligible. But the opposite is true: the discovery that cold alkali gases do scatter only made quantum gases possible. Experiment and theory heavily depend on it, both positively and negatively. It starts with basic problems: the scattering of cold atoms with a background gas for example can be a major loss process, which calls for an ultra-high vacuum apparatus. It is elastic scattering that makes atoms loose energy during evaporative cooling, while inelastic scattering leads to unwanted losses of the atoms. In theory, all the models we want to realize, like the forming of pairs in a molecular BEC or BCS superfluidity, are directly based on the elastic scattering problem. This is why it is important to understand scattering theory.

A very good description of the theory can already be found in textbooks (see for example references [43, 44]). We will, therefore, concentrate on key parts that are essential to the understanding of our experiments.

2.2.1 The stationary scattering problem

We will start by posing the problem in the form of a Schrödinger equation. Later, we will present a general ansatz for its solution and discuss its general properties. At this point we will focus on the differences between bosons and fermions at ultracold temperatures.

We want to solve the problem of two particles, in our case atoms, scattering against each other. The interaction potential for such a two-body system can, at least in our case, be written as $V(|\mathbf{r}_1 - \mathbf{r}_2|)$ since it depends on the distance between the two particles only. It is convenient to describe the problem in the center of mass frame, where the relative position of the two particles $\mathbf{r} = \mathbf{r}_1 - \mathbf{r}_2$ is the only variable.

We are now left with the problem of solving the stationary scattering problem, that is the time-independent Schrödinger equation $H\psi = E\psi$, with the Hamiltonian $H = \frac{p^2}{2\mu} + V(r)$, and the reduced mass $\mu = \frac{m_1 m_2}{m_1+m_2}$ where m_1 and m_2 are the masses of the atoms. We can now separate out the angular momentum component by invoking the ansatz $\psi(\mathbf{r}) = \frac{\chi(r)}{r} P_l(\cos\theta)$, ($P_l$ are the Legendre polynomials) leaving us with the radial problem

$$\chi'' + \left(\frac{2\mu}{\hbar^2}(E - V) - \frac{l(l+1)}{r^2}\right)\chi = 0 \tag{2.4}$$

The third term in this expression, the angular momentum term, can be considered to be part of the potential V. This means that an angular momentum $l > 0$ forms a centrifugal barrier. The height of this barrier is a few hundred mK. In experiments on cold atoms we reach much lower temperatures, such that normally we have nearly no contribution from partial waves with $l > 0$ and we are limited to s-wave scattering.

The wave function that we wish to calculate is a two-particle wave function. For two identical particles, this wave function has to be symmetric under the exchange of particles for bosons, or anti-symmetric for fermions. If the two particles are in the same internal state, this means that the wave function must be even for bosons or odd for fermions in the center of mass frame. From the properties of the Legendre polynomials, we know that they are even for even l and odd for odd l. This implies that for bosons we only have a contribution from the even waves s, d, ..., while for fermions we only have the odd waves p, f, ... Therefore, indistinguishable ultra-cold fermions hardly scatter, which can lead to problems. As an example, it makes evaporative cooling impossible. One should not forget that there is a simple way to overcome this problem: if the two particles are in different internal states, we can treat them like distinguishable particles. This means that we only have to

bring the fermions into two different internal states, very often different spin states, and there is no reason for them to refrain from scattering.

2.2.2 Scattering at low energies

Here we want to treat the special case of scattering at low energies, as this is the interesting case for cold atoms. A good understanding can be given by comparing the scattered wave function to the case when there is no potential, thus no scattering. In free space, we can describe a moving particle using plane waves $\psi(\mathbf{r}) = \exp(i\mathbf{k}\cdot\mathbf{r})$ [43]. We choose the particles to propagate along the z-axis. The scattered particles can leave in any direction, which we describe using spherical waves. At large distances, we can describe this situation using the wave function

$$\psi(r,\theta) = e^{ikz} + f(\theta)\frac{e^{ikr}}{r} \tag{2.5}$$

where we can ignore the azimuthal angle φ since the problem is symmetric around the axis between the two atoms. $f(\theta)$ is called the *scattering amplitude*, it is 0 if there is no scattering. Integrating $|f|^2$ over a sphere gives a measure of the scattering strength known as the scattering cross section σ.

For large distances compared to the range r_0 of the potential, where we can assume the potential to be 0, the wave function can be written as

$$\chi(r \gg r_0) = \sin(k(r-a)) \tag{2.6}$$

Comparing this with equation (2.5) (see also Landau and Lifshitz, §123 and §132 [43]), where we expand the plane wave in spherical waves, we can calculate the scattering amplitude [45]. We only take the s-wave term of the expansion, as we just saw that this is the only contributing partial wave. Then we find the scattering amplitude to be

$$f = \frac{e^{2ika}-1}{2ik} \approx a \qquad \text{for small } k \tag{2.7}$$

This means that the scattering amplitude is constant for small a. Integrating over θ, one obtains a scattering cross section of $\sigma = 4\pi a^2$. a is called the *scattering length*.

The scattering length is a good tool to "hide" the details of the interatomic potential. However, there are situations in which the shape of the potential does matter. Here we present one rather specific example,

a shape resonance. The treatment is very generic and holds for many scattering problems.

If there is a bound state in the scattering potential very close to the dissociation limit, the scattering length can take on very large values. This is called a shape resonance and the situation is sketched in figure 2.2.2. For large distances r we can neglect the potential V. In this case, a bound state wave function takes the form

$$\chi(r \gg r_0) = Ae^{-r\sqrt{2m|\varepsilon|}/\hbar} \tag{2.8}$$

where ε is the binding energy. At small distances and for cold atoms, we can neglect the total energy E in the Schrödinger equation $\chi'' - \frac{2m}{\hbar^2}U(r)\chi = E\chi$, since the potential energy is much larger. As we have neglected the total energy, all wave functions of low scattering energies are the same, including the bound state. The solutions to this equation must be connected to the solution for large distances at some point, and since this solution does not change much as $r \to 0$, we can do this formally at $r = 0$. We match the logarithmic boundary condition χ'/χ at $r = 0$ for the two limiting cases, equation 2.6 and 2.8 and get

$$\cot ka = -\sqrt{|\varepsilon|/E} \tag{2.9}$$

where E is the energy of the incoming particles, $E = \hbar^2k^2/2\mu$.

Here we see that the scattering length can become very large once the binding energy ε gets small. Our approximation performed in equation (2.7) does not hold anymore, it would lead to infinite cross sections, which has no physical meaning. Instead we can write that [46]

$$f = -\frac{a}{1 - \frac{1}{2}r^*k^2 + ika} \tag{2.10}$$

Here r^* is called the *effective range* of the potential. The effective range term does not follow from equation (2.7) but it is introduced to explain better the behavior at high momentum k. We can use it to explore the limits of our approximations: the effective range is very small in our experiments, and there is a natural cut-off for the momenta, the Fermi momentum k_F, such that the effective range term is normally negligible [47].

However, there are two noteworthy exceptions to this rule. Firstly, the group at Rice University studied the formation of molecules in the narrow Feshbach resonance [48], see the next section, where the effective range is large and negative, which complicated the interpretation of their data.

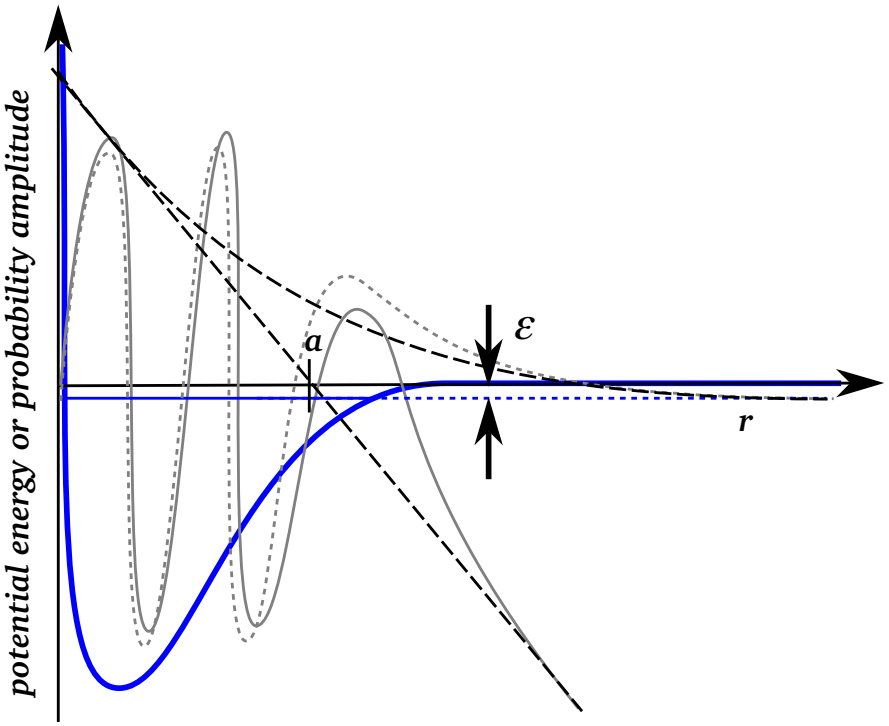

Figure 2.1: A sketch of a shape resonance. A bound state with binding energy ε is located just below the dissociation energy in the potential (thick solid line), its wave function is drawn as a grey dotted line, it exponentially decays for large distances r. The free state symbolized by the solid line is very close to the bound state, for large distances it will become a sine function with a very long wavelength. One extends the bound state exponential and free state sine function to the origin, as if there was no potential, drawn as dashed lines, and connects them there (The lower dashed line is not a straight line but the beginning of a sine with a very long wavelength). The distance where this extended wave function crosses zero is the scattering length a.

Secondly, before the gas is evaporatively cooled, the atoms also have a large momentum k. In ^{7}Li, the scattering cross section σ vanishes for energies around 6,6 mK, making evaporative cooling difficult to achieve as described in the thesis of Florian Schreck [38].

Such a bound state close to resonance exists for some atoms, like Cesium. It even exists in Lithium, but there the situation is more complicated, as we will see in the next section. There, we will also see that there is a way of artificially moving a bound state close to dissociation.

The treatment shown here thus far is very generic. The "bound state" could be above the dissociation limit, meaning that there is actually only a *virtual bound state*. While the physical notion of a bound state is incorrect in this situation, the presented calculation is still valid, as we abstract completely from the scattering potential, replacing it by a simple boundary condition at the origin.

We can artificially construct a pseudo potential, which imposes this boundary condition:

$$V(\mathbf{r}) = 2\pi\frac{\hbar a}{\mu}\delta(\mathbf{r})\frac{\partial}{\partial r}r \tag{2.11}$$

This pseudo potential is often used in many-body theory [49]. It leads to the same results as those presented in this thesis, see for example reference [50].

2.3 Feshbach resonances

In the last section it was mentioned that in order to get the fermionic atoms to scatter in the first place, we have to put them into two different internal states. For most of our experiments, we chose the two lowest Zeeman sub-levels of the atoms. In figure 2.2 we see that $|F = 1/2, m_F = 1/2\rangle$ and $|F = 1/2, m_F = -1/2\rangle$ are the lowest energy states at zero magnetic field. At high fields, this notion looses its meaning, so we simply use $|1\rangle$ and $|2\rangle$ as names for these two states. This mixture is stable against losses through inelastic collisions. As we have to conserve the total spin during the scattering process, the resulting pair after an inelastic collision would have a momentum $l = 1$, which is suppressed by the centrifugal barrier.

When two atoms are far apart, we can treat them as independent particles. We normally sum the angular momenta and spins of all the electrons and the nucleus, and consider the atom as a single particle with

a total angular momentum. Nevertheless, as the electrons of both atoms are indistinguishable, we have to anti-symmetrize their wavefunctions. When they are far apart, this hardly changes anything: the wavefunction of the two electrons overlap only negligibly, such that we can neglect the changes due to anti-symmetrization. During the scattering process, however, the atoms sufficiently approach each other for the electronic wavefunctions to overlap. This calls for a different treatment of the electrons, we would like to sum their spins, leading to singlet and a triplet state. Therefore, we introduce two different interaction potentials between the two atoms, one for the singlet, one for the triplet state, which is the antisymmetric or symmetric spin-wavefunctions, respectively. The two potentials coincide at large distances, as there the exchange and spin-spin interactions vanish, as described above.

Nevertheless, the electrons are still coupled to their nuclei. This means that the singlet and the triplet potentials are also coupled. Whenever a scattering process couples internal states of the scattered particles, this, in general scattering theory, is called coupled *channels*. We can treat such coupled channels by defining one scattering potential for each channel and say that the scattering particles are in a superposition of their internal states at every distance. In our case, the energy of the atoms is sufficiently low that the internal states of the atoms will not be changed while scattering. This means that at large distances the atoms are only in the lowest energy state and we call such a channel *open* as opposed to the *closed* channels, which only have an importance during the scattering process.

In our case, there are two different channels: the singlet and the triplet state of the electrons, shown in figure 2.3. As the singlet state has a total spin **S** of 0, only the triplet state can have magnetic quantum number $M_S \neq 0$, therefore, only the triplet state can couple to a magnetic field. For the lowest Zeeman states, the states we use for our experiments, the Zeeman effect will shift down the state with $M_S = -1$. In our case this is then the lowest energy state and the only open channel.

The singlet potential contains a bound state which is close to the dissociation limit. Using a magnetic field, we can shift down the triplet state until the continuum is at the same level as the weakly bound state in the singlet channel. The energy of the bound state and its dependence on the magnetic field is shown in figure 2.4. The existence of a bound state close to the dissociation limit drastically changes the scattering length of the atoms. From the theoretical standpoint, we have a bound state coupled to a continuum of scattering states. This was treated independently in nuclear physics by Feshbach [53] and in atomic physics

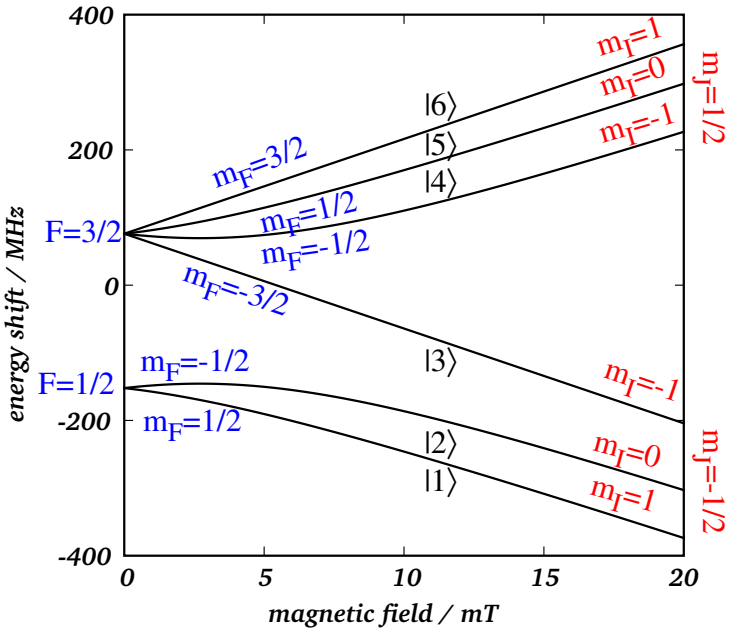

Figure 2.2: The energy levels of Lithium-6. For low magnetic fields we have a Zeeman effect, the total spin F of the atoms couples to the magnetic field. For high magnetic fields we are in the Paschen-Back regime, where the nuclear spin I and the total electron spin J decouple. In the center, we show the usual convention to give a number to each state.

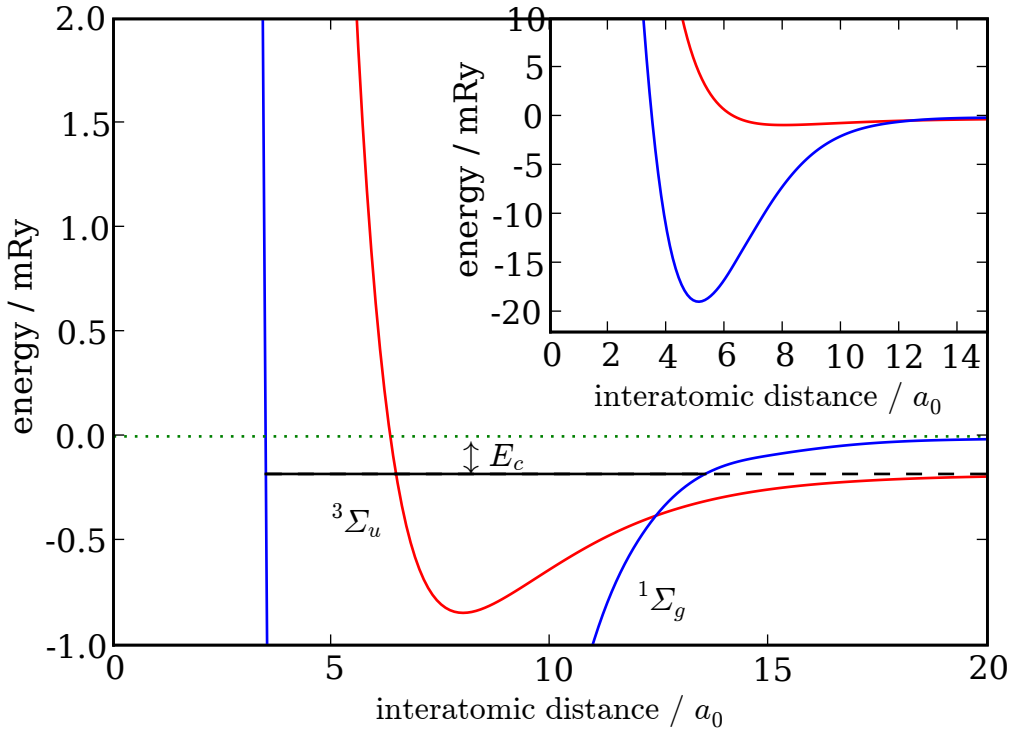

Figure 2.3: The two scattering potentials involved in the Lithium-6 Feshbach resonances. $^3\Sigma_u$ is the triplet, and $^1\Sigma_g$ is the singlet state. The singlet state contains bound states. The triplet state can be shifted using a magnetic field. Here, we show a shift down such that the dissociation energy of the triplet potential coincides with the bound state in the singlet state. This is what happens close to a Feshbach resonance. The binding energy E_c is not to scale, in reality the bound state is so close to dissociation that the difference would not be visible in this graph. The insert shows the overall picture at zero magnetic field. Data adopted from references [51,52].

by Fano [54], and is known in cold atoms as a *Feshbach resonance*.

The bound state in the singlet potential exists in different flavors. The total nuclear spin I leads to an energy shift, splitting the singlet potential into two, resulting in two Feshbach resonances. The same bound state exists also in the p-wave scattering potential, where it is shifted because of the centrifugal barrier mentioned above. As p-wave scattering is allowed even for fermions in the same internal state, they couple to all possible combinations of two atoms in the shown states, as shown in the inset of figure 2.4.

The different couplings call for a rather complicated coupled-channel treatment, as found in reference [47]. Here we choose a more simplified model potential [55,56], which we can actually calculate analytically. For the open channel, we choose a spherical potential well of depth $\hbar^2 q_o^2/m$ with an interaction range r_0, while we use a spherical box for the closed channel, where the bottom of the box is at $\hbar^2 q_c^2/m$ as, depicted in figure 2.5. We assume a coupling term Ω between the two potentials. This is much weaker than the short range potential between the atoms, so we can suppose that $\Omega \ll q_{o/c}^2$. This gives the Schrödinger equation

$$\frac{\hbar^2}{m}(-\nabla^2 + V)|\psi\rangle = E|\psi\rangle \tag{2.12}$$

$$\text{with } V = \begin{cases} -\begin{pmatrix} q_c^2 & \Omega \\ \Omega & q_o^2 \end{pmatrix} & \text{for } r < r_0 \\ \begin{pmatrix} 0 & 0 \\ 0 & \infty \end{pmatrix} & \text{for } r > r_0 \end{cases} \tag{2.13}$$

In the limit of zero scattering energy $E = 0$, and setting $\chi(r) = \frac{\psi(r)}{r}$ as above, we can write the general solution to this problem as

$$|\chi\rangle = (r - a)|o\rangle \qquad \text{for } r > r_0 \tag{2.14a}$$
$$|\chi\rangle = \cos\phi \sin(q_+ r)|+\rangle + \sin\phi \sin(q_- r)|-\rangle \qquad \text{for } r < r_0 \tag{2.14b}$$

a is the scattering length, $q_\pm$ are determined by inserting equations (2.14) into the Schrödinger equation. ϕ is fixed by the boundary conditions. $|o\rangle$ denotes the open channel, as $|c\rangle$ will denote the closed one. $|\pm\rangle$ are defined by

$$\begin{aligned} |+\rangle &= \cos\theta|o\rangle + \sin\theta|c\rangle \\ |-\rangle &= -\sin\theta|o\rangle + \cos\theta|c\rangle \end{aligned} \tag{2.15}$$

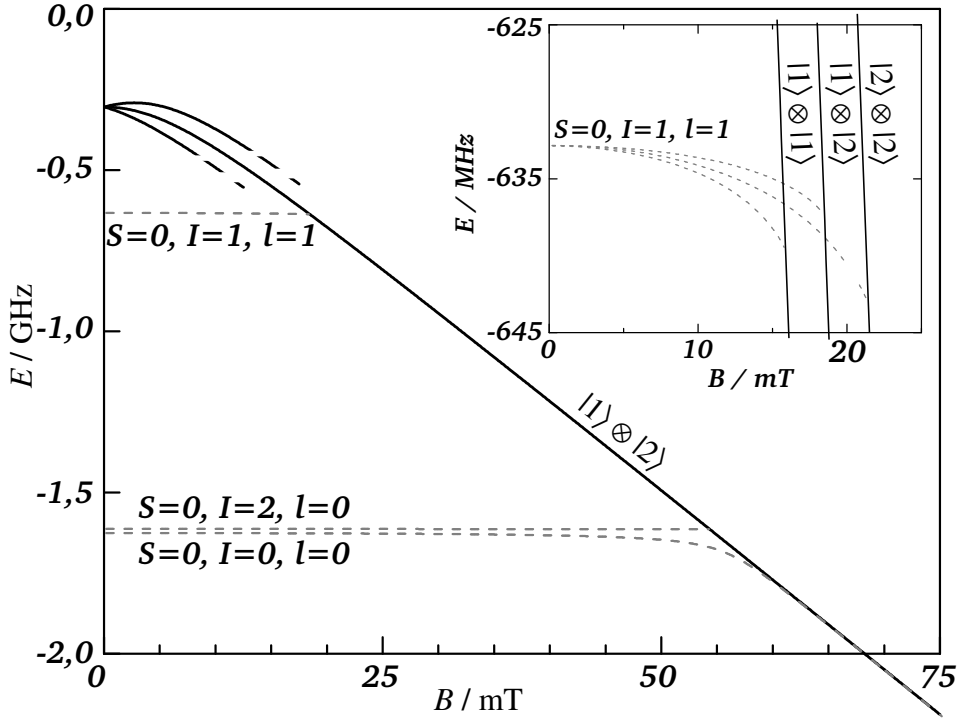

Figure 2.4: The bound states and the continuum state. The solid line is the Zeeman shift for two atoms, where the atoms are in the two lowest Zeeman states. The curves are essentially the sum of two curves of figure 2.2, the notation corresponding to that figure. The dashed lines are the bound states in the scattering potential. The total electronic spin is $S = 0$, as it is the singlet state. This is why the energy is independent of the magnetic field. The two lower states are the s-wave ($l = 0$) bound states. They differ in the orientations of the nuclear spins. Due to a coupling of the atomic state to the $I = 0$ s-wave state, close to the crossing, the states shift in energy. The same effect exists for the $I = 1$ state, but is much smaller, invisible on the scale of this figure. The p-wave ($l = 1$) states correspond to a higher rotational state of the same molecular bound state.

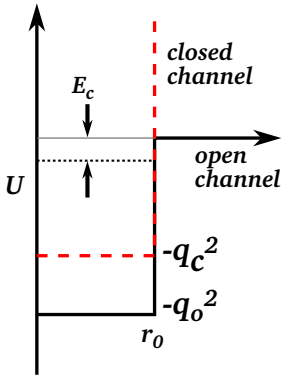

Figure 2.5: The potentials of the model described in the text. The dotted line is the bound state in the closed channel.

Inserting this into the Schrödinger equation gives $\tan 2\theta = 2\Omega/(q_o^2 - q_c^2)$. As the coupling Ω is small, the mixing angle θ will be small as well. We do not want any atoms outside the box in the closed channel, giving the boundary condition $\chi(r_0)|c\rangle = 0$, which enables us to calculate ϕ as

$$\tan\phi = -\tan\theta \frac{\sin q_+ r_0}{\sin q_- r_0} \tag{2.16}$$

For the open channel, we need to connect the two wave functions. We do this by setting the logarithmic derivative χ'/χ equal on both sides of the equation to give:

$$\frac{1}{r_0 - a} = \frac{q_+ \cos^2\theta}{\tan q_+ r_0} + \frac{q_- \sin^2\theta}{\tan q_- r_0} \tag{2.17}$$

The last term is usually small, as θ is small, but it can become very large if there is a bound state in the closed channel near the continuum of the open channel.[1] If this bound state has a binding energy of E_c, then its wavefunction vanishes at r_0, such that $n\pi = \sqrt{q_c^2 + \varepsilon_c} r_0 \approx q_c r_0 (1 + \varepsilon_c/(2q_c^2))$, where we have defined $\varepsilon_c = 2mE_c/\hbar^2$. The small coupling Ω leads to $q_- \approx q_c$, and we can approximate the denominator of the last term of equation (2.17) as $\tan q_- r_0 \approx \tan q_c r_0 \approx \tan(n\pi - r_0\varepsilon_c/2q_c) \approx -r_0\varepsilon_c/2q_c$.

At the same time, the middle term of equation (2.17) can be considered constant, since θ is small. It can be identified as a background scattering length a_{bg}. These simplifications lead us to the important equation

[1] We are indeed talking about the bound state in the closed channel – the two channel molecular states of the atoms, also known as the dressed state, will be discussed later.

relating the scattering length with the energy difference of the bound state:

$$\frac{1}{a - r_0} = \frac{1}{a_{bg} - r_0} + \frac{\gamma}{\varepsilon_c}, \tag{2.18}$$

where $\gamma = 2q_c^2\theta^2/r_0$ is a constant that contains the details of the potentials, i.e., the Feshbach coupling strength.

As described above, we can shift the energy levels by varying the magnetic field. We do so by replacing E_c by $E_c + \mu B$, with μ being the difference of the magnetic moments of the singlet and triplet state. In our case, $\mu = 2\mu_B$ [55]. The scattering length can then be written as

$$\frac{a}{a_{bg}} = 1 + \frac{\Delta B}{B - B_{res}} \tag{2.19}$$

where the resonance position B_{res} and the resonance width ΔB are

$$\begin{aligned} B_{res} &= -\frac{E_c}{\mu} + \Delta B \frac{a_{bg}}{a_{bg} - r_0} \approx -\frac{E_c}{\mu} + \Delta B \\ \Delta B &= -\frac{\hbar^2}{2m\mu}\gamma \frac{(a_{bg} - r_0)^2}{a_{bg}} \approx \frac{\hbar^2}{2m\mu}\gamma a_{bg} \end{aligned} \tag{2.20}$$

From the first formula, it can be seen immediately that the resonance is not at the position where the bound state crosses the continuum but at a magnetic field of ΔB higher.

The situation in lithium is certainly more complicated than the model just presented. It turns out that there is not only a bound state close to dissociation in the singlet channel, our closed channel, but also one in the triplet channel, our open channel. This leads to an unusually large background scattering length a_{bg}. As a surprise, just next to the predicted Feshbach resonance, another very narrow one was found at 54,325 mT [19]. The two resonances correspond to different values of the total nuclear spin, as shown in figure 2.4. It was intensely studied at Rice [48]. Our group normally uses the large resonance around 83 mT. We can describe both resonances with the presented model by using different parameter sets for each resonance. The parameters are shown in table 2.1. A complete treatment of the Feshbach resonance including the open channel resonance can be found in reference [57]. Figure 2.6 shows the dependence of the scattering length on the magnetic field.

Historically, experiments using the Feshbach resonance as a tool were often clouded by the uncertainty of the scattering length in the Feshbach resonance. However, recent precision measurements have cleared the situation: the group in Innsbruck claims in reference [58]

resonance	r_0/a_0	B_{res}/mT	ΔB/mT	a_{bg}/a_0	μ/μ_{B}	$\gamma^{-1/3}/a_0$
broad	29,9	83,415	30	-1405	2,0	101
narrow	29,9	54,326	-0,1	61,6	2,1	400

Table 2.1: The parameters of our model for the broad and narrow Feshbach resonances, from reference [55]. a_0 is the Bohr radius, $a_0 = 0{,}53 \cdot 10^{-10}\,\mathrm{m}$, and μ_{B} is the Bohr magneton, $\mu_{\mathrm{B}} = 9{,}3 \cdot 10^{-24}\,\mathrm{J/T}$.

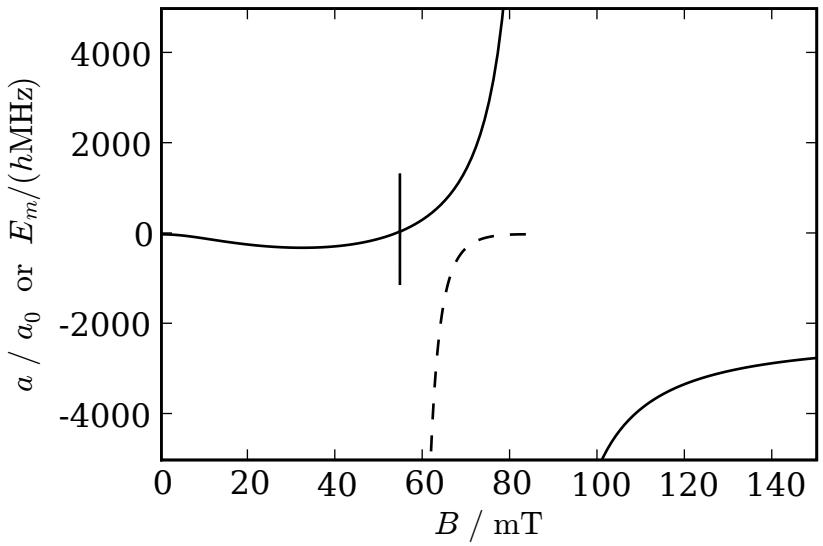

Figure 2.6: The scattering length a (solid line) and the molecular binding energy E_m (dashed line) by the magnetic field. The large resonance is centered at 83 mT. The narrow resonance at 54,325 mT is depicted by the vertical bar, it is too narrow to be shown otherwise. The scattering length crosses zero at 52,8 mT [19].

to fit the real scattering length with an accuracy better than 99% in the relevant range from 60 mT to 120 mT using the empirical formula

$$a = a_b \left(1 + \frac{\Delta}{B - B_0}\right)(1 + \alpha(B - B_0)) \tag{2.21}$$

with the fitted parameters $a_b = -1405a_0$, $B_0 = 83{,}4149\,\mathrm{mT}$, $\Delta = 30{,}0\,\mathrm{mT}$ and $\alpha = 0{,}0040\,\mathrm{mT}^{-1}$.

On the left side of the resonance, the existence of the bound state in the closed channel close to resonance leads to a molecular state of atom pairs. One should not get confused between the two: the bound state exists only in the closed channel. The molecular state which we are about to discuss, on the other hand, is a state that depends on both channels and is a stable state that can be occupied for macroscopic time scales.

Certainly, the molecular state is also a bound state in the sense that its wave function vanishes at large distances, leading to an exponentially decaying wave function

$$|\chi\rangle = \mathrm{e}^{-\sqrt{\varepsilon_m}r}|\mathrm{o}\rangle \text{ for } r > r_0 \tag{2.22}$$

where $-E_m = -(\hbar^2/m)\varepsilon_m$ is the binding energy of the molecule ($E_m > 0$), and the only change we have to apply to equation (2.14b) is to replace the wave vectors q by $\bar{q}_\pm^2 = q_\pm^2 - \varepsilon_m$, and the mixing angle ϕ by $\bar{\phi}$. Hence, (2.17) becomes

$$-\sqrt{\varepsilon_m} = \frac{\bar{q}_+ \cos^2\theta}{\tan \bar{q}_+ r_0} + \frac{\bar{q}_- \sin^2\theta}{\tan \bar{q}_- r_0} \tag{2.23}$$

Using the same approximations as above, we can calculate the molecular binding energy as

$$-\sqrt{\varepsilon_m} = \frac{1}{r_0 - a_{bg}} + \frac{\gamma}{\varepsilon_c + \varepsilon_m} \tag{2.24}$$

plotted in figure 2.6. If the molecular binding energy is small, we can compare this to equation (2.18). This gives us a simple relation between the scattering length and the binding energy:

$$E_m = \frac{\hbar^2}{ma^2} \tag{2.25}$$

This is the same result we get from a single channel calculation from equation 2.9. As long as the effective range r_0 is sufficiently short, we can use an effective single channel model in most cases.

2.4 BCS theory

When Bardeen, Cooper and Schrieffer (BCS) [9] presented their theory of superconductivity back in 1957, it was an important breakthrough for the microscopic description of superconductors. As a core of their theory they proposed a many-body ground state that incorporates pairing between electrons. They showed that it is this pairing which is the origin of superconductivity. Later, Eagles [59] and Leggett [60] realized that the BCS ground state is more general and can be used to describe more than just superconductivity. They realized that at large interaction strengths (compared to the Fermi energy), the diameter of a pair will become small and the pairs can be seen as independent bosons which may condensate into a Bose-Einstein condensate. As an important detail, this means that the condensation temperature and the pair binding temperature will not be the same as is the case in normal BCS theory. This also means that there is an intermediate region, a crossover between BCS-type pairing and Bose-Einstein condensation.

Large attention has been drawn on this subject after Randeria *et al.* suggested that such a crossover could be used to describe high critical temperature T_c superconductors [61]. They extended an older theory by Nozières and Schmitt-Rink, which treated the crossover for non-zero temperatures [62]. Shortly after Bose-Einstein condensation in cold atomic gases had been achieved, experimenters began working on obtaining a superfluid state also in fermionic gases, bearing in mind that the only ingredient necessary for BCS theory is an attractive interaction, which is easily achievable by means of a Feshbach resonance. Reaching low temperatures, however, turned out to be a bigger obstacle. Later, Holland *et al.* [10], following the theory by Randeria [61], predicted that the transition temperature in the crossover may become sufficiently high to be achieved in cold atoms, which created excitement in the community and hence the interest in this area.

2.4.1 The BCS ground state

The breakthrough of BCS was the realization that superconductivity can only be described using a theory that takes pair correlations between particles into account. Now we want to show the Hamiltonian they used to describe such a system and the ground state wavefunction they found.

We have fermions of two different spin states, which we call $\uparrow$ and $\downarrow$. They do not need to be spin-up and spin-down, any two different spin states will do. Atoms in these spin states interact via a potential U. In

second quantization, this is written as

$$H = \sum_{k,\sigma} \varepsilon_k a^\dagger_{k\sigma} a_{k\sigma} + \sum_{k,k'} U_{k,k'} a^\dagger_{-k'\downarrow} a^\dagger_{k'\uparrow} a_{k\uparrow} a_{-k\downarrow} \tag{2.26}$$

where $a^\dagger$ and a are the creation and annihilation operators, and the kinetic energy is $\varepsilon_k = \hbar^2\mathbf{k}^2/2m$. One immediately sees that in the last term, the interaction term, we only take into account pairs of atoms with opposite momentum. Conservation of energy and momentum must be satisfied in the interaction, which gives atoms of opposite momentum more possibilities to scatter than other pairs of atoms, as they can scatter in the whole sphere of same energy. Their interaction terms, therefore, dominate the total interaction, justifying our approximation. Normally however, the last term, the interaction term in the Hamiltonian, averages to zero also for atoms of opposite momentum. This is due to the Fermi-Dirac statistics, which alternates in sign under the exchange of particles. It might be instructive to try to write down a wave function where the interaction term does not cancel.

BCS deserve the credit to have found a state with an important contribution from the interaction term. Their idea is to construct a wave function which is a superposition of configurations where the atoms always occupy the momentum states in pairs, meaning that if there is one atom with momentum $\mathbf{k}$, there is also an atom with momentum $-\mathbf{k}$. This BCS ground state is

$$|\psi_{\text{BCS}}\rangle = \prod_k (u_k + v_k a^\dagger_{k\uparrow} a^\dagger_{-k\downarrow})|0\rangle \tag{2.27}$$

The v_k and u_k are the probability amplitudes that a pair state is occupied or not. For simplicity, they can be taken as real[2], and normalization yields $u_k^2 + v_k^2 = 1$. One notices that this wave function does not conserve the number of particles. We describe the system in the grand canonical ensemble. Efforts have been made to calculate the BCS problem without using the grand canonical ensemble, but it has turned out to be cumbersome at best and did not reveal any new physics [63].

2.4.2 The gap and number equations

Now we need to calculate the parameters u_k and v_k. We do this by minimizing the free energy $F = H - \mu N$, leading to $2u_k^2 = 1 + \xi_k/E_k$ and

[2]One can introduce a phase ϕ by $v_k = |v_k|e^{i\phi}$, which gives a macroscopic phase of the wave function and is needed to describe effects like the creation of vortices or Josephson junctions

$2v_k^2 = 1 - \xi_k/E_k$, $\xi_k = \varepsilon_k - \mu$, $E_k^2 = \xi_k^2 + \Delta_k^2$ and $\Delta_k = \sum_{k'} U_{k,k'} u_{k'} v_{k'}$. ξ_k is the energy of a particle measured from the Fermi level, which is the natural way to measure energies in the grand canonical ensemble. E_k can be understood as the energy of a quasi-particle (low-lying excited state of a system due to its response to an external perturbation). From its definition, we see that the minimum excitation energy is Δ_k. This is the excitation gap found in experiments.

This can be written in the form of the following two important equations, the gap-equation and the number-equation:

$$\Delta_k = \sum_{k'} U_{k,k'} \frac{\Delta_{k'}}{\sqrt{\xi_k^2 + \Delta_{k'}^2}} \tag{2.28}$$

$$N = \sum_k \frac{1}{2} \left(1 - \frac{\xi_k}{\sqrt{\xi_k^2 + \Delta_k^2}} \right) \tag{2.29}$$

2.4.3 Renormalization

Let us now consider the potential U. Certainly, it originates from our Feshbach resonance, but how is it related? Usually, this potential is taken to be constant, which on one hand allows for important simplifications in the calculations, but also leads to an ultraviolet divergence. In superconductors, one usually uses an energy cut-off at the Debye frequency to overcome this divergence.

Taking the potential U as constant is also a viable approach in our case. In real space the potential has a very small effective range, meaning that its Fourier transform, this is the $U_{k,k'}$ used in the BCS Hamiltonian (2.26), is nearly constant. In order to connect this potential to the theories we developed in the last sections, we calculate the scattering length of such a constant potential, and equate it to the one found for the Feshbach resonance.

In formal scattering theory, we use the T-matrix instead of the scattering amplitude, which is defined as $-\frac{V}{4\pi}\frac{2m}{\hbar^2}\langle \mathbf{k}|T|\mathbf{k}'\rangle = f(\mathbf{k} - \mathbf{k}')$, where V is the quantization volume. The T-matrix can be calculated as [44]

$$T(E) = U + UG(E)U + UG(E)UG(E)U + \cdots \tag{2.30}$$

where G is the resolving operator $G(E) = (E - \hbar^2 k^2/m)^{-1}$. Since U is taken to have constant elements, the second term on the right side in equation (2.30) can easily be calculated as

$$\langle \mathbf{k}|UG(E)U|\mathbf{k}'\rangle = \sum_{\mathbf{k}''} \langle \mathbf{k}|UG(E)|\mathbf{k}''\rangle\langle \mathbf{k}''|U|\mathbf{k}'\rangle = U^2 \sum_{\mathbf{k}} \frac{1}{E - \frac{\hbar^2 k^2}{2m}} \tag{2.31}$$

The other terms can be calculated in a similar manner. This way, we can calculate the whole sum as

$$\langle \mathbf{k}|T|\mathbf{k}'\rangle = U + U^2\Sigma + U^3\Sigma^2 + \cdots = \frac{U}{1 - U\Sigma} \tag{2.32}$$

where Σ is the sum over $\mathbf{k}$ in (2.31). We can now calculate the scattering length in the limit of small energies. We set $E = 0$ in equation (2.31) and remember that $f \approx a$ for low energies and get

$$\frac{m}{4\pi\hbar^2 a} = \sum_{\mathbf{k}} \frac{m}{\hbar^2 k^2} - \frac{1}{U} \tag{2.33}$$

One sees that the sum on the right side of this equation does not converge, but this is intentional: it exactly compensates the divergence in the gap equation. This technique is called *renormalization*. It is also possible to use the pseudo potential introduced in section 2.2.2 [64]. That technique leads to the same result. One might also note that this equation has a very similar form to equation (2.18). This gives a physical meaning to the two terms on the right hand side: the diverging part is the contribution from the background scattering length, while the interaction in the BCS theory is nothing else than the Feshbach coupling term.

As we have taken the potential to be constant, the gap Δ will be a constant as well. We divide the gap equation (2.28) by U and Δ and equate it to equation (2.33) and get the renormalized gap equation

$$\frac{m}{4\pi\hbar^2 a} = \frac{1}{2V}\sum_k \left(\frac{1}{\varepsilon_k} - \frac{1}{\sqrt{(\varepsilon_k - \mu)^2 + \Delta^2}} \right) \tag{2.34}$$

When working with cold atoms, it is easier to deal with densities rather than with number of atoms. This is easily done by dividing by the quantization volume. The number equation (2.29) then becomes

$$n_\sigma = \frac{1}{2V}\sum_k \left(1 - \frac{\varepsilon_k - \mu}{\sqrt{(\varepsilon_k - \mu)^2 + \Delta^2)}} \right) \tag{2.35}$$

We can now think about the physical meaning of the two equations. The gap equation gives a relation between the energy gap Δ and the chemical potential μ. Using this relation and the number equation we can then fix the chemical potential. Once we have calculated both parameters, we can go back to the BCS ground state (2.27). We can

now calculate the parameters v_k, and remember that this probability amplitude of the occupation of a momentum state. In the end we see that this is the same as removing the sum in the number equation 2.35, which gives us the momentum distribution., which gives us the momentum distribution.

2.4.4 Results

The BCS theory gives a good qualitative description of the whole crossover. In figure 2.7 we show the behavior of the chemical potential μ and the gap Δ at zero temperature in the crossover. While for a deep BCS state with weak interactions the chemical potential coincides with the Fermi energy, it decreases while crossing the resonance and even becomes negative on the BEC side, and eventually becomes asymptotically equal to the binding energy of the molecules. The Fermi edge washes out, as can be seen in figure 2.8, and once the chemical potential crosses zero it disappears completely. This illustrates that the pairs are not governed by the Fermi-Dirac distribution anymore, but follow the Bose-Einstein statistic and thus can be considered bosons. The gap, normally small in superconductors, opens up.

The critical temperature can also be deduced from BCS theory, usually by calculating the temperature T^* at which the gap vanishes, see references [65,66]. This is the dashed curve in figure 2.9. As we already stated, the pair creation and condensation do not coincide for strong interactions [59]. This becomes clear once we are on the BEC side of the crossover: the molecules exist even at higher temperatures and only condense into a BEC below a critical temperature T_c [60]. A similar effect is seen in high temperature superconductors and is known as the *pseudogap* [67,68].

This critical temperature was first studied by Nozières and Schmitt-Rink (NSR) [62]. They realized that the BCS approximation to only take pairs with zero momentum into account will fail at strong interactions, and considered thermal motion of bound molecules. A recent theoretical calculation, which agrees well with NSR, is shown in figure 2.9 together with experimental measurements. Further studies, which took beyond mean field fluctuations into account, revealed that the maximum visible in the figure should not exist, but the condensation temperature should increase steadily [69].

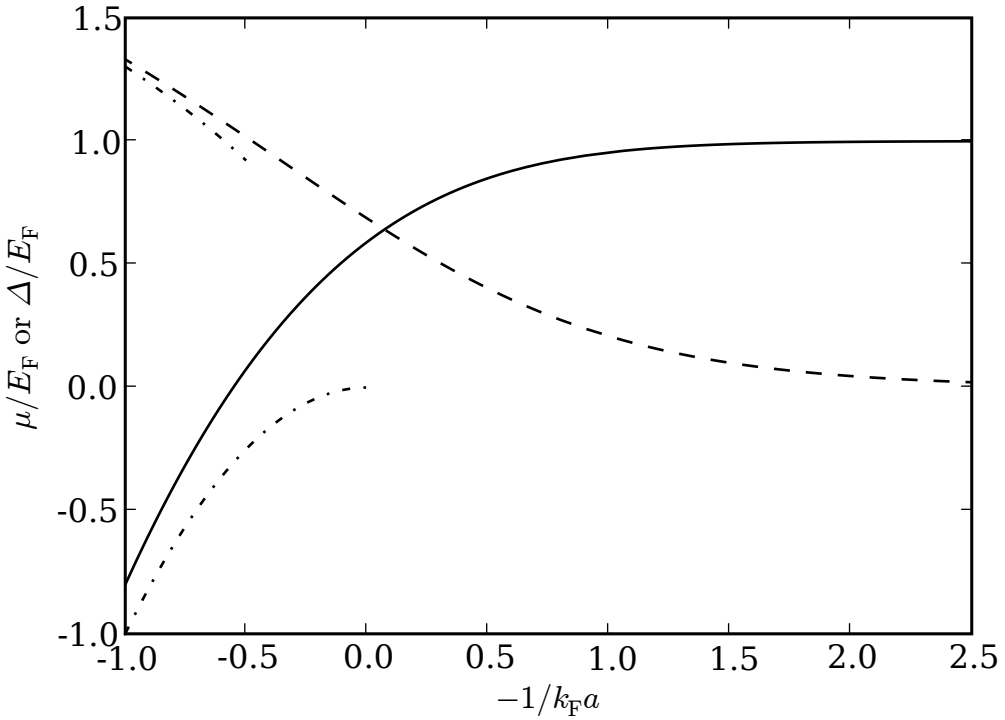

Figure 2.7: The gap Δ (dashed line) and the chemical potential μ (solid line) in the BEC-BCS crossover. The small dash-dotted lines are the approximations that we will discuss in section 5.1.3. The lower line corresponds to the binding energy of a molecule. In the experiment the parameter $1/k_F a$ decreases with increasing magnetic field, therefore, we introduce the minus sign in the abscissa to give the graph the same orientation as the graphs of the Feshbach resonance.

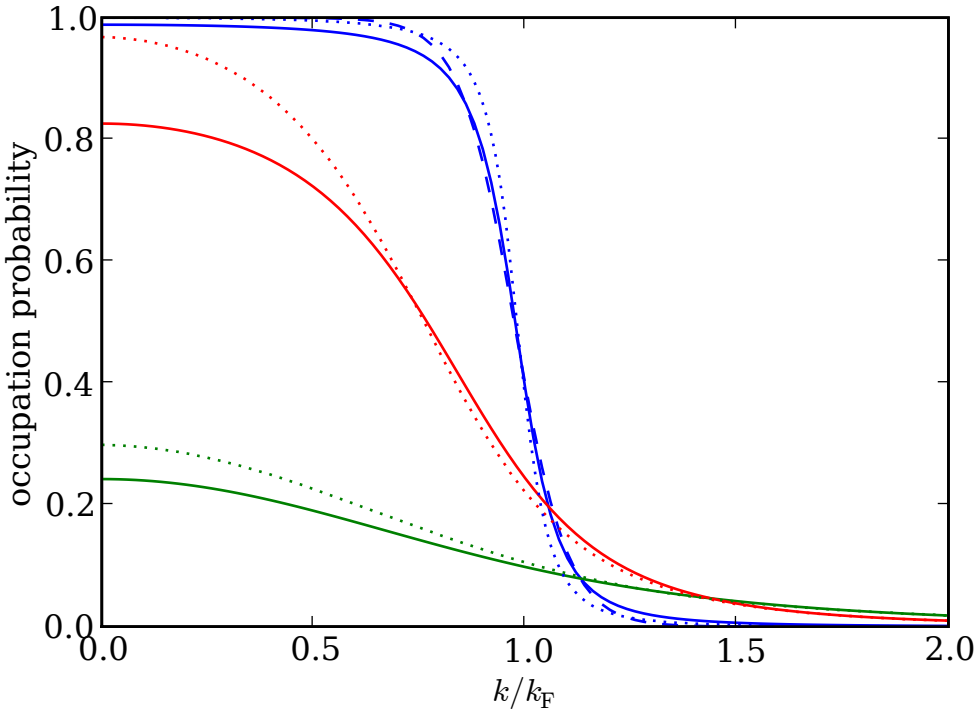

Figure 2.8: The momentum distribution in a homogeneous gas in the different limits of BCS theory. On the top the BCS limit, $k_F a = -1$. The dashed line shows a Fermi gas at the critical temperature for comparison. The center line is the unitarity limit ($1/k_F a = 0$) and the bottom line is the BEC limit ($k_F a = 1$). The dotted lines are the predictions from Astrakharchik *et al.* [70].

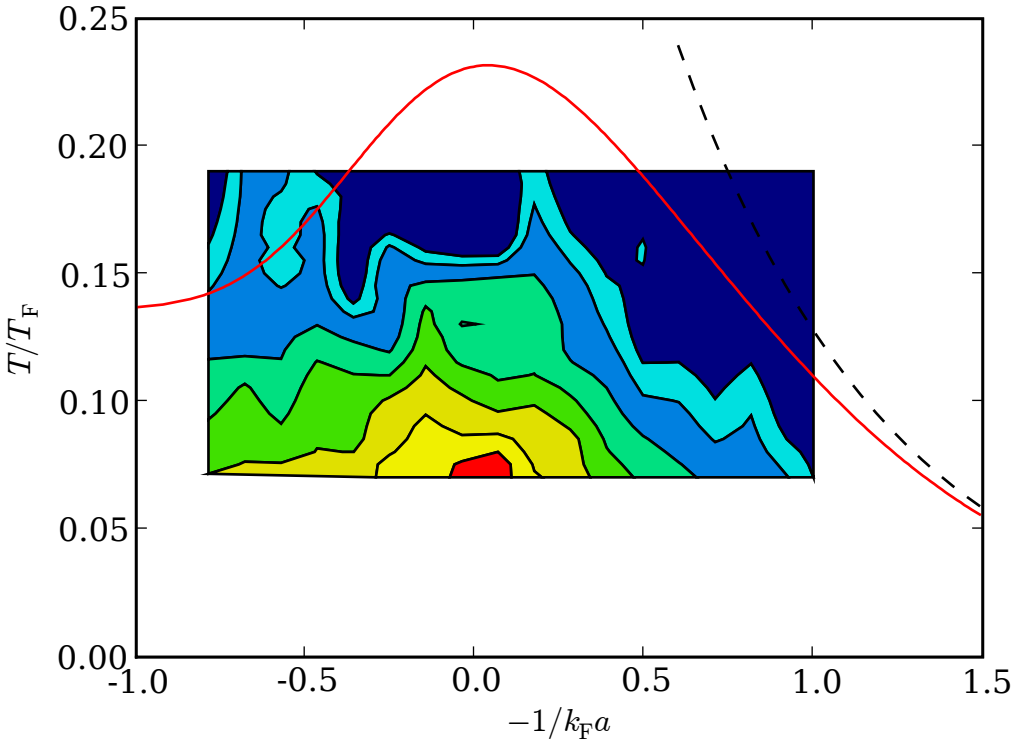

Figure 2.9: The transition temperature in the BEC-BCS crossover (solid line). The data in the background is a measurement taken in ^{40}K of the condensate fraction. Both theory and data is by Chen *et al.* [27]. The colors correspond to a condensate fraction between 0 (dark blue) and 15,5% (red). The curve is higher than the data since they could not measure a condensate fraction below 1%. The dashed line shows the transition temperature used to describe normal superconductors, it is the temperature below which pairing begins.

2.4.5 Beyond BCS theory

The use of BCS theory throughout the whole BEC-BCS crossover by Leggett was a bit adventurous, since the BCS approximations only hold for small attractive interactions. Nevertheless, his approach was justified later as his theory is a self-consistent theory which predicts experiments at least qualitatively.

This success had raised the bar for further theoretical research. The problem is indeed challenging: with the interactions being strong, we loose the last small parameter and approximations that hold on one side of the crossover not necessarily do so on the other.

The center of the crossover, where the scattering length diverges, is the best studied part. In general we can say that the chemical potential is proportional to the Fermi energy, where the proportionality depends on the scattering length, such that $\mu = f(1/k_F a)E_F$. At the center of the resonance a diverges, and we are left with a constant which is traditionally called $1 + \beta = f(0)$.

This β is independent of BCS theory, thus β is a meaningful constant even without BCS theory, in this meaning it can be considered universal. Therefore, it can be used as a test for BCS or beyond BCS theories. Furthermore, the definition does not contain any details on the interaction potential. It is thus valid even outside atomic physics, and indeed it is used in other fields, like the physics of neutron stars [11] or the quark-gluon plasma [7]. There has recently been a large effort, both theoretically and experimentally, to determine the value of β.

A first approximation is to calculate β from BCS theory by solving the gap equation, which results in $\beta = 0{,}41$. In our group, in order to determine β, we measured the energy released by a gas while expanding. The energy can be calculated from the size of the cloud. In a harmonic trap, the released energy is then $E_R = \sqrt{1+\beta}E_R^0$, where E_R^0 is the value for a gas without interactions. The square root comes from averaging over the trap, as described in the thesis of Julien Cubizolles [71]. The resulting values for β are described in the thesis of Thomas Bourdel [65], as well as in the paper in appendix A.1. There, we find a result of $\beta = -0{,}64(15)$. This value was based on a resonance position of 82 mT. Later, the position was more precisely determined to be 83 mT [58], such that we obtain a more accurate value of $\beta = -0{,}59(15)$, as written in the paper in appendix A.5. Similar to our work, the group in Innsbruck studied the size of the atomic cloud in the trap without releasing the atoms [72]. This is also a measure for β and after a correction similar to ours they obtained a value of $\beta = -0{,}73^{+12}_{-09}$ [73].

The same experiment was performed at Duke University and resulted in $\beta = -0{,}49(4)$, [31], while $\beta = -0{,}54(5)$ was found at Rice [74]. The group at JILA measured the potential energy in the trap for ^{40}K. They carefully studied temperature effects and where able to extrapolate a zero temperature value of $\beta = -0{,}54^{+05}_{-12}$ [75]. This nicely illustrates that β is universal, as it has the same value measured for both atoms.

Quantum Monte Carlo simulations predict values of β that fall into the same range as the experimental values. The theories are not immune to errors, as Carlson *et al.* also had to correct their value from $\beta = -0{,}56$ [76] to $\beta = -0{,}58$ [77], obviously not due to more precise knowledge of the resonance but because they simulated a larger number of atoms to achieve the latter value. Extending BCS theory by taking into account pairing fluctuation effects, Pieri *et al.* calculated a value of $\beta = -0{,}545$ [78].

Using Monte-Carlo simulation, Carlson *et al.* [76] studied the unitarity limit, where they calculated the chemical potential and the momentum distribution. Astrakharchik *et al.* [79] studied the whole crossover, calculating the energy per particle. They found that their results agree with the equation of state of a repulsive gas of molecules with a molecule-molecule scattering length of $a_m = 0{,}6a$. This is in direct contradiction to BCS theory, which sees a molecule just as a pair of two atoms and as such predicts a molecule-molecule scattering length of twice the atom-atom scattering length. By direct calculation, BCS theory was shown wrong before by Petrov *et al.* [22], who solved the molecular scattering problem and found the exact result of $a_m = 0{,}6a$.

Astrakharchik *et al.* [70] also used a Monte-Carlo simulation to calculate the momentum distribution of a Fermi gas in the crossover. Their results are shown in figure 2.8.

In this chapter we have shown the scattering properties of fermionic gases, and presented and introduction into the BCS theory. In chapter 5 we will use the results from these theories to develop a description of the experiments that we have performed.

Chapter 3

Experimental setup

LASER, subst. masc.
"Plante de la famille des Ombellifères" (Ac. 1878–1935).
Le laser à feuilles larges, à racine cylindrique, a des fleurs blanches disposées en ombelles larges et ouvertes (PRIVAT-FOC. 1870).
– Le Trésor de la Langue Française informatisé

This chapter gives a brief introduction to our experimental setup. As it is already described elsewhere in detail [38, 39], I will give a brief overview and make emphasis only on the parts that have been changed.

First I want to give a quick overview of the experimental procedure, to help in the general understanding of the following sections. Our experiment starts with the atoms in an oven, which is heated to create a gas jet. The atoms are slowed down in a Zeeman slower, after which we capture both isotopes, ^{6}Li and ^{7}Li, in a magneto-optical trap (MOT). Using a magnetic elevator, we transfer the atoms into a Ioffe-Pritchard trap, in which we perform forced evaporative cooling on the bosonic isotope ^{7}Li, at the same time sympathetically cooling the fermionic isotope ^{6}Li. In the end, the atoms are transferred into an optical dipole trap to enable us to study them in the states that are not magnetically trappable. After another evaporative cooling stage in the optical trap we can perform our experiments, which normally take place in a magnetic field around our Feshbach resonance at 83 mT. As a last step, we switch off the optical dipole trap and let the atoms expand, taking an absorption image at the end.

3.1 The vacuum chamber

As Lithium is a metal with a negligible vapor pressure at room temperature, the first step to make an atomic gas of it is to heat it. We do this in an oven which consists of a vertical stainless steel tube into which we put a few grams of Lithium. The oven is connected via a small tube to the vacuum chamber to create a collimated gas jet. Figure 3.1 shows the setup. A small metal mesh is installed in this collimator to recycle lithium into the oven via capillary forces. The oven is heated with an electric heating wire soldered around the tube. Originally, this wire had been only installed in the center of the tube, where the collimator leaves to the vacuum chamber. In order to have a more uniform heat distribution, we changed this design to heat the whole oven tube. This was a bad idea, since now there is no cold point in the oven anymore where lithium condenses. Instead, it will close the collimator albeit the mentioned recycling mesh. The solution to this problem was to also heat the collimator with a second heating wire, to temperatures comparable to the oven's temperature.

The most important drawback in our old setup was the very slow loading of the MOT. During the reconstruction, an important part of our efforts was to improve on that aspect. The loading times were mostly limited by the low flux of atoms in the gas jet. The flux of atoms in turn was limited by the small differential pumping tube between the oven part of our vacuum chamber and the experimental chamber. The obvious way to increase the flux, which is to open this differential pumping tube a bit more, had shown to degrade the vacuum to a point that the magnetic trap had lifetimes too low to work with. A second differential pumping stage was the solution. A 6-way cross was introduced between the oven chamber and the Zeeman slower to install a 25 l/s ion pump. The 6-way cross has windows on all ends, very helpful when measuring the flux of the atomic beam.

Let us estimate the efficiency of the differential pumping. The vapor pressure of Lithium in the oven can easily exceed 20 mbar, which means that we are in the transition region between viscous and molecular flow [80]. This region is very hard to calculate, so we trust the reading of the ion pump in the oven chamber which gives a current corresponding to a pressure of 10^{-7} mbar. The conductance of the differential pumping tubes can be calculated as $C = 0{,}26\bar{v}d^3/l$, where $\bar{v}$ is the average velocity of the particles, d is the diameter of the tube and l its length. The pressure ratio between the two ends of the tube that can be maintained is C/S if S is the pumping speed of the pump before the tube. Plugging in

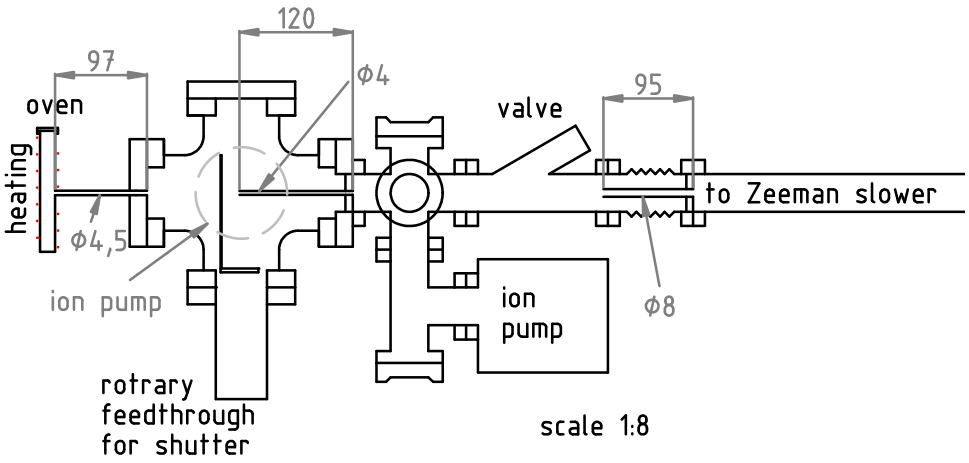

Figure 3.1: This is the beginning of the vacuum chamber, where the atomic jet gets collimated. A block of lithium is in the oven on the left, heated by the heating wire wound around the oven. The gas jet leaves the oven by the little tube between the oven and the chamber, in which we placed a metal mesh as described in the text. Afterwards the jet passes through two small collimation tubes, which also act as differential pumping stages. Here they are marked with their length and inner diameter. Each pumping stage has its own ion pump, one is shown and the other one is situated orthogonal to the represented plane, and indicated with the dashed circle. Between the oven chamber and the Zeeman slower is a 6-way cross with windows on all open ends and a valve to separate the oven from the main chamber in case we have to change the lithium. A bellow before the Zeeman slower allows for fine tuning of the gas jet's direction.

Figure 3.2: The Zeeman slower while being wound. One can see the layer structure of the coils. The cables are held in place using a cement mixed with silicon carbide, which gives a grey color. On the right on can se the end of the two parallel water cooling tubes which are below the coils.

our numbers, using a very conservative average velocity of $\bar{v} = 2000\,\mathrm{m/s}$, which is the average velocity of a lithium gas at 900 K, we get a ratio of 180 for the first tube and 9 for the second one. This gives a ratio 5 times better than the previous value of 270 for the smaller differential pumping tube we had before.

3.2 The Zeeman slower

In order to slow the atoms, a laser beam, detuned from the resonance, is shone counter-propagating onto the atomic gas jet. The momentum transfer to the atoms by the photons will slow the atoms down. This way, the Doppler shift of the resonance frequency changes, which we compensate using magnetic fields via the Zeeman effect. This is why such a setup is called a *Zeeman slower*.

From the technical point of view, the Zeeman slower consists of two cone-shaped coil wound around the vacuum chamber. This creates a decreasing magnetic field in the first coil, followed by an increasing field in the second one. As described in the thesis of Florian Schreck [38], the first coil consists of a cable which is wound in layers around the vacuum tube, held in place using a cement and cooled by water tubes, as illustrated in figure 3.2. The second coil is much smaller, it is a simple cable wound around the tube. As we did not change this second coil, we refer to Florian Schreck's thesis for its design.

One of the factors lowering the atomic flux was that the Zeeman slower was not working correctly, since some of the electric layers stopped working, as the wire was broken. After having dismantled the coils, we found out that those layers obviously had burnt down in some parts, and since we were working on the vacuum, we decided to wind a new slower.

We designed the slower in a way that it gives a high flux but does not burn down during bakeout. The high flux was easy to achieve: the old slower would have had a nice flux if all the windings had been functioning properly. Just to be on the safe side we added 10 cm of windings. We used a slightly thicker wire (cross section 2,5 mm^2, Garnisch GGCb250-K5-19), and added silicon carbide to the cement used before (Sauereisen No. 10) to increase its heat conductance. As a first layer we wound two coils that were only used for heating during bake out, since the burning of the coils had apparently occurred during that time. Should other layers of the slower stop functioning with time, one could consider using this layer instead. For cooling, we wound a layer of two parallel copper tubes with an outer diameter of 8 mm around the first layer. The two parallel tubes should increase the water flux by a factor of four compared to a single tube. After seven layers of cables, we added another cooling layer, and another cooling layer at the end.

The light for the Zeeman slower enters through a window at the end of the vacuum chamber. This window is under constant bombardment from lithium atoms from the jet. After many years of operation, this window was slightly covered with lithium. Not that it had prevented us from working, but as the chamber was already open, we decided to replace it with an anti-reflection coated window, hoping to improve the efficiency of the Zeeman slower. We were surprised that after only a few weeks the window was completely covered, the anti-reflection coating had apparently reacted with the lithium, and we had to replace it by a non-coated window.

When we shine a resonant laser onto the atom jet, the atoms will fluoresce. From the fluorescence we can measure the flux of atoms in the laser beam We do not adjust the laser beam perpendicular to the atomic jet, but leave a slight angle between the orthogonal of the jet and the laser beam. Then the those atoms will fluoresce, whose Doppler shift of the velocity component in the direction of the laser beam is exactly the detuning of the laser. As the atomic beam is collimated, the perpendicular velocity component is nearly negligible, which means that we directly measure the axial velocity of the atoms. Scanning the detuning of the laser, we can acquire the velocity distribution of the

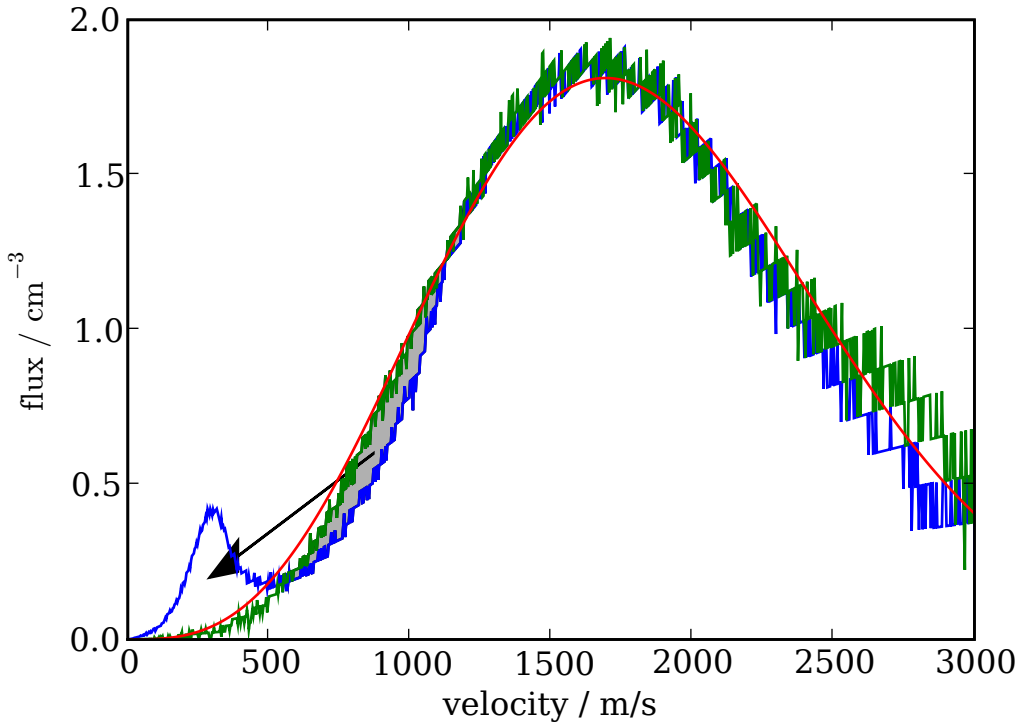

Figure 3.3: The velocity distribution after the Zeeman slower, at the position of the MOT. The small left peak is the slowed atoms. The other curve is the same distribution with the Zeeman slower switched off, shown for comparison. The grey area is the atoms that get slowed, they show up again in the peak on the left. The smooth curve is a fit with a Maxwell-Boltzmann distribution at a temperature of 500 °C. This is a bit lower than the nominal value of 550 °C that the oven was set to.

atoms. Figure 3.3 shows such a velocity distribution. The small peak on the left are the slowed atoms. Comparing to the distribution with the Zeeman slower switched off, one sees that there is less flux around for the velocity component of around 1000 m/s. It is those atoms which show up in the Zeeman slowed peak afterwards. This peak corresponds to a flux of about 10^{10} atoms/cm^{2}s.

3.3 The laser system

Our laser system is divided into several distinct parts, shown in figure 3.4. We placed our master lasers on a separate table, not disturbed by

the vibrations that the experiment creates. The lasers are extended cavity diode lasers, locked using saturated absorption spectroscopy onto three lines: the ^{6}Li D1 and D2 lines and the ^{7}Li D2 line. The lithium level structure is shown in figure 3.5. Using two double-pass acousto-optic modulators (AOM) we can generate the two hyperfine lines in ^{7}Li used as principal and repump beams. Due to the coincidence of the ^{7}Li D1 and the ^{6}Li D2 lines, we repump ^{6}Li on the D1 line. This is why we need an additional master laser for this line.

The mentioned double-pass AOMs together with those installed after the ^{6}Li lasers allows us to tune the lasers in the needed range. The resulting beams are injected into optical fibers and sent to the experiment, where they are used to inject slave lasers. As the power of the ^{7}Li master laser was not sufficient to stably inject the slave lasers on the experimental table, we injected diodes with each beam. These acted as amplifiers. Since we exchanged the ^{7}Li master laser with a more powerful diode, the need for this amplification stage has more or less disappeared, so we removed the amplifier for the ^{7}Li principal beam. The other amplifier might be uninstalled as well if the master laser turns out to be stable and powerful enough over a long time. In the meantime, the ^{6}Li principal laser has degraded to a point that we had to add an amplification stage to it.

After many years of successful operation, the tapered amplifier, used to amplify the light for the MOT, had died. The spontaneous emission background had raised to a level such that almost a third of the emitted power was not actually in the desired mode but formed a pedestal that was unfortunately too broad to be seen on a Fabry-Pérot interferometer. This resulted in an unstable MOT which became unusable. The replacement did not have a good fate: it died after only two weeks of operation. This left us with no tapered amplifier, since our model had gone out of production and no other model was available on the market (nowadays, Toptica produces tapered amplifiers for 670 nm). Fortunately, at the same time two models of high-power laser diodes became available. Both models (Mitsubishi ML101J27 and Hitachi HL6545MG) are specified for a wavelength of 660 nm and a power of 120 mW. For the Mitsubishi diodes, we managed to convince the distributor (Municom) to sell us diodes selected for a high wavelength, typically specified as 663 nm at room temperature. According to the specification, they should get to around 668 nm when heated to 60 °C. In the experiment, we usually heat them up to 80 °C. Near a current of 280 mA the wavelength reaches 670 nm, and we can inject the diodes, giving us more than 120 mW of power. Both temperature and current

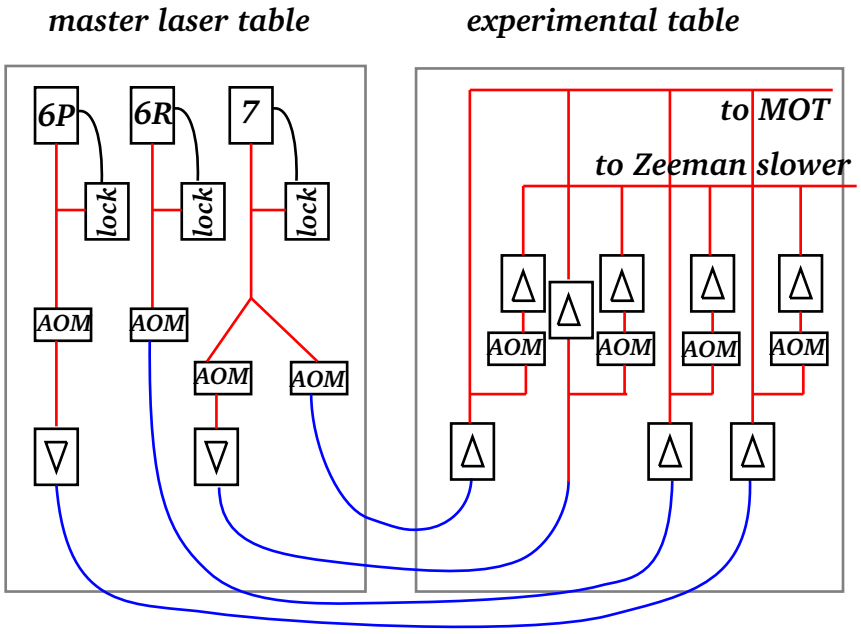

Figure 3.4: A bird's eye view of the laser system. Shown on the left is the master table, while the experimental table is on the right. The light is transported via fibers (shown on the bottom) from one table to the other. Three master lasers are locked via a feedback loop. Eight AOMs enable us to independently tune the four frequencies for the MOT and the Zeeman slower. All beams have to be amplified, symbolized by the boxes with a triangle.

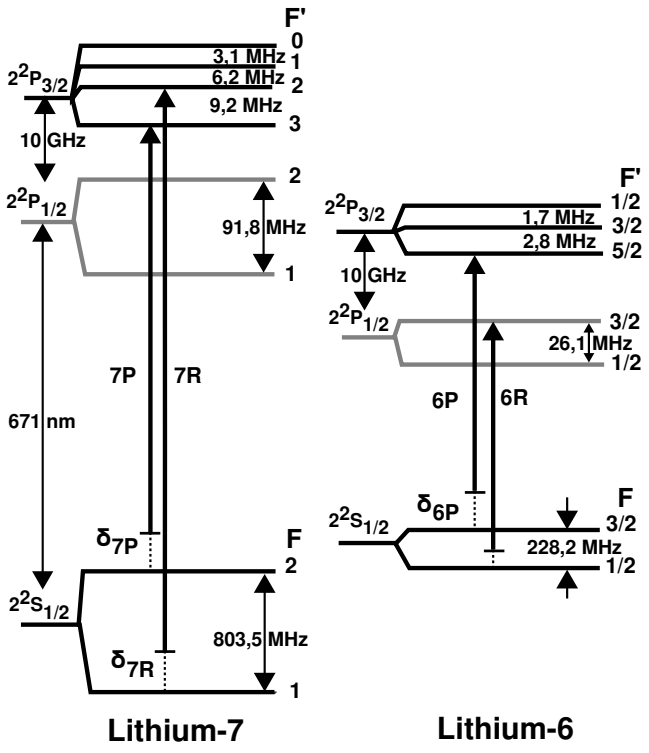

Figure 3.5: The energy levels of ^{6}Li and ^{7}Li.

are beyond the specifications of the diode.

The high current in combination with a high power is not easy to handle. Thermal isolation is crucial, as at high temperatures the losses by convection will be large, leading to an unstable diode. We glued rubber isolations on the inside of the laser housing, and closed it hermetically. Additionally, we used commercial diode mounts Newport Model 700 Series Temperature Controlled Mounts. Only the high price prevented us from using them for all diodes.

In case the temperature controller fails, the temperature drops rapidly and the diode will die, as the current is by far too high at ambient temperature. After having lost some diodes this way, we installed a temperature security system. We installed a temperature sensor LM35 into our own diode mounts and used the sensors AD592 in the Newport mounts to monitor the temperature. Once it leaves a predefined range, a relay installed in the current drivers will cut the supply to the diode.

During the evaporation of the atoms, it is imperative that we do not allow any light that resonates with the atoms, as even at low powers this leads to non-negligible heating. This is not easy to achieve if one has to block some 100 mW. In the old setup, we used to switch off the AOMs of the master lasers in order to disinject the lasers, such that they were not resonant with the atoms anymore. Unfortunately, some of the new lasers show an annoying behavior: while they are stable once injected, they will not re-inject after the injection beam has been switched off for a while. The diodes show a hysteresis behavior: one has to increase the diode current above the injection point and decrease it again for the laser to injection lock. As a first solution, we tried to constantly modulate the laser diode current. This made re-injection possible, but not to an extent that we could guarantee it. As this also affected long term stability on normal conditions, we abandoned this technique. Instead, we had to block the resonant light completely. This turned out to be harder than expected, as even after a switched off AOM and a shutter there was still enough light to decrease the lifetime of the atoms below a second. A shutter in front of a small aperture solved this problem.

Still, the tapered amplifier gave us about 500 mW of optical power, far from what the diodes are capable of. As luck would have it, this power is equally distributed over the four frequencies that we use. This means that we can use four lasers to generate the six beams needed for the MOT. In order to achieve this, we mix the four beams on non-polarizing beam splitters and use all four outputs, three of them are split again to make up the six beams of the MOT, while the fourth one is sent to a Fabry-Pérot interferometer to monitor the injection of the slave lasers

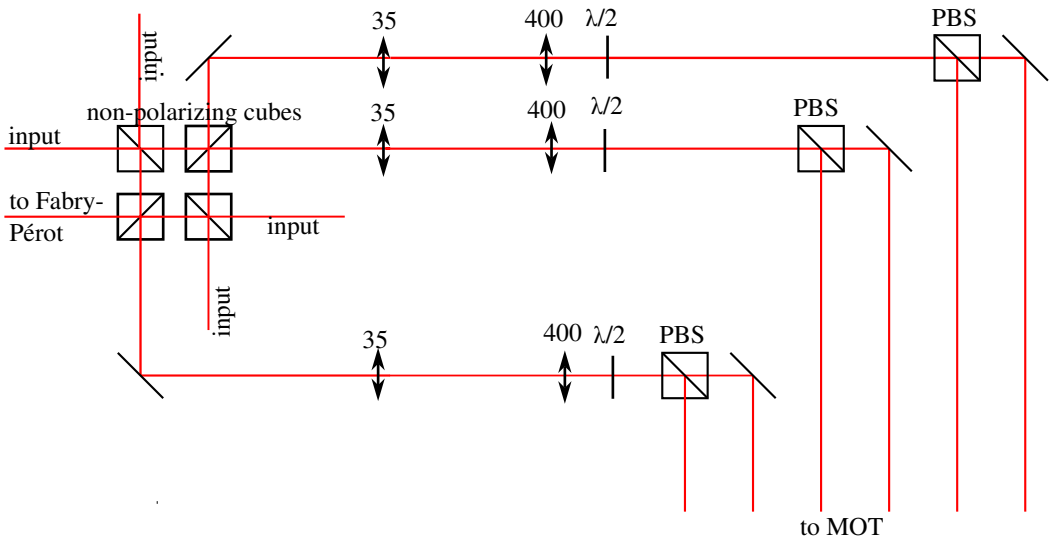

Figure 3.6: The optical setup for the MOT

(see Figure 3.6). In the end, we have a beam with a diameter of 25 mm and an intensity of 6 mW/cm^2 per line.

The high power of the MOT lasers also enables us to take some of their power to inject the lasers of the Zeeman slower. This makes the injection more stable, since we can now use all the power of a fiber coming from the master lasers to inject one laser, and we always have enough power to inject the Zeeman slower slave lasers, even though they are behind an AOM (see Figure 3.7). One exception is the laser for the MOT ^{7}Li principal line, since it has the highest need for power and we do not want to loose any without need.

In the old setup, the imaging beam used to be problematic. It was derived from the MOT lasers and mode cleaned in an optical fiber. After that optical fiber, the beam could be switched with an AOM, and was mode cleaned again using a pinhole. This design had several disadvantages: as the MOT lasers were disinjected during an experimental run, there was always a wait time of 20 ms to re-inject the lasers, during which time the experiment did nothing. The injection into the fiber was unstable, there was a high-frequency noise on the outgoing beam. We found out that this was due to the fiber acting as a cavity. The beam was injected into the fiber on the experimental table that vibrated while the magnetic coils were switched off. The AOM which was installed after the fiber distorted the beam, such that we needed a pinhole to clean the

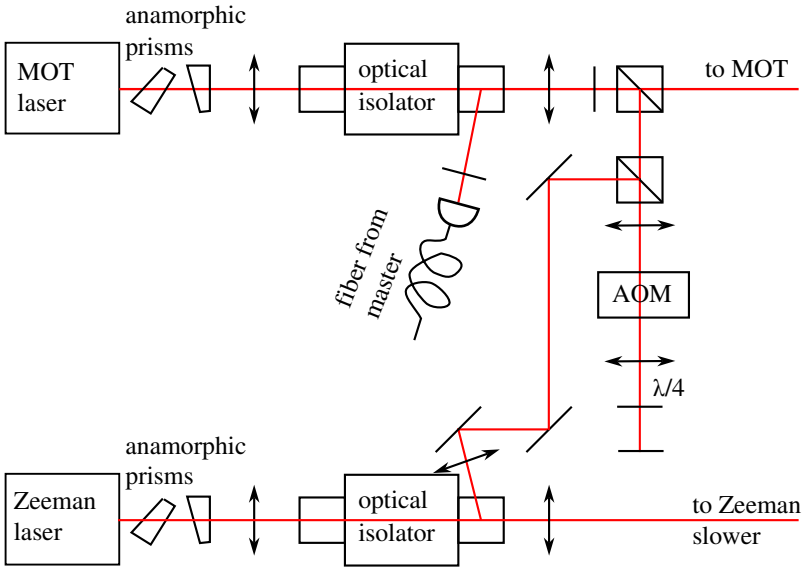

Figure 3.7: The principal optical setup for the lasers on the experimental table. Note that the ^{7}Li principal Zeeman laser is not injected by the MOT lasers, but directly from the fiber via the AOM.

mode again.

In the new setup we addressed all these problems. The AOMs to switch the beams are now placed on the table with the master lasers, with no vibrations from the coils switch-off, using beams coming directly from the amplifiers. This is shown in figure 3.3. A fiber cleaved with an angle on both ends eliminates the possible creation of a cavity, and the only optics after the fiber is a single lens which is placed directly after the exit of the fiber to collimate the beam, and some steering mirrors. This gives a virtually perfect Gaussian beam.

The Doppler cooling beam also had to be redesigned, as it was taken after the tapered amplifier, which does not exist anymore. We also simplified the beam path of the optical pumping beam.

3.4 The magnetic traps

After the atoms have been trapped in the MOT, we have to transfer them into the Ioffe-Pritchard trap where we perform the evaporative cooling. As the MOT coils are not perfectly on the axis of the Zeeman slower, we have some current in the transfer coils in order to lift the

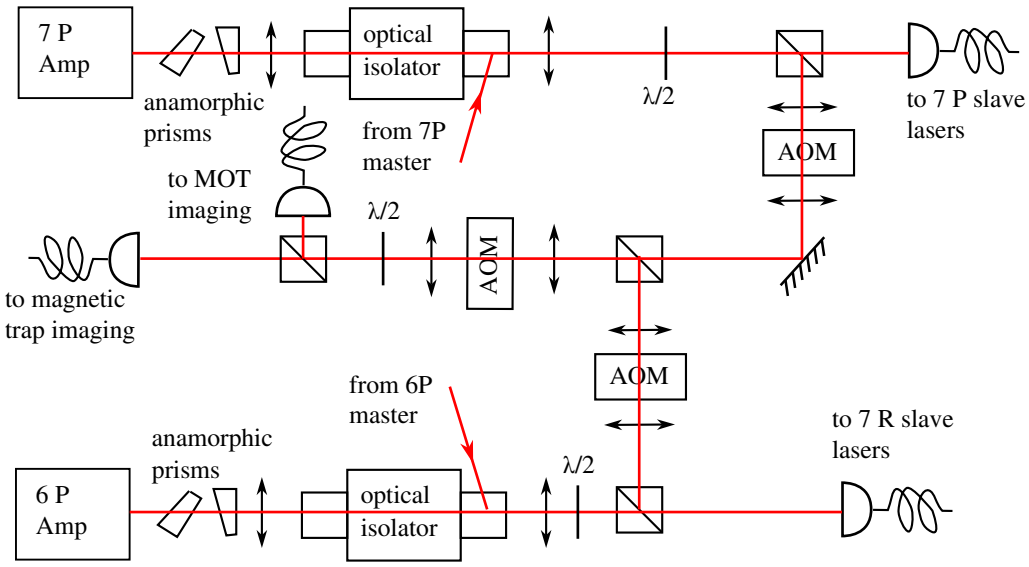

Figure 3.8: The setup of the MOT amplifiers and imaging lasers. The ^{7}Li principal and ^{6}Li principal beams are generated in a saturated absorption spectroscopy, tunable via an acousto-optic modulator. This is the beams entering into this picture. Two amplifiers give enough power for both the MOT slave lasers and the imaging. Three AOMs guarantee that there is always two AOMs switching the light, as stray light would be evil, and enable us to switch the to isotopes independently.

center of the atoms a bit. When the experiment starts, we shift down the MOT to the center of the coils. Afterwards, we detune the lasers closer to resonance while lowering their power and the magnetic field to cool the atoms more and compress them. We optically pump the atoms into the higher hyperfine states, the only states magnetically trappable.

When trapping cold atoms, one must do a trade-off: a MOT should be as big as possible as to trap as many atoms as possible. Later, while doing evaporation, one prefers high magnetic field gradients to achieve high densities. This is especially important in lithium, as it has rather low scattering cross sections in low magnetic fields. A high gradient means high currents close to the atoms, contradictory to a large MOT volume. The solution adopted here is to spatially separate the two traps, and transfer from one to the other.

The final magnetic trap is a classical Ioffe-Pritchard trap [81], illustrated in figure 3.9. It consists of four parallel bars, commonly called Ioffe bars, arranged around a common center line, where they create a magnetic field minimum in which the atoms will be trapped. At the end of the bars, two coils are posed. They are not in a Helmholtz configuration, but further apart, thus they create a magnetic field minimum in the center. This traps the atoms also in the direction parallel to the bars. These coils also create a large offset field, which is eliminated using a pair of large compensation coils with a current flowing in the opposite direction of the pinch coils' current. As the compensation is not exact, there is a small coil wound around the compensation coils connected to a different power supply used to fine-tune the offset field. The Ioffe-Pritchard trap is installed around a little appendix, which sticks out of the glass cell in which we make the MOT. The appendix is very small, enabling us to pose the trapping coils very close to the atoms, lowering the needed currents considerably.

We transfer the atoms magnetically. We ramp up a current in the transfer coils, centered around the Ioffe-Pritchard trap, and later lower the current in the MOT coils. This procedure moves the center of the quadrupole magnetic trap into the appendix. This technology, pioneered by our group, is used in many variations in several laboratories. While we use one coil to transfer the atoms, the group in Munich extended this concept by using many coils acting like a conveyor belt [82].

An important problem with the old setup was the fact that we lost most atoms during the transfer from the MOT into the magnetic trap because the little appendix on the glass cell was just too small. The atomic cloud has a $1/e$ radius of about 5 mm. As the inner *diameter* of the appendix was only 3 mm, we loose 90% of the atoms when

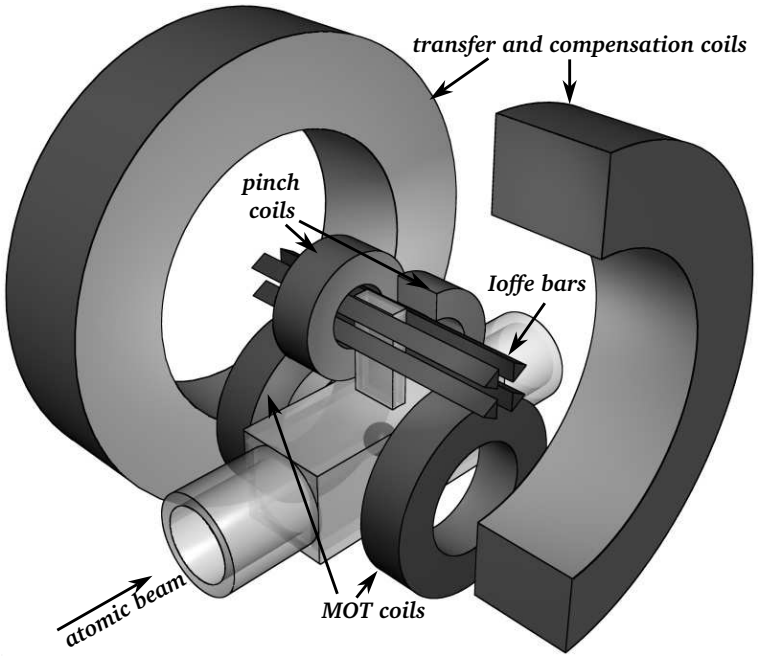

Figure 3.9: The magnetic coils setup.

transferring into the appendix. Increasing the inner diameter to 5 mm, the loss will decrease to only about 50% of the atoms, which can be easily calculated considering a cloud with a Gaussian distribution. This, admittedly oversimplified estimation, has been verified by a Monte-Carlo simulation by Andrea Alberti [83]. This means that we will be able to transfer five times more atoms into the Ioffe-Pritchard trap.

This change made a redesign of the coils around this appendix necessary. In order to reach the same confinement as before, the current in the Ioffe bars has to be increased significantly. In the old design we had three parallel wires for each bar, which we increased to four. This way, we can create a magnetic field gradient per current of $3\,\mathrm{GA^{-1}cm^{-1}}$, close to the $3{,}9\,\mathrm{Gcm^{-1}A^{-1}}$ in the old setup. Fortunately, we were driving a current of 400 A in the bars, well below their maximum current, such that we can compensate for this decrease. We expect that a current around 600 A will be necessary. We tested that the water cooling will be sufficient for these currents.

3.5 The optical dipole trap

As we just described, only atoms in a low field seeking states can be trapped using a magnetic trap. We prefer to use the lowest states of the atoms as they cannot scatter inelastically, reducing the losses from the trap. Therefore we installed an optical dipole trap, which can trap atoms in all states.

An optical dipole trap consists basically of a focused Gaussian beam of a wavelength higher than the atomic transition. The atoms are attracted to high laser intensities, giving us a trapping potential which is proportional to the intensity.

We use two crossed beams to create the optical trap. This enables us to change the shape of the trap by changing the relative intensities of the two laser beams. Originally, we used a 9,5 W Nd:YAG laser from Spectra Physics, which was split on a beam splitting cube for the two beams. One AOM per beam enabled us to change the intensity of the vertical and horizontal trap independently.

After years of successful operation, the old laser for the optical dipole trap started to decrease in power. As a replacement, we bought a Yb:YAG laser "VersaDisk" from ELS. The manufacturer specified an output power of 30 W at a wavelength of 1030 nm. Using a birefringent filter and an etalon, the laser should be able to work in single frequency mode, while still lasing at 15 W. This was a major design goal, as we will use this laser to create an optical lattice.

This laser had a big surprise for us: when we first tried to replace the old laser with it, the laser failed to trap the atoms, but instead heated them until they left the trap. The reason for this was that the laser showed a distinct noise peak at 3,4 kHz with a relative intensity noise (RIN) of -93 dB/Hz, on top of a noise background of -115 dB/Hz. This was far above the specified -160 dB/Hz. Similar results had been found by the group in Innsbruck.

The heating of an atomic cloud with a laser that has intensity noise was studied by Savard *et al.* [84]. They reported that the average energy of the particles in a trap created by a noisy laser increases exponentially,

$$\langle E(t)\rangle = \langle E(0)\rangle e^{t/\tau} \tag{3.1}$$

The heating rate τ in this equation relates to the noise of the laser as

$$\frac{1}{\tau} = \pi^2 \nu^2 S(2\nu) \tag{3.2}$$

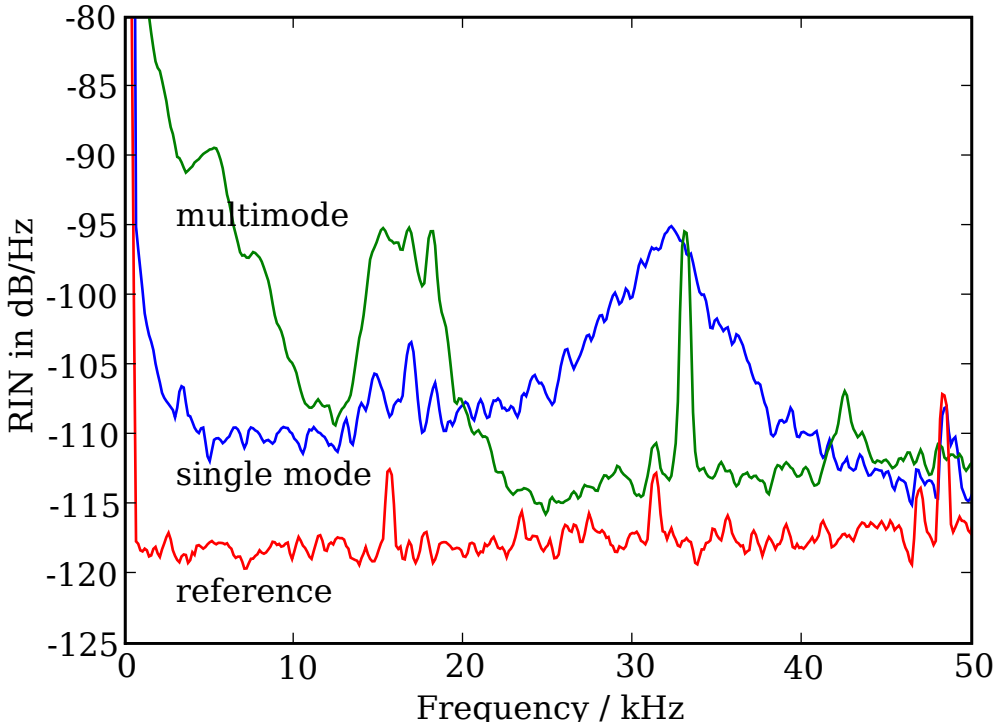

Figure 3.10: The noise of the laser in single mode and multi-mode operation, after it had been repaired but before we installed the active stabilization. The reference is the noise of the electronics.

where ν is the trap frequency and $S(\nu)$ is the power spectral density. Equation (3.2) shows that the most disturbing noise is around twice the trapping frequency, which we expect since parametric heating is the dominating process.

The laser was shipped back for repair. A feedback loop was installed in the factory, but this and various changes in the laser geometry had only minor effect, the peak noise did not drop below -100 dB/Hz. The good news was that the noise peak had moved to higher frequencies: the main peak was now at 32 kHz, see figure 3.10. The heating times calculated for the laser are shown in figure 3.11. Since we work at lower frequencies, the atoms see less of the noise. The noise is very different for single mode or multi-mode operation. The noise peak at 32 kHz is narrower, but the noise at low frequencies increases tremendously for multi-mode operation. This makes single mode the favorable way of operating.

The only way to use this laser was to install a feedback loop. A

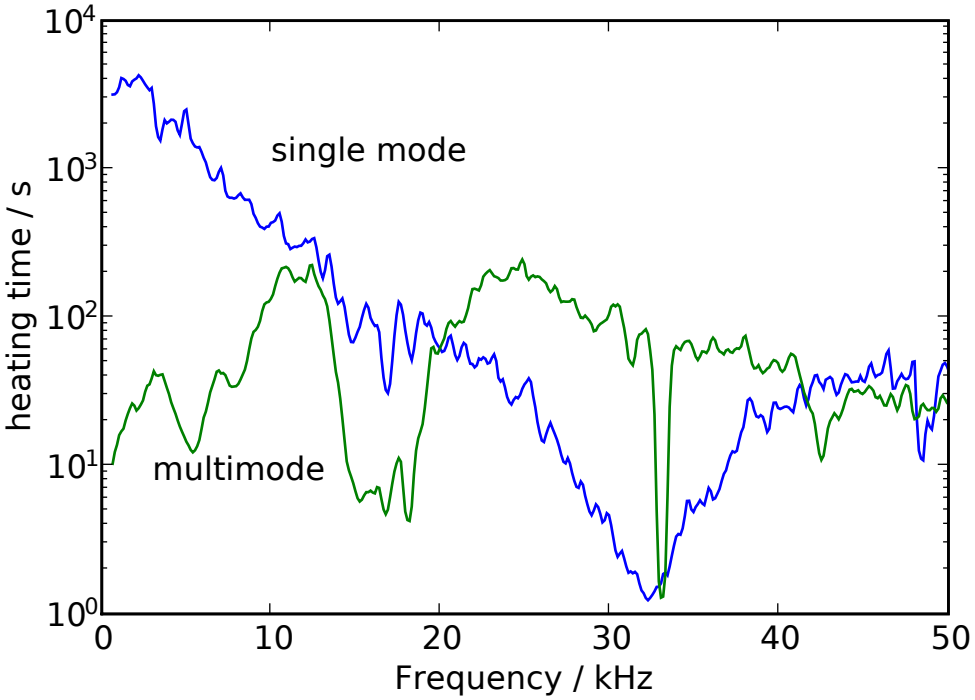

Figure 3.11: The heating induced by the laser noise from figure 3.10, calculated using equation (3.2)

photodiode, installed after the trap, detects the intensity of the laser. We designed a PI controller, which feeds back onto the AOM installed after the laser. The electronic circuit is shown in figure 3.12. The photodiode's signal enters on the left. It get summed with the reference voltage using an operational amplifier. As the photodiode's signal is negative, and the reference positive, the sum of the two give directly the error signal. A potentiometer, wired as a voltage divider, determines the overall gain of the feedback loop. The core part of the controller is the integrator in its center. The gain G of the shown circuit is proportional to

$$G \propto \frac{R_G R_\tau}{R_0} \left(1 + \frac{1}{i\omega R_\tau C}\right) \tag{3.3}$$

where R_G is the setting of the overall gain potentiometer and C is the value of the capacitor in the integrator. R_τ is the setting of the variable resistor named time constant in the figure, and looking at the equation we note that it can be indeed used to set the time constant $\tau = R_\tau C$ of the system.

The output from this controller is connected to voltage controlled attenuators (PAS-3 from Minicircuits) which attenuate the radio frequency power sent to the AOM. As their working point is normally not around 0 V, a last summing amplifier is installed in the electronics to add an offset to the output. The switch in the circuit can be used to disconnect the feedback loop, and the power of the RF can be controlled manually using the offset potentiometer.

In order to check the performance of the feedback loop, we studied the losses of the atomic cloud in the optical trap. Starting with $9 \cdot 10^5$ atoms at 20 μK, we saw an exponential decay with a time constant of 2,8 s when the laser was feedback stabilized. This is much worse than the predicted value shown in figure 3.11, apparently we are not limited by the laser noise. Without the stabilization the losses were much higher, and especially very non-deterministic, so that we were not even able to trace a loss curve.

After a short while the laser constantly dropped in power. We found out that this was due to an accumulation of dirt burnt into the laser crystal. This problem could only be solved by realigning the lasing cavity to use a different spot on the crystal. As this procedure can only be performed by ELS technicians, this is not a long term solution. We tried to overpressure the laser with filtered compressed air to reduce dust, but the final solution was that we bought laminar flow air filters which we installed on top of the experimental table.

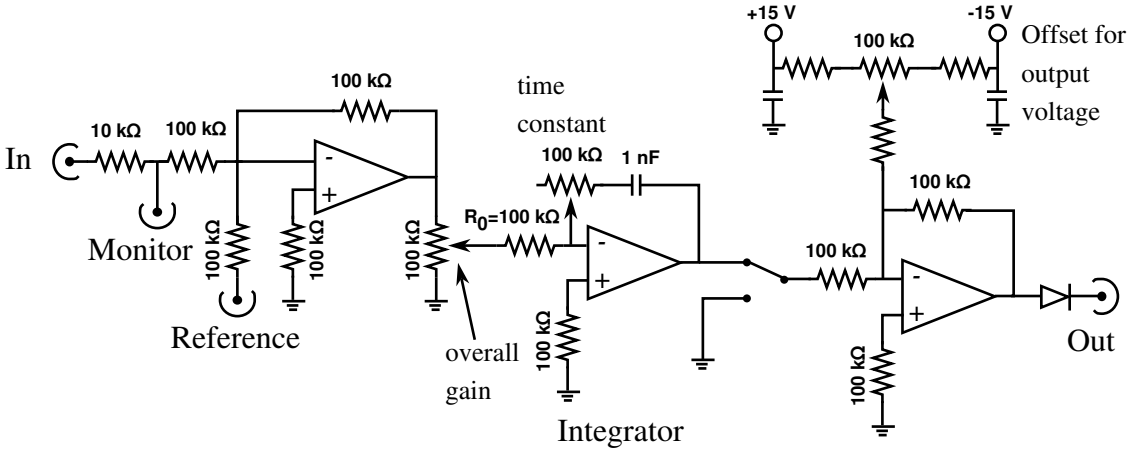

Figure 3.12: The controller electronics for the intensity feedback. All the operational amplifiers are of the type OP27.

The standard operation for the experiments described in this work was that we used the ELS laser for the horizontal trap and the Spectra Physics laser for the vertical.

3.6 The cooling strategy

In BEC experiments, the standard tool for creating quantum degenerate gases is forced evaporative cooling: one removes the most energetic atoms out of the trap and lets the remaining atoms rethermalize. Constantly lowering the energy above which one removes the atoms will cool the gas. It is elastic collisions which provide rethermalization, while inelastic collisions is the major limit of evaporative cooling, as it leads to heating.

As we have seen in section 2.2, *s*-wave collisions are forbidden for fermions. This decreases scattering to almost zero at low temperatures, which prevents the gas from rethermalizing. Two techniques are used to circumvent this: realizing that scattering is allowed once the fermions are in different internal states, the groups at Duke [85] and Innsbruck [86] are using the two lowest spin states of ^{6}Li in an optical trap. At JILA, they do the same in a magnetic trap using ^{40}K [13]. The other technique is to mix the fermions with a boson. One then cools the boson

evaporatively, and as the bosons and fermions scatter, the fermions are cooled sympathetically. This technique is used in many groups, the pioneers were the group at Rice [14] and our group [15] for the combination ^{6}Li-^{7}Li, the group at MIT for ^{23}Na-^{6}Li [16]. Many groups use nowadays the combination ^{87}Rb-^{40}K, pioneered at Florence [17] and JILA [87]. The obvious solution would be the combination ^{87}Rb-^{6}Li, as Rb is the most simple atom to deal with and Li is easier to handle than K. This was tried by the group at Tübingen [88]. They reported on a very low scattering length between the two atoms of $20a_0$, which reduces evaporation efficiency to a point that quantum degeneracy is hard to achieve.

We are using both techniques in our experiment. We start by performing sympathetic evaporative cooling in a magnetic trap. In order to start evaporative cooling, we first have to perform a Doppler cooling stage, the principle of cooling used in a MOT. This is necessary as evaporative cooling does not work for Lithium around 6 mK, corresponding to the cancellation of the scattering length described in section 2.2. In the MOT we can cool below 1 mK, but when we transfer the atoms into the magnetic trap we adiabatically compress the cloud, thus heating it. Using Doppler cooling we can decrease the temperature again below 1 mK.

A magnetic trap is a minimum of the magnetic field in free space. Atoms can be trapped in such a minimum, if they are prepared in a low field seeking state, this is a state whose energy increases with increasing magnetic field. Atoms in a high field seeking state, the other possibility, cannot be trapped as there is nothing like a magnetic field maximum in free space [89]. The situation of ^{6}Li is shown in figure 3.15. We can trap the atoms in the highest state. In order to remove the highest energy atoms from the trap, we drive an RF transition which transfers atoms into the untrapped lower states. As the transition depends on the magnetic field, only the atoms at a certain isomagnetic shell are removed, thus only those which are sufficiently energetic to get there. One commonly speaks of a *radio frequency knife* which "cuts" the high energetic tail of the atomic distribution.

Another way of seeing this is to look at a dressed state picture. The radio frequency effectively shifts the lower state upwards until it crosses the upper states, as shown in figure 3.6. This creates an avoided crossing, and the atoms will be able to leave the trap once they manage to cross the magnetic field of the RF knife. One can also trap the atoms in the upper minima, symbolized by the small circles in the figure. This gives an eggshell like trap, that was proposed by Zobay and Garraway [90],

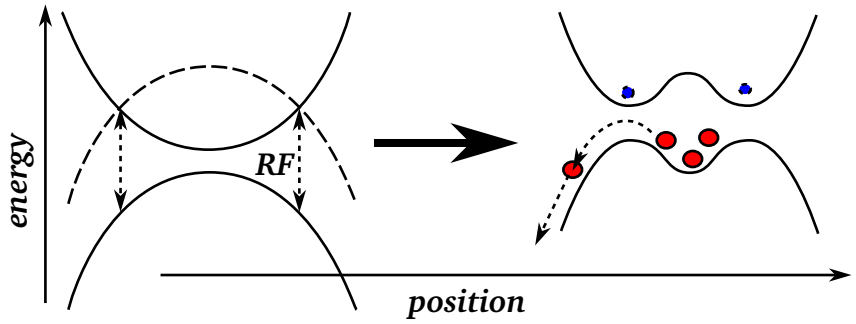

Figure 3.13: Evaporative cooling in a dressed state picture. The solid lines on the left represent the energy levels in the magnetic trap without the RF field, while the dashed line is the dressed state energy. On the right side we consider the avoided crossing and see that the atoms, symbolized as large circles, can leave the trap if they have sufficient energy. The small circles show how the atoms may be trapped in an eggshell trap, as described in the text.

and experimentally shown at Villetaneuse [91].

In the magnetic trap, we only evaporate ^{7}Li, as this way we are able to cool sufficiently low without loosing any of the fermions we want to work with later. Historically, we were using a sequence of linear ramps for the RF knife, that were optimized independently. It turned out that by proceeding this way we converged to an approximation of an exponential function by linear pieces, as shown in figure 3.14. Thus we replaced the ramp by a simple exponential sweep which can be easily tuned as a whole. The exponential sweep is followed by a linear ramp which goes down below the hyperfine splitting in order to clear the cloud from any remaining bosons.

We can improve the evaporation if we increase the scattering length by making use of the Feshbach resonance. There is a Feshbach resonance between the lowest spin states, which are not magnetically trappable. With an optical trap on the other hand, it is not easy to create a potential sufficiently deep and large as to trap the atoms directly from the MOT with good efficiency. This is why we evaporate first in the magnetic trap.[1] Once the atoms are sufficiently cold to be held in the optical trap, we transfer the atoms into it. Typical numbers are 10^6 atoms at $15\,\mu$K, while the optical trap depth is $500\,\mu$K. We overlap the magnetic trap with an optical trap which is similar in stiffness to its magnetic

[1]The group in Innsbruck decided to build a cavity around the vacuum chamber, leading to a power buildup which enables them to load directly from the MOT [86], while the group at Duke uses a 140 W CO_2 laser for the same purpose [85].

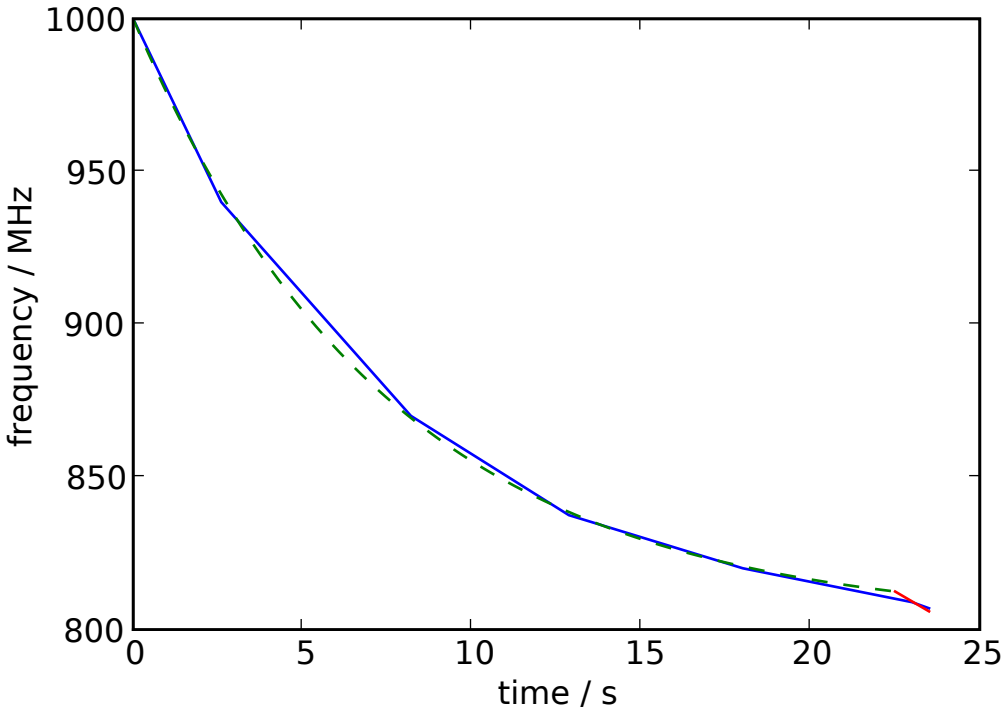

Figure 3.14: The evaporation ramp. The solid line shows the linear ramps used originally, while the dashed line shows the exponential ramp used later. One should note the little linear ramp a the end of the exponential ramp to eliminated all remaining bosons.

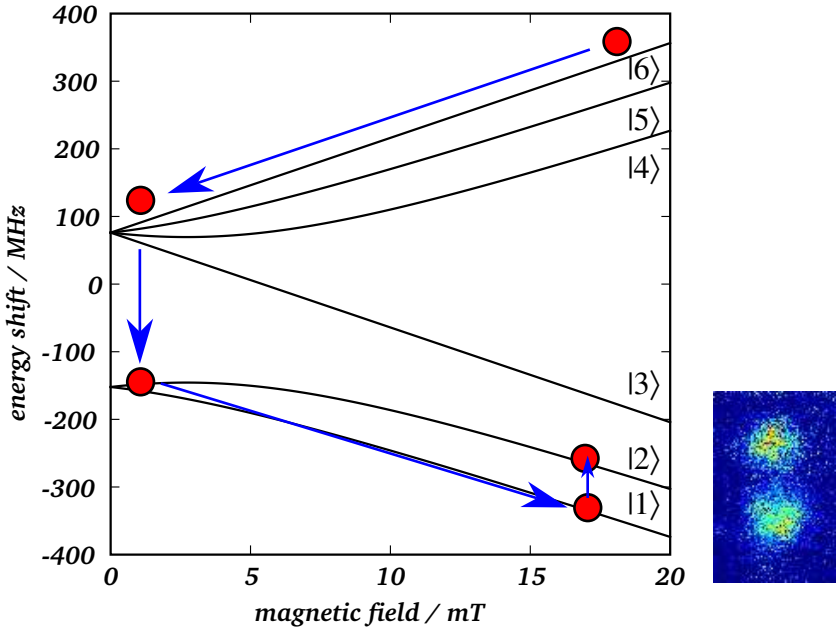

Figure 3.15: The atoms first get cooled down, and then get transferred to the lower spin states using an RF pulse. Then we ramp to high magnetic field where we generate the spin mixture using an RF sweep. On the right we show an absorption image where the two lowest spin states had been separated using the Stern-Gerlach effect.

counterpart, to minimize heating during the transfer. We ramp up the optical trapping laser in 1 s. Afterwards, we switch off the magnetic trap in 1,1 s only leaving some current in the pinch offset coils as a guiding field. At this stage, the atoms are still in the magnetically trappable higher hyperfine state. Using a RF transition we change from state $|6\rangle$ to state $|1\rangle$, as shown in figure 3.15. As this is the lowest state, inelastic collisions cannot lead to heating anymore, improving the stability of the cloud.

A rather complicated procedure follows to evaporatively cool the atoms in the optical trap, one may follow the description comparing the sketch in figure 3.6 to the setup shown in figure 3.9. The only coils which can generate the Feshbach field around the resonance and can be switched off rapidly are the pinch coils, as they are both small and close to the atoms. In the Ioffe-Pritchard trap they had been used to

trap the atoms axially, and as we are now in a high field seeking state, the trap acts as an anti-trap, pushing out the atoms. The "anti-trapping frequency" is around 100 Hz at the Feshbach resonance point. We can avoid the expulsion of the atoms by shining a second trapping laser vertically onto the atoms, but evaporative cooling is more efficient in the horizontal trap only. Therefore we use the compensation coils to create the magnetic field. In 15 ms we ramp them close to the minimum of the scattering length left of the resonance at 28 mT. There we create the mixture of the two lowest spin states using another RF sweep.

The parameters of this sweep are very sensitive to magnetic stray fields, and has to be verified regularly in a separate experimental run. A small additional coil, not shown in the figure, enables us to apply a magnetic field gradient. The spin states of the atoms will separate as in the Stern-Gerlach experiment, and we can image this separation to check the equality between the two spin states. Such a check is shown on the right of figure 3.15.

After the spin mixture has been created, we wait 1 s for the atoms to thermalize, followed by an exponential ramp down of the optical trap to a fourth of its initial power in 5 s, to perform evaporative cooling. There is no RF knife necessary in an optical trap, as it is naturally limited in size and the atoms are not trapped outside the small focus of the laser beam. At this point we are left with $5 \cdot 10^5$ atoms at 3 μK, meaning that we lost only half of the atoms while cooling down by a factor of five.

As we need to use the pinch coils to do experiments at the Feshbach resonance, we now have to ramp up a second, vertical laser that prevents the atoms from getting pushed out by the anti-trapping potential. This is the time to switch to the pinch coils. We want to cross the p-wave resonances at low field as fast as possible. This is why we first ramp up the pinch coils, in 5 ms, before we switch off the compensation coils, again in 5 ms, as it is much faster to ramp the small pinch coils. We stop at the center of the Feshbach resonance, at 83 mT, from where we can ramp to the desired magnetic field.

3.7 MOT imaging

When optimizing the MOT, it is of crucial importance to know the number and temperature of the trapped atoms. The old MOT imaging system had long stopped working, mostly due to the fact that the frame grabber card to read the camera did not fit into new computers. Therefore we decided to install a completely new system.

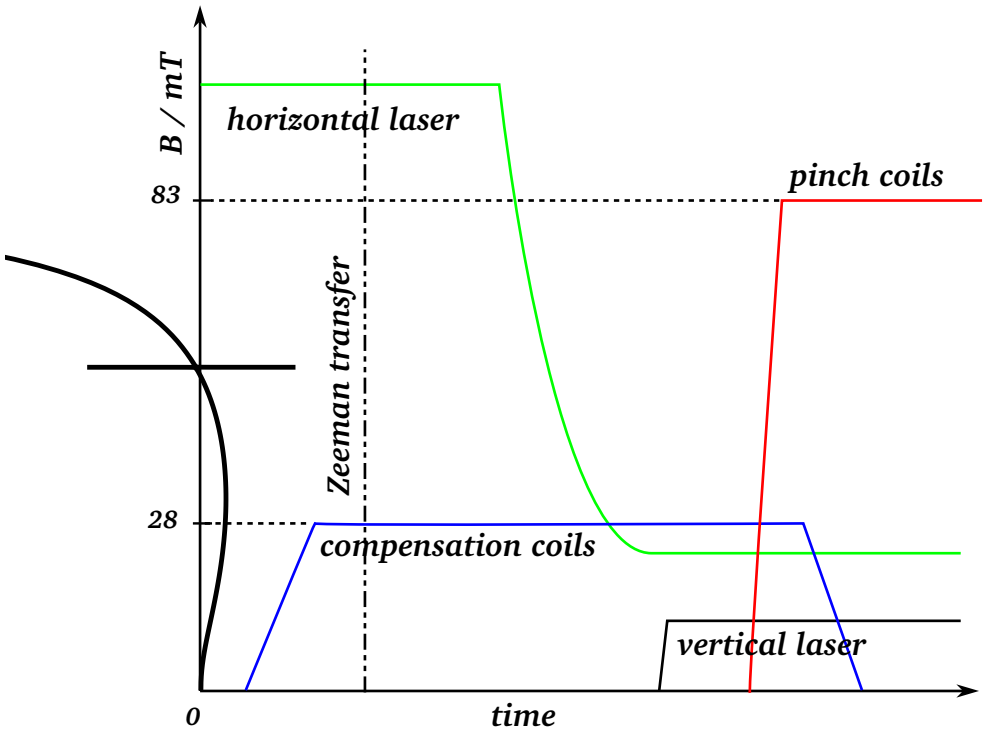

Figure 3.16: The magnetic field ramps, as described in the text. On the left is a sketch of the scattering length for comparison, as in figure 2.6. The time is not to scale. The two coils generate a field opposite to each other, the magnetic field thus crosses zero where the pinch coils get ramped up.

As for the camera, we decided to buy a cheap and especially small camera, as we do not need precision measurements for the characterization of the MOT. We chose the uEye UI-1410-M from IDS, an eight bit CMOS camera, which is triggerable via a TTL signal and can be connected to a computer using the USB port, which at the same time is its power supply, limiting the number of cables on the experimental table. There was a problem with that camera. A glass slide, meant to protect the camera, created strong fringes on the camera, such that the images were destroyed by the interference fringes. Unfortunately, while breaking this glass slide we destroyed some pixels on the camera, but there were enough left over to work with the camera.

As with the main imaging system, we use absorption imaging, since this gives an absolute number of atoms. Assuming we correctly installed the imaging lenses, each pixel of the camera will "see" a column of the imaged cloud. If the cross section of this column is A, and the scattering cross section of a photon with an atom is σ, a photon traveling along this column has a probability of σ/A to scatter with an atom. Considering many photons, there will be $1-\sigma/A$ of the incident light intensity transmitted. For N atoms $I_{\text{out}}/I_{\text{in}} = (1-\sigma/A)^N$ will be left, calling I_{in} and I_{out} the incident and transmitted light intensities, respectively. In order to know the number of atoms, we take the logarithm, leaving us with $N = \ln(I_{\text{out}}/I_{\text{in}})/\ln(1-\sigma/A) \approx -\ln(I_{\text{out}}/I_{\text{in}})A/\sigma$. Note that σ/A is normally sufficiently small that the last approximation is very good. The term $-\ln(I_{\text{out}}/I_{\text{in}})$ is called the *optical density*. The advantage of absorption imaging is clearly visible: the calculated number of atoms only depend on the ratio between two intensities, which can be easily determined by taking two images, one with, one without the atoms to be imaged, and we take the ratio of the two. Therefore there is no need to calibrate the calculated number of atoms. The formula for the scattering cross section is

$$\sigma = \frac{3c^2\lambda^2}{2\pi}(1 + 4(\Delta/\Gamma)^2)^{-1} \tag{3.4}$$

with $\lambda = 671\,\text{nm}$ the wavelength of the transition, $\Gamma = 5{,}9\,\text{MHz}$ its line width, c the corresponding Clebsch-Gordon coefficient, and Δ the detuning from the resonance. Special care has to be taken not to saturate the atoms: once the intensity reaches the order of the saturation intensity, the atoms absorb less photons, leading to a seemingly lower density. As a MOT usually has optical densities too high to be measured with the camera, we usually detune the lasers until saturation is sufficiently low. Figure 3.17 show examples of the MOT imaging.

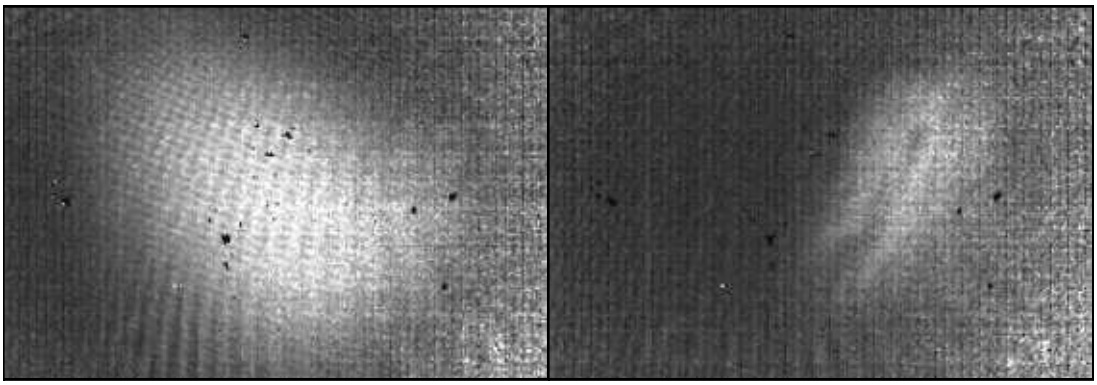

Figure 3.17: Two images of the MOT. On the left a normal MOT with $2 \cdot 10^9$ atoms, on the right side a compressed MOT, with $9 \cdot 10^8$ atoms left. The images show the same area. One can see that the CMOT is at a different position than the MOT, as described in section 3.4. The images are taken with a detuning of the probe laser of -10 MHz to reduce the absorption, otherwise the center of the cloud would be saturated.

3.8 Computer control

The whole experiment is controlled by an MS-DOS PC running a program written in Turbo Pascal. It commands an IO card which is multiplexed over a bus connected to two types of output boxes: a digital version with 16 outputs and an analog version containing 16 bit digital/analog converters. They had five address bits which we increased to six in order to double the number of boxes that can be connected.

Several other equipments are connected via a General Purpose Interface Bus (GPIB, IEEE754) namely the radio frequency generators, the function generator to generate the imaging pulses and a pulse generator.

Over the years, the computer control had grown chaotic to a point where the code could not be maintained. We rewrote the whole experimental sequence, adapting it to the new setup and removing large parts that had become unnecessary. During this rewrite we optimized the code interfacing with the bus, cutting in half the time between commands to 5 μs.

The cameras are connected to two different computers, which in turn are connected via serial ports to the control computer. We preferred to use two computers as the camera imaging the magnetical and optical

traps is connected to the computer via an old PCi card and we feared that it would not be compatible with modern computers, while the MOT camera is connected via USB 2.0 which is not compatible with the old computer.

The data acquisition program controlling the cameras had become even more cumbersome. Many different data analysis tools had been introduced which we were not able to manage. This led to frequent crashes of the program. When the new MOT camera arrived, it was nearly impossible to adapt the old program to the camera, so it was decided to write a new program from scratch. We chose Python as a programming language, since it has an easy to understand structure and automatic garbage collection, eliminating memory leaks which we think was the problem causing the frequent crashes. Our design goal was to keep the program as simple as possible, making it understandable as a whole. To achieve this task we used readily available libraries from the Internet wherever feasible. Namely we used Qt4 and PyQt for the graphical user interface, matplotlib [92] for plotting the acquired images and SciPy [93] for fitting our data. We could thus decrease the size of the program from more than 25000 lines to below 2000 lines. The running program is shown in figure 3.18. An important problem of the old program was, that the calculation of the physical values were distributed over the whole program. After a while they did not correspond to the actual experiment anymore, but it was cumbersome to change the code appropriately. The new program contains all physical calculations in one single file, shown in figure 3.19, which can even be changed during runtime.

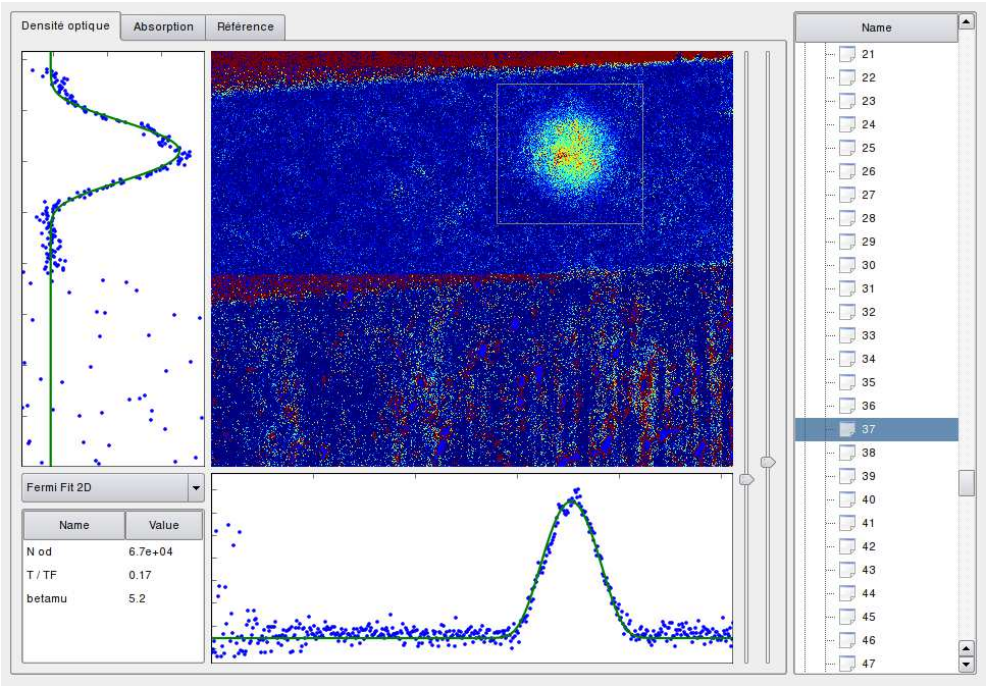

Figure 3.18: The data analysis program while performing a 2D Fermi fit. The program can show the optical density as well as absorption and reference images separately in the center of the screen. Left of the image and below integrals of a selected area are shown, with the fit superimposed. On the lower left the user can select the fitting method, and the fitting results are shown. On the very right is the selection of the images.

```
from scipy.special import erf
from math import pi, sqrt
from pygsl import sf

isotope = p["DetectIsotop"]
if isotope == 6: cgq = 1./2.  # cgq is the clebsch-gordon-coefficient squared
else: cgq = 7./15.
pixelsize = (1./17.3/1000)  # width of a pixel, in m
detuning = p["Probe7PrincipalDetuning"] # laser detuning, in MHz
gamma = 5.8724 # linewidth (in MHz)
lamda = 670.992421e-9 # wavelength, sorry, lambda is a reserved word in python...
# the scattering cross section
sigma = (3*cgq*lamda**2) / (2*pi) / (1 + 4 * (detuning / gamma)**2)

if fit == "Gaussian Fit":
        od = Hmax * Hsigma * 2 / ( # od is the optical density
                erf((bottom-Vmu) / (sqrt(2)*Vsigma)) - erf((top-Vmu)
                / (sqrt(2)*Vsigma))) * sqrt(2*pi)
        r["N hor"] = od * pixelsize**2 / sigma
        od = Vmax * Vsigma * 2 / (
                erf((right-Hmu) / (sqrt(2)*Hsigma)) - erf((left-Hmu)
                / (sqrt(2)*Hsigma))) * sqrt(2*pi)
        r["N ver"] = od * pixelsize**2 / sigma
        r["offset H"] = Hoffset
        r["chisq"] = Hchisq
        r["sigma horizontal / mm"] = Hsigma * pixelsize * 1000
        r["sigma vertical / mm"] = Vsigma * pixelsize * 1000
        r["TOF / ms"]=p["MOTImageTOF"]
elif fit == "Fermi Fit":
        max = (Hmax + Vmax) / 2
        od = 2 * pi * max * Hsigma * Vsigma
        r["N od"] = od * pixelsize**2 / sigma
        r["T / TF"] = (6*sf.fermi_dirac_2(Hfermi)[0])**(-1./3.)
        r["chisq"] = Hchisq
elif fit == "Gaussian Fit 2D":
        od = 2 * pi * max * Hsigma * Vsigma
        r["N"] = od * pixelsize**2 / sigma
        r["aspect ratio"] = Hsigma / Vsigma
        r["sigma horizontal / mm"] = Hsigma * pixelsize * 1000
        r["sigma vertical / mm"] = Vsigma * pixelsize * 1000
        r["od"] = max
elif fit == "Fermi Fit 2D":
        od = 2 * pi * max * sigmax * sigmay
        r["N od"] = od * pixelsize**2 / sigma
        r["T / TF"] = (6*sf.fermi_dirac_2(fermi)[0])**(-1./3.)
        r["betamu"] = fermi
elif fit == "Integrate": # simple summation of the optical density
        r["nint"] = integral * pixelsize**2 / sigma
        r["od"] = integral
```

Figure 3.19: The calculation of physical parameters, as it is currently used in the experiment. `fit` is the fitting method selected by the user, `p` contains the settings of the experimental parameters, `r` will be shown on screen. The calculations are done in a "physical" way, one can find, for example, the scattering cross section (equation (3.4)) or the temperature from equation (4.5).

Chapter 4

Data analysis

A correct data analysis is crucial to every experiment. In experiments on cold atoms, the raw data is normally the density distribution of the atoms acquired using absorption imaging techniques. Most often, the total number of the atoms and the extent of the cloud in the two directions is sufficient to interpret the data and can be achieved easily by performing an appropriate fit on the atomic distribution. Here we want to focus on a more advanced method of data analysis: firstly, the shape of the cloud contains important information about the temperature of the cloud, which can be extracted using appropriate fitting functions. Secondly, the cloud we see on the computer screen is only a two dimensional projection. Knowing that the original cloud has rotational symmetry, we can reconstruct the three dimensional distribution of the atoms.

4.1 Determination of the temperature of a fermionic gas

The temperature of a classical gas in a trap can be determined easily: after a time-of-flight expansion, the momentum distribution of the gas is known from which the temperature can be easily calculated. The case of a bosonic gas is very different: once the gas has condensed into a Bose-Einstein-Condensate, the fraction of the non-condensed atoms is directly related to the temperature of the gas. At very low temperatures, the condensate becomes nearly pure, and a temperature measurement becomes a task that is difficult to accomplish. The case of a fermionic gas is as tricky. At low temperatures, especially below the Fermi temperature, the momentum distribution shows no changes except that the smearing of the step in the Fermi distribution.

In order to determine the temperature of the gas, we release the atoms from their trap and study the momentum distribution. Since the gas is in the trap, this distribution will not have the shape of a Fermi distribution – the chemical potential varies in the trap. Instead, we obtain a bell-shaped distribution. At higher temperatures the width of this curve gives the temperature, while at low temperatures the width stays constant. This is an effect known as the *Fermi pressure* [14,15]. We determine the temperature of a fermionic cloud by fitting an image of the cloud to a theoretical function, which we want to develop in this section.

One of our former group members, Julien Cubizolles [71], has developed a fit based on the Sommerfeld approximation of the Fermi function. This fitting routine was useful, while limited, since he used approximations only valid in a certain temperature range, leading to a divergence of the fit once out of this range. A variation of the method we present here has been used in the group at Duke University. They claim that the fitting function developed here can also be used with a strongly interacting gas if one introduces and additional calibration parameter [31]. They developed a new technique to determine this parameter: they released the gas from the trap for a short while, recapturing it afterwards. The gas heats during this time in a controlled way. This way they created a reference scale using which they could determine the calibration parameter for their fitting routine.

Via absorption imaging, one measures the density of atoms integrated over the line of sight. Traditionally we integrate over a second direction to get a resulting curve which can then be fitted to a function. In case of a non-interacting Fermi gas, the density can be easily calculated.

For fermions, the occupation probability follows the well-known Fermi-Dirac distribution

$$f(E) = \frac{1}{e^{\beta(E-\mu)} + 1} \text{ with } \beta = \frac{1}{k_B T} \tag{4.1}$$

μ is the chemical potential. Using the local density approximation, the phase space density $w(\mathbf{r}, \mathbf{k})$ in a harmonic trap is given by

$$w(\mathbf{r}, \mathbf{p}) = (2\pi\hbar)^{-3} \left(e^{\beta\left(\frac{\mathbf{p}^2}{2m} + \frac{1}{2}m\sum_j \omega_j^2 \mathbf{r}^2 - \mu\right)} + 1 \right)^{-1} \tag{4.2}$$

As we want to use these functions to fit our data, we need to integrate over four or five dimensions, depending on whether we want to do a two- or one-dimensional fit. One should remember that we do not normally

see the spatial dimension of the cloud, but rather the momentum space since we do a time-of-flight measurement. Such an integration of two variables leads to:

$$\begin{aligned} n_{2D}(p_x,p_y) &= \int w(\mathbf{r},\mathbf{p})d\mathbf{r}dp_z \\ &= (2\pi^3\hbar^3 m\beta^2\omega_x\omega_y\omega_z)^{-1}\int_0^\infty \left(e^{\frac{\beta}{2m}(p_x^2+p_y^2)-\beta\mu+u^2}+1\right)^{-1} 2\pi^2 u^3 du \\ &= \frac{1}{2\pi}\frac{\beta}{m}6N\left(\frac{T}{T_F}\right)^3 F_1\left(\beta\mu-\frac{\beta}{2m}(p_x^2+p_y^2)\right) \\ &= \frac{N}{2\pi}\frac{\beta}{m}F_1\left(\beta\mu-\frac{\beta}{2m}(p_x^2+p_y^2)\right)/F_2(\beta\mu) \end{aligned} \tag{4.3}$$

$$\begin{aligned} n_{1D}(p_x) &= \int w(\mathbf{r},\mathbf{p})d\mathbf{r}dp_y dp_z \\ &= (\sqrt{2m\beta^5}\pi^3\hbar^3\omega_x\omega_y\omega_z)^{-1}\int_0^\infty \left(e^{\frac{\beta p_x^2}{2m}-\beta\mu+u^2}+1\right)^{-1}\frac{8\pi^2}{3}u^4 du \\ &= \frac{1}{\sqrt{2\pi}}\sqrt{\frac{\beta}{m}}6N\left(\frac{T}{T_F}\right)^3 F_{3/2}\left(\beta\mu-\frac{\beta p_x^2}{2m}\right) \\ &= \frac{N}{\sqrt{2\pi}}\sqrt{\frac{\beta}{m}}F_{3/2}\left(\beta\mu-\frac{\beta p_x^2}{2m}\right)/F_2(\beta\mu) \end{aligned} \tag{4.4}$$

with $F_j(x) = \frac{1}{\Gamma(j+1)}\int_0^\infty \frac{t^j}{\exp(t-x)+1}dt$ the complete Fermi-Dirac integral, which is easily available as a function in the GNU Scientific Library [94].

What information can we infer from such a fit? There are three parameters in the fit functions. The constant in front of the function will determine the height of the distribution and thus the number of atoms, while the two other parameters both contain β, which is the inverse temperature. The argument of the function F contains two terms: the first one $\beta\mu$ corresponds to the Fermi pressure. For high temperatures it is small, and the resulting distribution resembles a Gaussian, as the function F resembles an exponential. The width of the distribution at high temperatures is given by the other term in the argument, the kinetic energy term. Interestingly we only have one width parameter even in the two-dimensional case, resulting from the isotropy of the gas. At low temperatures, $\beta\mu$ becomes important and leads to a much

broader distribution than what one would expect from the kinetic energy term. This parameter is already interesting in itself since it is a unitless physical parameter of the trapped gas. In addition, it is strongly related to the parameter this whole fitting was developed for: the ratio T/T_F. To see this, we integrate over all dimensions:

$$\begin{aligned} N &= \int w(\mathbf{r},\mathbf{p}) d\mathbf{p} d\mathbf{r} \\ &= (\beta^3\hbar^3\omega_x\omega_y\omega_z\pi^3)^{-1} \int_0^\infty (e^{u^2-\beta\mu}+1)^{-1}\pi^3 u^5 du \\ &= (\beta^3\hbar^3\omega_x\omega_y\omega_z)^{-1} F_2(\beta\mu) = 6N\left(\frac{T}{T_F}\right)^3 F_2(\beta\mu) \end{aligned} \tag{4.5}$$

Meaning that $T/T_F = (6F_2(\beta\mu))^{-1/3}$. This is the parameter we are finally interested in.

Once we have calculated those functions, we use the least square fitting function "leastsq" of SciPy [93] to fit them to our data. Figure 4.1 shows a one-dimensional fit of n_{1D} to the integrated optical density. One can see that the Fermi function gives a better fit than a Gaussian, especially in the wings, where the information about the temperature lies.

The quality of a fit is usually measured by means of the χ^2 test. We calculate the sum of squares of the differences between the fitting function and the data points. For normalization, this has to be divided by the variance of a single datapoint. This is commonly divided by the number of datapoints reduced by the number of parameters, which is called the reduced χ^2. Correctly normalized, one can thus compare different fitting methods. The lower the reduced χ^2, the better the fitting function suits the data. A value of $\chi^2 = 1$ represents an optimal fit. Values significantly below 1 are usually caused by major mistakes during the data analysis.

In the the one-dimensional case, the reduced χ^2 is 1,06 for the Fermi fit, but 1,16 for the Gaussian, for the sample in the figure. The two-dimensional fit has a typical χ^2 of 1,2 for a Fermi function, while it is at 1,7 for a Gaussian function. The higher χ^2 value for those fits first seems to make them unfavorable, but the higher difference in χ^2 between a Gaussian and a Fermi fit shows that the two-dimensional fit is better suited to attain an information about the temperature. Nonetheless, the higher value for the two-dimensional fit is an artifact in most cases. Our images often show a fluctuating offset in the vertical direction. As we did

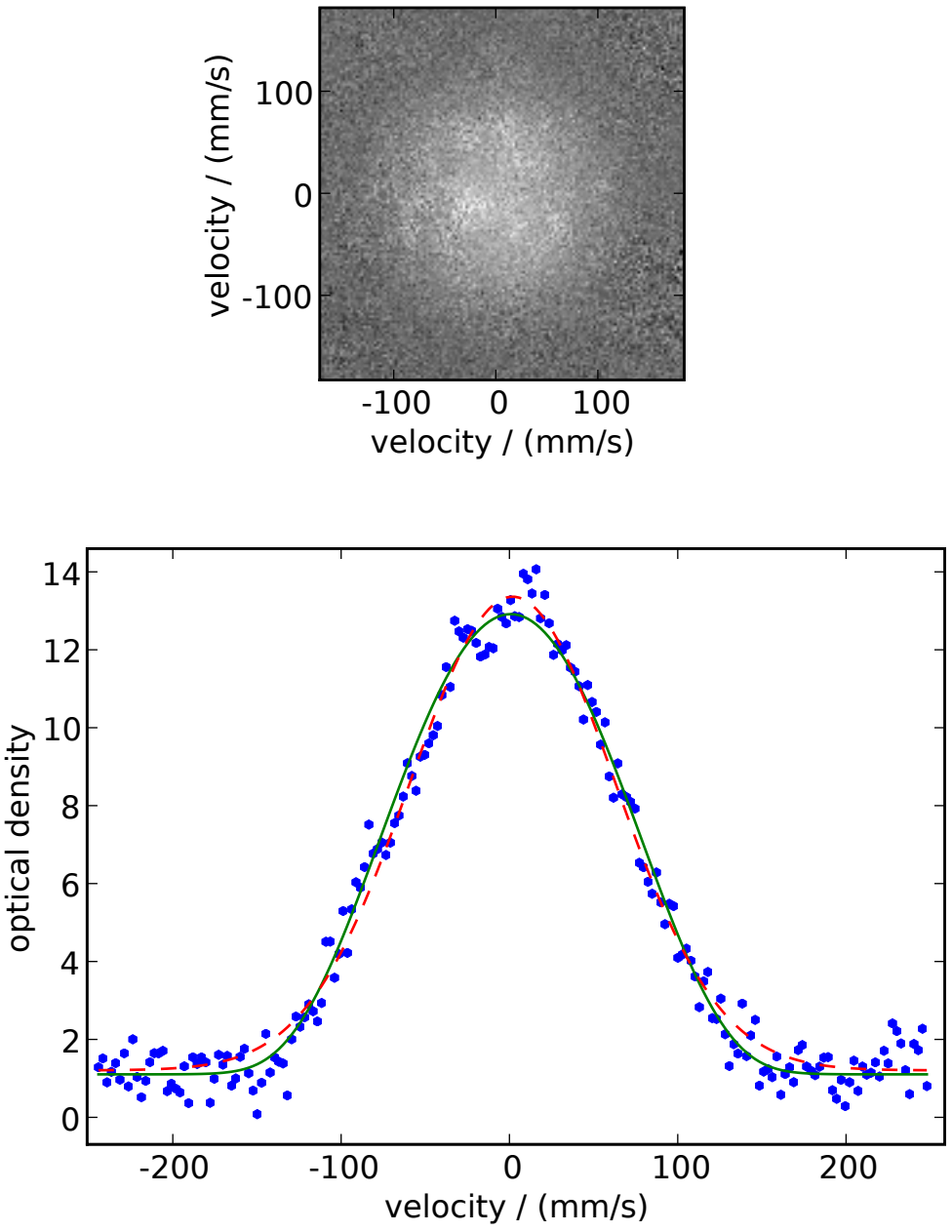

Figure 4.1: An example for a Fermi gas. The upper picture shows the optical density in a false-color plot. The lower picture is an integration over the vertical axis. The solid line is a fit with the Fermi-Dirac integral, while the dashed line shows a fit with a Gaussian for comparison. The parameters of the solid curve are $T = 0{,}7\,\mu\mathrm{K}$, $T/T_\mathrm{F} = 0{,}2$ and $N = 1{,}4 \cdot 10^5$

the one-dimensional fits in the horizontal direction, these fluctuations are simply averaged out for the one-dimensional fit.

While using the fit, it is important to check that the fitting algorithm correctly finds the baseline of the data, as the temperature information is mostly in the wings of the function which are just misplaced if the baseline is incorrect. It turns out that in most of the cases, the Fermi fit is much better at finding the baseline than the Gaussian fit. If this is not the case, the data is most likely too bad to give any information about the temperature, since the reason why the baseline could not be found is that the algorithm could not find the typical sharp wings of the Fermi function.

At very low temperatures, the shape of the expanded cloud shows no changes. This makes fitting problematic and casts doubts on its result. Thus, we tested the algorithm by letting it fit theoretical distributions where a Gaussian noise was added. The results are shown in figure 4.2. This shows that the one-dimensional fit is reliable below $T = 0{,}7T_F$, given reasonable noise levels. The error is around $0{,}1T_F$, and as this becomes slightly bigger for lower temperatures, we are not able to measure temperatures below $0{,}15T_F$, this is also where we stopped the simulation. At high temperatures, we do not have need for this fit, as we can take the size of the cloud as a measure for the temperature. The same simulation performed for the two-dimensional fit appears to be more stable at first sight, given the much higher noise levels the fit works at. This appearance is deceptive, since for the one-dimensional fit we average over one direction, giving us much lower noise levels than in two dimensions. In practice, the difference between the two fitting methods is negligible. The noise on the data is normally below 30 % for the two-dimensional fit, and below 3 % for the one-dimensional.

4.2 Three-dimensional reconstruction

In most of the experiments we have at least one axis of symmetry. This enables us to deconvolute the data to get the original distribution, not integrated over the line of sight. In the case of cylindrical symmetry, we have to cut the image into slices perpendicular to the axis of symmetry, and deconvolute each slice. In the case of spherical symmetry, we could do the same, since spherical symmetry is cylindrical symmetry with an additional symmetry axis. We can make use of this additional axis. We find the center of the distribution and integrate over same distances around this central point. This gives a one-dimensional distribution

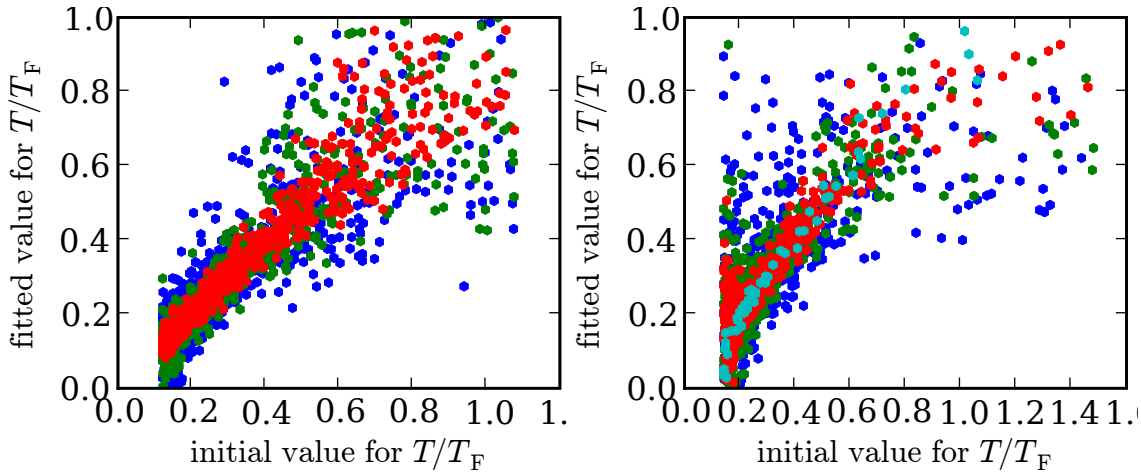

Figure 4.2: The stability of the fit. The graph shows the fitted values for a distribution with a given value for T/T_F with Gaussian noise added. On the left graph a one-dimensional fit is performed. The noise level is 1 % for the innermost, light, points, 2 % for the intermediate points and 3 % for the outer, dark points. The right panel shows the same for a two dimensional fit. Noise levels are 30 % for the outermost, dark points, 20 % and 10 % for the intermediate shades and 5 % for the light curve.

which is then to be deconvoluted.

Both cases can be treated with the same mathematical method. The one-dimensional distribution $\rho(k)$ is

$$\rho(k_r) = \int_{-\infty}^{\infty} n(\sqrt{k_r^2 + k_z^2})dk_z \tag{4.6}$$

with k_r being the distance from the axis for cylindrical symmetry or the distance from the center for spherical symmetry. k_z is the line of sight over which we integrate. We take a Fourier-transform of both sides and change to polar coordinates to obtain

$$\hat{\rho}(r) = \int_{-\infty}^{\infty}\int_{-\infty}^{\infty} n(\sqrt{k_r^2 + k_z^2})e^{ik_r r}dk_z dk_r = 2\pi\int_0^{\infty} n(k_\rho)J_0(rk_\rho)k_\rho dk_\rho \tag{4.7}$$

J_0 is the zero order Bessel function. The last part of this equation is the Hankel-transform. This transform is its own inverse, which allows us to calculate the original distribution n in terms of the measured distribution ρ as

$$n(k) = \frac{1}{2\pi}\int_0^{\infty} \hat{\rho}(r)J_0(kr)rdr \tag{4.8}$$

In total, this gives us a good method for deconvoluting the data: we first Fourier-transform the data, which is easily done using the fast Fourier transform algorithm, and then use the Hankel transform. As the Hankel transform is linear, it is just a matrix multiplication whose coefficients can be calculated analytically [95].

We tried this deconvolution on both spherical and cylindrical symmetric data. It works well in the case of spherical symmetry and has been used to create the curves presented in chapter 5 for the momentum distribution curves, which are spherically symmetric. The cylindrically symmetric data, however, namely the hydrodynamic expansion later described in that chapter, is by far too noisy to be deconvoluted. This is because the summation over same distances done for the spherical symmetric data has an important smoothing effect, which is not possible for cylindrically symmetric data.

Chapter 5

Experimental results

Well roared, Lion.
– W. Shakespeare *A Midsummer Night's Dream*

The heart of an experimental physics thesis is the presentation of the results achieved in the experiment. Our interest is to study superfluidity in the BEC-BCS crossover. The two main sections of this chapter are devoted to the study of the momentum distribution and the hydrodynamic expansion of a gas in the crossover region. An outline of similar experiments reported by other groups will be given. In addition, we developed a new analysis of an older experiment on molecular BECs. We accompany these experiments with measurements of the creation of molecules happening while crossing the Feshbach resonance. We extended the older experiments using slow magnetic field sweeps to high sweep rates.

Finally results on heteronuclear Feshbach resonances are presented, with initial measurements on this interesting extension of our current work.

5.1 Momentum distribution

One of the main ingredients to BCS theory is the prediction of the the momentum distribution for superfluid fermions: even at zero temperature, it does not follow a Fermi-Dirac distribution as one would expect but the step of this distribution is smeared out. At zero temperature, the momentum distribution resembles closely the Fermi distribution of a non-interacting gas at the condensation temperature. The momentum distribution is accessible in experiments (this is illustrated in figure 2.8).

If we switch off both the trapping potential and the interactions at the same time, the gas will expand freely and the momentum distribution gets mapped onto a distribution in real space which we can measure using absorption imaging.

In this section, we want to calculate the momentum distribution in the BEC-BCS crossover and compare it to experimental data. The momentum distribution is directly connected to the microscopic behavior of the atom, thus we can derive it directly from BCS theory. Wherever possible, we compare to more advanced theories.

From the gap and number equations (2.34) and (2.35), we can calculate μ and Δ for a given scattering length a and density n. In our case, this is not necessarily a simple task as the density n is not constant since the atoms are in a harmonic trap. Therefore, we need to solve the equations at each point $\mathbf{r}$ in the trap. After the gas has expanded, we measure the momentum distribution, so we have to integrate the density at each point over the whole space,

$$n(\mathbf{k}) = \int \frac{d^3r}{(2\pi)^3} n_{\mathbf{k}}(\mathbf{r}) = \int \frac{d^3r}{(2\pi)^3} \left(1 - \frac{\varepsilon_k - \mu(\mathbf{r})}{\sqrt{(\varepsilon_k - \mu(\mathbf{r}))^2 + \Delta^2(\mathbf{r})}}\right) \tag{5.1}$$

leaving us with the problem of determining the local parameters μ and Δ. In order to determine μ we use the local density approximation. We consider the "global" chemical potential μ to be constant over the whole cloud, which is the sum of the local chemical potential and the external potential: $\mu = \mu(\mathbf{r}) + V_{\text{ext}}(\mathbf{r})$.

5.1.1 Unitarity limit

Let us start with the distribution at the unitarity limit, where $a = \pm\infty$. This has the advantage that the left side of equation (2.34) vanishes, and gives us a simple proportionality between μ and Δ. As we have seen in section 2.4.5, the chemical potential can be written as $\mu(r) = (1+\beta)E_F(r)$, with $1+\beta$ being a unitless proportionality constant.

The local Fermi energy is $\tilde{E}_F = \frac{\hbar^2 \tilde{k}_F^2}{2m}$, and with the Fermi wave vector $\tilde{k}_F^3 = 6\pi^2 n$ we can directly calculate the density as

$$n(r) = \frac{1}{6\pi}\left(\frac{2m}{\hbar^2(1+\beta)}\right)^{3/2}\left(\mu - \frac{1}{2}m\omega^2 r^2\right)^{3/2} \tag{5.2}$$

and upon normalization (see also Appendix C of [71]) leads to $\mu = \hbar\omega(6N)^{1/3}\sqrt{1+\beta}$.

Now we have all the ingredients together, we can just plug everything into 5.1, which leads to [96]

$$n(k) = \frac{(1+\beta)^{3/4}}{2\pi k_F^3} \int_0^1 \left(1 - \frac{k^2/k_F^2 - \sqrt{1+\beta}(1-r^2)}{\sqrt{\left(\frac{k^2}{k_F^2} - \sqrt{1+\beta}(1-r^2)\right)^2 + \frac{(1-r^2)^2}{1+\beta}(\frac{\Delta}{E_F})^2}} \right) r^2 dr \tag{5.3}$$

The parameter $k_F = (48N)^{1/6}/a_{ho}$ is the Fermi wave vector for a noninteracting gas in a harmonic trap with a harmonic oscillator length of $a_{ho} = \sqrt{\hbar/m\omega}$. This integral can only be solved numerically. Using the mean-field BCS theory as described in section 2.4, the parameter Δ/E_F appearing in the denominator can be calculated from the gap and number equations and is found to be $\Delta = 0{,}69E_F$.

5.1.2 The crossover

The problem becomes more complicated once we leave the unitarity limit. The relationship between the Fermi energy and the chemical potential is no longer linear. For simplicity, we use BCS theory, as it can be written in a closed form. More complicated treatments have been proposed [97], but the differences are not large enough to be seen in our experiment.

We introduce the unitless variables[1] $x^2 = \varepsilon_k/\Delta$ and $x_0 = \mu/\Delta$. After replacing the sums by integrals, the gap and number equations respectively read as

$$\frac{1}{a} = \sqrt{2m\Delta}\mathcal{G}(x_0) \qquad\qquad n = \frac{1}{2\pi^2}(2m\Delta)^{3/2}\mathcal{N}(x_0) \tag{5.4}$$

where we have introduced the gap and number integrals

$$\mathcal{G}(x_0) = \frac{2}{\pi}\int_0^\infty \left(\frac{1}{x^2} - \frac{1}{\sqrt{(x^2-x_0)^2+1}}\right) x^2 dx \tag{5.5}$$

$$\mathcal{N}(x_0) = \int_0^\infty \left(1 - \frac{x^2-x_0}{\sqrt{(x^2-x_0)^2+1}}\right) x^2 dx \tag{5.6}$$

These integrals have been solved analytically by means of elliptic integrals [98]. We can use them to calculate the functions appearing in

[1] The square in the presented substitution is purely technical, it later brings the equations into the form of an elliptic integral.

equation (5.1):

$$\Delta(x_0) = E_F(x_0)\left(\frac{2}{3\mathcal{N}(x_0)}\right)^{2/3} \tag{5.7}$$

$$\frac{1}{a\tilde{k}_F(x_0)} = \left(\frac{2}{3\mathcal{N}(x_0)}\right)^{1/3}\mathcal{G}(x_0) \tag{5.8}$$

The parameter x_0 can be calculated using

$$\mu(x_0) = x_0\Delta(x_0) = x_0\frac{\hbar^2}{2ma^2}\mathcal{G}^{-2}(x_0) = \mu_0 - \frac{1}{2}m\omega^2 r^2 \tag{5.9}$$

which we substitute into equation (5.1) to become:

$$n(k) = \frac{a_{ho}^6}{2a^3}\int_{x_0\Delta(x_0)=\mu_0}^{\infty}\left(1 - \frac{a^2k^2\mathcal{G}^2(x_0) - x_0}{\sqrt{(a^2k^2\mathcal{G}^2(x_0) - x_0)^2 + 1}}\right) \cdot\sqrt{\frac{4\mu_0 a^2 m}{\hbar^2} - \frac{x_0}{\mathcal{G}^2(x_0)}}\frac{\mathcal{G}(x_0) - 2x_0\mathcal{G}'(x_0)}{\mathcal{G}^3(x_0)}\frac{dx_0}{(2\pi)^3} \tag{5.10}$$

This function is plotted in figure 5.1 for different values of $k_F a$. In the same graph, we show the distribution in the unitarity limit (equation (5.3)) and in the limiting cases of a noninteracting gas, using the same equations as in chapter 4. Furthermore, we show the momentum distribution of a molecular condensate that we will discuss in the next section. One sees that the transition between the different parameter ranges are smooth, although they are derived from different formulae. The steepest curve corresponds to the noninteracting gas. It actually goes to zero at the Fermi momentum. The central density decreases while traversing the crossover, and the distribution broadens.

5.1.3 Molecular condensate

For weak repulsive interactions, meaning that $0 < k_F a \ll 1$, the atoms form deeply bound molecules, as seen at the end of section 2.3. In this case the binding energy of the molecules dominates over the interaction energy, and the momentum distribution is determined by the molecular wavefunction.

In section 2.4.4 we saw that in the molecular regime, the chemical potential becomes negative and the gap becomes large, as shown in figure 2.7. This means that $x_0 = \mu/\Delta \to -\infty$. We can develop equation

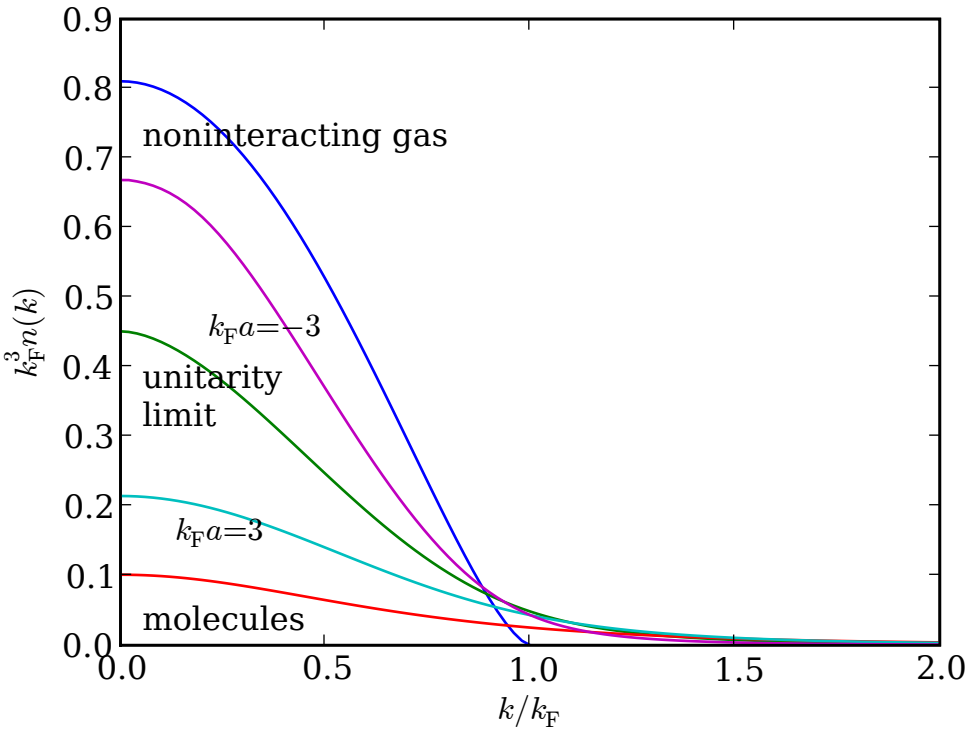

Figure 5.1: The calculated momentum distributions in a harmonic trap. The curves are normalized to $\int_0^\infty n(k)k^2dk = 1$. The areas under the curves are not equal as the number of atoms is proportional to the density multiplied by the surface of the sphere with radius k. k_F is the Fermi wave vector calculated for the noninteracting gas.

(5.8) for $x_0^{-1} \to -0$ and get $na^3 = 3\pi/16x_0^2$, or $\Delta^2 = 16E_F^2/3\pi k_F a$. We also find that $x_0/\mathcal{G}^2(x_0) \to -1$ for $x_0 \to \infty$. Then from (5.9) we see that $\mu = -\hbar^2/2ma^2$. This is exactly the binding energy of a molecule that is been found in equation (2.25). Developing the summands in the number equation (2.35) for small values of Δ/μ, in combination with the result from this paragraph, leads to

$$n_k = \frac{4}{3\pi}(k_F a)^3 \frac{1}{(k^2a^2+1)^2} \tag{5.11}$$

This result is very interesting as it is the Fourier transform of a molecular bound state. This means that the center of mass motion of the molecules is condensed into $p = 0$ and only the relative motion of the atoms in the molecule is relevant. This shows that in the BEC limit the BCS wavefunction indeed describes a Bose-Einstein-Condensate of molecules.

5.1.4 Experiments

We measure the momentum distribution at three different magnetic fields: at the unitarity limit at 83 mT, in the molecular regime and on the BCS side of the Feshbach resonance.

We perform evaporative cooling as described in section 3.6. At the end of this cooling stage we lower both trapping lasers to 10% of their initial power, leading to transverse trapping frequencies of 2 kHz in both the horizontal and vertical beam. The desired field is then ramped in 500 ms to the desired magnetic field.

At this point we would like to verify that we are indeed sufficiently cold to be condensed into the superfluid state. The easiest way to achieve that is to ramp the field to the BEC side of the resonance and let the gas expand in the presence of the field. If the expanded gas is elliptic, we know that the gas is Bose-Einstein condensed (we will go into more details on this in section 5.3). But this will only happen if the trap is non-isotropic in the observed plane, which is not the case. Therefore, we recompress the horizontal beam in 200 ms to a trap frequency of 5,5 kHz. Technically, it would not be necessary to recompress the horizontal beam for the momentum distribution experiments, but as it does not disturb the momentum distribution we prefer to keep the verified state as is.

At the end, we switch off the trap, which takes about 5 μs. The gas expands for 0,5 ms, after which we take an absorption image. In order to reconstruct the three-dimensional distribution, we perform an inverse Abel transform as described in section 4.2.

While taking these measurements, we realized that we were not imaging all the atoms. Instead, a non-negligible part of the atoms formed molecules during the switch-off of the magnetic field, which are invisible to our absorption imaging. We will discuss this in detail in the next section.

These lost atoms are the only unknown parameter that prevents us from comparing directly to theory. We determine this loss parameter by fitting the measured data to the theory in the BCS limit, as this is the region where our theory is most trustworthy. This is shown in figure 5.4. Once we know this factor, we can plot theory and experiment in the same graph for other positions in the crossover. Figure 5.2 shows this in the unitarity limit. From this figure, it is seen that the BCS theory slightly overestimates the broadening of the cloud. This was already predicted by Astrakharchik *et al.*. We integrated their prediction (see figure 2.8) over the trap and included the result in figure 5.2. We see that their theory underestimates the broadening. Figure 5.3 shows the experiments in the BEC region at 78 mT. Again we see that BCS theory overestimates the broadening, as predicted by Astrakharchik *et al.* Unfortunately, in this case we cannot compare to their theory as the local Fermi wave vector $\tilde{k}_F$ varies over the trap, and they calculated the momentum distribution only for a specific value of $\tilde{k}_F a$.

Similar experiments have been performed by the JILA group [99]. They study the momentum distribution in a gas of ^{40}K. They fit their data to an empirical function, which enables them to quantify the broadening of the distribution. There is an important difference between the two experiments: as the Feshbach resonance in ^{40}K is shaped differently, there is no need to cross the Feshbach resonance in order to take absorption images and thus they have no losses from molecule formation. They use a more detailed theory which includes the ramp to zero field [97]. Similar to us, they find that the mean-field BCS theory underestimates the broadening of the distribution. In a second experiment, they analyzed the temperature dependency of the distribution [100].

5.2 Molecule creation

When measuring the momentum distribution of the atoms, we assumed that the magnetic field switch off happens instantaneously. Certainly, this can never be exactly true. With only 5 μs, the switch off of the coils is very fast and we expected this to be sufficient. Nevertheless, we found that in experiments where we switch off the coils *after* the expansions

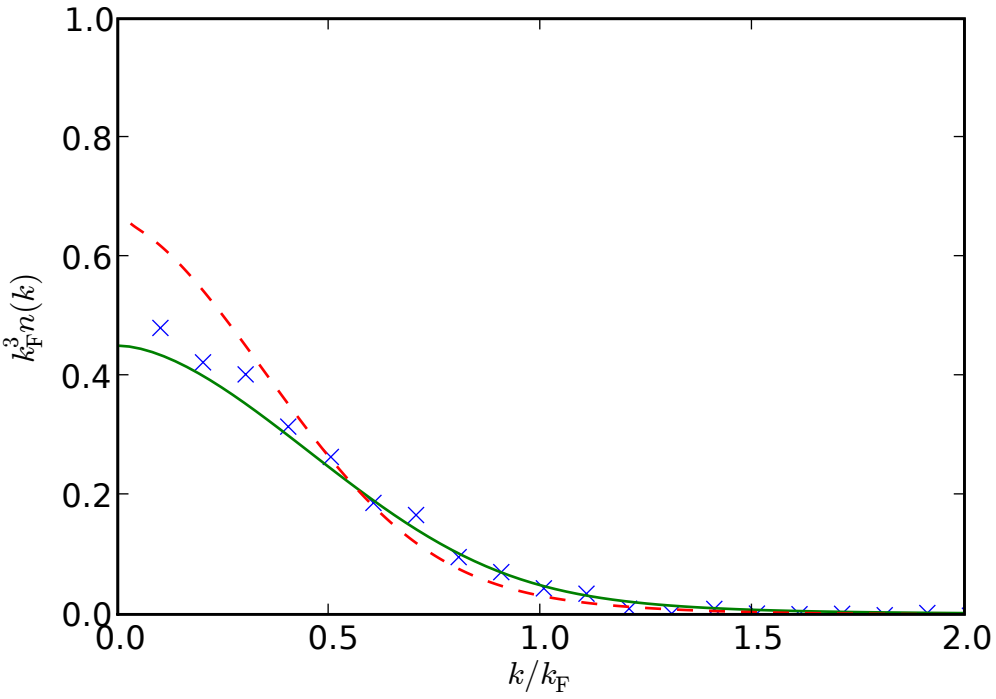

Figure 5.2: The momentum distribution of a gas at the unitarity limit. The crosses are the inverse Abel transform of the cloud. The solid curve is the distribution at zero temperature as calculated in section 5.1.1. The dashed line is the prediction by Astrakharchik *et al.* [70]. The data is averaged over three images.

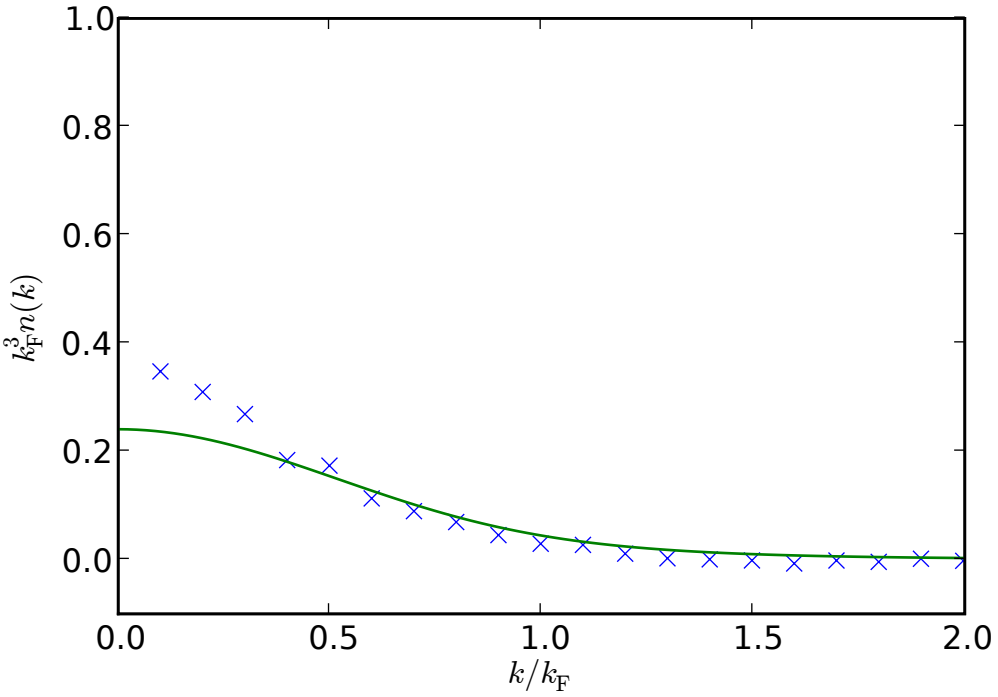

Figure 5.3: The momentum distribution of a gas in the molecular regime. $k_F a = 3$, with about $1{,}5 \cdot 10^5$ atoms. The data (crosses) is averaged over three images. The solid line shows the theoretical predictions explained in the text.

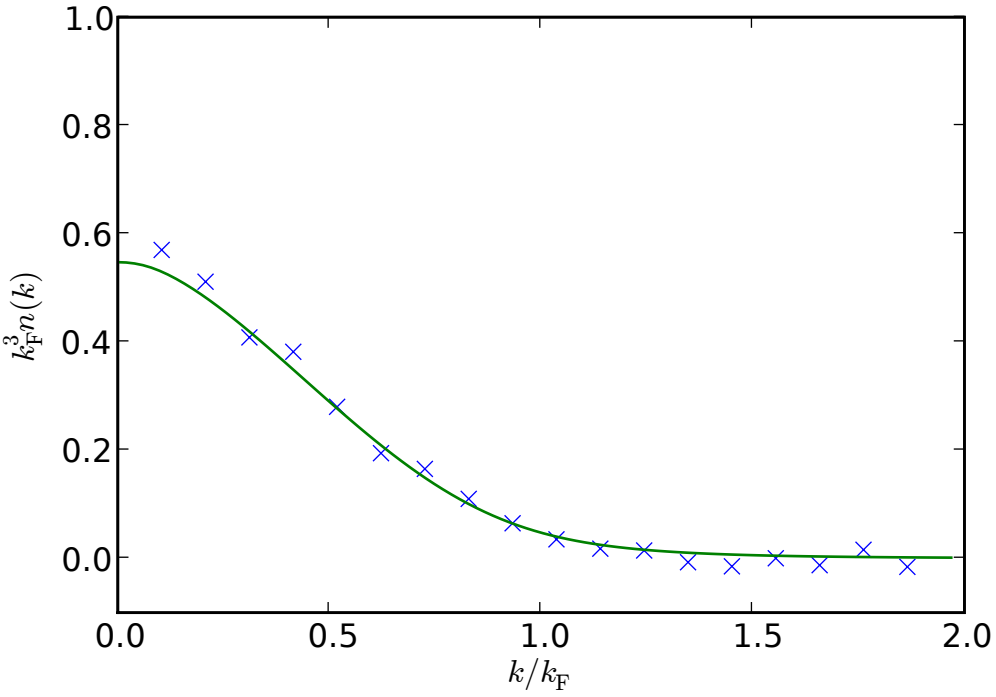

Figure 5.4: The momentum distribution of a gas on the BCS side of the resonance. $k_F a = -3{,}5$, with about $1{,}5 \cdot 10^5$ atoms, averaged over two images. The crosses are the experimental points, while the solid line shows the BCS predictions (see text).

systematically had higher optical density than the momentum distribution experiments, where the coils get switched off before expansion.

This convinced us that we were creating molecules while ramping the field, which cannot be seen in absorption imaging. If we leave the magnetic field on during the expansion, the density of the cloud decreases, down to densities too low to create molecules during the magnetic field switch off.

We did a systematic scan of this effect, since it could be crucial to the validity of our data. We let the atoms expand for a variable time τ in the magnetic field, switch it off and let the atoms expand for 0,5 ms more before imaging them. Figure 5.5 shows the detected number of atoms after this procedure. One can clearly see that for short expansion times, less atoms are detected than for long expansion times. During the expansion, the density of atoms drops and less atoms get converted into molecules.

We can fit this result to a simple Landau-Zener model [101, 102]. In this model we treat the Feshbach resonance as an avoided crossing of the molecular and the atomic levels, similar to figure 2.4. When sweeping the magnetic field infinitely slowly coming from infinitely high magnetic fields over the resonance, the atoms should follow adiabatically into the molecular state. At faster ramping speeds, the atoms can change into the atomic state. This change is possible while they are in the resonance region, during a time $\Delta B/\dot{B}$, where ΔB is the resonance width from section 2.3, and $\dot{B}$ is the sweeping rate. The typical time for an interaction is the time t_{inter} the atoms are close to each other in the open channel of the resonance, and is thus proportional to the density n. A detailed analysis by Góral *et al.* [103] leads to $t_{\text{inter}} = 4\pi\hbar a_{\text{bg}} n/m$.

The presented model is only a crude simplification of the real process. We do not start the magnetic field sweep at infinite magnetic field, but instead from the center of the resonance. The sweep is also not slow, but actually faster than all relevant time scales, the fastest being the interaction time, which is about $t_{\text{inter}} = 10\,\mu\text{s}$. Using a mean field approach to calculate this time is also questionable given the strength of the interactions. Despite these problems, we will see that this model gives a good qualitative and even reasonable quantitative description of the observations.

According to the Landau-Zener theory, the probability of changing states is the exponentially suppressed ratio of the time to cross the resonance by the interaction time t_{inter}:

$$P = e^{-An/\dot{B}} \tag{5.12}$$

where $A = 4\pi\Delta B a_{bg}/m$ is a parameter which contains the details of molecule creation. During the expansion, the radius of the cloud changes as $r^2(t) = r_0^2(1 + \omega^2 t^2)$, where ω is the trap frequency. Therefore, the density changes as $n(t) = n_0/(1 + \omega^2 t^2)^{3/2}$. We insert this into equation (5.12) and fit it to our data. This way, we can determine the molecule creation parameter A as $A = 7 \cdot 10^{-15}\,\mathrm{Tm}^3/\mathrm{s}$. This is about three times larger than the value measured by the MIT group, where $A = 2{,}4 \cdot 10^{-15}\,\mathrm{Tm}^3/\mathrm{s}$ [104]. Calculating A using the values from table 2.1 gives $A = 1{,}9 \cdot 10^{-15}\,\mathrm{Tm}^3/\mathrm{s}$. This agrees rather well with the experimental values, given the approximations explained above.

It should be mentioned that the fit is best when we take the time zero of the expansion to be $50\,\mu$s before the switch-off of the magnetic coils. This is of the same order as the time between two commands executed by the computer control. In the future, special care should be taken to ensure that this does not happen.

5.3 Hydrodynamic expansion

While the momentum distribution presented in the last section is a good tool to test theories in the BEC-BCS crossover, the superfluidity of the gas is not as apparent. If we leave the magnetic field on while the gas is expanding, it will stay superfluid at least in the beginning of the expansion. Using the equations of hydrodynamics, we can calculate the expansion of the gas, as we will show in this section.

5.3.1 General properties

After we have released the gas from the trap, it will expand ballistically if there is no or only negligible interactions. Since the momentum distribution is isotropic, the expanded cloud will also be isotropic. There is an important exception to this rule: if the atoms in the gas are condensed into a Bose-Einstein condensate, they all occupy the same macroscopic quantum state. The expansion of this quantum state determines the shape of the final cloud, see reference [105] for theoretical calculations of this. In bosons, an anisotropic expansion is a clear signature for Bose-Einstein condensation.

One has to be careful about judging whether an expansion is anisotropic or not: the ellipticity of the expanded cloud is not a clear signature, as the cloud will always be elliptic initially if the trap is not isotropic. An anisotropically expanding cloud will eventually invert its

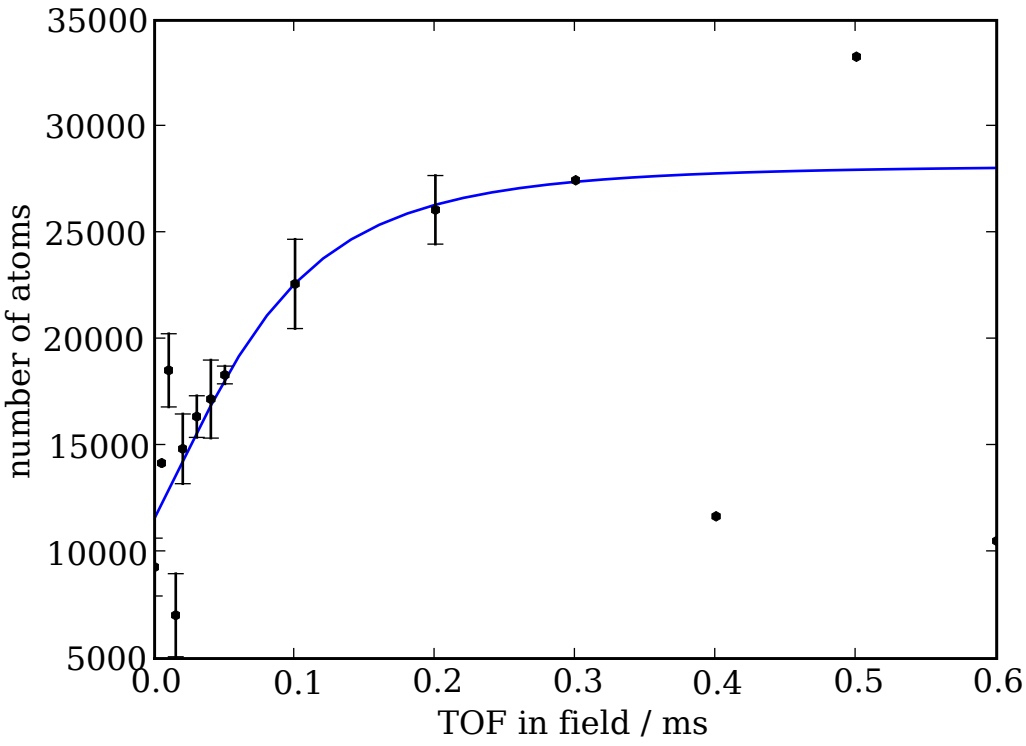

Figure 5.5: The number of detected atoms as function of the time of flight τ in magnetic field at the unitarity limit. The error bars are one standard error, the points without error bars are single points, thus the error is not defined. The line is a fit with the Landau-Zener model described in the text.

ellipticity. As this will never happen for an isotropically expanding cloud, this *ellipticity inversion* is a clear signature of an anisotropic expansion.

The situation with fermions is more complicated. In order to achieve any kind of condensation we need interactions, as the non-interacting Fermi gas shows no phase transition. Therefore we have to treat three different cases: At very low interaction strength, the gas will behave collisionless and show ballistic expansion, this is the *noninteracting* regime. For stronger interactions we enter into the *collisional* regime where the gas behaves like a normal fluid. In both situations, the gas can condense into a *superfluid* below a certain temperature, which is the third case to consider.

We now want to estimate which regime the atoms are in, in our experiment. We calculate the expected collision rate in the gas, and compare it to the relevant time scale in our system, the trapping frequency. The interactions reach their maximum at the unitarity limit, therefore we chose this point as reference.

The scattering rate Γ can be calculated as $\Gamma = n\sigma v$, where n is the density of scatterers, σ is the scattering cross section and v is the average velocity of the atoms. At the unitarity limit, the scattering cross section is $\sigma = 4\pi/k^2$. The average velocity can be calculated from the temperature of the gas to be $v = \sqrt{3k_B T/m}$. Now we can compare this scattering rate with the trap frequency and define the collisional parameter $\phi = \Gamma/\omega$. As we have two different trapping frequencies, we actually have two parameters $\phi_\perp = \Gamma/\omega_\perp$ and $\phi_z = \Gamma/\omega_z = \phi_\perp/\lambda$, with the definitions from section 2.1. To get a typical value for this parameter, we calculate it at the Fermi temperature, and use k_F to calculate the scattering cross section, which leads to

$$\phi_\perp = \frac{(3\lambda N)^{1/3}}{6\pi} \tag{5.13}$$

This calculation can only be approximate, since we have ignored completely the changes in the scattering length k. A detailed calculation by Gehm *et al.* [106][2] showed that we need to correct this value by a temperature-dependent factor shown in figure 5.6. Comparing to their experiments in reference [107], they find that a gas is to be treated as collisional above a collisional parameter of $\phi = 0{,}4$. Our results usually have an atom number around $2 \cdot 10^4$ atoms, and the temperature is typically $T = 0{,}2T_F$. This means that at unitarity we have $\phi_\perp \approx 3$, so

[2]This paper uses the term "collisional hydrodynamics" for what we call the collisional regime. Given that there is no well-established theory for this regime, using the term *hydrodynamic* is a bit adventurous.

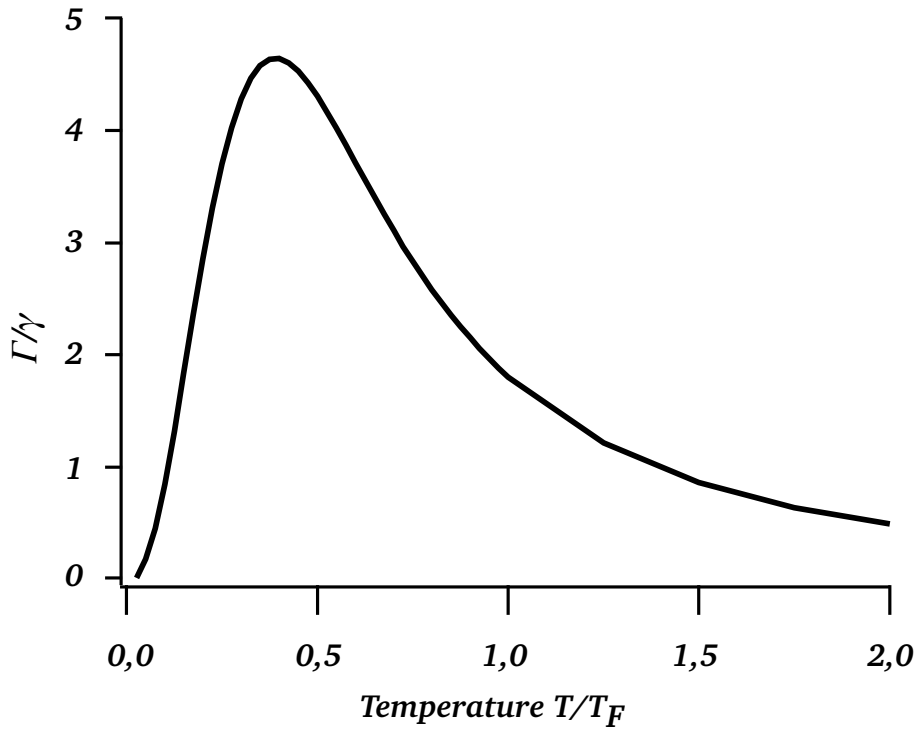

Figure 5.6: The correction factor between the typical scattering rate γ resulting from the calculations in the text and the real scattering rate Γ as a function of the temperature. The scattering rate decreases for high temperatures as does the scattering cross section. At low temperatures the Pauli exclusion principle reduces the scattering rate. This can decrease scattering down to values found in the noninteracting regime, but as the gas condenses at these low temperatures, it will become hydrodynamic. Figure taken from reference [106]

we are clearly in the collisional regime. This changes once we leave unitarity: the scattering cross section will decrease or even vanish at the point where $a = 0$, so that we can expect to enter into the collisionless regime at some point.

In the experiment we want to distinguish the superfluid state from a normal state. Originally, it was proposed to take the same path as for bosons and take the ellipticity inversion as a signature for superfluidity [108]. For the collisional regime, however, it was pointed out by Jackson *et al.* [109] [3] that at very strong interactions the cloud will also show

[3]This paper uses the term "hydrodynamic" only for the superfluid state as we do, opposed to Gehm *et al.*, see last footnote

ellipticity inversion, but this effect is much smaller than the ellipticity resulting from a superfluid cloud.

5.3.2 The scaling ansatz

We now want to calculate the ellipticity of an expanding superfluid. In a superfluid, all particles have condensed into one macroscopic wavefunction ψ. This wavefunction follows the continuity equation of quantum mechanics,

$$\frac{\partial|\psi|^2}{\partial t} + \nabla \mathbf{j} = 0 \tag{5.14}$$

where the probability current $\mathbf{j}$ is defined by $2m\mathbf{j} = \psi\nabla\psi^* - \psi^*\nabla\psi$. We write the wave function as $\psi = |\psi| \exp i\phi$. Then the density is $n = |\psi|^2$ and the probability current becomes $\mathbf{j} = (\hbar/m)n\nabla\phi$. After having defined a velocity $\mathbf{v} = \mathbf{j}/n$, we are left with the continuity equation of classical fluid mechanics:

$$\frac{\partial n}{\partial t} + \nabla(n\mathbf{v}) = 0 \tag{5.15}$$

A superfluid is a liquid with vanishing viscosity. Such a liquid is described by the Euler equation, which reads, after having used the Gibbs-Duhem relation [40], as

$$m\frac{\partial \mathbf{v}}{\partial t} + \nabla\left(\mu(n) + V_{\text{ext}}(\mathbf{r}) + \frac{1}{2}mv^2\right) = 0 \tag{5.16}$$

Now we are supposed to plug in the results from BCS theory, see section 2.4, for the equation of state $\mu(n)$. Unfortunately, this leads to coupled differential equations which are only numerically solvable. A good approximation is to use a polytropic equation of state, $\mu(n) \propto n^\gamma$, where γ is the *polytropic exponent* [108].

Recently, a large amount of literature was published regarding this exponent since it is crucial in describing the Innsbruck [29] and Duke [110] experiments on collective excitations. The idea is to take the real equation of state and calculate an effective polytropic exponent

$$\gamma = \frac{n}{\mu}\frac{\partial\mu}{\partial n} \tag{5.17}$$

which coincides with the actual one for a polytropic equation of state. In section 2.4 we calculated $\mu(n)$, which we could use to calculate γ, shown in figure 5.8. Hu *et al.* [111] improved this approach by averaging over

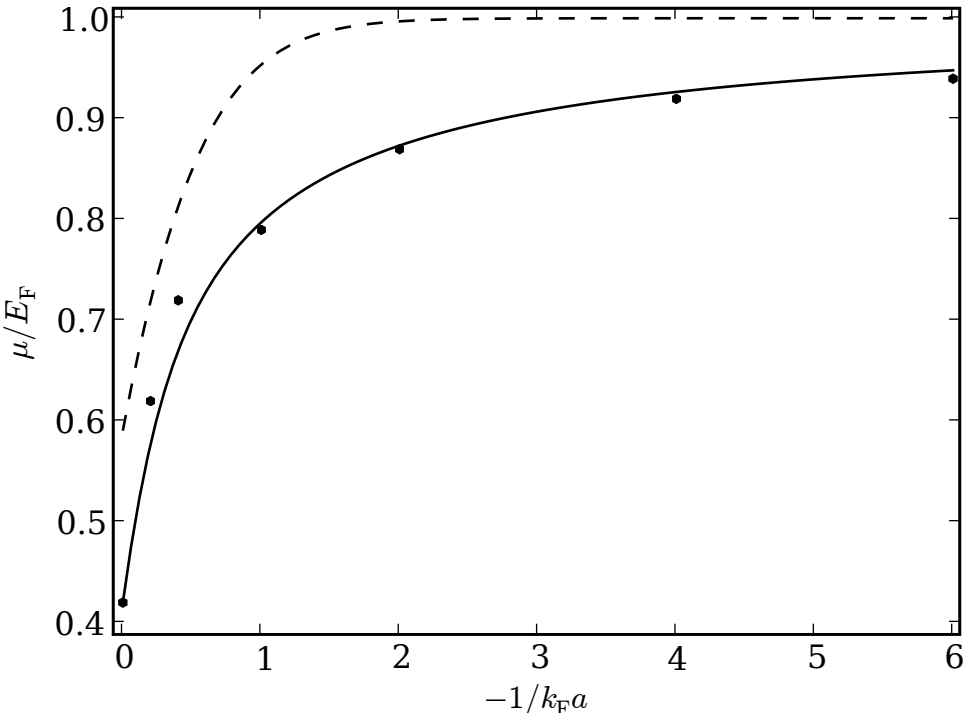

Figure 5.7: The chemical potential as a function of the inverse gas parameter in the homogeneous case. The points are Monte-Carlo simulations from reference [79], the solid line is the fit presented in reference [112], while the dashed line is the prediction from mean-field BCS theory.

the trap. Astrakharchik *et al.* [79] performed a quantum Monte Carlo simulation to achieve a better approximation, and Manini *et al.* [112] used an empiric fitting function to fit their data. The data and the fitted function are presented in figure 5.7. We can use 5.17 to extract the effective polytropic exponent, shown in figure 5.8.

The external potential V_{ext} is the potential of the optical dipole trap. By setting the partial derivatives with respect to time in the Euler equation 5.16 to zero we can find the equilibrium solution $n_0 \propto (\mu_0 - V_{\text{ext}})^{1/\gamma}$. To model the switch-off of the trap, we set V_{ext} to zero for times $t > 0$, and solve the Euler equation (5.16). The choice of a polytropic equation of state now pays back, as we can solve it using the scaling ansatz [113]

$$n(r_x, r_y, r_z, t) = \frac{n_0\left(\frac{x}{b_x}, \frac{y}{b_y}, \frac{z}{b_z}\right)}{b_x b_y b_z} \quad \text{and} \quad u_i(r_i, t) = \frac{\dot{b}_i}{b_i} r_i \tag{5.18}$$

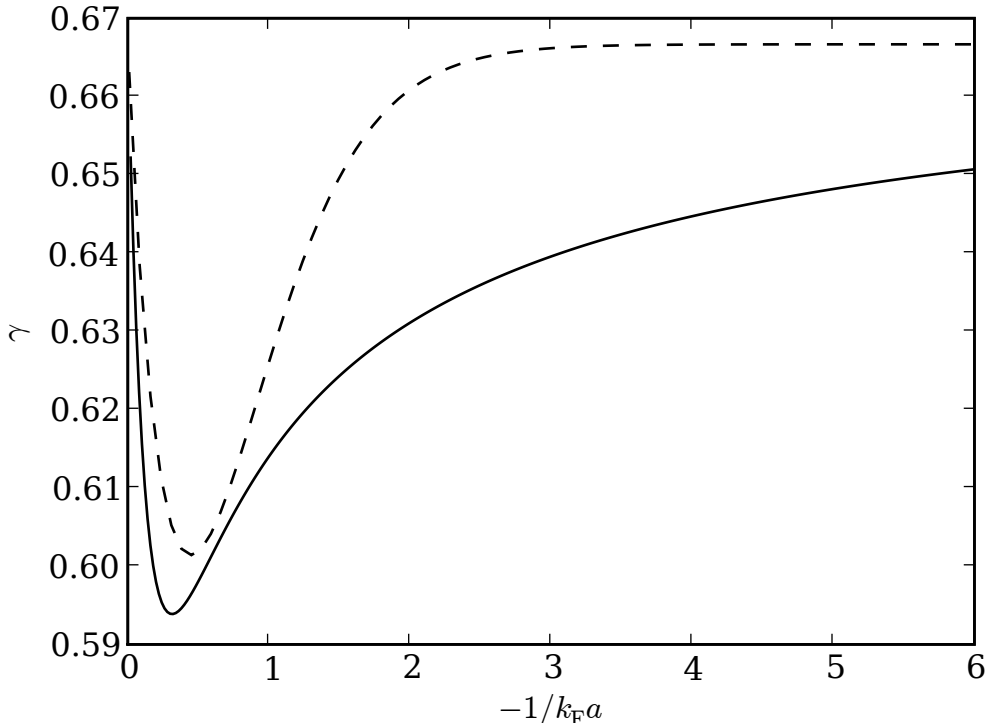

Figure 5.8: The effective polytropic exponent γ as a function of the inverse gas parameter. The solid line is calculated from the fit in figure 5.7, while the dashed line is the mean-field BCS theory.

where the b_i are the time dependent scaling parameters. Inserting this ansatz into the Euler equation (5.16) leads to the coupled differential equations

$$\ddot{b}_i = \frac{\omega_i^2}{(b_x b_y b_z)^\gamma b_i} \tag{5.19}$$

The scaling ansatz is the method of choice if one wants to avoid extensive numerical simulations. Nevertheless, it is only an approximation as we do not have a polytropic equation of state. It has been shown that a scaling ansatz is correct in an isotropic trap [114]. Recently it has been proposed to study the expansion not after a sudden switch off of the trap, but to perform a special ramp of the trap which would lead to an expansion where a scaling ansatz is exact [115].

For very elongated cylindrically symmetric traps the scaling ansatz (5.19) has been integrated analytically [113]. Our trap is neither very elongated nor cylindrically symmetric, thus we had to integrate numerically. At the same time, we have taken into account the fact that the magnetic field for the Feshbach resonance is not completely homogeneous and thus forms an anti-trapping potential. As we switch off this field after a while to enable imaging, we have to remove that field for later times from our calculation. The result of such a numerical integration is shown in figure 5.9.

A very similar treatment has been performed by Diana *et al.* [116] for our older data presented in the articles in the appendix. Unfortunately, they were not aware of the anti-trapping potential, so their theory seems to disagree with our data. Although they attribute this to the finite temperature of the cloud, the anti-trapping is a far more likely reason.

5.3.3 Experiments

Let us now turn to the realization of the presented experiments. After evaporation, we transfer $1{,}7 \cdot 10^6$ atoms into the crossed dipole trap, where we create a mixture of the two lowest Zeeman states as described for the momentum distribution experiments. Two linear evaporations of 1 s, each down to 50% and 25% of the initial trap depth, respectively, are followed by a ramp of the vertical beam down to 5% of its initial value in 500 ms. This leaves us with optical trap frequencies of $\omega_x = 2\pi \cdot 1{,}24\,\mathrm{kHz}$ in the horizontal direction, $\omega_y = 2\pi \cdot 2{,}76\,\mathrm{kHz}$ in the vertical direction and $\omega_z = 2\pi \cdot 3{,}03\,\mathrm{kHz}$ in the direction perpendicular to both laser beams. This means that we have a nearly cigar-shaped trap with an ellipticity of $\omega_y/\omega_x = 2{,}23$.

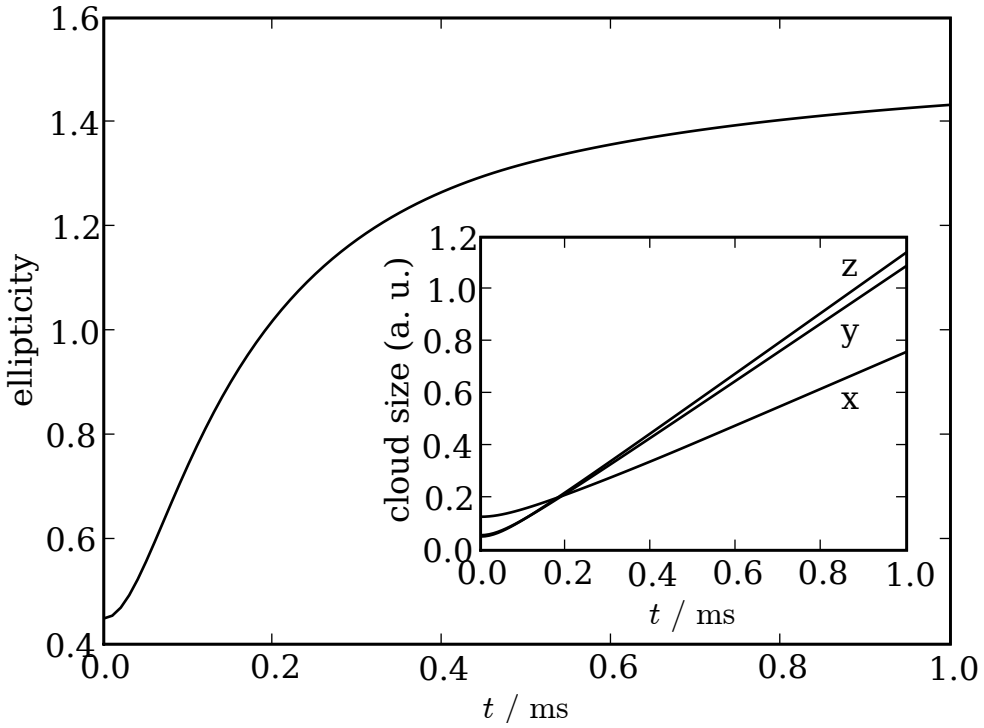

Figure 5.9: The ellipticity of an atomic cloud while expanding in a magnetic field. The parameters are the same as for the experiments which will be shown in the experimental section, namely in figure 5.10. The inset illustrates the behavior of the diameter of the three axes, the notation of the axis is described in the text.

At this time we are only left with less than 10^5 atoms, which makes it difficult to determine the temperature of the cloud. Thus we have also stopped the ramp of the vertical beam at 10% of the initial value, giving us enough atoms to fit with a fermionic distribution function. This gave a result of $T = 0{,}17 T_F$.

In 5 ms we ramp to the resonance point, where we let the atoms rethermalize for 200 ms. It takes the same time to ramp the magnetic field to the desired field value. Once there, we switch off the optical dipole trap and let the cloud expand in 0,5 ms, when we also switch off the magnetic field and wait another 0,5 ms before we take an image. We fit these images to a two-dimensional Gaussian distribution function to calculate the ellipticity of the cloud. The results can be seen in figure 5.10. In image 5.11 we show the same data, where we plot the ellipticity as a function of the interaction parameter $-1/k_F a$. In this graph we the step at $-1/k_F a = 0{,}3$, which is the point where we expect the transition from a superfluid to a collisionless behavior, according to the theoretical predictions shown in figure 2.9. We cannot give a theoretical curve, as the ellipticity depends strongly on the antitrapping potential described above, which is independent of $-1/k_F a$.

One might argue that the experimental procedure does not correspond to the theoretical calculations, as we are switching off the magnetic field during the expansion and our theory is not valid in this case. This argument is correct, but misleading: superfluidity is due to interactions, which in turn strongly depend on the density of the atoms. This means that all the interesting effects occur while the cloud is still dense. During this time, the original anisotropy in real space is turned into an anisotropy in momentum space, and lacking any further interactions the cloud will simply expand ballistically. This is also why the ellipticity converges to a constant value, as shown in figure 5.9. On the other hand, after the 0,5 ms that we let the cloud expand, one might argue, the ellipticity did not yet converge, as it is visible in the very same figure. We could not increase this time any further as the density drops too much to be imaged. In order to verify the validity of our data, we repeated the experiment, stopping the magnetic field after different times, while leaving the expansion without field constant at 0,5 ms. The result is shown in figure 5.12. In this figure, we see that the cloud already reaches its final ellipticity after 0,2 ms. It is worth noting that this measurement does *not* correspond to figure 5.9. The two curves present different situations: the experimental data have an additional expansion time without field during which the ellipticity changes. The point at zero expansion time in field is actually a momentum distribution measurement. This is not true for the

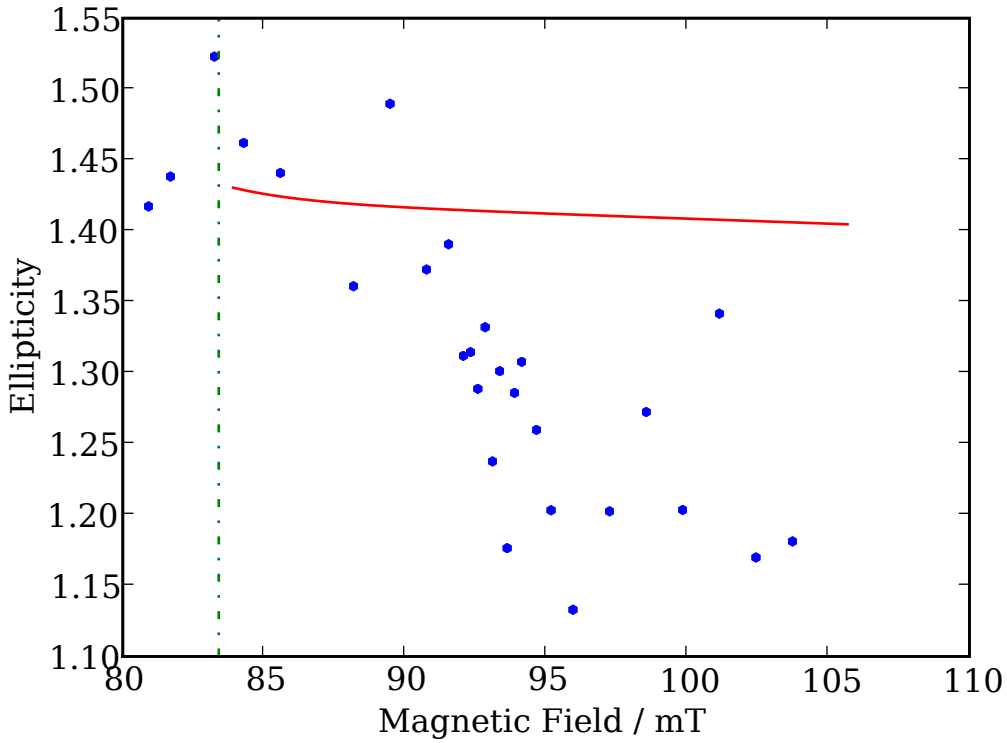

Figure 5.10: Ellipticity of the gas after expansion in a magnetic field on the BCS side of the crossover. The temperature was determined with a two-dimensional Fermi fit to be $T = 0{,}17 T_F$. The solid line shows the theoretical expectation, as calculated in section 5.3. The dashed line marks the position of the Feshbach resonance. While at the resonance the experimental points agree with a superfluid hydrodynamic expansion, they leave this function in a step-like manner. We average images at same magnetic fields before applying the gaussian fit.

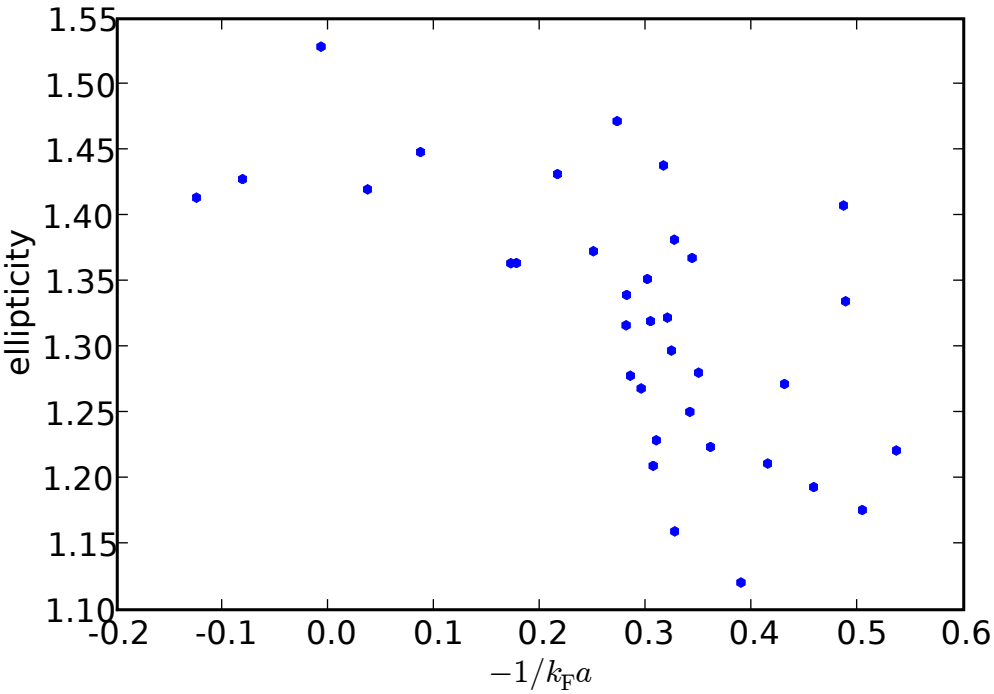

Figure 5.11: The ellipticity as a function of $-1/k_F a$. The step happens at a gas parameter of about $k_F a = 0{,}3$. Since the temperature is about $T = 0{,}17 T_F$ (see text), this is consistent with the predicted transition temperature in figure 2.9.

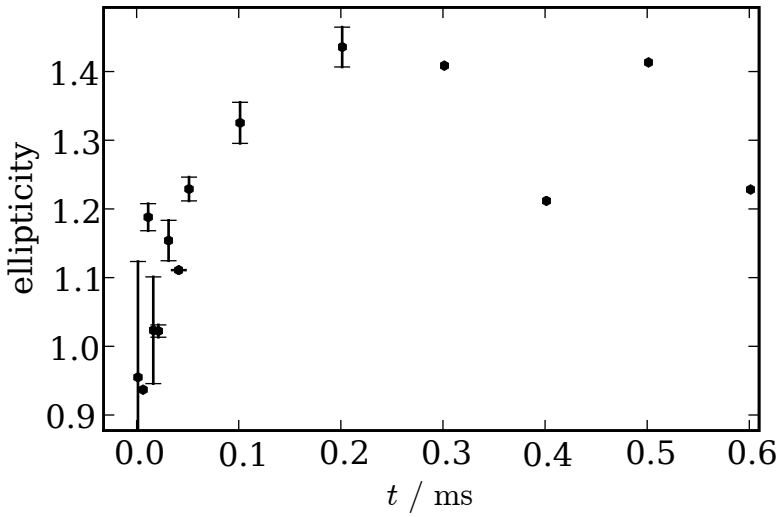

Figure 5.12: The ellipticity of the cloud for various times in the magnetic field at the unitarity limit. The expected ellipticity for long expansion times is 1,4. This is the same dataset as figure 5.5, the error bars are calculated in the same way.

other points, as one cannot expect the cloud which already expanded in field to be small compared to the final size. This is necessary for the momentum distribution measurements to be valid.

We repeated the same curve using the evaporation scheme described for the momentum distribution, shown in figure 5.13. This way we have more atoms left, leading to a better signal to noise ratio. The temperature of the gas is significantly higher. A Fermi fit to the noninteracting gas gave $T = 0{,}3T_F$. At this temperature we can only expect to be condensed very close to the unitarity limit, as we see from figure 2.9. And indeed, we observe that the step seen at lower temperatures has disappeard. We are near the predicted ellipticity for a hydrodynamic gas at the resonance.

Our data are complementary to the data taken by the Innsbruck group [117]. They measured the quadrupole mode in a cigar-shaped harmonic trap along the long axis. They found its frequency and damping to change around $1/k_F a = -0{,}8$. They attributed this to the transition from a hydrodynamic to collisionless behavior. Their gas is colder than ours, below $T = 0{,}1T_F$. Studying the temperature behavior, they found that heating up the gas to $T = 0{,}2T_F$, the transition moves above $1/k_F a = -0{,}66$, which is in agreement with our measurements.

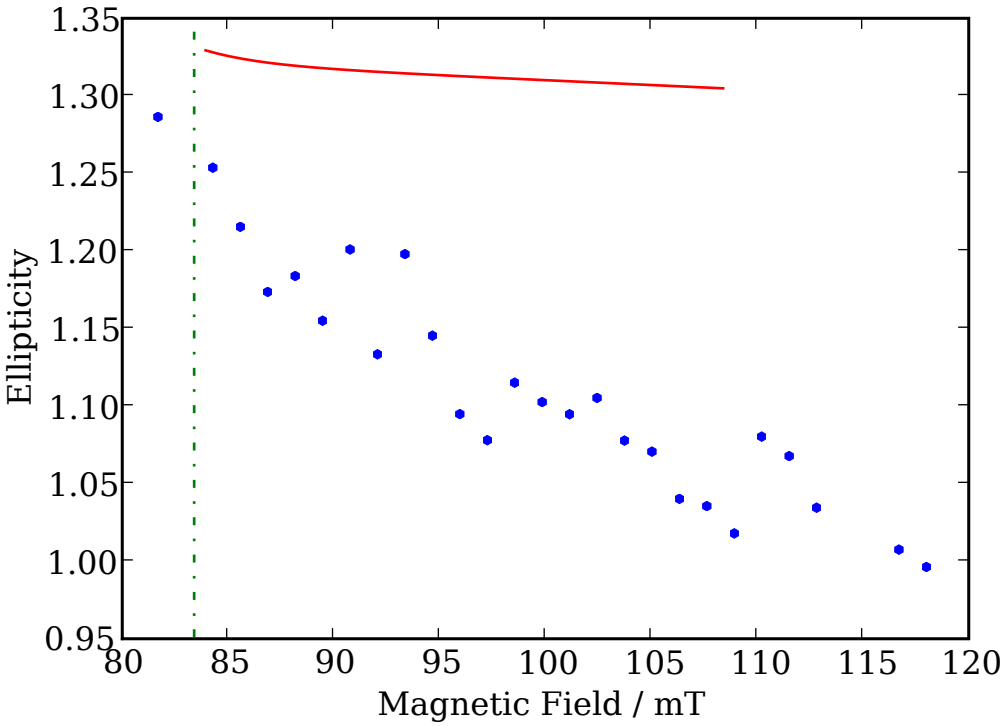

Figure 5.13: The ellipticity in the crossover at higher temperatures: here $T = 0{,}3T_F$. The step has disappeared. The residual ellipticity is lower than its superfluid counterpart in figure 5.10

5.4 Molecular condensate

On the molecular side of the Feshbach resonance, we performed additional studies on the molecular Bose-Einstein condensates expected there. As a BEC is superfluid, we expect the same behavior as in the last sections. But more than that, we expect the momentum distribution after time of flight to show a bimodality, a landmark of Bose-Einstein condensation. Indeed, this behavior was observed both in ^{40}K at JILA [24], as well as in ^{6}Li at MIT [25]. In our experiments, however, we saw that the ellipticity corresponds to condensation, but the bimodality was not obvious, as it can be seen in the paper in appendix A.1. This is due to the much stronger interactions that we have compared to the usual condensation of bosonic atoms. The group in Innsbruck ramped the magnetic field down to 68 mT, a value where the bimodality becomes visible [72]. We attempt to model the expansion of the cloud with strong interactions.

The theory of Bose-Einstein condensation is too wide a field to be treated here in depth, it can be found in textbooks (e.g. reference [40]). The condensate wave function follows the Gross-Pitaevskii equation

$$i\hbar\frac{\partial\psi}{\partial t} = (-\frac{\hbar^2\nabla^2}{2m} + V_{\text{ext}}(\mathbf{r}) + g|\psi|^2)\psi \tag{5.20}$$

This equation can be seen as a Schrödinger equation with a kinetic and potential energy and an interaction term in the Hamiltonian. The interaction part is proportional to the condensate density $n_c = |\psi|^2$. The proportionality constant is the coupling $g = 4\pi\hbar^2 a_m/m$. Here, a_m is the scattering length between molecules. In section 2.4.5 we saw that $a_m = 0{,}6a$, where a is the atom-atom scattering length.

We suppose that there is a BEC in the center of the trap, which is expanding after switching off the trap. Around this condensate is a cloud of thermal molecules. We only consider interactions between the molecules in the thermal cloud and the BEC as a whole. Then the BEC acts as a potential for the thermal cloud. This way, we can write the Hamiltonian of the molecules in the thermal cloud:

$$H(\mathbf{r},\mathbf{p}) = \frac{\mathbf{p}^2}{2m} + \frac{1}{2}m\sum_{i\in\{x,y,z\}}\omega_i^2 r_i^2 + 2gn_c(\mathbf{r}) \tag{5.21}$$

The term gn_c is exactly twice the interaction energy which appears in the Gross-Pitaevskii equation. The factor two is owed to the exchange interaction of bosonic particles. One might note here that the two is

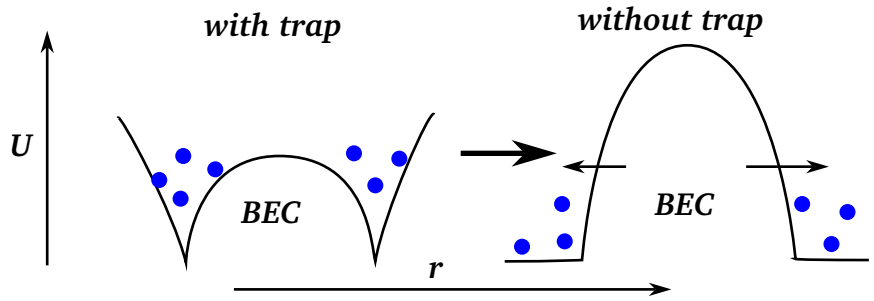

Figure 5.14: Illustration of the model used in the text. The points represent the thermal cloud. They are trapped in a potential created by the BEC before the trap is switched off, and pushed outwards afterwards by the expanding BEC.

not the BCS result of the molecule-molecule interaction being twice the atom-atom interaction, as our basic particle is already a molecule.

In the trap, this gives a Mexican hat potential as illustrated in figure 5.14. We start our simulation by generating a random distribution of up to one million atoms following the Bose-Einstein distribution function $n(\mathbf{r},\mathbf{p}) \propto (\exp(\beta(H-\mu))-1)^{-1}$, with H being the Hamiltonian in the trap. Then we numerically integrate the path of each atom with the BEC as a time-varying potential. As we are deeply on the BEC side of the resonance, we can calculate the expansion of the cloud using the formulae of the last section, knowing that in this limit the polytropic exponent is just 1.

The result of such a simulation is shown in figure 5.15. It is a simulation of a condensate of 1000 molecules and some 3000 atoms in the thermal cloud (technically, we simulated one million atoms and divided the result appropriately to get a smoother curve). The expansion time is 12 times the trap frequency period, corresponding to the example data shown in the background. Unfortunately, we had to change the parameters to get a curve that is similar to experimental data: we simulated a scattering length between molecules of $a = 0{,}02a_{\mathrm{ho}}$, while the experiments are done at $a = 0{,}1a_{\mathrm{ho}}$. The number of molecules is also much higher in the experiment, about $2 \cdot 10^4$. Those discrepancies are probably due to neglecting the interactions between the molecules in the thermal cloud. Another possibility is that the cloud contains a fraction of unbound atoms. Further investigation in this problem will be necessary.

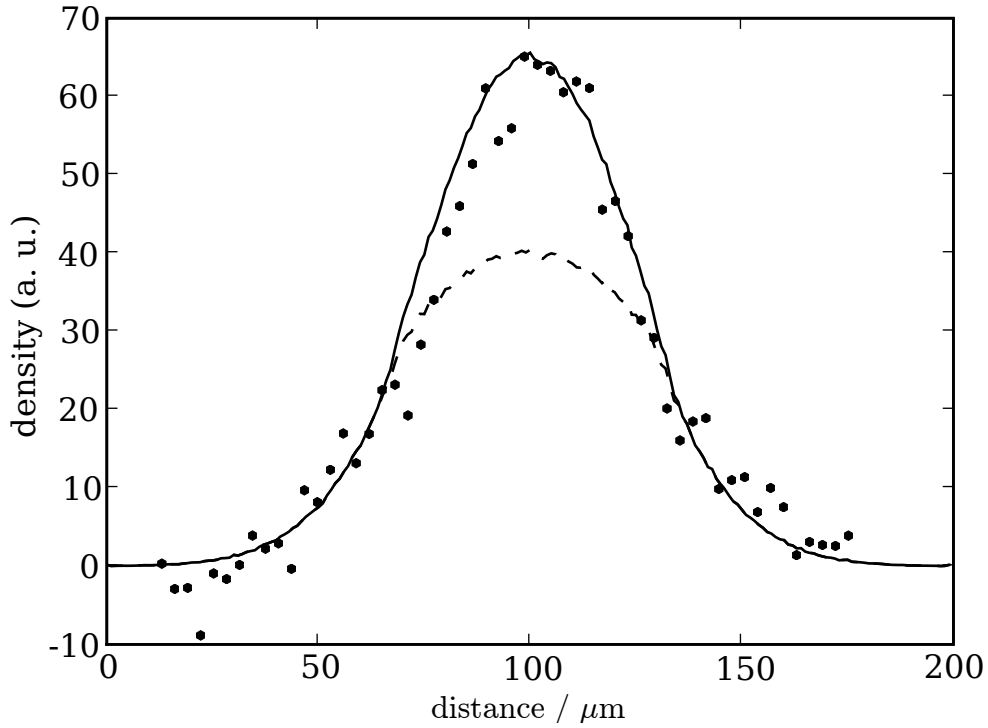

Figure 5.15: Simulation of a molecular Bose-Einstein condensate. The solid line is the atomic density, the dashed line is the thermal cloud. The points are experimental data. The data is taken at $k_F a \approx 1$.

5.5 Heteronuclear Feshbach resonances

After atoms had been successfully cooled and trapped, various efforts have been made to extend this field to ultra-cold molecules. This is not a simple task, as laser cooling is difficult to achieve, as the level structure of molecules is too complicated. There are two possible paths to ultra-cold molecules: one can develop cooling mechanisms that work with molecules, or one can laser cool atoms and create molecules once they are cold. An example for the first approach is the use of Stark slowers, the electrostatic counterpart of the Zeeman slower, which has been successfully used to slow various molecular gases [118]. Efforts to create molecules using photoassociation, particularly interesting as this is a new state of matter which does not exist in nature [119], falls into the second category.

The most advanced approach, however, is the one presented in this thesis. Using a Feshbach resonance, we can easily create molecules and we even achieved molecular Bose-Einstein condensation. However, the molecules we are studying are a very particular example, as they consist of two atoms not only of the same element but even of the same isotope. But we can do better. Since our experimental setup also cools the bosonic isotope of Lithium, we can work on creating molecules between these two isotopes. Taking the same approach as for homonuclear molecules, we were searching Feshbach resonances between the two isotopes.

Heteronuclear molecules can have a large electric dipole moment. This adds dipole-dipole interactions to the usual contact interactions used in the physics of cold atoms so far. New quantum states, like a quantum ferrofluid, can be realized using these interactions. Another option to create dipolar interactions is to use atoms with a large magnetic dipole moment. Using this approach, quantum ferrofluid has recently been demonstrated in Chromium [120]. It has also been proposed to use heavy polar molecules to measure the electric dipole moment of the electron [121], in the search for violations of the standard model.

Such resonances had been predicted before [122]. As one can see in figure 5.16, the situation is comparable to the usual Feshbach resonances described in section 2.3. Several molecular states exist below the dissociation limit and can be tuned to this limit using a magnetic field. One obvious difference is that the bound states in the closed channel also depend on the magnetic field. This is due to their fermionic nature, which means that they cannot have a spin of 0 and thus a magnetic spin component $m_F \neq 0$. We have been searching for these resonances by

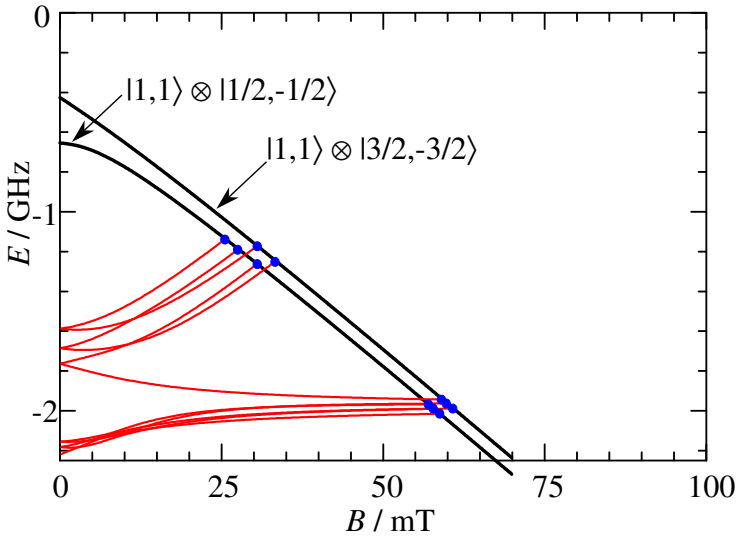

Figure 5.16: The bound states and Feshbach resonances for a mixture of ^{7}Li and ^{6}Li. This figure corresponds to figure 2.4, which describes the same situation in ^{6}Li only. We only searched for the resonances between the lowest Zeeman states, as in such a gas inelastic collisions are suppressed. Image taken from reference [122]

looking at the atom loss, which is large close to a resonance.

During the time we performed our experiments, other combination of atoms have been studied, namely ^{6}Li and ^{23}Na by the group at MIT [123], as well as ^{87}Rb and ^{40}K at JILA [124]. In the meantime, inter-species resonances have become a standard tool in atomic physics:

- The group in Hamburg studied mixtures of fermionic ^{40}K and bosonic ^{87}Rb both in a harmonic trap [125] and in an optical lattice [126]. They found an enhancement of the mean-field energy of a Bose-Einstein condensate by the fermions on the attractive side of the resonance, and a phase separation on the repulsive side, both in the harmonic trap. In the lattice they showed the creation of heteronuclear molecules.

- At the ETH in Zürich they studied the same mixture in a lattice, and found that the phase coherence between the bosons diminishes as the fermions are added [127].

- Purely bosonic mixtures between ^{85}Rb and ^{87}Rb have been studied at JILA, where molecules could be formed and observed [128].

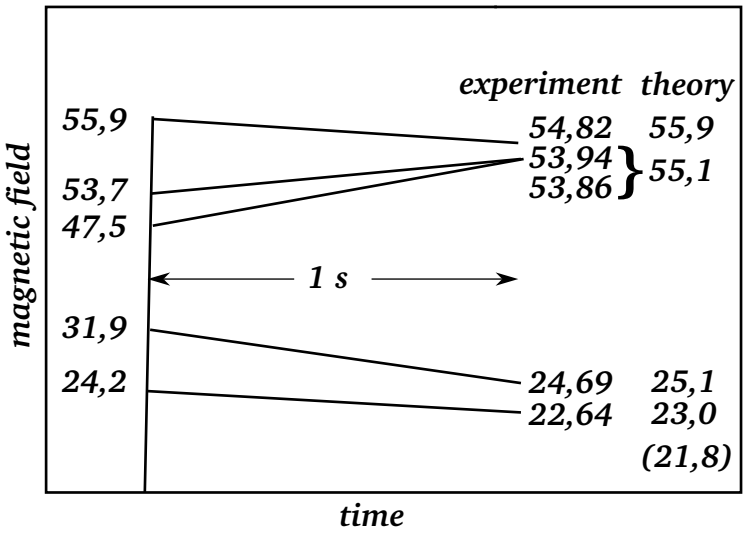

Figure 5.17: The magnetic field ramps used to search the heteronuclear resonances. On the left we mark the starting magnetic field of the final ramps, on the right we mark the found resonances and compare them to the theoretical values from reference [122]. We also find that one of the resonances changes in position depending on the ramping speed. A fifth resonance, predicted at 21,9 mT, was not searched for. Graph not to scale.

The experimental procedure is similar to the experiments on ^{6}Li only, as described in section 3.6. In order to have some ^{7}Li left in the trap, we stop the evaporation prematurely. We evaporatively cool for 27 s, leaving $2 \cdot 10^5$ atoms of both ^{6}Li and ^{7}Li. In the optical dipole trap, we apply two RF fields in order to transfer the atoms from the $|3/2, 3/2\rangle$ and $|2,2\rangle$ state into the $|1/2,1/2\rangle$ and $|1,1\rangle$ states, with a small guiding field of 8 G.

During 1 ms we ramp the magnetic field close to the searched resonance, as shown in figure 5.17. We try to ramp as fast as possible in order to prevent a loss of atoms at other resonances than the one under investigation. It is possible that the current supplies are not fast enough to actually follow, therefore, we have to stop far enough from the resonance so that we do not reach the resonance during a possible overshoot. A last slow ramp of 1 s leads us to the point we are looking for. At the end, we wait for 20 ms before taking an image of ^{7}Li. Once the end of the ramp is close to a resonance, we loose the atoms very rapidly. The losses were too fast as to characterize a lifetime.

We found four resonances, shown in figure 5.17. One of the mea-

surements is particularly interesting, as the position of the resonance seems to have changed depending on the starting point of the ramp. Figure 5.18 shows the raw data. One can see that the number of atoms drops at different magnetic fields for the different ramps. The most probable explanation for this behavior is an overshoot of the magnetic field after the ramp. For the higher ramping speed the losses seem to appear earlier, as the magnetic field is a bit higher at the end of the ramp than demanded from the current supply.

The sharpness of the heteronuclear resonances asks for a very careful calibration of the magnetic field. As a first step, we performed an RF spectroscopy of the transition from state $|6\rangle$ to state $|1\rangle$ of ^{6}Li at high field (28 mT). At this field, we performed RF sweeps, and could determine the transition frequency with an accuracy of 0,1% by searching for the frequency where the transfer is most efficient. Knowing the Zeeman splitting (see for eample references [71, 129]), we can calculate the magnetic field with the same accuracy.

We also need to include the small offset coils mentioned at the end of section 3.4, which provide an additional magnetic field. We were able to calibrate the field by locating the p-wave Feshbach resonances (in essentially the same way that we located the heteronuclar resonances), which are very narrow, for different values of the offset field. Figure 5.19 shows this result. The accuracy is not as good as for the pinch coils, around 1%, but as the generated field is more then 10 times lower than the field generated by the pinch coils, we get the same accuracy for the final results.

5.6 Other experiments and outlook

The large interest in the work described in this thesis becomes visible seeing the many groups working in the field of strongly interacting fermionic gases. Namely, the groups of W. Ketterle at MIT, J. Thomas at Duke, R. Grimm at Innsbruck, R. Hulet at Rice and D. Jin at JILA contributed important results to this field. We want to give here a rough overview of their work.

5.6.1 The collective oscillation modes

In the experiments presented in this thesis, the gas is statically confined in a trap until the trap is switched off. Superfluidity is seen in the expansion of the gas, which eventually leaves the superfluid state. Therefore, we

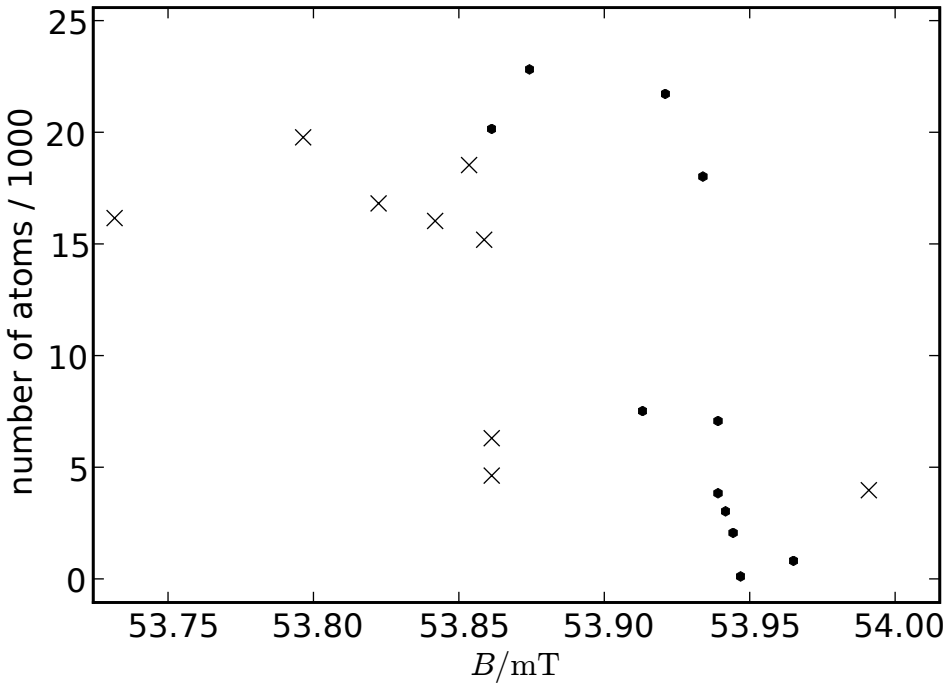

Figure 5.18: An example for the measurement of the position of a heteronuclear Feshbach resonance. Here we show the most interesting of the four resonances, where the position changed with the ramping speed. The magnetic field was ramped in 1 s from lower values, 47,5 mT for the crosses, 53,7 mT for the dots, to the value indicated in this graph. One sees a sharp loss of atoms.

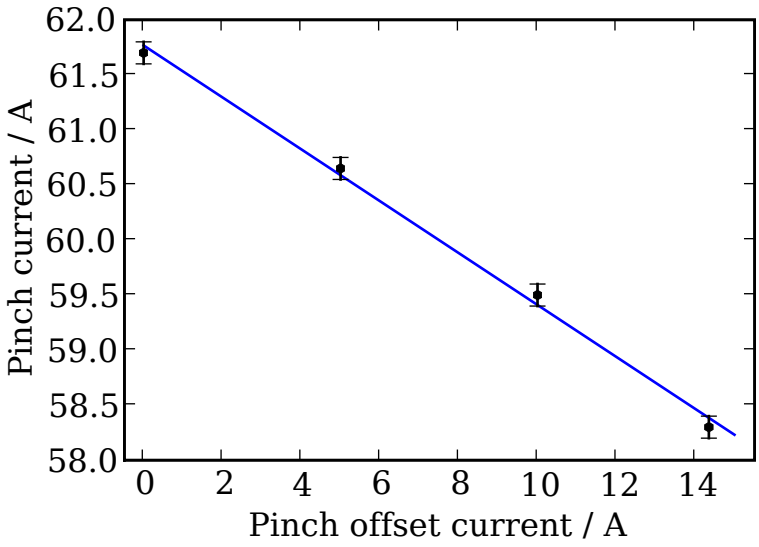

Figure 5.19: Calibration of the magnetic fields of the two coil systems. The points are the position of the p-wave resonance $|1/2,1/2\rangle + |1/2,1/2\rangle$. The fit of the points gives a calibration of $I_{\text{pinch}} = 0{,}24 I_{\text{offset}}$.

never see a superfluid *flow*. Another approach was taken in Innsbruck: the dynamics of the gas after a sudden change of the trap was studied. The group used an AOM to displace the trap rapidly which leads to the gas oscillating in the trap.

In a first experiment, they studied the radial sloshing and compression oscillations [30]. The measurements have a very high precision, as they were able to see the beat note between the two frequencies in two orthogonal directions of the trap. As the compression mode depends on the pressure of the gas, it was shown [130] that one can trace the whole equation of state using this technique.

A second experiment was a study of the radial quadrupole mode [117]. This mode is a pure surface mode, the compressibility does not enter. It was predicted [131] that in the hydrodynamic regime the quadrupole mode has a frequency of $\omega_q = \sqrt{2}\omega_r$, where ω_r is the radial trapping frequency. In a collisionless gas on the other hand, the frequency is twice the trapping frequency. One notes that here the equation of state does not enter, making it simple to compare theory to experiment.

Interestingly, they find that the gas changes from hydrodynamic to collisionless behavior near the position where we see the step in

the ellipticity, around 95 mT, and $1/k_F a \approx -0{,}8$. They find that the frequency of the quadrupole mode corresponds to predictions in the hydrodynamic regime, and it drops just before it does a step upward to reach the frequency expected in the collisionless regime. They also find that the damping of the mode is increased just around that step. This damping has been interpretated as the position where the pair breaking energy has become sufficiently low to break a pair during the oscillations [132].

5.6.2 Spin-polarized Fermi gases

Shortly after the development of BCS theory, theorists started to ask what would happen if the electrons were spin-polarized, for example by a magnetic field. This is hard to achieve in superconductors, as normally the Meissner effect prevents the magnetic field from entering the superconductor. Recently an experimental realization of such a state became possible in cold atoms. This created excitement in the community, especially since some of the results seem contradictory. These experiments showed the great advantage of the physics of cold atoms: we can easily vary the polarization state of the atoms in a controlled way, just by changing the RF pulse which depolarizes the gas appropriately.

It started with an experiment at Rice [74]. They created fermionic gases with different spin populations, and substracted the absorbtion images of the two spin states from each other. They found that both spin state form clouds of the same size if the polarization is lower than a certain limit. Above this limit they see a core of bound atom pairs, surrounded by a shell of unpaired atoms.

A more detailed analysis revealed that the experiment showed a breakdown of the local density approximation. An explanation for this would be the existence of a surface tension between the two phases [133]. A second experiment seemed to support this strongly: they observe that the unpaired atoms get pushed to the ends of their highly elongated trap [134].

In a much less elongated trap, the group at MIT found significantly different results [135]. Instead of the two phases from the Rice experiment, they saw a third phase appearing between the superfluid core and the unpaired single atoms. This phase contains particles of both spin states, but not equal in number. They also developed a new variation of phase contrast imaging, where they can directly image the density

difference between the two states.

The seemingly contradictory results from the two groups opened a sometimes heated discussion in the community. The discussion is still ongoing, we try here to present the main lines of argumentation. A rather general idea of the situation is presented in figure 5.20, following the results of Gubbels *et al.* [136]. One of the oldest theoretical results is the prediction by Clogston [137]: at some point it becomes energetically favorable to align spins, Cooper pairs will break. Above this limit no superfluidity is possible. The two groups who have studied spin-polarized gases disagree on the position of this limit, the Rice group claiming that it is too high to be seen in experiments.

At lowest temperatures, one expects the gas to be phase separated, meaning that there exists a superfluid core and a normal shell around. At higher temperatures, we expect a third shell to appear between the two, a phase of gapless superfluidity which allows for spin-imbalanced fermions, first predicted by Sarma [138]. A phase transition is predicted between this Sarma phase and the separated phase, as shown in figure 5.20. A tri-critical point should appear where the two phase transition lines cross, which is the subject of current experimental studies. Other authors introduce different phases into the phase diagram [139, 140]. Most important is a phase proposed independently by Fulde, Ferrel [141], Larkin and Ovchinnikov [142], who predict that a BCS state can tolerate a small spin imbalance if we allow the Cooper pairs to have non-zero momentum. This leads to a gap that fluctuates in the gas.

Good predictions of the experiments were also made using a very different approach: Combescot *et al.* [143] considered a single atom in one spin state immersed in a sea of atoms in the other spin state. Using a many-body variational approach in combination with a Monte-Carlo simulation, they were able to predict the macroscopic quantities of a spin-polarized gas, especially the three different phases found in the MIT experiment. As their model is independent of BCS theory, their results should hold independently from the outcome of the discussion about the various states mentioned in the last paragraph.

In another experiment the MIT group could prove that the core of the spin-polarized gas is actually superfluid by rotating the cloud and observing vortices [32]. In a recent study they showed that pairing occurs at very low temperatures in the absence of superfluidity once the population imbalance becomes too large [144]. They demonstrated the existence of pairs using radio frequency spectroscopy, a method pioneered at Innsbruck to study the pairing gap in the BEC-BCS crossover [28]. The method was recently improved at MIT to be position

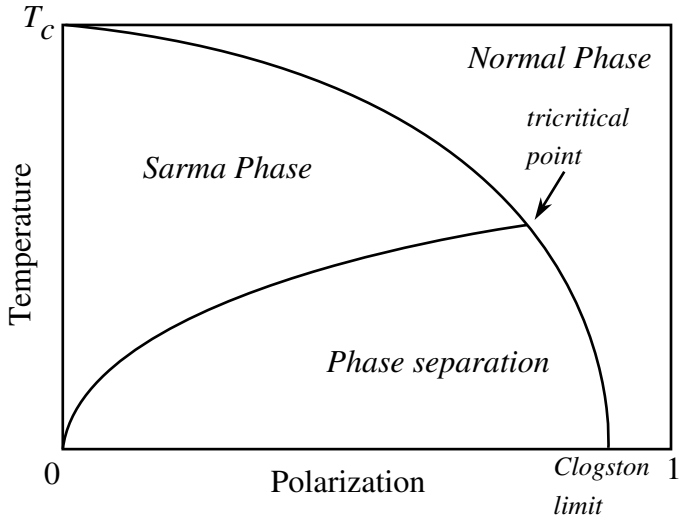

Figure 5.20: A sketch of the phase diagram of a spin-polarized Fermi gas. The temperature is given in the unit of the transition temperature T_c for a polarized gas. A polarization of 1 means that all spins are oriented in the same direction, while 0 means that the gas is completely depolarized. Figure adopted from reference [136]

dependent by using a tomography technique [145].

5.6.3 p-wave resonances

In section 2.3 we saw that there is also p-wave Feshbach resonances. We searched these resonances and performed a first study of their behavior, published in the article in appendix A.2. For fermions, p-wave scattering is allowed between the same spin state. Since we were usually studying mixtures of the lower two spin states of the atoms, there are three different resonances for the different possible combinations of the internal states of the atoms. This was already shown in figure 2.4.

We detected the resonances by studying the losses near the resonance point. Taking into account two- and three- body losses, one expects the number of atoms N to follow the law

$$\frac{\dot{N}}{N} = -G_2\langle n\rangle - L_3\langle n^2\rangle \tag{5.22}$$

The coefficents G_2 and L_3 are the two-body and three-body loss coefficients, respectively, and n is the density of the atoms. We find that for the

resonance between two atoms in the state $|1\rangle$, the three-body coefficient L_3 domiates. As both atoms are in the lowest Zeeman state, they cannot scatter inelastically, and thus two-body collisions are suppressed. Once at least one of the atoms is in a higher Zeeman state, namely state $|2\rangle$, two-body collisions become possible, and the two-body loss coefficient G_2 dominates the process, in agreement with the experiments.

The main difference between an *s*-wave resonance and its *p*-wave counterpart is the centrifugal barrier which we talked about in section 2.2. While the molecular state in the *s*-wave resonance becomes large, this does not happen in *p*-wave resonances, as the molecular state is localized behind the centrifugal barrier, as we have shown in the paper in appendix A.4. This also means that the scattering is not dominated anymore by the low energy scattering, but by collisions around the energy of the molecular state, as the atoms need to tunnel through the potential barrier. This also leads to a temperature dependence of the losses: the maximum of losses is located at the magnetic field where the maximum of the momentum distribution of the atoms is equal to the binding energy of the molecules. Interestingly this means that the maximum of losses happens above the actual resonance position. This is very interesting if we want to create *p*-wave molecules: at the exact resonance position, the lifetime of the atomic cloud could be sufficiently long to study the molecules.

The group at JILA found and studied the *p*-wave resonances in ^{40}K [33]. The group in Zürich studied *p*-wave resonances in an optical lattice, allowing them to show that a *p*-wave resonance is not isotropic, as the direction of the spin-alignment changes the scattering properties [146]. We found preliminary indication of *p*-wave molecule formation with an efficiency of 20% and a lifetime below 20 ms.

In a recent experiment, the group at JILA demonstrated the existence of *p*-wave molecules. As the gas near such a resonance is very unstable, they could not use the usual technique to slowly ramp the magnetic field to the resonance, but they modulated the magnetic field with a frequency which corresponds to the molecule's binding energy. They were able to take images of the non-isotropic momentum distribution inside a *p*-wave molecule [147]. Unfortunately, the lifetimes of these molecules are only around 2 ms, making it unlikely to achieve p-wave condensates.

5.6.4 Other experiments

In the group of John Thomas [31], a new technique for thermometry was developed: the gas is released from its trap for a short time to be retrapped shortly after. This adds a defined quantity of energy into the gas, which changes the shape of the cloud, from which the heat capacity of the cloud can be determined. They find that the heat capacity deviates from the behavior of a normal Fermi gas at low temperatures. They were also able to use this method to create a relative temperature scale. This scale is proportional to the real temperature. The proportionality constant, however, is not precisely known, but this scale is nowadays a generaly accepted method to perform temperature dependent measurements.

The creation of vortices in a rotating gas is seen as a proof for its superfluidity. The usual method to rotate a gas is to "stir" it using a blue detuned laser beam. After having been used in bosonic gases [148], it was used to show superfluidity of a fermionic gas at MIT [149]. Until now, this is the only direct proof of the superfluidity of the gas. An interesting detail is that it seems not to be possible to image the vortices in the crossover. They had to ramp the magnetic field to 74 mT, well below the resonance point, during the expansion of the gas, in order to observe vortices above 81 mT. Their explanation is that the pairs will break during the expansion if they omit the described ramp. This detection of vortices is also the technique that was used to observe superfluidity in spin-polarized gases, mentioned in the last subsection.

The direct measurments of the pair correlation is possible by measuring the correlations of the noise in the absorption images. This method was introduced by the group at JILA [150]. They studied the noise correlations of two images of the momentum distribution, one for each spin state of the atoms. They dissociated weakly bound molecules in the crossover, and were able to observe the correlation of the resulting atoms in momentum space.

Chapter 6

Conclusions

In this thesis we have studied the behavior of an ultracold fermionic gas in the vicinity of a Feshbach resonance. We have seen that the gas becomes superfluid below a critical temperature. This state is normally only found in Helium and is very similar to the behavior of superconductors. The crossover can be separated into three regions: the BCS regime, which corresponds to superconductivity in metals, a BEC regime, where the atoms form molecules which can condense into a Bose-Einstein condensate, like atoms in cold bosonic gases, and a strongly interacting regime comparable to high temperature superconductors. In the center of the crossover, where the scattering length diverges, one reaches the unitarity limit, a state common to all strongly interacting Fermi systems, which can hence be called universal.

We have shown that the BCS theory, originally developped for superconductors, can be extended to the whole crossover region. One ingredient of this theory is a prediction of the momentum distribution of the particles. The Fermi edge seen for a noninteracting Fermi gas smears out even at zero temperature. We have calculated the momentum distribution in the crossover using the BCS theory, comparing to more advanced theories. We presented an experimental measurment of the momentum distribution of a strongly interacting Fermi gas in a harmonic trap, and have found it to agree well with the predictions.

As superfluidity is in its roots a dynamic process, studying its dynamics is crucial for the comprehension of this phenomenon. We studied the expansion of a superfluid gas with strong interactions around the unitarity limit and on the BCS side of the resonance. We found that superfluidity suddenly breaks down when interactions drop below a certain value. This value moves to higher interaction strengths once we measure at higher temperatures.

Stable molecules can be formed by preparing the gas around the unitarity point and slowly ramping down the magnetic field into the BEC region. In this thesis we present experimental measurements which show that this molecule creation also happens for fast sweep rates if the density of the gas is sufficiently high. This can occur when we switch off the magnetic field in order to take an absorption picture of a cloud in the crossover, and can disturb the measured distribution.

The development of new data analysis methods allowed us to determine more precisely the temperature of the gas. We also presented an algorithm to deconvolute absorption images into the original three dimensional density distribution.

The presented experiments have also shown that we are at the limits at what our setup is capable of. Therefore, we have started with the construction of a second generation experimental apparatus. We have installed a new laser system, which is more flexible and stable than its predecessor. The vacuum system was rebuilt in large parts, including a complete rebuild of the Zeeman slower. As a result, the loading rate of the atoms is now ten times higher than before, enabling us to increase the repetition rate of our experiment, leading to better statistics. At the same time we optimized the geometry of the magnetic traps, which will enable us to increase the number of trapped atoms by about an order of magnitude. A new imaging system for the magneto-optical trap is an important tool in the characterisation of the new setup.

In the near future, we plan to set up an optical lattice in our system. An optical lattice is a standing wave overlapped with the atomic cloud. Similar to an optical dipole trap, atoms will be trapped in the intensity maxima of the standing wave. Many different configurations are possible. We can successively "freeze out" the spatial degrees of freedom, enabling us to study atomic gases in low dimensions. For bosons, optical lattices have already become a standard tool, we refer to reference [151] for a review.

Optical lattices open the possiblity to experimentally realize theoretical many-body models, without the problems appearing in solid state physics, such as lattice defects or impurities. One example is the Fermi-Hubbard model. Hubbard proposed in 1963 a simple model for electrons in a lattice [152] whose Hamiltonian contains only two terms, a next-neighbor tunneling and an on-site interaction term. It is a very simple model, but exhibits phenomena like a metal-insulator transition, ferromagnetism or superconductivity. For a review we refer to reference [153]. This model is still a challenge to theoretical physics, as no complete solution has been found yet.

Cold fermions in optical lattices can be seen as a direct experimental implementation of this model [154]. Its bosonic counterpart has already been experimentally realized [155]. Pioneering experiments have been performed for fermions. The group in Florence studied transport phenomena in optical lattices [156]. The MIT group reported on evidence for superfluidity in a lattice [157]. We already mentioned the efforts made by the group in Hamburg to study Bose-Fermi mixtures in optical lattices in section 5.5, and the study of p-wave resonances in optical lattices in Zürich in section 5.6.3. We see that optical lattices are an exciting future project, which will lead to a merge of cold atoms and solid state physics.

Appendix A

Articles

A.1 Experimental Study of the BEC-BCS Crossover Region in Lithium 6

T. Bourdel, L. Khaykovich, J. Cubizolles, J. Zhang, F. Chevy, M. Teichmann, L. Tarruell, S.J.J.M.F. Kokkelmans, and C. Salomon,

Physical Review Letters **93**, page 050401, 27 July 2004.

Experimental Study of the BEC-BCS Crossover Region in Lithium 6

T. Bourdel, L. Khaykovich, J. Cubizolles, J. Zhang, F. Chevy, M. Teichmann, L. Tarruell, S. J. J. M. F. Kokkelmans, and C. Salomon

Laboratoire Kastler-Brossel, ENS, 24 rue Lhomond, 75005 Paris

(Received 2 March 2004; revised manuscript received 14 April 2004; published 27 July 2004)

We report Bose-Einstein condensation of weakly bound $^6Li_2$ molecules in a crossed optical trap near a Feshbach resonance. We measure a molecule-molecule scattering length of 170^{+100}_{-60} nm at 770 G, in good agreement with theory. We study the 2D expansion of the cloud and show deviation from hydrodynamic behavior in the BEC-BCS crossover region.

DOI: 10.1103/PhysRevLett.93.050401 PACS numbers: 03.75.Ss, 05.30.Fk, 32.80.Pj, 34.50.–s

By applying a magnetic field to a gas of ultracold atoms, it is possible to tune the strength and the sign of the effective interaction between particles. This phenomenon, known as Feshbach resonance, offers in the case of fermions the unique possibility to study the crossover between situations governed by Bose-Einstein and Fermi-Dirac statistics. Indeed, when the scattering length a characterizing the 2-body interaction at low temperature is positive, the atoms are known to pair in a bound molecular state. When the temperature is low enough, these bosonic dimers can form a Bose-Einstein condensate (BEC) as observed very recently in ^{40}K [1] and ^{6}Li [2,3]. On the side of the resonance where a is negative, one expects the well-known Bardeen-Cooper-Schrieffer (BCS) model for superconductivity to be valid. However, this simple picture of a BEC phase on one side of the resonance and a BCS phase on the other is valid only for small atom density n. When $n|a|^3 \gtrsim 1$ the system enters a strongly interacting regime that represents a challenge for many-body theories [4–6] and that now begins to be accessible to experiments [7–9].

In this Letter, we report on Bose-Einstein condensation of ^{6}Li dimers in a crossed optical dipole trap and a study of the BEC-BCS crossover region. Unlike all previous observations of molecular BEC made in single beam dipole traps with very elongated geometries, our condensates are formed in nearly isotropic traps. Analyzing free expansions of pure condensates with up to 4×10^4 molecules, we measure the molecule-molecule scattering length $a_m = 170^{+100}_{-60}$ nm at a magnetic field of 770 G. This measurement is in good agreement with the value deduced from the resonance position [9] and the relation $a_m = 0.6\,a$ of Ref. [10]. Combined with tight confinement, these large scattering lengths lead to a regime of strong interactions where the chemical potential μ is on the order of $k_B T_C$ where $T_C \simeq 1.5\,\mu$K is the condensation temperature. As a consequence, we find an important modification of the thermal cloud time of flight expansion induced by the large condensate mean field. Moreover, the gas parameter $n_m a_m^3$ is no longer small but on the order of 0.3. In this regime, the validity of mean field theory becomes questionable [11–13]. We show, in particular, that the anisotropy and gas energy released during expansion varies monotonically across the Feshbach resonance.

Our experimental setup has been described previously [14,15]. A gas of ^{6}Li atoms is prepared in the absolute ground state $|1/2, 1/2\rangle$ in a Nd-doped yttrium aluminum garnet crossed beam optical dipole trap. The horizontal beam (respectively vertical) propagates along x (y), has a maximum power of $P_o^h = 2$ W ($P_o^v = 3.3$ W) and a waist of $\sim 25\,\mu$m ($\sim 40\,\mu$m). At full power, the ^{6}Li trap oscillation frequencies are $\omega_x/2\pi = 2.4(2)$, $\omega_y/2\pi = 5.0(3)$, and $\omega_z/2\pi = 5.5(4)$ kHz, as measured by parametric excitation, and the trap depth is $\sim 80\,\mu$K. After sweeping the magnetic field B from 5 to 1060 G, we drive the Zeeman transition between $|1/2, 1/2\rangle$ and $|1/2, -1/2\rangle$ with a 76 MHz rf field to prepare a balanced mixture of the two states. As measured very recently [9], the Feshbach resonance between these two states is peaked at 822(3) G, and for $B = 1060$ G, $a = -167$ nm. After 100 ms the coherence between the two states is lost and plain evaporation provides $N_\uparrow = N_\downarrow = N_{tot}/2 = 1.5 \times 10^5$ atoms at $10\,\mu\text{K} = 0.8 T_F$, where $k_B T_F = \hbar^2 k_F^2/2m = \hbar(3N_{tot}\omega_x\omega_y\omega_z)^{1/3} = \hbar\bar{\omega}(3N_{tot})^{1/3}$ is the Fermi energy. Lowering the intensity of the trapping laser to $0.1\,P_0$, the Fermi gas is evaporatively cooled to temperatures T at or below $0.2\,T_F$ and $N_{tot} \approx 7 \times 10^4$.

Then, sweeping the magnetic field to 770 G in 200 ms, the Feshbach resonance is slowly crossed. In this process atoms are reversibly transformed into cold molecules [14,16] near the BEC critical temperature as presented in Fig. 1(a). The onset of condensation is revealed by bimodal and anisotropic momentum distributions in time of flight expansions of the molecular gas. These images are recorded as follows. At a fixed magnetic field, the optical trap is first switched off. The cloud expands typically for 1 ms and then the magnetic field is increased by 100 G in 50 μs. This converts the molecules back into free atoms above resonance without releasing their binding energy [3]. Switching the field abruptly off in 10 μs, we detect free ^{6}Li atoms by light absorption near the D2 line. Using this method, expansion images are not altered by the adiabatic following of the molecular state to a

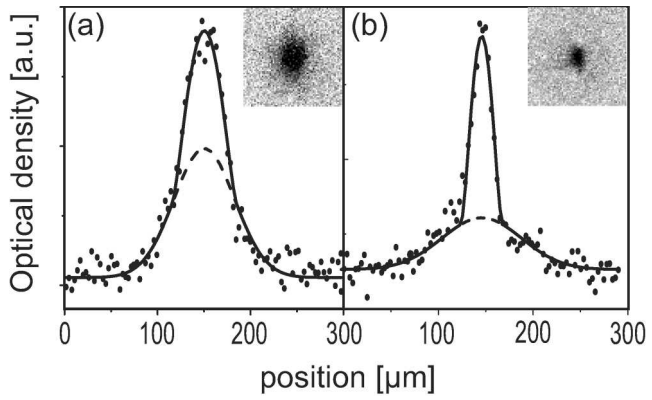

FIG. 1. Onset of Bose-Einstein condensation in a cloud of 2×10^4 ^{6}Li dimers at 770 G (a) and of 2×10^4 ^{7}Li atoms at 610 G (b) in the same optical trap. (a) 1.2 ms expansion profiles along the weak direction x of confinement. (b) 1.4 ms expansion. The different sizes of the condensates reflect the large difference in scattering length $a_m = 170$ nm for ^{6}Li dimers and $a_7 = 0.55$ nm for ^{7}Li. Solid line: Gaussian+Thomas-Fermi fit. Dashed line: Gaussian component. Condensate fractions are both 28%. $\omega_x/2\pi = 0.59(4)$ kHz, $\omega_y/2\pi = 1.6(1)$ kHz, and $\omega_z/2\pi = 1.7(1)$ kHz in (a). $\omega_x/2\pi = 0.55(4)$ kHz, $\omega_y/2\pi = 1.5(1)$ kHz, and $\omega_z/2\pi = 1.6(1)$ kHz in (b).

deeper bound state during switch-off as observed in our previous work [14]. Furthermore, we check that there are no unpaired atoms before expansion. In Fig. 1(b), a Bose-Einstein condensate of ^{7}Li atoms produced in the same optical trap is presented. The comparison between the condensate sizes after expansion reveals that the mean field interaction and scattering length are much larger for $^6Li_2$ dimers [Fig. 1(a)] than for ^{7}Li atoms [Fig. 1(b)].

To measure the molecule-molecule scattering length, we produce pure molecular condensates by taking advantage of our crossed dipole trap. We recompress the horizontal beam to full power while keeping the vertical beam at the low power of $0.035P_0^v$ corresponding to a trap depth for molecules $U = 5.6\,\mu$K. Temperature is then limited to $T \leq 0.9\,\mu$K assuming a conservative $\eta = U/k_BT = 6$, whereas the critical temperature increases with the mean oscillation frequency. Consequently, with an axial (respectively radial) trap frequency of 440 Hz (respectively 5 kHz), we obtain $T/T_C^0 \leq 0.3$, where $T_C^0 = \hbar\bar{\omega}(0.82N_{tot}/2)^{1/3} = 2.7\,\mu$K is the noninteracting BEC critical temperature. Thus, the condensate should be pure as confirmed by our images. After 1.2 ms of expansion, the radius of the condensate in the x (respectively y) direction is $R_x = 51\,\mu$m ($R_y = 103\,\mu$m). The resulting anisotropy $R_y/R_x = 2.0(1)$ is consistent with the value 1.98 [17] predicted the scaling equations [18,19]. Moreover, this set of equations leads to an *in-trap* radius $R_x^0 = 26\,\mu$m (respectively $R_y^0 = 2.75\,\mu$m). We then deduce the molecule-molecule scattering length from the Thomas-Fermi formula $R_{x,y}^0 = a_{ho}\bar{\omega}/\omega_{x,y}(15N_{tot}a_m/2a_{ho})^{1/5}$, with $a_{ho} = \sqrt{\hbar/2m\bar{\omega}}$. Averaging over several images, this yields $a_m = 170^{+100}_{-60}$ nm at 770 G. Here, the statistical uncertainty is negligible compared to the systematic uncertainty due to the calibration of our atom number. At this field, we calculate an atomic scattering length of $a = 306$ nm. Combined with the prediction $a_m = 0.6\,a$ of [10], we obtain $a_m = 183$ nm in good agreement with our measurement. For ^{7}Li, we obtain with the same analysis a much smaller scattering length of $a_7 = 0.65(10)$ nm at 610 G also in agreement with theory [20].

Such large values of a_m bring our molecular condensates into a novel regime where the gas parameter $n_m a_m^3$ is no longer very small. Indeed, $a_m = 170$ nm and $n_m = 6 \times 10^{13}$ cm^{-3} yield $n_m a_m^3 = 0.3$. As a first consequence, corrections due to beyond mean field effects [11,21] or to the underlying fermionic nature of atoms may play a role, since the average spacing between molecules is then of the order of the molecule size $\sim a/2$. Second, even in a mean field approach, thermodynamics is expected to be modified. For instance, in the conditions of Fig. 1(a), we expect a large shift of the BEC critical temperature [11–13]. The shift calculated to first order in $n^{1/3}a$ [12], $\Delta T_C/T_C^0 = -1.4$, is clearly inapplicable and a more refined approach is required [22]. Third, we observe that partially condensed cloud expansions are modified by interactions. Indeed, double structure fits lead to temperatures inconsistent with the presence of a condensate. In Fig. 1, we find $T = 1.6\,\mu$K, to be compared with $T_C^0 = 1.4\,\mu$K, whereas for the ^{7}Li condensate $T = 0.7\,\mu\text{K} = 0.6T_C^0$.

This inconsistency results from the large mean field interaction which modifies the thermal cloud expansion. To get a better estimate of the temperature, we rely on a release energy calculation. We calculate the Bose distribution of thermal atoms in a Mexican hat potential that is the sum of the external potential and the repulsive mean field potential created by the condensate. For simplicity we neglect the mean field resulting from the thermal component. The release energy is the sum of the thermal kinetic energy, condensate interaction energy, and Hartree-Fock interaction energy between the condensate and thermal cloud. The temperature and chemical potential are then adjusted to fit the measured atom number and release energy. For Fig. 1(a), we obtain a condensate fraction of 28% and $\mu = \hbar\bar{\omega}/2(15N_C a_m/2a_{ho})^{2/5} = 1.4\,\mu$K. The temperature $T = 0.9\,\mu$K is then found below $T_C^0 = 1.4\,\mu$K.

The condensate lifetime is typically $\sim$300 ms at 715 G ($a_m = 66$ nm) and $\sim 3\,s$ at 770 G ($a_m = 170$ nm), whereas for $a = -167$ nm at 1060 G, the lifetime exceeds 30 s. On the BEC side, the molecule-molecule loss rate constant is $G = 0.26^{+0.08}_{-0.06} \times 10^{-13}$ cm^3/s at 770 G and $G = 1.75^{+0.5}_{-0.4} \times 10^{-13}$ cm^3/s at 715 G with the fit procedure for condensates described in [23]. Combining similar results for four values of the magnetic field ranging from 700 to 770 G, we find $G \propto a^{-1.9\pm0.8}$. Our data are in

agreement with the theoretical prediction $G \propto a^{-2.55}$ of Ref. [10] and with previous measurements of G in a thermal gas at 690 G [14] or in a BEC at 764 G [8]. A similar power law was also found for ^{40}K [24].

We now present an investigation of the crossover from a Bose-Einstein condensate to an interacting Fermi gas (Figs. 2 and 3). We prepare a nearly pure condensate with 3.5×10^4 molecules at 770 G and recompress the trap to frequencies of $\omega_x = 2\pi \times 830$ Hz, $\omega_y = 2\pi \times 2.4$ kHz, and $\omega_z = 2\pi \times 2.5$ kHz. The magnetic field is then slowly swept at a rate of 2 G/ms to various values across the Feshbach resonance. The 2D momentum distribution after a time of flight expansion of 1.4 ms is then detected as previously.

Figure 2 presents the observed profiles (integrated over the orthogonal direction) for different values of the magnetic field. At the lowest field values $B \leq 750$ G, $n_m a_m^3 \ll 1$, condensates number are relatively low because of the limited molecule lifetime. As B increases, the condensate width gradually increases towards the width of a noninteracting Fermi gas, and nothing dramatic happens on resonance. At the highest fields ($B \geq 925$ G), where $k_F|a| \leq 3$, distributions are best fitted with zero temperature Fermi profiles. More quantitatively, Fig. 3(b) presents both the gas energy released after expansion E_{rel} and the anisotropy η across resonance. These are calculated from Gaussian fits to the density after time of flight: $E_{rel} = m(2\sigma_y^2 + \sigma_x^2)/2\tau^2$ and $\eta = \sigma_y/\sigma_x$, where σ_i is the rms width along i, and τ is the time of flight [17]. On the BEC side at 730 G, the measured anisotropy is $\eta \sim 1.6(1)$, in agreement with the hydrodynamic prediction, 1.75. It then decreases monotonically to 1.1 at 1060 G on the BCS side. On resonance, at zero temperature, superfluid hydrodynamic expansion is expected [25] corresponding to $\eta = 1.7$. We find, however, $\eta = 1.35(5)$, indicating a partially hydrodynamic behavior that could be due to a reduced superfluid fraction. On the $a < 0$ side, the decreasing anisotropy would indicate a further decrease of the superfluid fraction that could correspond to the reduction of the condensed fraction of fermionic atom pairs away from resonance observed in [7,9]. Interestingly, our results differ from that of Ref. [26] where hydrodynamic expansion was observed at 910 G in a more elongated trap for $T/T_F \simeq 0.1$.

In the BEC-BCS crossover regime, the gas energy released after expansion E_{rel} is also smooth [Fig. 3(c)]. E_{rel} presents a plateau for $B \leq 750$ G, and then increases monotonically towards that of a weakly interacting Fermi

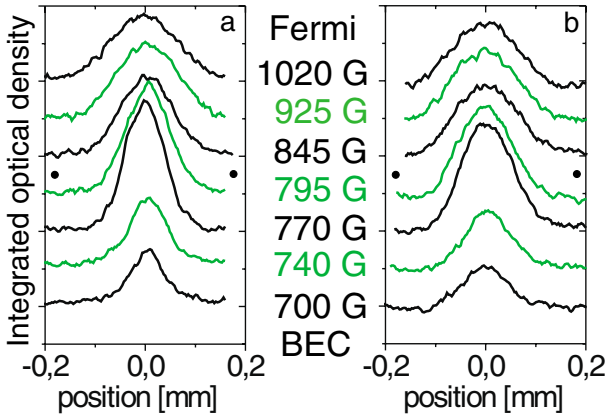

FIG. 2 (color online). Integrated density profiles across the BEC-BCS crossover region. 1.4 ms time of flight expansion in the axial (a) and radial (b) direction. The magnetic field is varied over the whole region of the Feshbach resonance from $a > 0$ ($B < 822$ G) to $a < 0$ ($B > 822$ G). ●: Feshbach resonance peak.

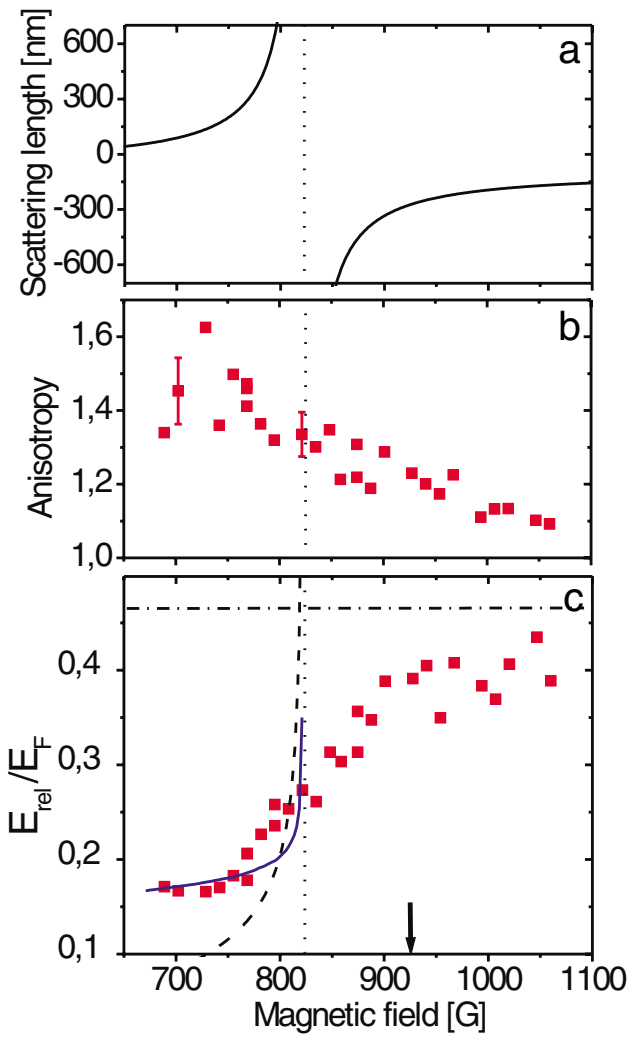

FIG. 3 (color online). (a) scattering length between the $|1/2, 1/2\rangle$ and $|1/2, -1/2\rangle$ ^{6}Li states. The Feshbach resonance peak is located at 822 G (dotted line). (b): anisotropy of the cloud, (c) release energy across the BEC-BCS crossover region. In (c), the dot-dashed line corresponds to a $T = 0$ ideal Fermi gas. The dashed curve is the release energy from a pure condensate in the Thomas-Fermi limit. The solid curve corresponds to a finite temperature mean field model described in the text with $T = 0.6\,T_C^0$. Arrow: $k_F|a| = 3$.

gas. The plateau is not reproduced by the mean field approach of a pure condensate (dashed line). This is a signature that the gas is not at $T = 0$. It can be understood with the mean field approach we used previously to describe the behavior of the thermal cloud. Since the magnetic field sweep is slow compared to the gas collision rate [14], we assume that this sweep is adiabatic and conserves entropy [27]. We then adjust this entropy to reproduce the release energy at a particular magnetic field, $B = 720$ G. The resulting curve as a function of B (solid line in Fig. 3(c)] agrees well with our data in the range 680 G $\leq B \leq$ 770 G, where the condensate fraction is 40%, and the temperature is $T \approx 0.6T_C^0 = 1.4\ \mu$K. This model is limited to $n_m a_m^3 \lesssim 1$. Near resonance the calculated release energy diverges and clearly departs from the data. On the BCS side, the release energy of a $T = 0$ ideal Fermi gas gives an upper bound for the data (dot-dashed curve), as expected from negative interaction energy and a very cold sample. This low temperature is supported by our measurements on the BEC side and the assumption of entropy conservation through resonance which predicts $T = 0.1\,T_F$ [27].

On resonance the gas is expected to reach a universal behavior, as the scattering length a is not a relevant parameter any more [5]. In this regime, the release energy scales as $E_{rel} = \sqrt{1+\beta}E_{rel}^0$, where E_{rel}^0 is the release energy of the noninteracting gas and β is a universal parameter. From our data at 820 G, we get $\beta = -0.64(15)$. This value is larger than the Duke result $\beta = -0.26 \pm 0.07$ at 910 G [26], but agrees with that of Innsbruck $\beta = -0.68^{+0.13}_{-0.10}$ at 850 G [8], and with the most recent theoretical prediction $\beta = -0.56$ [6]. Around 925 G, where $a = -270$ nm and $(k_F|a|)^{-1} = 0.35$, the release energy curve displays a change of slope. This is a signature of the transition between the strongly and weakly interacting regimes. It is also observed near the same field in [8] through *in situ* measurement of the trapped cloud size. Interestingly, the onset of resonance condensation of fermionic atom pairs observed in ^{40}K [7] and ^{6}Li [9], corresponds to a similar value of $k_F|a|$.

In summary, we have explored the whole region of the ^{6}Li Feshbach resonance, from a Bose-Einstein condensate of fermion dimers to an ultracold interacting Fermi gas. The extremely large scattering length between molecules that we have measured leads to novel BEC conditions. We have observed hydrodynamic expansions on the BEC side and nonhydrodynamic expansions at and above resonance. We suggest that this effect results from a reduction of the superfluid fraction and we point to the need of a better understanding of the dynamics of an expanding Fermi gas.

We are grateful to Y. Castin, C. Cohen-Tannoudji, R. Combescot, J. Dalibard, G. Shlyapnikov, and S. Stringari for fruitful discussions. This work was supported by CNRS, Collège de France, and Région Ile de France. S. Kokkelmans acknowledges a Marie Curie grant from the E.U. under Contract No. MCFI-2002-00968. Laboratoire Kastler-Brossel is Unité de recherche de l'Ecole Normale Supérieure et de l'Université Pierre et Marie Curie, associée au CNRS.

[1] M. Greiner, C. A. Regal, and D. S Jin, Nature (London) **426**, 537 (2003).
[2] S. Jochim *et al.*, Science **302**, 2101 (2003).
[3] M.W. Zwierlein *et al.*, Phys. Rev. Lett. **91**, 250401 (2003).
[4] A. J. Leggett, J. Phys. C (Paris) **41**, 7 (1980); P. Nozières and S. Schmitt-Rink, J. Low Temp. Phys. **59**, 195 (1985); C. Sá de Melo, M. Randeria, and J. Engelbrecht, Phys. Rev. Lett. **71**, 3202 (1993); M. Holland, S. Kokkelmans, M. Chiofalo, and R. Walser, Phys. Rev. Lett. **87**, 120406 (2001); Y. Ohashi and A. Griffin, Phys. Rev. Lett. **89**, 130402 (2002); J. N. Milstein, S. J. J. M. F. Kokkelmans, and M. J. Holland, Phys. Rev. A **66**, 043604 (2002); R. Combescot, Phys. Rev. Lett. **91**, 120401 (2003); G. M. Falco and H. T. C. Stoof, cond-mat/0402579.
[5] H. Heiselberg, Phys. Rev. A **63**, 043606 (2001).
[6] J. Carlson, S-Y Chang, V. R. Pandharipande, and K. E. Schmidt, Phys. Rev. Lett. **91**, 050401 (2003).
[7] C. A. Regal, M. Greiner, and D. S. Jin, Phys. Rev. Lett. **92**, 040403 (2004).
[8] M. Bartenstein *et al.*, Phys. Rev. Lett. **92**, 120401 (2004).
[9] M. Zwierlein *et al.*, Phys. Rev. Lett. **92**, 120403 (2004).
[10] D. S. Petrov, C. Salomon, and G.V. Shlyapnikov, cond-mat/0309010.
[11] G. Baym *et al.*, Eur. Phys. J. B **24**, 107 (2001).
[12] F. Dalfovo, S. Giorgini, L. P. Pitaevskii, and S. Stringari, Rev. Mod. Phys. **71**, 463 (1999).
[13] F. Gerbier *et al.*, Phys. Rev. Lett. **92**, 030405 (2004).
[14] J. Cubizolles *et al.*, Phys. Rev. Lett. **91**, 240401 (2003).
[15] T. Bourdel *et al.*, Phys. Rev. Lett. **91**, 020402 (2003).
[16] C. A. Regal, C. Ticknor, J. L. Bohn, and D. S. Jin, Nature (London) **424**, 47 (2003).
[17] We correct our data for the presence of a magnetic field curvature which leads to an antitrapping frequency of 100 Hz at 800 G along x.
[18] Yu. Kagan, E. L. Surkov, and G.V. Shlyapnikov, Phys. Rev. A **54**, 1753(R) (1996).
[19] Y. Castin and R. Dum, Phys. Rev. Lett. **77**, 5315 (1996).
[20] L. Khaykovich *et al.*, Science **296**, 1290 (2002).
[21] L. Pitaevskii and S. Stringari, Phys. Rev. Lett. **81**, 4541 (1998).
[22] A mean field self-consistent calculation of the molecular density profile in the trap at T_C leads to $T_C^{mf} = 0.58T_C^0 \approx 0.8\,\mu$K. S. Kokkelmans (to be published).
[23] J. Söding *et al.*, Appl. Phys. B **69**, 257 (1999).
[24] C. Regal, M. Greiner, and D. Jin, Phys. Rev. Lett. **92**, 083201 (2004).
[25] C. Menotti, P. Pedri, and S. Stringari, Phys. Rev. Lett. **89**, 250402 (2002).
[26] K. O'Hara *et al.*, Science **298**, 2179 (2002); M. Gehm *et al.*, Phys. Rev. A **68**, 011401 (2003).
[27] L. D. Carr, G.V. Shlyapnikov, and Y. Castin, Phys. Rev. Lett. **92**, 150404 (2004).

A.2 P-wave Feshbach resonances of ultra-cold ^{6}Li

J. Zhang, E.G.M. van Kempen, T. Bourdel, L. Khaykovich, J. Cubizolles, F. Chevy, M. Teichmann, L. Tarruell, S.J.J.M.F. Kokkelmans, and C. Salomon,

Physical Review A, volume **70**, page 030702(R), 30 September 2004.

PHYSICAL REVIEW A **70**, 030702(R) (2004)

P-wave Feshbach resonances of ultracold ^{6}Li

J. Zhang,[1,2] E. G. M. van Kempen,[3] T. Bourdel,[1] L. Khaykovich,[1,4] J. Cubizolles,[1] F. Chevy,[1] M. Teichmann,[1] L. Tarruell,[1] S. J. J. M. F. Kokkelmans,[1,3] and C. Salomon[1]

[1]*Laboratoire Kastler-Brossel, ENS, 24 rue Lhomond, 75005 Paris, France*

[2]*SKLQOQOD, Institute of Opto-Electronics, Shanxi University, Taiyuan 030006, People's Republic of China*

[3]*Eindhoven University of Technology, P.O. Box 513, 5600 MB Eindhoven, The Netherlands*

[4]*Department of Physics, Bar Ilan University, Ramat Gan 52900, Israel*

(Received 18 June 2004; published 30 September 2004)

We report the observation of three *p*-wave Feshbach resonances of ^{6}Li atoms in the lowest hyperfine state $f=1/2$. The positions of the resonances are in good agreement with theory. We study the lifetime of the cloud in the vicinity of the Feshbach resonances and show that, depending on the spin states, two- or three-body mechanisms are at play. In the case of dipolar losses, we observe a nontrivial temperature dependence that is well explained by a simple model.

DOI: 10.1103/PhysRevA.70.030702 PACS number(s): 34.50.−s, 03.75.Ss, 05.30.Fk, 32.80.Pj

In the presence of a magnetic field, it is possible to obtain a quasidegeneracy between the relative energy of two colliding atoms and that of a weakly bound molecular state. This effect, known as a Feshbach resonance, is usually associated with the divergence of the scattering length and is the key ingredient that led to the recent observation of superfluids from fermion atom pairs of ^{6}Li [1–4] and ^{40}K [5]. Up to now these pairs were formed in *s*-wave channels but it is known from condensed matter physics that fermionic superfluidity can arise through higher angular momentum pairing: *p*-wave Cooper pairs have been observed in ^{3}He [6] and *d*-wave cooper pairs in high-T_c superconductivity [7]. Although Feshbach resonances involving *p* or higher partial waves have been found in cold atom systems [8–10], *p*-wave atom pairs have never been directly observed.

In this paper we report the observation of three narrow *p*-wave Feshbach resonances of ^{6}Li in the lowest hyperfine state $f=1/2$. We measure the position of the resonance as well as the lifetime of the atomic sample for all combinations $|f=1/2,m_f\rangle+|f=1/2,m_f'\rangle$, henceforth denoted (m_f,m_f'). We show that the position of the resonances are in good agreement with theory. In the case of atoms polarized in the ground state $(1/2,1/2)$, the atom losses are due to three-body processes. We show that the temperature dependence of the losses at resonance cannot be described by the threshold law predicted by [11] on the basis of the symmetrization principle for identical particles. In the case of atoms polarized in $(-1/2,-1/2)$ or that of a mixture $(1/2,-1/2)$, the losses are mainly due to two-body dipolar losses. These losses show a nontrivial temperature dependence that can nevertheless be understood by a simple theoretical model with only one adjustable parameter. In the $(1/2,-1/2)$ channel, we take advantage of a sharp decrease of the two-body loss rate below the Feshbach resonance to present a first evidence for the generation of *p*-wave molecules.

The *p*-wave resonances described in this paper have their origin in the same singlet $(S=0)$ bound state that leads to the *s*-wave Feshbach resonances located at 543 G and ~830 G. The latter has been used to generate stable molecular Bose-Einstein condensates [1–4]. In order to discuss the origin of these resonances, it is useful to introduce the molecular basis quantum numbers S,I, and l, which correspond to the total electron spin $\boldsymbol{S}=\boldsymbol{s}_1+\boldsymbol{s}_2$, total nuclear spin $\boldsymbol{I}=\boldsymbol{i}_1+\boldsymbol{i}_2$, and orbital angular momentum $\boldsymbol{l}$. Furthermore, the quantum numbers must fulfill the selection rule

$$S+I+l=\text{even}, \tag{1}$$

which is a result of the symmetrization requirements of the two-body wave function. Since the atomic nuclear spin quantum numbers are $i_1=i_2=1$, and $S=0$, there are two possibilities for the total nuclear spin in combination with an *s*-wave $(l=0)$ collision: $I=0$ and $I=2$. These two states give rise to the two aforementioned *s*-wave Feshbach resonances. For *p*-wave $(l=1)$ collisions only $I=1$ is possible. This bound state may then give rise to the three *p*-wave Feshbach resonances of Fig. 1. This threshold state does not suffer from exchange decay, and is therefore relatively stable. Our predicted resonance field values B_F (Table I) result from an analysis which takes into account the most recent experimental data available for ^{6}Li. The calculation has been performed for all spin channels (m_f,m_f') and a typical collision energy

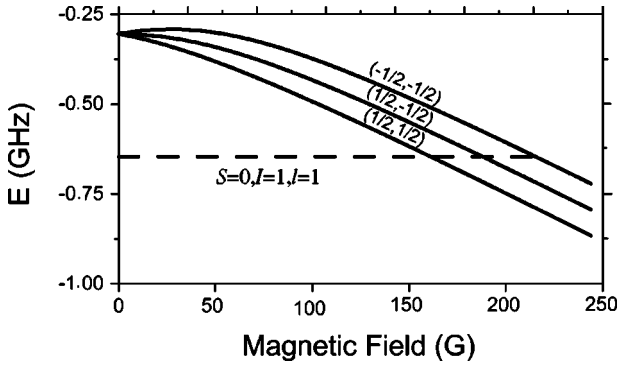

FIG. 1. Coupled channels calculation of *p*-wave binding energies, which give rise to Feshbach resonances at threshold. The two-atom states (full line) are indicated by their quantum number (m_{f_1},m_{f_2}), while the bound state (dashed line) is labeled by the molecular quantum numbers S,I, and l.

TABLE I. Theoretical and experimental values of the magnetic field B_F at the p-wave Feshbach resonance for ^{6}Li atoms in $|f_1=1/2,m_{f_1}\rangle$ and $|f_1=1/2,m_{f_2}\rangle$.

(m_{f_1},m_{f_2})	Theory (G)	Experiment (G)
$(1/2,1/2)$	159	160.2(6)
$(1/2,-1/2)$	185	186.2(6)
$(-1/2,-1/2)$	215	215.2(6)

of 15 μK. A more detailed analysis will be published elsewhere [12].

Experimentally, we probe these p-wave resonances using the setup described in previous papers [13,14]. After evaporative cooling in the magnetic trap, we transfer $\sim 5\times 10^5$ atoms of ^{6}Li in $|f=3/2,\ m_f=3/2\rangle$ in a far-detuned crossed optical trap at low magnetic field. The maximum power in each arm is $P_h^0=2$ W and $P_v^0=3.3$ W in the horizontal and vertical beam, respectively, and corresponds to a trap depth of $\sim 80\ \mu$K. The oscillation frequencies measured by parametric excitation are, respectively, $\omega_x=2\pi\times 2.4(2)$ kHz, $\omega_y=2\pi\times 5.0(3)$ kHz, $\omega_z=2\pi\times 5.5(4)$ kHz, where the $x(y)$ direction is chosen along the horizontal (vertical) beam. A first radio-frequency (rf) sweep brings the atoms to $|f=1/2,\ m_f=1/2\rangle$ and, if necessary, we perform a second rf transfer to prepare the mixture $(1/2,-1/2)$ or the pure $(-1/2,-1/2)$. The variable magnetic field B is the sum of two independent fields B_0 and B_1. B_0 offers a wide range of magnetic field while B_1 can be switched off rapidly. After the radio-frequency transfer stage, we ramp the magnetic field to $B_0\sim 220$ G with $B_1\sim 8$ G in 100 ms. When needed, we reduce in 100 ms the power of the trapping beams to further cool the atoms. For the coldest samples, we obtain at the end of this evaporation sequence $N\sim 10^5$ atoms at a temperature $\sim 5\ \mu$K. This corresponds to a ratio $T/T_F\sim 0.5$, where $k_BT_F=\hbar(6N\omega_x\omega_y\omega_z)^{1/3}$ is the Fermi energy of the system. To reach the Feshbach resonance, we reduce B_0 in 4 ms to its final value $B_{0,f}\sim B_F$, near the Feshbach resonance. At this stage, we abruptly switch off B_1 so that the total magnetic field is now close to resonance. After a waiting time in the trap $t_{\rm wait}=50$ ms, we switch off the trapping and the magnetic field and we measure the remaining atom number after a 0.35 ms time of flight.

We show in Fig. 2 the dependence of the atom number on the final value of $B_{0,f}$ in the case of the spin mixture $(1/2,-1/2)$ at a temperature $T\sim 14\ \mu$K. As expected from theory, we observe a sharp drop of the atom number for values of the magnetic field close to 186 G. The other two p-wave Feshbach resonances have a similar loss signature and Table I shows that for all spin channels, the resonance positions are in good agreement with predictions. Note that in Table I the uncertainty is mainly due to the magnetic field calibration while the short term stability is $\lesssim 50$ mG.

To evaluate the possibility of keeping p-wave molecules in our trap, we have studied the lifetime of the gas sample at the three Feshbach resonances. We have measured the number N of atoms remaining in the trap after a variable time $t_{\rm wait}$. Accounting for two- and three-body processes only, N should follow the rate equation

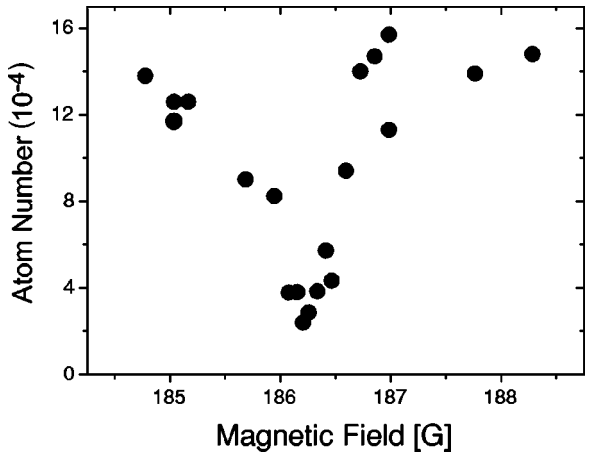

FIG. 2. Atom number vs magnetic field $B_{0,f}$ after a 50 ms wait for atoms in the spin mixture $(1/2,-1/2)$ at $T\sim 14\ \mu$K. The sharp drop close to $B_0\sim 186$ G over a range $\simeq 0.5$ G is the signature of the p-wave Feshbach resonance predicted by theory.

$$\frac{\dot{N}}{N}=-G_2\langle n\rangle-L_3\langle n^2\rangle, \tag{2}$$

where n is the atom density and $\langle n^a\rangle=\int d^3r\, n^{a+1}/N$ $(a=1,2)$ is calculated from the classical Boltzman distribution. In this equation, we can safely omit one-body losses since the measured decay time is ~ 100 ms, much smaller than the one-body lifetime ~ 30 s.

In the $(1/2,1/2)$ channel, we find that three-body losses are dominant. The dependence of L_3 with temperature is very weak [Fig. 3(a)]. A theoretical calculation of the temperature dependence of three-body loss rate has been performed in [11] and it predicts that in the case of indistinguishable fermions L_3 should be proportional to T^λ, with $\lambda\geqslant 2$. Although this prediction seems in disagreement with our experimental

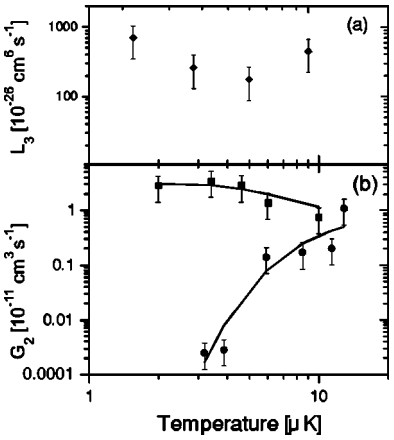

FIG. 3. Variations of (a) three-body and (b) two-body loss rates vs temperature at the Feshbach resonance. (a) ♦: atoms in the Zeeman ground state $|f=1/2,m_f=1/2\rangle$, $B_{0,f}\sim 159$ G. (b) ■: atoms polarized in $|f=1/2,m_f=-1/2\rangle$, $B_{0,f}\sim 215$ G. ●: the mixture $|f=1/2,m_f=1/2\rangle+|f=1/2,m_f=-1/2\rangle$, $B_{0,f}\sim 186$ G. In both cases, the full line is a fit to the data using the prediction of Eq. (4) with the magnetic field as the only fitting parameter.

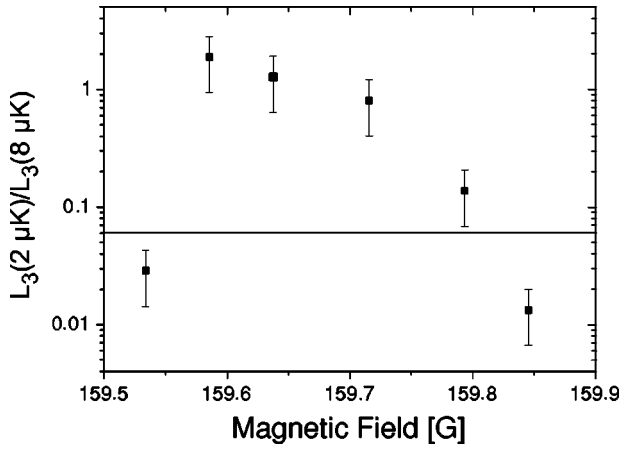

FIG. 4. Ratio $L_3(T=2\ \mu\text{K})/L_3(T=8\ \mu\text{K})$ of the three-body decay rate for two different temperatures for a gas of atoms polarized in $|f=1/2, m_f=1/2\rangle$. The full line is the threshold law $L_3 \sim T^2$.

results, the analysis of [11] relies on a Wigner threshold law, i.e., a perturbative calculation based on the Fermi golden rule. At the Feshbach resonance where the scattering cross section is expected to diverge, this simplified treatment is not sufficient. This suggests that three-body processes must be described by a more refined formalism, analogous to the unitary limited treatment of the *s*-wave elastic collisions [15]. To confirm this assumption, we have compared the loss rates at two given temperatures ($T=2\ \mu$K and $T=8\ \mu$K, respectively) for various values of the magnetic field (Fig. 4). If the threshold law is valid, then the ratio $L_3(2\ \mu\text{K})/L_3(8\ \mu\text{K})$ should always be smaller than $(2/8)^2 \sim 0.0625$ (full line of Fig. 4). As seen before, experimental data show no significant variation of L_3 with temperature near resonance. However, when the magnetic field is tuned out of resonance we recover a dependence in agreement with [11].

In contrast to *s*-wave Feshbach resonances where dipolar losses are forbidden in the $f=1/2$ manifold [16], the losses at resonance are found to be dominantly two body in the $(1/2,-1/2)$ and $(-1/2,-1/2)$ channels. The variations of the two-body loss rate with temperature are displayed in Fig. 3(b). The temperature dependence appears very different in the two cases. We show now that this is the consequence of a strong sensitivity to magnetic field detuning from resonance, rather than a specific property of the states involved. In an extension of the work presented in [17], we describe inelastic collisions by two noninteracting open channels coupled to a single *p*-wave molecular state [18]. This model leads to an algebra close to the one describing photoassociation phenomena [19] and the two-body loss rate at energy E is given by

$$g_2(E) = \frac{KE}{(E-\delta)^2 + \gamma^2/4}. \tag{3}$$

Here $\delta = \mu(B - B_F)$ is the detuning to the Feshbach resonance and K, μ, and γ are phenomenological constants, depending on the microscopic details of the potential [21]. For each channel, these parameters are estimated from our coupled-channel calculation (Table II). To compare with experimental

TABLE II. Parameters characterizing the two-body loss rates for $(1/2,-1/2)$ and $(-1/2,-1/2)$ spin channels.

(m_{f_1}, m_{f_2})	K ($\text{cm}^3\ \mu\text{K s}^{-1}$)	γ (μK)	μ ($\mu\text{K G}^{-1}$)
$(1/2,-1/2)$	1.21×10^{-13}	0.05	117
$(-1/2,-1/2)$	7.33×10^{-13}	0.08	111

data, Eq. (3) is averaged over a thermal distribution and for $\delta > 0$ and $\delta \gg \gamma$ we get

$$G_2 \sim 4\sqrt{\pi}\frac{K}{\gamma}\left(\frac{\delta}{k_B T}\right)^{3/2} e^{-\delta/k_B T}. \tag{4}$$

Equation (4) is used to fit the data of Fig. 3(b), with $B - B_F$ as the only fitting parameter. We get a fairly good agreement if we take $B - B_F = 0.04$ G (0.3 G) for the $(-1/2, -1/2)[(1/2,-1/2)]$ channel, illustrating the extreme sensitivity of G_2 to detuning and temperature. This feature was also qualitatively tested by measuring the variations of G_2 with magnetic field at constant temperature. Another interesting feature of Eq. (4) is that it predicts that the width δB of the Feshbach resonance, as measured by atom losses, should scale like $k_B T/\mu$. For a typical temperature $T \sim 15\ \mu$K, this yields $\delta B \sim 0.15$ G, in agreement with the resonance width shown in Fig. 2.

From Eq. (4) we see that G_2 nearly vanishes at $\delta = 0$. The thermal average of Eq. (4) for $\delta = 0$ yields $G_2(\delta=0) \propto K k_B T$. The ratio between the maximum two-body loss rate ($\delta = 3k_B T/2$) and that at $\delta = 0$ is then $\sim k_B T/\gamma$, $\sim 10^2$ for $\sim 10\ \mu$K. In the region $\delta < 0$ where we expect to form molecules, we benefit from a $1/\delta^2$ further reduction of the two-body losses [see Eq. (4)].

We have checked the production of molecules in $(1/2, -1/2)$ by using the scheme presented in [13,22]. We first generate molecules in $|S=0, I=1, l=1\rangle$ by ramping in 20 ms the magnetic field from 190 G $> B_F$ to $B_{\text{nuc}} = 185$ G $< B_F$. At this stage, we can follow two paths before detection (Fig. 5). Path 1 permits us to measure the number N_1 of free atoms: by ramping *down* in 2 ms the magnetic field from 185 G to 176 G, we convert the molecules into deeply bound molecu-

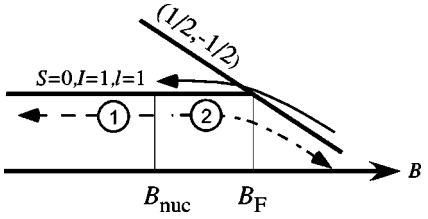

FIG. 5. Molecules are generated by ramping from a magnetic field higher than B_F to $B_{\text{nuc}} < B_F$. From there, two paths are used. In path 1 (dashed line), the magnetic field is decreased to create tightly bound molecules that will not appear on absorption images. In path 2 (dashed-dotted line), the magnetic field is ramped up across resonance to dissociate the molecules. The efficiency of the molecule production is simply given by $(1 - N_1/N_2)$, where N_i is the atom number measured after path i.

lar states that decay rapidly by two-body collisions. Path 2 gives access to the total atom number N_2 (free atoms + atoms bound in *p*-wave molecules). It consists of ramping *up* the magnetic field in 2 ms from B_{nuc} to 202 G$>B_F$ to convert the molecules back into atoms. Since the atoms involved in molecular states appear only in pictures taken in path 2, the number of molecules in the trap is $(N_2-N_1)/2$. In practice, both sequences are started immediately after reaching B_{nuc} and we average the data of 25 pictures to compensate for atom number fluctuations. We then get $N_1=7.1(5)\times10^4$ and $N_2=9.1(7)\times10^4$ which corresponds to a molecule fraction $1-N_1/N_2=0.2(1)$. Surprisingly, we failed to detect any molecule signal when applying the same method to $(1/2,1/2)$ atoms.

Since the dramatic reduction of inelastic losses close to a *s*-wave Feshbach resonance [23] was a key ingredient to the recent observation of fermionic superfluids, the formation of stable atom pairs requires a full understanding of the decay mechanisms at play close to a *p*-wave resonance. In this paper we have shown that in the particular case of two-body losses, the maximum losses take place when the detuning is positive. Since stable dimers are expected to be generated for negative detuning, dipolar losses should not present a major hindrance to further studies of *p*-wave molecules.

We thank Z. Hadzibabic for very helpful discussions. S.K. acknowledges support from the Netherlands Organization for Scientific Research (NWO). E.K. acknowledges support from the Stichting FOM, which is financially supported by NWO. This work was supported by CNRS, and Collège de France. Laboratoire Kastler Brossel is *Unité de recherche de l'École Normale Supérieure et de l'Université Pierre et Marie Curie, associée au CNRS*.

[1] S. Jochim *et al.*, Science **302**, 2101 (2003).
[2] M. W. Zwierlein *et al.*, Phys. Rev. Lett. **91**, 250401 (2003).
[3] T. Bourdel *et al.*, e-print cond-mat/0403091.
[4] J. Kinast *et al.*, Phys. Rev. Lett. **92**, 150402 (2004).
[5] M. Greiner, C. A. Regal, and D. S Jin, Nature (London) **426**, 537 (2003).
[6] D. M. Lee, Rev. Mod. Phys. **69**, 645 (1997).
[7] C. C Tsuei and J. R. Kirtley, Phys. Rev. Lett. **85**,182 (2000).
[8] C. Chin *et al.*, Phys. Rev. Lett. **85**, 2717 (2000).
[9] C. A. Regal *et al.*, Phys. Rev. Lett. **90**, 053201 (2003).
[10] T. Weber *et al.*, Phys. Rev. Lett. **91**, 123201 (2003).
[11] B. D. Esry, C. H. Greene, and H. Suno, Phys. Rev. A **65**, 010705 (2002).
[12] E. G. M. van Kempen *et al.*, e-print cond-mat/0406722.
[13] J. Cubizolles *et al.*, Phys. Rev. Lett. **91** 240401 (2003).
[14] T. Bourdel *et al.*, Phys. Rev. Lett. **91**, 020402 (2003).
[15] H. Suno, B. D. Esry, and C. H. Greene, Phys. Rev. Lett. **90**, 053202 (2003).
[16] K. Dieckmann *et al.*, Phys. Rev. Lett. **89**, 203201 (2002).
[17] M. Holland *et al.*, Phys. Rev. Lett. **87**, 120406 (2001).
[18] We also neglect the splitting between the different m_l predicted by [20].
[19] R. Napolitano *et al.*, Phys. Rev. Lett. **73**, 1352 (1994)
[20] C. Ticknor *et al.*, Phys. Rev. A **69**, 042712 (2004).
[21] Note that in our case μ is positive. This corresponds to molecular states stable at low field.
[22] C. A. Regal *et al.*, Nature (London) **424**, 47 (2003).
[23] D. S. Petrov, Phys. Rev. A **67**, 010703 (2003).

A.3 Expansion of a lithium gas in the BEC-BCS crossover

J. Zhang, E. G. M. van Kempen, T. Bourdel, L. Khaykovich, J. Cubizolles, F. Chevy, M. Teichmann, L. Tarruell, S.J.J.M.F. Kokkelmans, and C. Salomon,

Proceedings of the XIX International Conference on Atomic Physics, ICAP 2004, AIP Conference Proceedings **770**, page 228, 5 May 2005.

Expansion of a lithium gas in the BEC-BCS crossover

J.Zhang[a,b], E. G. M. van Kempen[c], T. Bourdel[a], L. Khaykovich[a,d], J. Cubizolles[a], F. Chevy[a]
M. Teichmann[a] L. Tarruell[a], S. J. J. M. F. Kokkelmans[a,c], and C. Salomon[a]
Laboratoire Kastler-Brossel, ENS, 24 rue Lhomond, 75005 Paris,
[b] *SKLQOQOD, Institute of Opto-Electronics, Shanxi University, Taiyuan 030006, P.R. China,*
[c] *Eindhoven University of Technology, P.O. Box 513, 5600 MB Eindhoven, The Netherlands,*
[d] *Department of Physics, Bar Ilan University, Ramat Gan 52900, Israel.*

We report on experiments in ^{6}Li Fermi gases near Feshbach resonances. A broad s-wave resonance is used to form a Bose-Einstein condensate of weakly bound $^6Li_2$ molecules in a crossed optical trap. The measured molecule-molecule scattering length of 170^{+100}_{-60} nm at 770 G is found in good agreement with theory. The expansion energy of the cloud in the BEC-BCS crossover region is measured. Finally we discuss the properties of p-wave Feshbach resonances observed near 200 Gauss and new s-wave resonances in the heteronuclear ^{6}Li- ^{7}Li mixture.

Strongly interacting fermionic systems occur in a variety of physical processes, ranging from nuclear physics, to high temperature superconductivity, superfluidity, quark-gluon plasmas, and ultra-cold dilute gases. Thanks to the phenomenon of Feshbach resonances, these gases offer the unique possibility to tune the strength and the sign of the effective interaction between particles. In this way, it is possible to study the crossover between situations governed by Bose-Einstein and Fermi-Dirac statistics.

BEC-BCS CROSSOVER NEAR ^{6}LI S-WAVE RESONANCE

When the scattering length a characterizing the 2-body interaction at low temperature is positive, the atoms can pair in a weakly bound molecular state. When the temperature is low enough, these bosonic dimers can form a Bose-Einstein condensate (BEC) as observed very recently in ^{40}K [1] and ^{6}Li [2–4]. On the side of the resonance where a is negative, one expects the well known Bardeen-Cooper-Schrieffer (BCS) model for superconductivity to be valid. However, this simple picture of a BEC phase on one side of the resonance and a BCS phase on the other is valid only for small atom density n. When $n|a|^3 \gtrsim 1$ the system enters a strongly interacting regime that represents a challenge for many-body theories [5]. In the recent months, this regime has been the subject of intense experimental activity [4, 6–11].

Here we first report on Bose-Einstein condensation of ^{6}Li dimers in a crossed optical dipole trap, and a study of the BEC-BCS crossover region. Unlike all previous observations of molecular BEC made in single beam dipole traps with very elongated geometries, our condensates are formed in nearly isotropic strongly confining traps. The experimental setup has been described previously [12, 13]. A gas of ^{6}Li atoms is prepared in the absolute ground state $|1/2, 1/2\rangle$ in a Nd-YAG crossed beam optical dipole trap. The horizontal beam (resp. vertical) propagates along x (y), has a maximum power of $P_o^h = 2$ W ($P_o^v = 3.3$ W) and a waist of $\sim 25\,\mu$m ($\sim 40\,\mu$m). At full power, the ^{6}Li trap oscillation frequencies are $\omega_x/2\pi = 2.4(2)$ kHz, $\omega_y/2\pi = 5.0(3)$ kHz, and $\omega_z/2\pi = 5.5(4)$ kHz, as measured by parametric excitation, and the trap depth is $\sim 80\,\mu$K. After sweeping the magnetic field B from 5 G to 1060 G, we drive the Zeeman transition between $|1/2, 1/2\rangle$ and $|1/2, -1/2\rangle$ with a 76 MHz RF field to prepare a balanced mixture of the two states. As measured recently [11], the Feshbach resonance between these two states is peaked at 834(2) G, and for B=1060 G, $a = -167$ nm. After 100 ms the coherence between the two states is lost and plain evaporation provides $N_\uparrow = N_\downarrow = N_{\rm tot}/2 = 1.5 \times 10^5$ atoms at $10\,\mu$K=$0.8\,T_{\rm F}$, where $k_{\rm B}T_{\rm F} = \hbar^2 k_{\rm F}^2/2m = \hbar(3N_{\rm tot}\omega_x\omega_y\omega_z)^{1/3} = \hbar\bar{\omega}(3N_{\rm tot})^{1/3}$ is the Fermi energy. Lowering the intensity of the trapping laser to $0.1\,P_0$, the Fermi gas is evaporatively cooled to temperatures T at or below $0.2\,T_{\rm F}$ and $N_{\rm tot} \approx 7 \times 10^4$.

Then, sweeping the magnetic field to 770 G in 200 ms, the Feshbach resonance is slowly crossed. In this process atoms are adiabatically and reversibly transformed into cold molecules [13, 14] near the BEC critical temperature as presented in figure 1a. The onset of condensation is revealed by bimodal and anisotropic momentum distributions in time of flight expansions of the molecular gas. These images are recorded as follows. At a fixed magnetic field, the optical trap is first switched off. The cloud expands typically for 1 ms and then the magnetic field is increased by 100 G in 50 μs. This converts the molecules back into free atoms above resonance without releasing their binding energy [3]. Switching the field abruptly off in 10 μs, we detect free ^{6}Li atoms by light absorption near the D2 line. We have checked that, in the trap before expansion, there are no unpaired atoms. In figure 1b, a Bose-Einstein condensate of ^{7}Li atoms produced in the same optical trap is presented. The comparison between the condensate sizes after expansion dramatically reveals that the mean field interaction and scattering length are much larger for $^6Li_2$ dimers (Fig. 1a) than for ^{7}Li atoms (Fig. 1b).

To measure the molecule-molecule scattering length, we produce pure molecular condensates by taking advantage of our crossed dipole trap. We recompress the horizontal beam to full power while keeping the vertical beam at the low power of $0.035\,P_0^v$ corresponding to a trap depth for molecules $U = 5.6\,\mu$K. Temperature is then limited to $T \leq 0.9\,\mu$K assuming a conservative $\eta = U/k_{\rm B}T = 6$, whereas the critical temperature increases with the mean oscillation frequency. Consequently, with an axial (resp. radial) trap frequency of 440 Hz (resp. 5 kHz), we obtain $T/T_{\rm C}^0 \leq 0.3$, where $T_{\rm C}^0 = \hbar\bar{\omega}(0.82N_{\rm tot}/2)^{1/3}$ =2.7 μK is the non interacting BEC critical temperature. Thus, the condensate should be pure as confirmed by our images. After 1.2 ms of expansion, the radius of the condensate in the x (resp. y) direction is $R_x = 51$ μm ($R_y = 103$ μm). The resulting anisotropy

$R_y/R_x = 2.0(1)$ is consistent with the value 1.98 [15] predicted the scaling equations [16, 17]. Moreover, this set of equation leads to an *in-trap* radius $R_x^0 = 26\mu$m (resp. $R_y^0 = 2.75\mu$m). We then deduce the molecule-molecule scattering length from the Thomas-Fermi formula $R_{x,y}^0 = a_{\rm ho}\bar{\omega}/\omega_{x,y}(15N_{\rm tot}a_{\rm m}/2a_{\rm ho})^{1/5}$, with $a_{\rm ho} = \sqrt{\hbar/2m\bar{\omega}}$. Averaging over several images, this yields $a_{\rm m} = 170^{+100}_{-60}$ nm at 770 G. Here, the statistical uncertainty is negligible compared to the systematic uncertainty due to the calibration of our atom number. At this field, we calculate an atomic scattering length of $a = 306$ nm. Combined with the prediction $a_{\rm m} = 0.6\,a$ of [18], we obtain $a_{\rm m} = 183$ nm in good agreement with our measurement. For ^{7}Li, we obtain with the same analysis a much smaller scattering length of a_7=0.65(10) nm at 610 G also in agreement with theory [19].

The condensate lifetime is typically ∼300 ms at 715 G ($a_{\rm m} = 66$ nm) and ∼3 s at 770 G ($a_{\rm m} = 170$ nm), whereas for $a = -167$ nm at 1060 G, the lifetime exceeds 30 s. On the BEC side, the molecule-molecule loss rate constant is $G = 0.26^{+0.08}_{-0.06}\times10^{-13}$ cm^3/s at 770 G and $G = 1.75^{+0.5}_{-0.4}\times10^{-13}$ cm^3/s at 715 G with the fit procedure for condensates described in [20]. Combining similar results for four values of the magnetic field ranging from 700 G to 770 G, we find $G \propto a^{-1.9\pm0.8}$ (figure 2). Our data are in agreement with the theoretical prediction $G \propto a^{-2.55}$ of ref. [18] and with previous measurements of G in a thermal gas at 690 G [13] or in a BEC at 764 G [6]. A similar power law was also found for ^{40}K [21].

We then made an investigation of the crossover from a Bose-Einstein condensate to an interacting Fermi gas (Fig. 1.c and d). We prepare a nearly pure condensate with 3.5×10^4 molecules at 770 G and recompress the trap to frequencies of $\omega_x = 2\pi\times830$ Hz, $\omega_y = 2\pi\times2.4$ kHz, and $\omega_z = 2\pi\times2.5$ kHz. The magnetic field is then slowly swept at a rate of 2 G/ms to various values across the Feshbach resonance. The 2D momentum distribution after a time of flight expansion of 1.4 ms is then detected as previously. As B increases from the regime of weak interactions the condensate size gradually increases towards the width of a non interacting Fermi gas. Nothing particular happens on resonance. Fig. 1.c and 1.d present respectively the anisotropy of the cloud after expansion η and the corresponding released energy $E_{\rm rel}$. These are calculated from gaussian fits to the density after time of flight: $E_{\rm rel} = m(2\sigma_y^2 + \sigma_x^2)/2\tau^2$ and $\eta = \sigma_y/\sigma_x$, where σ_i is the rms width along i, and τ is the time of flight. The anisotropy monotonically decreases from ∼1.6 on the BEC side, where hydrodynamic expansion predicts 1.75, to 1.1, at 1060 G, on the BCS side. On resonance, at zero temperature, a superfluid hydrodynamic expansion is expected [22] and would correspond to $\eta = 1.7$. We find however $\eta = 1.35(5)$, indicating a partially hydrodynamic behavior that could be due to a reduced superfluid fraction. On the $a < 0$ side, the decreasing anisotropy would indicate a further decrease of the superfluid fraction that could correspond to the reduction of the condensed fraction of fermionic atom pairs away from resonance observed in [7, 8]. Interestingly, our results differ from that of ref.[23] where hydrodynamic expansion was observed at 910 G in a more elongated trap for $T/T_{\rm F} \simeq 0.1$.

In the BEC-BCS crossover regime, the gas energy released after expansion $E_{\rm rel}$ is also smooth (Fig. 1.d). $E_{\rm rel}$ presents a plateau for $B \leq 750$ G, and then increases monotonically towards that of a weakly interacting Fermi gas. The plateau is not

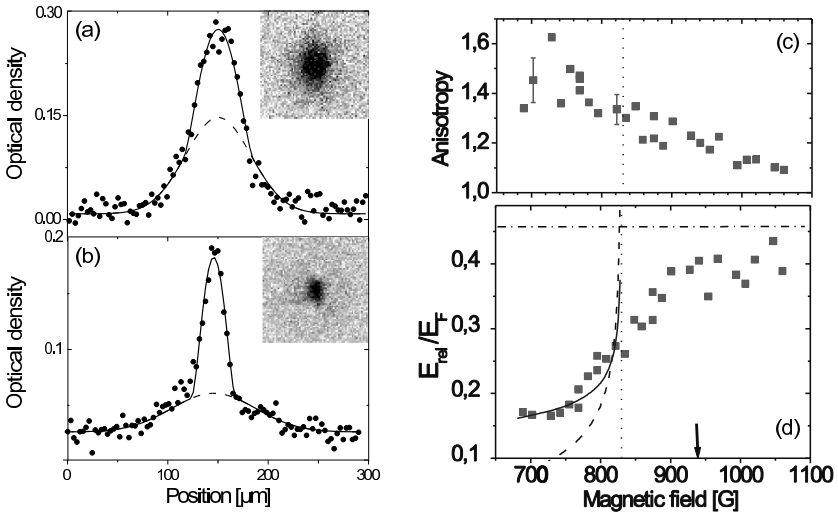

FIG. 1: a,b: Onset of Bose-Einstein condensation in a cloud of 2×10^4 ^{6}Li dimers at 770 G (a) and of 2×10^4 ^{7}Li atoms at 610 G (b) in the same optical trap. (a): 1.2 ms expansion profiles along the weak direction x of confinement. (b): 1.4 ms expansion. The different sizes of the condensates reflect the large difference in scattering length $a_{\rm m} = 170$ nm for ^{6}Li dimers and $a_7 = 0.55$ nm for ^{7}Li. Solid line: Gaussian+Thomas-Fermi fit. Dashed line: gaussian component. Condensate fractions are 44 % in (a) and 28% in (b). c,d: BEC-BCS crossover. (c): anisotropy of the cloud. (d): release energy across the BEC-BCS crossover region. In (d), the dot-dashed line corresponds to a $T = 0$ ideal Fermi gas. The dashed curve is the release energy from a pure condensate in the Thomas-Fermi limit. The solid curve corresponds to a finite temperature mean field model with $T = 0.5\,T_C^0$. Arrow: $k_{\rm F}|a| = 3$.

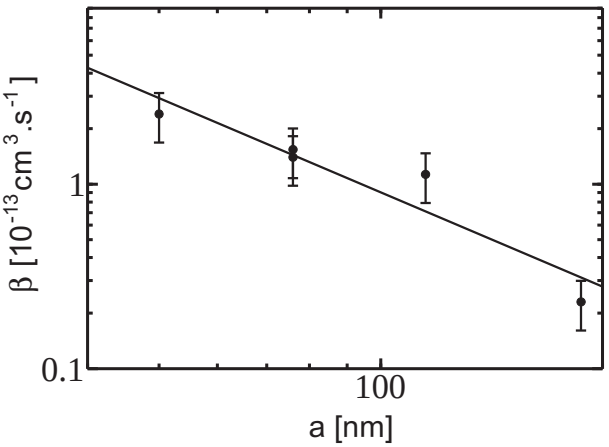

FIG. 2: Molecular condensate loss rate β as a function of the atomic scattering length a near the 834 G s-wave Feshbach resonance. The line is a power law fit with $\beta \sim a^{-1.9\pm0.8}$ in agreement with theory, $\beta \sim a^{-2.55}$ [18].

reproduced by the mean field approach of a pure condensate (dashed line). This is a signature that the gas is not at $T = 0$. It can be understood with the mean field approach we used previously to describe the behavior of the thermal cloud. Since the magnetic field sweep is slow compared to the gas collision rate [13], we assume that this sweep is adiabatic and conserves entropy [24]. We then adjust this entropy to reproduce the release energy at a particular magnetic field, $B = 720\,\mathrm{G}$. The resulting curve as a function of B (solid line in Fig. 1.d) agrees well with our data in the range $680\,\mathrm{G} \leq B \leq 770\,\mathrm{G}$, where the condensate fraction is 40%, and the temperature is $T \approx T_C^0/2 = 1.4\,\mu\mathrm{K}$. This model is limited to $n_m a_m^3 \lesssim 1$. Near resonance the calculated release energy diverges and clearly departs from the data. On the BCS side, the release energy of a $T = 0$ ideal Fermi gas gives an upper bound for the data (dot-dashed curve), as expected from negative interaction energy and a very cold sample. This low temperature is supported by our measurements on the BEC side and the assumption of entropy conservation through resonance which predicts $T = 0.1\,T_\mathrm{F}$ on the BCS side [24].

On resonance the gas is expected to reach a universal behavior, as the scattering length a is not a relevant parameter any more [25]. In this regime, the release energy scales as $E_\mathrm{rel} = \sqrt{1+\beta} E_\mathrm{rel}^0$, where E_rel^0 is the release energy of the non-interacting gas and β is a universal parameter. From our data at 820 G, we get $\beta = -0.64(15)$. This value is larger than the Duke result $\beta = -0.26 \pm 0.07$ at 910 G [23], but agrees with that of Innsbruck $\beta = -0.68^{+0.13}_{-0.10}$ at 850 G [6], and with the most recent theoretical prediction $\beta = -0.56$ [26, 27]. Around 925 G, where $a = -270\,\mathrm{nm}$ and $(k_\mathrm{F}|a|)^{-1} = 0.35$, the release energy curve displays a change of slope. This is a signature of the transition between the strongly and weakly interacting regimes. It is also observed near the same field in [6] through *in situ* measurement of the trapped cloud size. Interestingly, the onset of resonance condensation of fermionic atom pairs observed in ^{40}K [7] and ^{6}Li [8], corresponds to a similar value of $k_\mathrm{F}|a|$.

P-WAVE RESONANCES

Recently, both experimental [28–30] and theoretical [31] papers have devoted interest to the p-wave Feshbach resonances. The goal of these experiments is to nucleate molecules with internal angular momentum $l = 1$, that could lead to the observation of some non-conventional superconductivity, analogous to that observed in superfluid ^{3}He [32].

In the manifold $f = 1/2$ corresponding to the hyperfine ground state of ^{6}Li, coupled channels calculations have demonstrated that three Feshbach resonances could be observed in p-wave channels. The position of the resonances are calculated using the most recent experimental data available on ^{6}Li and are presented in Tab. I. The predicted values of the resonance position are compared with the location we obtained experimentally using the following procedure: we prepare ^{6}Li atoms in the dipole trap with the required spin state (m_f, m_f') using radiofrequency transfer. We then ramp up the magnetic field from 0 to a value B_1 slightly higher than the predicted position of the Feshbach resonance. The magnetic field is then abruptly decreased to a variable value B close to resonance. After a waiting time of 50 ms in the trap, we measure the atom number by time of flight imaging. In Fig. 3.a, we show the evolution of the atom number vs magnetic field in the channel (1/2,-1/2). We observe a sharp decrease of the atom number at ~ 186.5 G, close to the predicted value 185 G. The two other channels display similar losses in the vicinity of the theoretical position of the Feshbach resonances (Tab. I). Note that in this table the experimental uncertainty is mainly due to the magnetic field calibration.

One of the main issue of the physics of Feshbach resonances is related to the lifetime of the molecules, and more generally of the atoms, at resonance. Indeed, one of the key element that led to the experiments on the BEC-BCS crossover was the increase of the lifetime of molecules composed of fermions close to resonance. To address this issue, we have measured the time evolution of the atom number N in the sample at the three Feshbach resonances. Since the one-body lifetime is ~ 30 s, much longer than the measured decay time (~ 100 ms), we can fit the time evolution using the rate equation

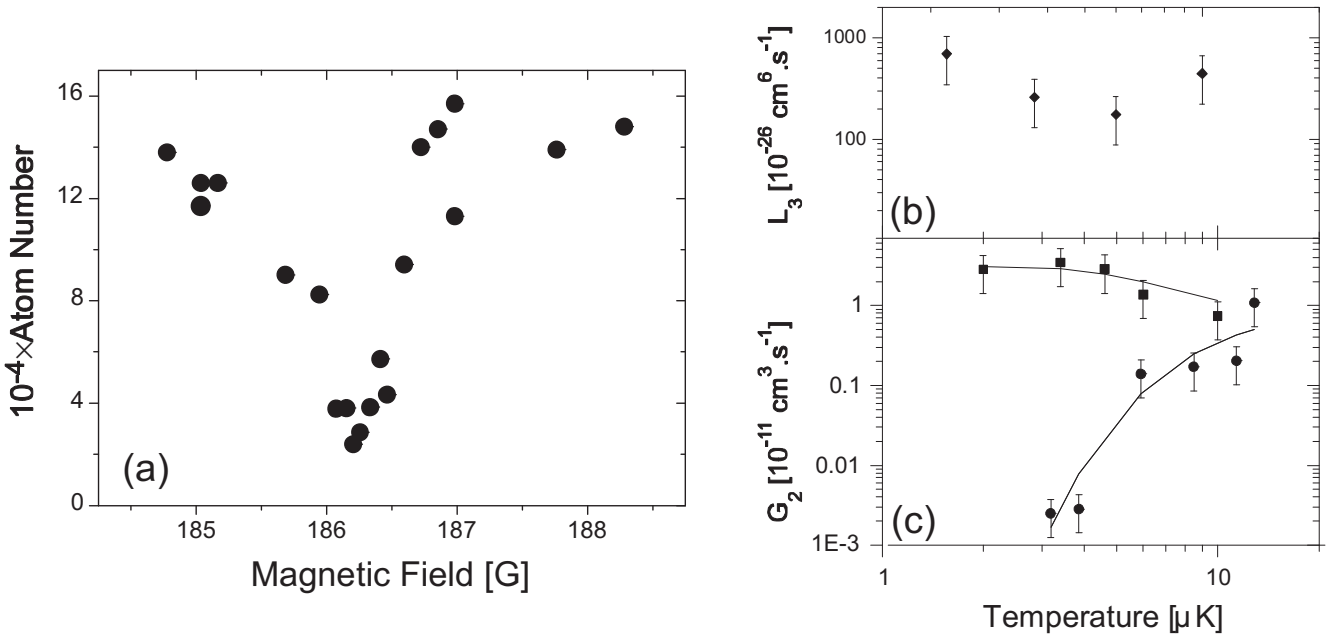

FIG. 3: (a) Atom number vs. magnetic field $B_{0,\mathrm{f}}$ after a 50 ms wait for atoms in the spin mixture $(1/2,-1/2)$ at $T\sim 14\mu$K. The sharp drop close to $B_0\sim 186$ G over a range $\simeq 0.5$ G is the signature of the p-wave Feshbach resonance predicted by theory. (b) (resp. (c)) Variations of 3-body (2-body) loss rates vs temperature at the Feshbach resonance. (b): ♦: atoms in the Zeeman ground state $|f=1/2,m_f=1/2\rangle$, $B_{0,\mathrm{f}}\sim 159$ G. (c): ■: atoms polarized in $|f=1/2,m_f=-1/2\rangle$, $B_{0,\mathrm{f}}\sim 215$ G. •: mixture $|f=1/2,m_f=1/2\rangle+|f=1/2,m_f=-1/2\rangle$, $B_{0,\mathrm{f}}\sim 186$ G. In both cases, the full line is a fit to the data using prediction of Eq. 3 with the magnetic field as the only fitting parameter.

$$\frac{\dot N}{N}=-G_2\langle n\rangle-L_3\langle n^2\rangle, \tag{1}$$

where n is the atom density and $\langle n^a\rangle=\int \mathrm{d}^3r\, n^{a+1}/N$ $(a=1,2)$ is calculated from the classical Boltzman distribution.

In contrast to s-wave Feshbach resonances where dipolar losses are forbidden in the $f=1/2$ manifold [33], the losses near a p-wave resonance are found to be dominantly 2-body in the (1/2,-1/2) and (-1/2,-1/2) channels. The variations of the 2-body loss rate with temperature are displayed in Fig. 3.c and show very different behaviors in these two channels. This non trivial dependence is actually not the consequence of some specific property of the states involved (eg., the quantum statistics) but can be recovered using a very simple three-state model. We describe inelastic processes by two non interacting open channels, respectively the incoming and decay channels, that are coupled to a single p-wave molecular state . This model leads to a very simple algebra that can be treated analytically [34] and yields for the two-body loss-rate at a given energy E

$$g_2(E)=\frac{KE}{(E-\delta)^2+\gamma^2/4}. \tag{2}$$

Here $\delta=\mu(B-B_{\mathrm{F}})$ is the detuning to the Feshbach resonance and K, μ and γ are phenomenological constants depending on the microscopic details of the potential. For each channel, these parameters are estimated from our numerical coupled-channel calculation (Tab. I).

Eqn. (2) shows that, contrarily to s-wave processes that can be described accurately by their low energy behavior, p-wave losses are dominated by the resonance peak located at $E=\delta$ where the losses are maximum. In other word, the so-called "threshold laws", that give the low energy scattering behavior, are insufficient to describe a Feshbach resonance associated with p-wave molecular states (and, more generally, any non zero angular momentum molecular state).

To compare with experimental data, Eq. (2) is averaged over a thermal distribution and for $\delta>0$ and $\delta\gg\gamma$ we get:

$$G_2\sim 4\sqrt{\pi}\frac{K}{\gamma}\left(\frac{\delta}{k_{\mathrm{B}}T}\right)^{3/2}\mathrm{e}^{-\delta/k_{\mathrm{B}}T}. \tag{3}$$

Eqn. 3 is used to fit the data of Fig. 3.b, with $B-B_{\mathrm{F}}$ as the only fitting parameter. We get a fairly good agreement if we take $B-B_{\mathrm{F}}=0.04$ G (resp. 0.3 G) for the (-1/2,-1/2) (resp. (1/2,-1/2)) channel, illustrating the extreme sensitivity of G_2 to detuning and temperature. This feature was also tested by measuring the variations of G_2 with magnetic field at constant temperature. Note that the width of the resonance, as given by Eqn. 3, is of the order of $k_{\mathrm{B}}T/\mu$. At $\sim 10\,\mu$K, this yields a width of ~ 0.1 G, which is comparable with the one observed in Fig. 3.a.

(m_{f_1}, m_{f_2})	$B_{\rm th}$	$B_{\rm exp}$	K	γ	μ
	G	G	$\rm cm^3 \cdot \mu K \cdot s^{-1}$	μK	$\mu \rm K \cdot G^{-1}$
(1/2,1/2)	159	160.2(6)	–	–	–
(1/2,-1/2)	185	186.2(6)	1.21×10^{-13}	0.05	117
(-1/2,-1/2)	215	215.2(6)	7.33×10^{-13}	0.08	111

TABLE I: Position and two-body losses parameters of the p-wave Feshbach resonances of ^{6}Li atoms in $|f_1 = 1/2, m_{f_1}\rangle$ and $|f_2 = 1/2, m_{f_2}\rangle$.

In the (1/2,1/2) channel, dipolar losses are forbidden and we indeed find that 3-body losses are dominant. The dependence of L_3 with temperature is very weak (Fig. 3.b) and contradicts the low energy theoretical calculation of the temperature dependence of three-body loss rate performed in [35]. Indeed, Wigner threshold law predicts that at low energy, L_3 should be proportional to T^λ, with $\lambda \geq 2$ for indistinguishable fermions. However, as we noticed earlier in the case of two-body losses, the threshold law is probably not sufficient to describe losses at resonance due to the existence of a resonance peak that might also be present in three-body processes. This suggests that 3-body processes must be described by a more refined formalism, analogous to the unitary limited treatment of the s-wave elastic collisions [36].

Finally, we have checked the production of molecules in (1/2,-1/2)mixture by using the scheme presented in [13, 14]. We first generate p-wave molecules by ramping in 20 ms the magnetic field from 190 G$> B_{\rm F}$ to $B_{\rm nuc} = 185$ G$< B_{\rm F}$. At this stage, we can follow two paths before detection. Path 1 permits to measure the number N_1 of free atoms: by ramping *down* in 2 ms the magnetic field from 185 G to 176 G, we convert the molecules into deeply bound molecular states that decay rapidly by 2-body collisions. Path 2 gives access to the total atom number N_2 (free atoms + atoms bound in p-wave molecules). It consists in ramping *up* the magnetic field in 2 ms from $B_{\rm nuc}$ to 202 G$> B_{\rm F}$ to convert the molecules back into atoms. Since the atoms involved in molecular states appear only in pictures taken in path 2, the number of molecules in the trap is $(N_2 - N_1)/2$. In practice, both sequences are started immediately after reaching $B_{\rm nuc}$ and we average the data of 25 pictures to compensate for atom number fluctuations. We then get $N_1 = 7.1(5) \times 10^4$ and $N_2 = 9.1(7) \times 10^4$ which corresponds to a molecule fraction $1 - N_1/N_2 = 0.2(1)$. Surprisingly, we failed to detect any molecule signal when applying the same method to (1/2,1/2) atoms.

HETERONUCLEAR FESHBACH RESONANCES

So far, the Feshbach resonances used in this paper were involving atoms of the same species (namely ^{6}Li). However, it was recently pointed out that the observation of Feshbach resonances between two different atom species could lead to a host of interesting effects ranging from the observation of supersolid order [37] to the study polar molecules [38]. In the case of a mixture of bosons and fermions, these molecules are fermions and are expected to be long lived. Indeed, Pauli principle keeps molecules far apart and prevents inelastic collisions. Such resonances were observed experimentally in ^{6}Li-^{23}Na [39] and ^{40}K-^{87}Rb [40] mixtures. In the case of ^{6}Li-^{7}Li in the stable Zeeman ground state $|f = 1/2, m_f = 1/2\rangle \otimes |f = 1, m_f = 1\rangle$, the existence and the position of heteronuclear Feshbach resonances were predicted in [41]. In that work, the ^{6}Li-^{7}Li interaction potential was extracted from the data on ^{6}Li-^{6}Li scattering properties by mean of a simple mass-scaling. Using coupled channels calculation it was found that this system exhibited five Feshbach resonances whose position is displayed in Tab. II [42].

Experimentally, we probed these Feshbach resonances using a mixture of respectively $N_6 \sim N_7 \sim 10^5$ atoms of ^{6}Li and ^{7}Li in the absolute Zeeman ground state $|1/2, 1/2\rangle \otimes |1, 1\rangle$. The gas is cooled at a temperature of $4\,\mu$K in the cross dipole trap and we locate the resonance by sweeping down in 1 s the magnetic field from a value located about 20 G above the predicted position of the resonance to a variable value B. By looking for the value of B at which we start loosing atoms, we were able to detect four of the five resonances at a value very close to that predicted by theory (Tab. II). The discrepancy between the experimental and theoretical values is larger in this case than in the case of th p-wave resonance. This is probably due to a breakdown of the Born-Oppenheimer approximation that one expects in the case of light atoms such as lithium and that forbids the use of the mass scaling [41]. Note also that the missing resonance is predicted to be very narrow ($\sim$1 mG).

As noticed in [43], the width of a Feshbach resonance strongly influences the molecule lifetime that can be much higher close to a wide resonance. Since the Feshbach resonances we found in $|1/2, 1/2\rangle \otimes |1, 1\rangle$ are very narrow (~ 0.1 G) it might prove interesting to look for wider Feshbach resonances. In the case of ^{6}Li-^{7}Li, a wide resonance is predicted to exist in the stable state $|3/2, 3/2\rangle \otimes |1, 1\rangle$ at ~ 530 G, in agreement with our observation of a large atom loss located between ~ 440 G and ~ 540 G.

[1] M. Greiner, C. A. Regal, and D. S Jin, Nature **426**, 537 (2003).
[2] S. Jochim *et al.*, Science **302**, 2101 (2003).
[3] M. W. Zwierlein *et al.*, Phys. Rev. Lett. **91**, 250401 (2003).
[4] T. Bourdel *et al.*, Phys. Rev. Lett. **93**, 050401 (2004)

$B_{\rm th}$ (G)	$B_{\rm exp}$ (G)
218	not seen
230	226.3(6) G
251	246.0(8) G
551	539.9(8) G
559	548.6(9) G

TABLE II: Predicted and observed positions of the heteronuclear Feshbach resonances of a ^{6}Li-^{7}Li gas. First column: resonance position as predicted by coupled channel calculation. Secund column: experimental determination of the resonances. The experimental error bars are due to the systematic uncertainty on the calibration of the magnetic field. The first Feshbach resonance is extremely narrow and could not be detected with our experimental resolution.

[5] A.J. Leggett, J. Phys. C. (Paris) **41**,7 (1980); P. Nozières and S. Schmitt-Rink, J. Low Temp. Phys. **59** 195 (1985); C. Sá de Melo, M. Randeria, and J. Engelbrecht, Phys. Rev. Lett. **71**, 3202 (1993); M. Holland, S. Kokkelmans, M. Chiofalo, and R. Walser, Phys. Rev. Lett. **87** 120406 (2001); Y. Ohashi and A. Griffin, Phys. Rev. Lett. **89**, 130402 (2002); J. N. Milstein, S. J. J. M. F. Kokkelmans, and M. J. Holland, Phys. Rev. A **66**, 043604 (2002); R. Combescot, Phys. Rev. Lett. **91**, 120401 (2003); G. M. Falco and H. T. C. Stoof, cond-mat/0402579.
[6] M. Bartenstein *et al.*, Phys. Rev. Lett. **92**, 120401 (2004).
[7] C. A Regal, M. Greiner, and D. S. Jin Phys. Rev. Lett. **92**, 040403 (2004).
[8] M. Zwierlein *et al.*, Phys. Rev. Lett. **92**, 120403 (2004).
[9] M. Greiner *et al.*, e-print cond-mat/0407381.
[10] J. Kinast *et al.*, Phys. Rev. Lett. *92*, 150402 (2004)
[11] C. Chin *et al.*, Science **305**, 1128 (2004).
[12] T. Bourdel *et al.*, Phys. Rev. Lett. **91**, 020402 (2003).
[13] J. Cubizolles *et al*, Phys. Rev. Lett. **91** 240401 (2003).
[14] C. A. Regal, C. Ticknor, J. L. Bohn, and D. S. Jin, Nature **424**, 47 (2003).
[15] We correct our data for the presence of a magnetic field curvature which leads to an anti-trapping frequency of 100 Hz at 800 G along x.
[16] Yu. Kagan, E. L. Surkov, and G. V. Shlyapnikov, Phys. Rev. A **54**, R1753 (1996).
[17] Y. Castin and R. Dum, Phys. Rev. Lett. **77**, 5315 (1996).
[18] D. S. Petrov, C. Salomon, and G. V. Shlyapnikov, Phys. Rev. Lett. **93**, 090404 (2004).
[19] L. Khaykovich *et al.*, Science **296**, 1290 (2002).
[20] J. Söding, *et al*, Applied Physics **B69**, 257 (1999)
[21] C. Regal, M. Greiner and D. Jin, Phys. Rev. Lett. **92**, 083201 (2004).
[22] C. Menotti, P. Pedri, and S. Stringari, Phys. Rev. Lett. **89**, 250402 (2002).
[23] K. O'Hara *et al.*, Science **298**, 2179 (2002). M. Gehm *et al.*, Phys. Rev. A **68**, 011401 (2003).
[24] L. D. Carr, G. V. Shlyapnikov, and Y. Castin, cond-mat/0308306.
[25] H. Heiselberg, Phys. Rev. A **63**, 043606 (2001).
[26] J. Carlson, S.Y. Chang, V. R. Pandharipande, and K. E. Schmidt, Phys. Rev. Lett. **91**, 050401 (2003).
[27] G. E. Astrakharchik, J. Boronat, J. Casulleras, and S. Giorgini, cond-mat 0406113 (2004).
[28] C. A. Regal, C. Ticknor, J. L. Bohn, and D. S. Jin Phys. Rev. Lett. **90**, 053201 (2003).
[29] J. Zhang *et al.*, Phys. Rev. A **70**, 030702 (2004)
[30] C. H. Schunck *et al.*, e-print cond-mat/0407373.
[31] T.L. Ho and N. Zahariev, e-print cond-mat/0408469; T.L. Ho and R.B. Diener, e-print cond-mat/0408468.
[32] D. M. Lee, Rev. Mod. Phys. **69**, 645 (1997).
[33] K. Dieckmann *et al.*, Phys. Rev. Lett. **89**, 203201 (2002).
[34] F. Chevy *et al.*, to be published.
[35] B. D. Esry, C. H. Greene, and H. Suno, Phys. Rev. A **65**, 010705 (2002).
[36] H. Suno, B. D. Esry, and C. H. Greene, Phys. Rev. Lett. 90, 053202 (2003).
[37] H.P. Büchler and G. Blatter, Phys. Rev. Lett. **91**,130404 (2003).
[38] M.A. Baranov, M.S. Mar'enko, V.S. Rychkov and G. Shlyapnikov, Phys. Rev. A **66** 013606 (2002).
[39] C.A. Stan *et al.*, Phys. Rev. Lett. **93**, 143001 (2004).
[40] S. Inouye *et al.*, e-print cond-mat/0406208.
[41] E.G.M. van Kempen, B. Marcellis and S.J.J.M.F Kokkelmans, e-print cond-mat/0406722.
[42] Note that the absence of symmetrization constraint in the case of a heteronuclear system allows for many more resonances than for a pure system.
[43] R. Combescot, Phys. Rev. Lett. **91**, 120401 (2003); G.M. Bruun and C. J. Pethick, Phys. Rev. Lett. **92**, 140404 (2004).

A.4 Resonant scattering properties close to a p-wave Feshbach resonance

Frédéric Chevy, E.G.M. Van Kempen, T. Bourdel, J. Zhang, L. Khaykovich, M. Teichmann, L. Tarruell, S.J.J.M.F. Kokkelmans, and C. Salomon,

Physical Review A **71**, page 062710, 22 June 2005.

Resonant scattering properties close to a *p*-wave Feshbach resonance

F. Chevy,[1] E. G. M. van Kempen,[2] T. Bourdel,[1] J. Zhang,[3] L. Khaykovich,[4] M. Teichmann,[1] L. Tarruell,[1] S. J. J. M. F. Kokkelmans,[2] and C. Salomon[1]

[1]*Laboratoire Kastler-Brossel, ENS, 24 rue Lhomond, 75005 Paris*

[2]*Eindhoven University of Technology, P. O. Box 513, 5600 MB Eindhoven, The Netherlands*

[3]*SKLQOQOD, Institute of Opto-Electronics, Shanxi University, Taiyuan 030006, People's Republic of China*

[4]*Department of Physics, Bar Ilan University, Ramat Gan 52900, Israel*

(Received 15 December 2004; published 22 June 2005)

We present a semianalytical treatment of both the elastic and inelastic collisional properties near a *p*-wave Feshbach resonance. Our model is based on a simple three-channel system that reproduces more elaborate coupled-channel calculations. We stress the main differences between *s*-wave and *p*-wave scattering. We show in particular that, for elastic and inelastic scattering close to a *p*-wave Feshbach resonance, resonant processes dominate over the low-energy behavior.

DOI: 10.1103/PhysRevA.71.062710 PACS number(s): 34.50.−s, 03.75.Ss, 05.30.Fk, 32.80.Pj

I. INTRODUCTION

The observation of molecular gaseous Bose-Einstein condensates (BECS) and the subsequent experimental study of the BEC-BCS crossover [1–5] were made possible by the possibility of tuning interatomic interactions using a magnetic field (the so-called Feshbach resonances). Although all these experiments were based on *s*-wave interatomic interactions, it is known from condensed matter physics that superfluidity of fermionic systems can also arise through higher-order partial waves. The most famous examples of this nonconventionnal superfluidity are ^{3}He [6], for which the Cooper pairs spawn from *p*-wave interactions, and high-T_c superconductivity, in which pairs are known to possess *d*-wave symmetry [7]. Recent interest in *p*-wave interactions in cold atom gases stemmed from these possibilities and resulted in the observation of *p*-wave Feshbach resonances in ^{40}K [8] and ^{6}Li [9,10], as well as theoretical studies on the superfluidity of cold atoms interacting through *p*-wave pairing [11,12].

The present paper is devoted to the study of *p*-wave interactions close to a Feshbach resonance and it derives some results presented in [9]. In a first part, we present the model we use to describe both elastic and inelastic processes that are discussed in the second part. We stress in particular the main qualitative differences between *p*-wave and *s*-wave physics and show that contrarily to the case of the *s* wave, which is dominated by low-energy physics, *p*-wave scattering is dominated by a resonance peak associated to the quasibound molecular state. Finally, we compare our analytical results to numerical coupled-channel calculations.

II. MODEL FOR *p*-WAVE INTERACTIONS

We consider the scattering of two identical particles of mass m. As usual when treating a two-body problem, we work in the center-of-mass frame and consider only the motion of a fictitious particle of mass $m/2$ interacting with a static potential. In order to study the *p*-wave Feshbach resonance, we use a model based on the separation of open and closed channels. In this framework, the Feshbach resonance arises in an open channel as a result of the coupling with a closed channel [13]. At resonance, scattering properties are dominated by resonant effects and we can neglect all "background" scattering (i.e., we assume there is no scattering far from resonance).

(1) We restrict ourselves to a three-channel system, labeled 1, 2, and 3, which correspond to the different two-body spin configurations (Fig. 1). Channels $|1\rangle$ and $|2\rangle$ are open channels. We focus on the situation where atoms are prepared initially in state $|1\rangle$. Atoms may be transferred to state $|2\rangle$ after an inelastic process. Channel $|3\rangle$ is closed and hosts the bound state leading to the Feshbach resonance.

Let us consider, for instance, the case of ^{6}Li atoms prepared in a mixture of $|F=1/2,m_F=1/2\rangle$ and $|F'=1/2,m_F'=-1/2\rangle$. In this system, the only two-body decay channel is associated with the flipping of an $m_F'=-1/2$ atom to $m_F'=1/2$. If we denote by (m_F,m_F') the symmetrized linear combination of the states $|F=1/2,m_F\rangle$ and $|F'=1/2,m_F'\rangle$, then $|1\rangle=(1/2,-1/2)$ and $|2\rangle=(1/2,1/2)$.

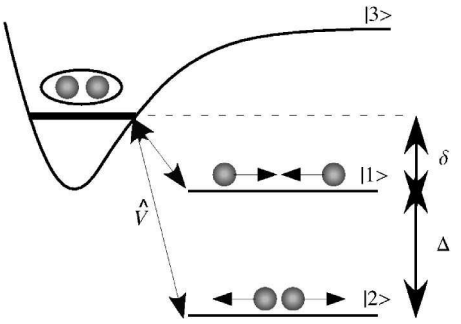

FIG. 1. The *p*-wave model: we consider three internal states, labeled $|1\rangle$, $|2\rangle$, and $|3\rangle$. States $|1\rangle$ and $|2\rangle$ are two open channels corresponding, respectively, to the incoming and decay channels. The released energy in an inelastic collision bringing an atom initially in $|1\rangle$ to $|2\rangle$ is denoted Δ. State $|3\rangle$ is a closed channel that possesses a *p*-wave bound state of energy δ nearly resonant with state $|1\rangle$. Finally, we assume that these three channels interact through a potential $\hat{V}$ acting only on the internal states and coupling the two open channels to the closed channel.

(2) The Feshbach resonances studied here are all located at values of the magnetic field where the Zeeman splitting is much larger than the hyperfine structure. In a first approximation we can therefore assume that the internal states are described by uncoupled electronic and nuclear spin states. In the absence of any dipolar or hyperfine coupling between the electronic singlet and triplet manifolds, we assume we have no direct interaction in channels 1 and 2 so that the eigenstates are plane waves characterized by their relative wave vector k and their energy $E_1(k)=\hbar^2k^2/m$ (channel 1) and $E_2(k)=-\Delta+\hbar^2k^2/m$ (channel 2). $\Delta>0$ is the energy released in an inelastic process leading from 1 to 2. Δ can be considered as independent of the magnetic field and is assumed to be much larger than any other energy scales (in the case relevant to our experiments, $\Delta/h\sim 80$ MHz is the hyperfine splitting of ^{6}Li at high field).

(3) In channel 3, we consider only a p-wave bound state nesting at an energy δ quasiresonant with channel 1. In the case of ^{6}Li atoms in the $F=1/2$ hyperfine state, $\delta=2\mu_B(B-B_0)$, where B is the magnetic field and B_0 is the position of the "bare" Feshbach resonance. If the projection of the angular momentum (in units of $\hbar$) is denoted by $m_{\mathbf{u}}$ for a quantization axis chosen along some vector $\mathbf{u}$, the eigenfunctions associated with this bound state can be written as $g(r)Y_1^{m_{\mathbf{u}}}(\theta,\phi)$, where (r,θ,ϕ) is the set of polar coordinates and the Y_l^m are the spherical harmonics.

(4) The coupling $\hat{V}$ between the various channels affects only the spin degrees of freedom. Therefore the orbital angular momentum is conserved during the scattering process and we restrict our analysis to the p-wave manifold. This is in contrast to the situation in heavy alkalimetals where incoming particles in the s wave can be coupled to molecular states of higher orbital angular momentum [14,15].

We assume also that the only nonvanishing matrix elements are between the closed and the open channels (i.e., $\langle 1,2|\hat{V}||3\rangle$ and $\langle 3|\hat{V}|1,2\rangle$).

Let us denote a state of the system by $|\alpha,\chi\rangle$, where $\alpha\in\{1,2,3\}$ and χ describe, respectively, the internal (spin) and the orbital degrees of freedom. According to assumption ((4)), the matrix element $\langle\alpha,\chi|\hat{V}|\alpha',\chi'\rangle$ is simply given by

$$\langle\alpha,\chi|\hat{V}|\alpha',\chi'\rangle=\langle\chi|\chi'\rangle\langle\alpha|\hat{V}|\alpha'\rangle, \tag{1}$$

and is therefore simply proportional to the overlap $\langle\chi|\chi'\rangle$ between the external states.

Let us now particularize to the case where $\alpha\in\{1,2\}$, and $|\chi\rangle=|\mathbf{k}\rangle$ is associated with a plane wave of relative momentum $\hbar\mathbf{k}$. According to hypothesis ((4)), this state is coupled only to the closed channel $|3\rangle$. Moreover, using the well-known formula $e^{ikz}=\Sigma_l i^l\sqrt{4\pi(2l+1)}j_l(kr)Y_l^0(\theta,\phi)$, where the j_l are the spherical Bessel functions, we see that $|\chi\rangle$ is coupled only to the state $|\alpha'=3,\mathbf{k}=\mathbf{0}\rangle$ describing the pair in the bound state $|\alpha'=3\rangle$ with zero angular momentum in the $\mathbf{k}$ direction. The matrix element then reads

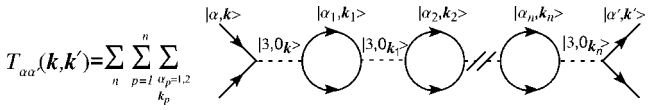

FIG. 2. Diagrammatic expansion of the T matrix. The full (dashed) lines represent free atoms (molecules). $|\alpha,\mathbf{k}\rangle$ is the scattering state of the two particles, in the internal state $\alpha=1,2$. $|3,0_{\mathbf{k}}\rangle$ represents the state of a p-wave molecule with orbital angular momentum component zero on the $\mathbf{k}$ direction.

$$\langle\alpha,\mathbf{k}|\hat{V}|3,m_{\mathbf{k}}\rangle=i\delta_{m_{\mathbf{k}},0}\sqrt{\frac{12\pi}{L^3}}\langle\alpha|\hat{V}|3\rangle\int g^*(r)j_1(kr)r^2dr, \tag{2}$$

where L^3 is a quantization volume. Since for small k we have $j_1(kr)\sim kr/3$, the matrix element $\langle\alpha,\mathbf{k}|\hat{V}|3,m_{\mathbf{k}}\rangle$ takes the general form

$$\langle\alpha,\mathbf{k}|\hat{V}|3,m_{\mathbf{k}}\rangle=\delta_{m_{\mathbf{k}},0}\frac{kF_\alpha(k)}{\sqrt{L^3}}, \tag{3}$$

where $F_\alpha(k)$ has a finite (in general nonzero) limit when k goes to zero.

Later on, we shall also need the coupling between $|\alpha,\mathbf{k}\rangle$ and $|3,m_{\mathbf{k}'}=0\rangle$ (that will be denoted by $|3,0_{\mathbf{k}'}\rangle$), where the momentum $\mathbf{k}$ and the direction of quantization $\mathbf{k}'$ are no longer parallel. The calculation presented above yields readily

$$\langle\alpha,\mathbf{k}|\hat{V}|3,0_{\mathbf{k}'}\rangle=\frac{kF_\alpha(k)}{\sqrt{L^3}}\langle 0_{\mathbf{k}}|0_{\mathbf{k}'}\rangle=\frac{kF_\alpha(k)}{\sqrt{L^3}}\cos(\widehat{\mathbf{k},\mathbf{k}'}), \tag{4}$$

where $(\widehat{\mathbf{k},\mathbf{k}'})$ is the angle between $\mathbf{k}$ and $\mathbf{k}'$ [16].

III. T MATRIX

From general quantum theory, it is known that the scattering properties of a system are given by the so-called T matrix $\hat{T}$. It can be shown in particular that $\hat{T}$ is given by the following expansion in powers of the coupling potential:

$$\hat{T}(E)=\hat{V}+\hat{V}\hat{G}_0(E)\hat{V}+\hat{V}\hat{G}_0(E)\hat{V}\hat{G}_0(E)\hat{V}+\cdots, \tag{5}$$

where $\hat{G}_0(E)=1/(E-\hat{H}_0)$ and $\hat{H}_0=\hat{H}-\hat{V}$ is the free Hamiltonian of the system.

Let us consider $|\alpha,\mathbf{k}\rangle$ and $|\alpha',\mathbf{k}'\rangle$, two states of the *open channels*, and let us set $T_{\alpha\alpha'}(\mathbf{k},\mathbf{k}',E)=\langle\alpha,\mathbf{k}|\hat{T}(E)|\alpha',\mathbf{k}'\rangle$. According to formula (5), this matrix element is the sum of terms that can be represented by the diagram of Fig. 2 and we get after a straightforward calculation

$$T_{\alpha\alpha'}(\mathbf{k},\mathbf{k}',E)=\frac{kk'}{L^3}F_\alpha(k)F^*_{\alpha'}(k')\sum_{n=0}^{\infty}R_n\Lambda(E)^nG_0^{(m)}(E)^{n+1}.$$

Here $G_0^{(m)}(E)=1/(E-\delta)$ is the free propagator for the molecule, $\Lambda=\Lambda_1+\Lambda_2$ with

$$\Lambda_\alpha(E) = \int \frac{q^4 dq}{(2\pi)^3} \frac{|F_\alpha(q)|^2}{E - E_\alpha(q)} \tag{6}$$

the results of the integration on the loops, and finally

$$R_n = \int d^2\Omega_1 \cdots d^2\Omega_n \cos(\widehat{\mathbf{k},\mathbf{k}_1}) \times \cos(\widehat{\mathbf{k}_1,\mathbf{k}_2}) \cdots \cos \widehat{\mathbf{k}_n,\mathbf{k}'},$$

where Ω_p is the solid angle associated with $\mathbf{k}_p$, arises from the pair-breaking vertices $|3,0_{\mathbf{k}_i}\rangle \rightarrow |\alpha_{i+1},\mathbf{k}_{i+1}\rangle$. This last integral can be calculated recursively and we get $R_n = (4\pi/3)^n \cos(\widehat{\mathbf{k},\mathbf{k}'})$, that is, for the T matrix

$$T_{\alpha\alpha'}(\mathbf{k},\mathbf{k}',E) = \frac{1}{L^3} \frac{kk' F_\alpha(k) F^*_{\alpha'}(k')}{E - \delta - \Sigma_1 - \Sigma_2} \cos(\widehat{\mathbf{k},\mathbf{k}'}),$$

with $\Sigma_\alpha = 4\pi\Lambda_\alpha/3$.

This expression can be further simplified since, according to Eq. (2), the width of $F_\alpha(q)$ is of the order of $1/R_e$, where R_e is the characteristic size of the resonant bound state. In the low-temperature limit, we can therefore expand Σ_α with the small parameter kR_e.

From Eq. (2), we see that replacing $F_\alpha(q)$ by its value at $q=0$ leads to a q^2 divergence. This divergence can be regularized by the use of counterterms in the integral, namely, by writing that

$$\Sigma_\alpha(E) = \int |F_\alpha(q)|^2 \left[\frac{q^4}{E - E_\alpha(q)} + \frac{mq^2}{\hbar^2} + \frac{m^2}{\hbar^4}[E - E_\alpha(0)] \right] \frac{dq}{6\pi^2} - \int |F_\alpha(q)|^2 \frac{mq^2}{\hbar^2} \frac{dq}{6\pi^2} - [E - E_\alpha(0)] \int |F_\alpha(q)|^2 \frac{m^2}{\hbar^4} \frac{dq}{6\pi^2},$$

where we have assumed that F_α was decreasing fast enough at large q to ensure the convergence of the integrals. $|F_\alpha(q)|^2$ can now be safely replaced by $\lambda_\alpha = |F_\alpha(0)|^2$ in the first integral and we finally get

$$\Sigma_\alpha = -i \frac{\lambda_\alpha}{6\pi} \frac{m}{\hbar^2} \left(\frac{m}{\hbar^2}[E - E_\alpha(0)] \right)^{3/2} - \delta_{0,\alpha} - \eta_\alpha [E - E_\alpha(0)],$$

with

$$\delta_0^{(\alpha)} = \int |F_\alpha(q)|^2 \frac{mq^2}{\hbar^2} \frac{dq}{6\pi^2},$$

$$\eta_\alpha = \int |F_\alpha(q)|^2 \frac{m^2}{\hbar^4} \frac{dq}{6\pi^2}.$$

If we assume that the release energy Δ is much larger than E and if we set $\delta_0 = \delta_0^{(1)} + \delta_0^{(2)}$ and $\eta = \eta_1 + \eta_2$, we get for the T matrix

$$T_{\alpha\alpha'}(\mathbf{k},\mathbf{k}',E) \simeq \frac{1}{L^3} \frac{kk' F_\alpha(0) F^*_{\alpha'}(0) \cos(\widehat{\mathbf{k},\mathbf{k}'})/(1+\eta)}{E - \tilde{\delta} + i\hbar\gamma(E)/2} \tag{7}$$

with

$$\hbar\gamma(E) = \left(\frac{m}{\hbar^2} \right)^{5/2} \frac{(\lambda_2 \Delta^{3/2} + \lambda_1 E^{3/2})}{3\pi(1+\eta)},$$

$$\tilde{\delta} = \frac{(\delta - \delta_0)}{1+\eta}.$$

We note that this expression for the T matrix is consistent with the general theory of multichannel scattering resonances [13], where resonantly enhanced transitions to other channels are readily included. In a similar context of two open channels and a Feshbach resonance, a recent experiment was analyzed [15] that involved the decay of a molecular state formed from a Bose-Einstein condensate.

IV. *s* WAVE VS *p* WAVE

This section is devoted to the discussion of the expression found for the T matrix. In addition to the scattering cross section, the study of the T matrix yields important information on the structure of the dressed molecular state underlying the Feshbach resonance and we will demonstrate important qualitative differences between the behaviors of *p*-wave and *s*-wave resonances.

A. Molecular state

The binding energy E_b of the molecule is given by the pole of T. In the limit $\delta \sim \delta_0$, it is therefore given by

$$E_b = \tilde{\delta} - i\hbar\gamma(\tilde{\delta})/2,$$

We see that the real part of E_b (the "physical" binding energy) is $\sim\tilde{\delta}$ and therefore scales linearly with the detuning $\delta - \delta_0$. This scaling is very different from what happens for *s*-wave processes where we expect a $(\delta - \delta_0)^2$ behavior. This difference is in practice very important: indeed, the molecules can be trapped after their formation only if their binding energy is smaller than the trap depth. The scaling we get for the *p*-wave molecules means that the binding energy increases much faster when we increase the detuning than what we obtain for *s*-wave molecules (this feature was already pointed out in [11]). Hence, *p*-wave molecules must be looked for only in the close vicinity of the Feshbach resonance—for instance, for $\eta \ll 1$ (relevant for ^{6}Li, as we show below) and a trap depth of 100 μK, the maximum detuning at which molecules can be trapped is $\simeq 0.1$ G.

This asymptotic behavior of the binding energy is closely related to the internal structure of the molecule. Indeed, the molecular wave function $|\psi_m(B)\rangle$ can be written as a sum $|\text{open}\rangle + |\text{closed}\rangle$ of its projections on the closed and open channels, which correspond, respectively, to short- and long-range molecular states. If we neglect decay processes by setting $\lambda_2 = 0$, we can define the magnetic moment of the molecule (relative to that of the free atom pair) by

$$\Delta\mu_{\rm eff}(B) = -\frac{\partial E_b}{\partial B} = -\frac{\partial\tilde{\delta}}{\partial B},$$

that is, in the case of ^{6}Li where $\delta = 2\mu_B(B - B_0)$,

$$\Delta\mu_{\rm eff}(B) = -\frac{2\mu_B}{1+\eta}. \tag{8}$$

On the other hand, we can also write $E_b = \langle\psi_m(B)|\hat{H}(B)|\psi_m(B)\rangle$. Since in the absence of any decay channel, the molecular state is the ground state of the two-body system, we can write using the Hellmann-Feynman relation

$$\Delta\mu_{\rm eff} = -\frac{\partial E_b}{\partial B} = -\langle\psi_m(B)|\frac{\partial\hat{H}(B)}{\partial B}|\psi_m(B)\rangle.$$

In our model, the only term of the Hamiltonian depending on the magnetic field is the energy $\delta = 2\mu_B(B - B_0)$ of the bare molecular state in the closed channel and we finally have

$$\Delta\mu_{\rm eff} = -2\mu_B\langle{\rm closed}|{\rm closed}\rangle. \tag{9}$$

If we compare Eqs. (8) and (9), we see that the probability $P_{\rm closed} = \langle{\rm closed}|{\rm closed}\rangle$ to be in the closed channel is given by

$$P_{\rm closed} = 1/(1+\eta).$$

In other words, unless $\eta = \infty$, there is always a finite fraction of the wave function in the tightly bound state. In practice, we will see that in the case of ^{6}Li, $\eta \ll 1$. This means that the molecular states that are nucleated close to a Feshbach resonance are essentially short-range molecules. On the contrary, for *s*-wave molecules, $E_b \propto (\delta - \delta_0)^2$ leads to $\Delta\mu_{\rm eff} = -2\mu_B\langle{\rm closed}|{\rm closed}\rangle \propto (\delta - \delta_0)$. This scaling leads to a zero probability of occupying the bare molecular state near an *s*-wave resonance.

We can illustrate these different behaviors in the simplified picture of Fig. 3. For small detunings around threshold, the *p*-wave potential barrier provides a large forbidden region, which confines the bound state behind this barrier. The bound-state wave function decays exponentially inside the barrier and the tunneling remains nearly negligible. Since there is no significant difference for the shape of the *p*-wave bound state for small positive and negative detunings, the linear dependence of the closed channel on magnetic field will be conserved for the bound state, and therefore the binding energy will also linearly approach the threshold. We note that the linear dependence close to threshold can also be found from the general Breit-Wigner expression for a resonance, in combination with the *p*-wave threshold behavior of the phase shift [13].

The imaginary part of E_b corresponds to the lifetime of the molecule. In the case of *s*-wave molecules for which two-body decay is forbidden [20,21], the only source of instability is the coupling with the continuum of the incoming channel that leads to a spontaneous decay when $\tilde{\delta} > 0$ [see Fig. 3(a)]. By contrast, we get a finite lifetime in the *p* wave even at $\tilde{\delta} < 0$: due to dipolar relaxation between its constituents, the molecule can indeed spontaneously decay toward state $|2\rangle$. For $\tilde{\delta} \sim 0$, the decay rate γ_0 associated with this process is given by

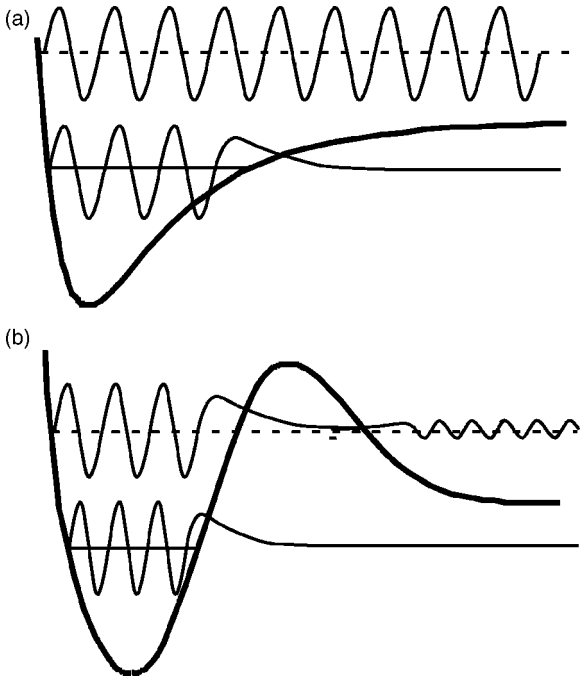

FIG. 3. Effect of the centrifugal barrier on the bound state in *p*-wave Feshbach resonances. (a) Case of *s*-wave scattering: the bare molecular state goes from $\delta < 0$ (full line) to $\delta > 0$ (dashed line). In the process, the molecular state becomes unstable and the wave function becomes unbounded. (b) In the case of a *p*-wave bound state, the presence of the centrifugal barrier smooths the transition from $\delta > 0$ to $\delta < 0$. Even for $\delta > 0$, the wave function stays located close to the bottom of the well.

$$\gamma_0 = \gamma(0) = \frac{\lambda_2}{1+\eta}\frac{m}{3\pi\hbar^3}\left(\frac{m\Delta}{\hbar^2}\right)^{3/2}.$$

B. Elastic scattering

The scattering amplitude $f(\mathbf{k},\mathbf{k}')$ for atoms colliding in the channel 1 can be extracted from the *T* matrix using the relation

$$f(\mathbf{k},\mathbf{k}') = -\frac{mL^3}{4\pi\hbar^2}T_{11}(\mathbf{k},\mathbf{k}', E = \hbar^2k^2/m),$$

that is,

$$f(\mathbf{k},\mathbf{k}') = -\frac{m\lambda_1}{4\pi\hbar^2}\left(\frac{k^2\cos(\widehat{\mathbf{k},\mathbf{k}'})/(1+\eta)}{\hbar^2k^2/m - \tilde{\delta} - i\hbar\gamma/2}\right).$$

The $\cos(\widehat{\mathbf{k},\mathbf{k}'})$ dependence is characteristic of *p*-wave processes and, once again, this expression shows dramatic differences from the *s*-wave behavior. First, at low k, $f(\mathbf{k},\mathbf{k}')$ vanishes like k^2. If we introduce the so-called scattering volume V_s [13] defined by

$$f(\mathbf{k},\mathbf{k}') = -V_s k^2,$$

then we have

$$V_s = \frac{-m\lambda_1}{4\pi\hbar^2[\delta - \delta_0 + i(1+\eta)\hbar\gamma_0/2]} \sim \frac{-m\lambda_1}{2\pi\hbar^2(\delta-\delta_0)},$$

if we neglect the spontaneous decay of the molecule. We see that in this approximation, the binding energy E_b of the molecule is given by

$$E_b = -\frac{m\lambda_1}{2\pi\hbar^2(1+\eta)}\frac{1}{V_s}.$$

In *s*-wave processes, the binding energy and the scattering length are related through the universal formula $E_b = -\hbar^2/ma^2$. This relationship is of great importance since it allows one to describe both scattering properties and the molecular state with only one scattering length, without having to be concerned care with any other detail of the interatomic potential. In the case of the *p* wave, we see that no such universal relation exists between the scattering volume and E_b, a consequence of the fact that we have to deal with short-range molecular states, even at resonance. We therefore need two independent parameters to describe both the bound states and the scattering properties.

In the general case, the elastic cross section σ_{el} is proportional to $|f|^2$. According to our calculation, we can put σ_{el} under the general form

$$\sigma_{\mathrm{el}}(E) = \frac{CE^2}{(E-\tilde{\delta})^2 + \hbar^2\gamma^2/4}, \tag{10}$$

where $E=\hbar^2k^2/m$ is the kinetic energy of the relative motion and C is a constant depending on the microscopic details of the system. Noticeably, the energy dependence of the cross section exhibits a resonant behavior at $E=\tilde{\delta}$ as well as a plateau when $E\to\infty$, two features that were observed in the numerical coupled-channel calculations presented in [17]. Once again, this leads to physical processes very different from what is expected in *s*-wave scattering. Indeed, we know that in *s*-wave scattering, we have $f\sim -a$, as long as $ka \ll 1$. Since a is in general nonzero, the low-energy behavior gives a non-negligible contribution to the scattering processes. By contrast, we have just seen that in the case of the *p* wave, the low-energy contribution is vanishingly small ($\sigma_{\mathrm{el}}\sim E^2$) so that the scattering will be dominated by the resonant peak $E\sim\tilde{\delta}$.

C. Inelastic scattering.

For two particules colliding in channel 1 with an energy $E=\hbar^2k^2/m$, the probability to decay to channel 2 is proportional to $\rho_2(k')|T_{12}(\mathbf{k},\mathbf{k}',E)|^2$ where ρ_2 is the density of states in channel 2. Since k' is given by the energy conservation condition $\hbar^2k'^2/m-\Delta=E$, and in practice $\Delta \gg E$, we see that $k'\sim\sqrt{m\Delta/\hbar^2}$ is therefore a constant. Using this approximation, we can write the two-body loss rate $g_2(E)$ for particles of energy E as

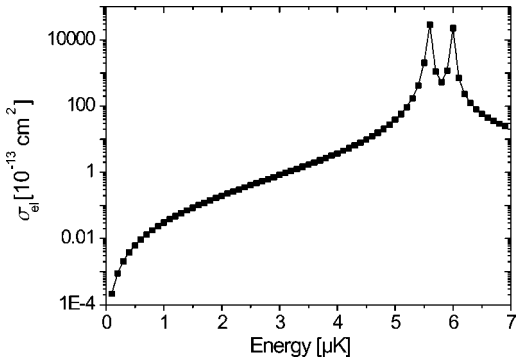

FIG. 4. Energy dependence of the elastic cross section. Dots: numerical closed-channel calculation. The left peak corresponds to $m_l=0$ and the right peak to $m_l=\pm 1$. Full line: Fits using Eq. (11).

$$g_2(E) = \frac{DE}{(E-\tilde{\delta})^2 + \hbar^2\gamma^2/4},$$

where D is a constant encapsulating the microscopic details of the potential.

V. COMPARISON WITH COUPLED-CHANNEL CALCULATION

The quantities such as C, D, γ_0, etc., that were introduced in the previous section were only phenomenological parameters to which we need to attribute some value to be able to perform any comparison with the experiment. These data are provided by *ab initio* numerical calculations using the coupled-channel scheme described in [18]. The result of this calculation for the elastic scattering cross section is presented in Fig. 4. The most striking feature of this figure is that it displays two peaks instead of one, as predicted by Eq. (10). This difference can be easily understood by noting that the dipolar interaction that couples the molecular state to the outgoing channel provides a "spin-orbit" coupling that modifies the relative orbital angular momentum of the pair [17]. In other words, each resonance corresponds to a different value of the relative angular momentum m_l (the $m_l=+1$ and $m_l=-1$ resonances are superimposed because the frequency shift induced by the dipolar coupling is proportional to m_l^2, as noted in [17]).

As the spin-orbit coupling is not included in our simplified three-level model, we take the multiple peak-structure into account by fitting the data of Fig. 4 using a sum of three laws (10) with a different set of phenomenological parameters for each value of the angular momentum:

$$\sigma_{\mathrm{el}}(E) = \sum_{m_l=-1}^{+1} \frac{C_{m_l}E^2}{(E-\tilde{\delta}_{m_l})^2 + \hbar^2\gamma_{m_l}^2/4}, \tag{11}$$

where $\tilde{\delta}_{m_l}$ is related to the magnetic field through $\tilde{\delta}_{m_l}=\mu(B-B_{F,m_l})$ and $\gamma_{m_l}=\gamma_{0,m_l}+a_{m_l}E^{3/2}$. Using this law, we obtain a perfect fit to the elastic as well as inelastic data obtained from the coupled-channel calculations. The values obtained

TABLE I. Values of the phenomenological parameters obtained after a fit to the coupled-channel calculation data of Fig. 4. δB_F is the shift between the $m_l=\pm 1$ and $m_l=0$ resonances.

Channel	$(1/2,-1/2)$			$(-1/2,-1/2)$		
m_l	-1	0	1	-1	0	1
$C(10^{-13}\ \mathrm{cm}^2)$	0.22	0.22	0.22	0.87	0.88	0.87
$D(10^{-13}\ \mathrm{cm}^2\ \mu\mathrm{K/s})$	0.00002	0.59	0.56	3×10^{-5}	1.54	5.72
$\gamma_0(\mathrm{s}^{-1})$	$<10^{-2}$	110	110	<1	220	830
$a(\mu\mathrm{K}^{-1/2})$	0.0017	0.0017	0.0017	0.0024	0.0024	0.0024
η	0.22	0.22	0.22	0.23	0.23	0.23
$\delta B_F(\mathrm{G})$	-0.0036	0	-0.0036	-0.012	0	-0.012

for the different phenomenological parameters are presented on Table I.

From these data, we see first that the "elastic" properties are independent of m_l. This comes from the fact that the elastic scattering is mainly a consequence of the hyperfine coupling that does not act on the center-of-mass motion of the atoms. However, we see that both the inelastic collision rate constant D and the molecule lifetime γ_0 exhibit large variations with the relative angular momentum [22]. First, the spontaneous decay rate γ_0 of a molecule in $m_l=0,+1$ is always larger than $\sim 10^2\ \mathrm{s}^{-1}$, which corresponds to a maximum lifetime of about 10 ms. Second, we observe a strong reduction of the losses in the $m_l=-1$ channel, in which no significant spontaneous decay could be found. An estimate of γ_0 can nevertheless be obtained by noting that, since the elastic parameters are independent of m_l, the ratio D/γ_0 should not depend on m_l [this can be checked by comparing the ratios D/γ_0 for $m_l=0$ and $m_l=+1$ in the $(-1/2,-1/2)$ channel]. Using this assumption we find that $\gamma_0\sim 4\times10^{-3}\ \mathrm{s}^{-1}$ both in $(1/2,-1/2)$ and $(-1/2,-1/2)$. The reason for this strong increase of the lifetime of the molecules in $m_l=-1$ is probably because, due to angular momentum conservation, the outgoing pair is expected to occupy a state with $l=3$ after an inelastic process. Indeed, if we start in a two-body state (m_F,m_F') and if the dipolar relaxation flips the spin m_F', then the atom pair ends up in a state $(m_F,m_F'+1)$. This increase of the total spin of the pair must be compensated by a decrease of the relative angular momentum. Therefore, if the molecule was associated with a relative angular momentum m_l, it should end up with m_l-1. In the case of $m_l=-1$, this means that the final value of the relative angular momentum is $m_l=-2$, i.e., $l\geqslant 2$. But, according to selection rules associated with spin-spin coupling, the dipolar interaction can only change l by 0 or 2. Therefore, starting from a p-wave $(l=1)$ compound, this can only lead to $l=3$. Let us now assume that the coupling between the molecular state and the outgoing channel is still proportional to the overlap between the two states [see Eq. (1)], even in the presence of a dipolar coupling: the argument above indicates that the ratio $\rho=\gamma_{0,m_l=-1}/\gamma_{0,m_l'\neq-1}$ between the decay rate of molecules in $m_l=-1$ and the one of molecules in $m_l'\neq 1$ is then of the order of

$$\rho\sim\left|\frac{\int g^*(r)j_3(kr)r^2dr}{\int g^*(r)j_1(kr)r^2dr}\right|^2,$$

where $k=\sqrt{m\Delta/\hbar^2}$ is the relative momentum of the atoms after the decay. For lithium, we have $R_e\sim 3$ Å [23] which yields $kR_e\sim 7\times10^{-2}$. This permits us to approximate the spherical Bessel functions j_l by their expansion at low k, $j_l(kr)\sim(kr)^l$, that is,

$$\rho\sim k^4\left|\frac{\int g^*(r)r^5dr}{\int g^*(r)r^3dr}\right|^2\sim(kR_e)^4.$$

With the numerical value obtained for kR_e, we get $\rho\sim 2\times10^{-5}$, which is, qualitatively, in agreement with the numerical coupled-channel calculations presented above.

VI. TEMPERATURE AVERAGING

In realistic conditions, the two-body loss rate G_2 needs to be averaged over the thermal distribution of atoms. G_2 is therefore simply given by

$$G_2(E)=\sqrt{\frac{\pi}{4(k_BT)^3}}\int_0^\infty g_2(E)e^{-E/k_BT}E^{1/2}dE.$$

The evolution of G_2 vs detuning is displayed in Fig. 5 and shows a strongly asymmetric profile that was already noticed in previous theoretical and experimental papers [8,10].

This feature can readily be explained by noting that in situations relevant to experiments, γ_0 is small with respect to temperature. We can therefore replace g_2 by a sum of Dirac functions centered on δ_{0,m_l}. When the δ_{0,m_l} are positive, G_2 takes the simplified form

$$G_2=4\sqrt{\pi}\sum_{m_l}\left(\frac{D_{m_l}}{\hbar\gamma_{m_l}(\tilde{\delta}_{m_l})}\right)\left(\frac{\tilde{\delta}_{m_l}}{k_BT}\right)^{3/2}e^{-\tilde{\delta}_{m_l}/k_BT}.$$

Moreover, if we neglect the lift of degeneracy due to the dipolar interaction coupling and we assume all the $\tilde{\delta}_{m_l}$ to be equal to some $\tilde{\delta}$, we get

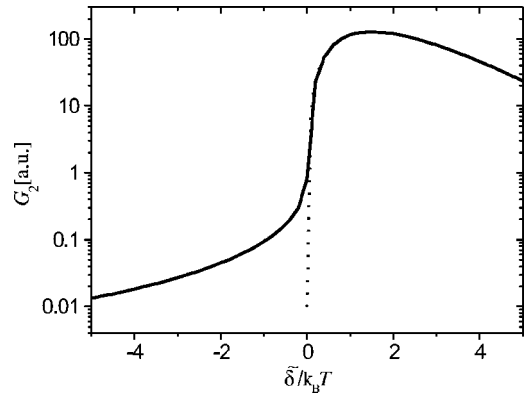

FIG. 5. Full line: numerical calculation of the loss rate for $T=10\ \mu$K. Dotted line: asymptotic expansion (12).

$$G_2 = 4\sqrt{\pi}\left(\frac{\overline{D}}{\hbar\,\overline{\gamma}(\tilde{\delta})}\right)\left(\frac{\tilde{\delta}}{k_BT}\right)^{3/2} e^{-\tilde{\delta}/k_BT}, \tag{12}$$

with $\overline{D}=\Sigma_{m_l}D_{m_l}$ and $\overline{D}/\overline{\gamma}=\Sigma_{m_l}D_{m_l}/\gamma_{m_l}$ [19].

For $\tilde{\delta}<0$ and $|\tilde{\delta}|\gg k_BT$, we can replace the denominator of g_2 by $\tilde{\delta}^2$ and we get the asymptotic form for G_2

$$G_2 = \frac{3}{2}k_BT\sum_{m_l}\frac{D_{m_l}}{\tilde{\delta}_{m_l}^2}. \tag{13}$$

Let us now comment on the two equations (12) and (13) .

(1) We note that the maximum value of G_2 is obtained for $\tilde{\delta}/k_BT=3/2$. It means that when tuning the magnetic field (i.e., $\tilde{\delta}$), the maximum losses are not obtained at the resonance $\tilde{\delta}=0$, but at a higher field, corresponding to $\tilde{\delta}=3k_BT/2$. For a typical experimental temperature $T=10\ \mu$K, this corresponds to a shift of about 0.1 G.

(2) Similarly, the width of $G_2(\tilde{\delta})$ scales like k_BT. Expressed in terms of magnetic field, this corresponds to $\sim$0.1 G for $T=10\ \mu$K. This width is a consequence of the resonance nature of the scattering in *p*-wave processes. As seen earlier, both elastic and inelastic collisions are more favorable when the relative energy $E=\tilde{\delta}$. When $\tilde{\delta}<0$, the resonance conditions cannot be satisfied, since there are no states in the incoming channel with negative energy. The scattering is then formally analogous to optical pumping or other second-order processes and yields the $1/\tilde{\delta}^2$ obtained in Eq. (13). When $\tilde{\delta}\gg k_BT$, the resonance condition is satisfied by states that are not populated (since for a thermal distribution, we populate states up to $E\sim k_BT$).

VII. CONCLUSION

In this paper, we have developed a simple model capturing the main scattering properties close to a *p*-wave Feshbach resonance. The analytical formulas we obtained show very good agreement with both numerical coupled-channel calculations and experimental measurements from our group [9] and from Chin and Grimm [24]. We have shown that the line shape of the resonance is very different from what is expected for an *s*-wave process: while *s*-wave scattering is mainly dominated by low-energy processes, *p*-wave scattering is rather dominated by collisions at energies equal to that of the molecular state. Regarding *p*-wave molecules, we have seen that at resonance their wave function was dominated by the short-range bare molecular state. Finally, the study of the spontaneous decay of these molecules has shown a very different lifetime depending on the relative angular momentum of its constituents, since molecules in $m_l=-1$ could live 10^4 times longer than those in $m_l=0,+1$. This very intriguing result might prove to be a valuable asset for the experimental study of *p*-wave molecules since it guarantees that $m_l=-1$ dimers are very stable against two-body losses in the absence of depolarizing collisions.

ACKNOWLEDGMENTS

We thank Z. Hadzibabic, J. Dalibard, and Y. Castin for very helpful discussions. S.K. acknowledges support from the Netherlands Organisation for Scientific Research (NWO) and E.U. Contract No. HPMF-CT-2002-02019. E.K. acknowledges support from the Stichting FOM, which is financially supported by NWO. M.T. acknowledges support from E.U. Contracts No. HPMT-2000-00102 and No. MEST-CT-2004-503847. This work was supported by CNRS, by the ACI photonique and nanosciences programs from the French Ministry of Research, and by Collège de France. Laboratoire Kastler Brossel is "Unité de recherche de l'École Normale Supèrieure et de l'Université Pierre et Marie Curie, associée au CNRS."

[1] S. Jochim, M. Bartenstein, A. Altmeyer, G. Hendl, S. Riedl, C. Chin, J. Hecker Denschlag, and R. Grimm, Science **302**, 2101 (2003).
[2] M. W. Zwierlein, C. A. Stan, C. H. Schunck, S. M. F. Raupach, S. Gupta, Z. Hadzibabic, and W. Ketterle, Phys. Rev. Lett. **91**, 250401 (2003).
[3] T. Bourdel, L. Khaykovich, J. Cubizolles, J. Zhang, F. Chevy, M. Teichmann, L. Tarruell, S. J. J. M. F. Kokkelmans, and C. Salomon, Phys. Rev. Lett. **93**, 050401 (2004).
[4] J. Kinast, S. L. Hemmer, M. E. Gehm, A. Turlapov, and J. E. Thomas, Phys. Rev. Lett. **92**, 150402 (2004).
[5] M. Greiner, C. A. Regal, and D. S. Jin, Nature (London) **426**, 537 (2003).
[6] D. M. Lee, Rev. Mod. Phys. **69**, 645 (1997).
[7] C. C. Tsuei and J. R. Kirtley, Phys. Rev. Lett. **85**, 182 (2000).
[8] C. A. Regal *et al.*, Phys. Rev. Lett. **90**, 053201 (2003).
[9] J. Zhang, E. G. M. van Kempen, T. Bourdel, L. Khaykovich, J. Cubizolles, F. Chevy, M. Teichmann, L. Tarruell, S. J. J. M. F. Kokkelmans, and C. Salomon, Phys. Rev. A **70**, 030702(R) (2004).

[10] C. H. Schunck, M. W. Zwierlein, C. A. Stan, S. M. F. Raupach, W. Ketterle, A. Simoni, E. Tiesinga, C. J. Williams, and P. S. Julienne, e-print cond-mat/0407373.
[11] T. L. Ho and N. Zahariev, e-print cond-mat/0408469; T. L. Ho and R. B. Diener, e-print cond-mat/0408468.
[12] Y. Ohashi, e-print cond-mat/0410516.
[13] J. R. Taylor, *Scattering Theory* (John Wiley, New York, 1972); H. Feshbach, *Theoretical Nuclear Physics* (John Wiley, New York, 1992).
[14] C. Chin, V. Vuletic, A. J. Kerman, and S. Chu, Phys. Rev. Lett. **85**, 2717 (2000); P. J. Leo, C. J. Williams, and P. S. Julienne, *ibid.* **85**, 2721 (2000).
[15] Thomas Volz, Stephan Drr, Niels Syassen, Gerhard Rempe, Eric van Kempen, and Servaas Kokkelmans, e-print cond-mat/0410083.
[16] A. R. Edmunds, *Angular Momentum in Quantum Mechanics* (Princeton University Princeton, NJ, Press, 1996).
[17] C. Ticknor, C. A. Regal, D. S. Jin, and J. L. Bohn, Phys. Rev. A **69**, 042712 (2004).
[18] E. G. M. van Kempen, B. Marcelis, and S. J. J. M. F. Kokkelmans, e-print cond-mat/0406722.
[19] For the sake of simplicity, these averaged parameters only were presented in [9].
[20] K. Dieckmann, C. A. Stan, S. Gupta, Z. Hadzibabic, C. H. Schunck, and W. Ketterle, Phys. Rev. Lett. **89**, 203201 (2002).
[21] H. T. C. Stoof, J. M. V. A. Koelman, and B. J. Verhaar, Phys. Rev. B **38**, 4688 (1988).
[22] Note that the different lifetimes calculated for the three m_l states do not violate any rotational symmetry. Indeed, the magnetic field used to reach the Feshbach resonance provides a preferred direction to the system.
[23] We evaluate R_e by identifying it with the relative distance r at which the total (centrifugal + long-range) potential $3\hbar^2/mr^2 - C_6/r^6 - C_8/r^8 - C_{10}/r^{10}$ cancels and we used the $C_{8,9,10}$ coefficients of [24]. Z.-C. Yan *et al.*, Phys. Rev. A **54**, 2824 (1996).
[24] C. Chin and R. Grimm (private communication).

A.5 Expansion of an ultra-cold lithium gas in the BEC-BCS crossover

Leticia Tarruell, Martin Teichmann, Jason McKeever, Thomas Bourdel, Julien Cubizolles, Lev Khaykovich, Jing Zhang, Nir Navon, Frédéric Chevy, Christophe Salomon,

Proceedings of the 2006 Enrico Fermi summer school on Fermi gases, Varenna 2006.

Expansion of a lithium gas in the BEC-BCS crossover

L. Tarruell[1], M. Teichmann[1], J. McKeever[1], T. Bourdel[1], J. Cubizolles[1], L. Khaykovich[2], J. Zhang[3], N. Navon[1], F. Chevy[1], and C. Salomon[1]

[1] *Laboratoire Kastler Brossel, École normale supérieure, 24, rue Lhomond, 75005 Paris, France*
[2] *Department of Physics, Bar Ilan University, 52900 Ramat Gan, Israel*
[3] *SKLQOQOD, Institute of Opto-Electronics, Shanxi University, Taiyuan 030006, P. R. China*

Summary. — We present an experimental study of the time of flight properties of a gas of ultra-cold fermions in the BEC-BCS crossover. Since interactions can be tuned by changing the value of the magnetic field, we are able to probe both non interacting and strongly interacting behaviors. These measurements allow us to characterize the momentum distribution of the system as well as its equation of state. We also demonstrate the breakdown of superfluid hydrodynamics in the weakly attractive region of the phase diagram, probably caused by pair breaking taking place during the expansion.

1. – Introduction

Feshbach resonances in ultra cold atomic gases offer the unique possibility of tuning interactions between particles, thus allowing one to study both strongly and weakly interacting many-body systems with the same experimental apparatus. A recent major achievement was the experimental exploration of the BEC-BCS crossover [1, 2, 3, 4, 5, 6], a scenario proposed initially by Eagles, Leggett, Nozières and Schmitt-Rink to bridge the gap between the Bardeen-Cooper-Schrieffer (BCS) mechanism for superconductivity in metals, and the Bose-Einstein condensation of strongly bound pairs [7, 8, 9]. Here, we present a study of the crossover using time of flight measurements. This technique gives access to a wide range of physical properties of the system and has been successfully used in different fields of physics. The observation of elliptic flows was for instance used to demonstrate the existence of quark-gluon plasmas in heavy ion collisions [10]. In cold atoms, the ellipticity inversion after free flight is a signature of Bose-Einstein condensation [11, 12]. In an optical lattice the occurrence of interference peaks can be used as the signature of the superfluid to insulator transition [13] and, with fermions, it can be used

to image the Fermi surface [14]. Two series of time-of-flight measurements are presented: expansion of the gas without interactions, which gives access to the momentum distribution, a fundamental element in the BEC-BCS crossover, or with interactions, which allows us to characterize the equation of state of the system, and probe the validity of superfluid hydrodynamics.

2. – Experimental method

In a magnetic trap, a spin polarized gas of $N = 10^6$ ^{6}Li atoms in $|F = 3/2, m_F = +3/2\rangle$ is sympathetically cooled by collisions with ^{7}Li in $|F = 2, m_F = +2\rangle$ to a temperature of 10 μK. This corresponds to a degeneracy of $T/T_F \sim 1$, where $T_F = \hbar\bar{\omega}(6N)^{1/3}/k_\mathrm{B}$ is the Fermi temperature of the gas. The magnetic trap frequencies are 4.3 kHz (76 Hz) in the radial (axial) direction, and $\bar{\omega} = (\omega_x\omega_y\omega_z)^{1/3}$ is the mean frequency of the trap. Since there are no thermalizing collisions between the atoms in a polarized Fermi gas, the transfer into our final crossed dipole trap, which has a very different geometry (Fig. 1), is done in two steps. We first transfer the atoms into a mode-matched horizontal single beam Yb:YAG dipole trap, with a waist of ~ 23 μm. At maximum optical power (2.8 W), the trap depth is ~ 143 μK (15 T_F), and the trap oscillation frequencies are 6.2(1) kHz (63(1) Hz) in the radial (axial) direction. The atoms are transferred in their absolute ground state $|F = 1/2, m_F = +1/2\rangle$ by an RF pulse. We then sweep the magnetic field to 273 G and drive a Zeeman transition between $|F = 1/2, m_F = +1/2\rangle$ and $|F = 1/2, m_F = -1/2\rangle$ to prepare a balanced mixture of the two states (better than 5%). At this magnetic field, the scattering length between both states is $-280\,a_0$ (Fig. 2). After 100 ms the mixture has lost its coherence, initiating collisions in the gas. During the thermalization process about half of the atoms are lost. We then perform a final evaporative cooling stage by lowering the trap depth to $\sim 36\,\mu$K. At this point, we ramp up a vertical Nd:YAG laser beam (power 126 mW and waist $\sim 25\,\mu$m), obtaining our final crossed dipole trap configuration (Fig. 1). The measured degeneracy is $T/T_F \lesssim 0.15$. The magnetic field is then increased to 828 G (in the vicinity of the Feshbach resonance, see Fig. 2), where we let the gas thermalize for 200 ms before performing subsequent experiments.

3. – Momentum distribution

In standard BCS theory, the ground state of an homogeneous system is described by a pair condensate characterized by the many-body wave function

$$|\psi\rangle = \prod_{\boldsymbol{k}} (u_{\boldsymbol{k}} + v_{\boldsymbol{k}} a^\dagger_{\boldsymbol{k},\uparrow} a^\dagger_{-\boldsymbol{k},\downarrow})|0\rangle,$$

where $|0\rangle$ is the vacuum and $a^\dagger_{\boldsymbol{k},\sigma}$ is the creation operator of a fermion with momentum $\boldsymbol{k}$ and spin σ. In this expression, $|v_{\boldsymbol{k}}|^2$ can be interpreted as the occupation probability in momentum space, and is displayed in Fig. 3a for several values of the interaction

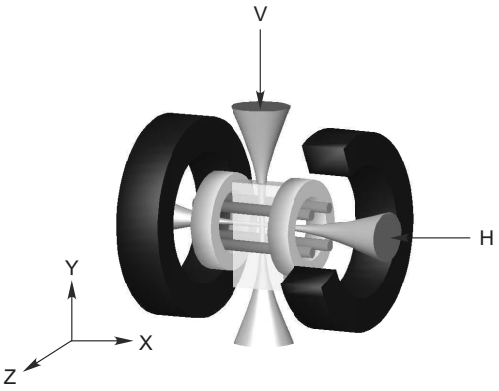

Fig. 1. – Ioffe-Pritchard trap and crossed dipole trap used for the experiments. The crossed geometry allows us to change the aspect ratio of the trap.

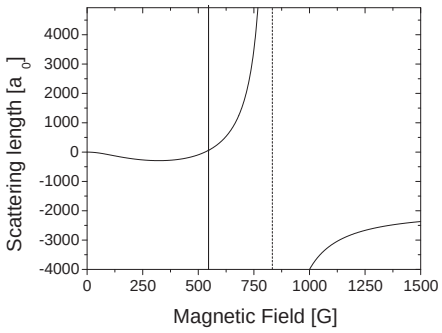

Fig. 2. – ^{6}Li Feshbach resonance between $|F = 1/2, m_F = +1/2\rangle$ and $|F = 1/2, m_F = -1/2\rangle$. The broad Feshbach resonance is located at 834 G. The balanced mixture is prepared at 273 G.

parameter $1/k_F a$, where k_F is the Fermi wave vector of the non interacting Fermi gas ($E_F = \hbar^2 k_F^2/2m$). One effect of the pairing of the atoms is to broaden the momentum distribution. In the BCS limit ($1/k_F a \to -\infty$), the broadening with respect to the momentum distribution of an ideal Fermi gas is very small, of the order of the inverse of the coherence length ξ. In the unitary limit ($1/k_F a \to 0$) it is expected to be of the order of k_F. In the BEC limit ($1/k_F a \to \infty$) we have molecules of size a so the momentum distribution, which is given by the Fourier transform of the molecular wave function, has a width $\hbar/a$.

In a first series of expansion experiments, we have measured the momentum distribution of a trapped Fermi gas in the BEC-BCS crossover. Similar experiments have been performed at JILA on ^{40}K [15].

In order to measure the momentum distribution of the atoms, the gas must expand freely, without any interatomic interactions. To achieve this, we quickly switch off the magnetic field so that the scattering length is brought to zero (see FIG. 2) [16]. We prepare $N = 3 \times 10^4$ atoms at 828 G in the crossed dipole trap with frequencies $\omega_x = 2\pi \times 2.78$ kHz, $\omega_y = 2\pi \times 1.23$ kHz and $\omega_z = 2\pi \times 3.04$ kHz. The magnetic field is adiabatically swept in 50 ms to different values in the crossover region. Then, we simultaneously switch off both dipole trap beams and the magnetic field (with a linear ramp of 296 G/μs). After 1 ms of free expansion, the atoms are detected by absorption imaging. The measured density profiles give directly the momentum distribution of the gas integrated along the imaging direction.

In FIG. 3, we show the measured momentum distributions for three different interaction parameters, corresponding to the BCS side of the resonance, the unitary limit and the BEC side of the resonance. Together with our data, we have plotted the predictions

of mean field BCS theory at $T = 0$, taking into account the trapping potential with a local density approximation [17]. k_F^0 is now the Fermi wave-vector calculated at the center of the harmonic trap for an ideal gas.

Some precautions need to be taken concerning this type of measurements due to possible density dependent losses during the magnetic field switch-off. If the magnetic field is not turned off fast enough, some atoms can be bound into molecules while the Feshbach resonance is crossed. The molecules are not detected with the imaging light and therefore will appear as a loss of the total number of atoms. Even if, as in our case, the Feshbach resonance is crossed in only 1 μs, this time may not be small compared to the typical many-body timescale ($\hbar/E_F \sim 1.3\,\mu s$ for Fig. 3 data).

To investigate quantitatively this effect, we have performed an additional experiment in a more tightly confining trap. We prepare a gas of 5.9×10^4 atoms at 828 G in a trap with frequencies $\omega_x = 2\pi \times 1.9$ kHz, $\omega_y = 2\pi \times 3.6$ kHz and $\omega_z = 2\pi \times 4.1$ kHz. The total peak density in the trap is 1.3×10^{14} atoms/cm^3. We let the gas expand at high field for a variable time t_B, then switch off B and detect the atoms after 0.5 ms of additional free expansion. Assuming hydrodynamic expansion at unitarity we calculate the density after t_B [18] and obtain the fraction of atoms detected as a function of the density of the gas when the resonance is crossed. For instance, we detect $\simeq 60\%$ fewer atoms for $t_B = 0$ compared to $t_B = 0.5$ ms, where the density is a factor $\simeq 10^3$ lower. The results are nicely fitted by a Landau-Zener model :

$$N_{\mathrm{detected}}/N_{\mathrm{total}} = \exp\left(-A\frac{n(t_B)}{2\dot{B}}\right),$$

where $n(t_B)$ is the total density at t_B, $\dot{B}$ the sweep rate and A the coupling constant between the atoms and the molecules. We determine $A \simeq 5 \times 10^{-12}$ G m^3/s. Our result is five times smaller than the MIT value $A \simeq 24 \times 10^{-12}$ G m^3/s [19], measured at a total peak density of 10^{13} atoms/cm^3 (one order of magnitude smaller than in our experiment). The theoretical prediction, assuming only two body collisions, is $A = 19 \times 10^{-12}$ G m^3/s [20]. The difference between our measurement and theory may suggest that many-body effects are important in our case. Finally, using our value of A the model predicts an atom number loss of about 27% for the momentum distribution measurements of Fig. 3. This loss is comparable to our shot-to-shot fluctuations in atom number and therefore was not unambiguously observed.

In conclusion, we have performed a measurement of the momentum distribution of a trapped Fermi gas. The results are found in reasonable agreement with BCS theory despite the fact that it is not expected to be quantitatively correct in the strongly interacting regime. In future work, experiments at lower density will be performed, in order to avoid the observed loss effect. This should allow us to distinguish between BCS and more exact theories [21]. It would also be interesting to perform measurements at different temperatures as in Ref. [22].

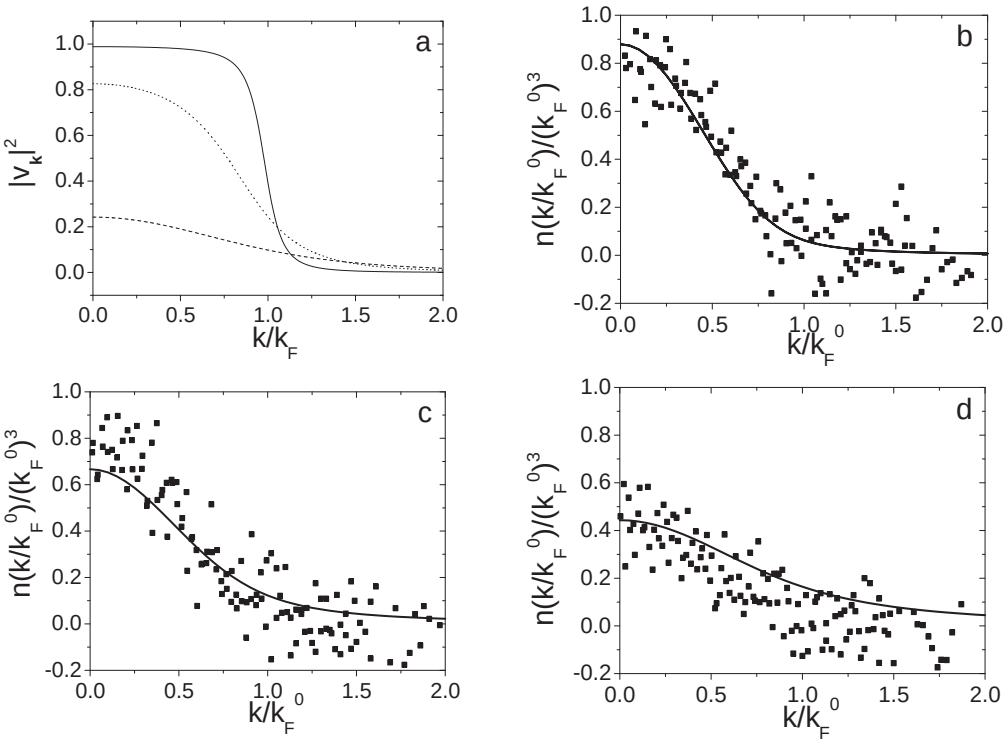

Fig. 3. – (a): Momentum distribution of a uniform Fermi gas for $1/k_F a = -1$ (solid line), $1/k_F a = 0$ (dotted line) and $1/k_F a = 1$ (dashed line) calculated from mean field BCS theory at $T = 0$ [17]. The results obtained from quantum Monte Carlo simulations [21] show that BCS theory slightly underestimates the broadening; (b): Measured momentum distribution of a trapped Fermi gas on the BCS side of the resonance ($1/k_F^0 a = -0.42$); (c): Unitary limit ($1/k_F^0 a = 0$); (d): BEC side of the resonance ($1/k_F^0 a = 0.38$). The solid lines in (b), (c) and (d) are the predictions of BCS mean field theory taking into account the trapping potential with a local density approximation [17]. k_F^0 is defined in the text.

4. – Release energy

In a second series of experiments, we have performed expansions at constant magnetic field, thus keeping the interactions present during the time of flight. The analysis of size measurement across the BEC-BCS crossover yields valuable information on the influence of interactions on the properties of the system. In particular, we have measured the release energy of the gas in the BEC-BCS crossover [3]. On resonance ($1/k_F^0 a = 0$), the gas reaches a universal behavior [23]. The chemical potential μ is proportional to the Fermi energy $\mu = (1 + \beta)E_F$. We have determined the universal scaling parameter β from our release energy measurement.

The starting point for the experiment is a nearly pure molecular condensate of 7×10^4 atoms at 770 G, in an optical trap with frequencies $\omega_x = 2\pi \times 830$ Hz, $\omega_y = 2\pi \times 2.4$ kHz, and $\omega_z = 2\pi \times 2.5$ kHz. We slowly sweep the magnetic field at a rate of 2 G/ms to various values across the Feshbach resonance. We detect the integrated density profile after a time of flight expansion of 1.4 ms in several stages: 1 ms of expansion at high magnetic field, followed by a fast ramp of 100 G in 50 μs in order to dissociate the molecules and, after the fast switch-off of the magnetic field, 350 μs of ballistic expansion.

Fig. 4 presents the gas energy released after expansion, which is calculated from gaussian fits to the optical density after time of flight: $E'_{\rm rel} = m(2\sigma_y^2 + \sigma_x^2)/2\tau^2$, where σ_i is the rms width along i and τ is the time of flight. We assume that the size σ_z (which is not observed) is equal to σ_y. Note that both in the weakly interacting case and unitarity limit the density has a Thomas-Fermi profile and the release energy can be calculated from the exact profiles. However, we have chosen this gaussian shape to describe the whole crossover region with a single fit function. This leads to a rescaling of the release energy. In particular, the ideal Fermi gas release energy in an harmonic trap is $E_{\rm rel} = 3/8 E_F$ but when using the gaussian fit to the Thomas-Fermi profile we get instead $E'_{\rm rel} = 0.46 E_F$ as shown in Fig. 4.

The release energy in the BEC-BCS crossover varies smoothly. It presents a plateau for $-1/k_F a \leq -0.5$, (BEC side) and then increases monotonically towards that of a weakly interacting Fermi gas. On resonance, the release energy scales as $E_{\rm rel} = \sqrt{1+\beta}\, E^0_{\rm rel}$, where $E^0_{\rm rel}$ is the release energy of the non interacting Fermi gas. The square root comes from the average over the trap. At 834 G, we get $\beta = -0.59(15)$. This value is slightly different from our previous determination $\beta = -0.64(15)$, where the resonance was assumed to be located at 820 G instead of 834 G [3]. Our result agrees with other measurements performed on ^{6}Li and with some theoretical predictions (see Table I). Remarkably, the recent ^{40}K measurement at JILA is also in very good agreement, thus proving the universality of the unitarity regime.

5. – Ellipticity

Nontrivial information can be extracted from the measurement of the aspect ratio of the cloud after expansion. For instance, in the first days of gaseous Bose-Einstein condensates, the onset of condensation was characterized by an ellipticity inversion after time of flight, a dramatic effect compared to the isotropic expansion of a non condensed Boltzmann gas. In the case of strongly interacting Fermi gases, ellipticity measurements can be used as probes for the hydrodynamic behavior of the system, and constitute an indirect signature of the appearance (or breakdown) of superfluidity.

We have studied the ellipticity of the cloud as a function of the magnetic field for different temperatures. As before, the density profiles are fitted with gaussians, and the ellipticity is defined as $\eta = \sigma_y/\sigma_x$. We prepare $N = 3 \times 10^4$ atoms at 828 G in a crossed dipole trap. The magnetic field is adiabatically swept in 50 ms to different values in the crossover region. Then, we switch off both dipole trap beams and let the gas expand

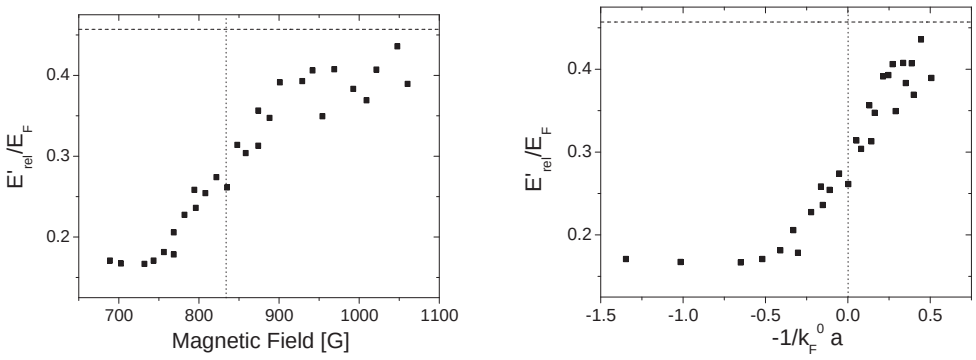

Fig. 4. – Rescaled release energy $E'_{\rm rel}$ of a trapped Fermi gas in the BEC-BCS crossover as a function of the magnetic field and as a function of $-1/k_F^0 a$ [3]. The dashed line is the rescaled release energy of a $T = 0$ non interacting Fermi gas. From the measurement at resonance we extract $\beta = -0.59(15)$.

		β
Experimental results on ^{6}Li at finite T	This work	$-0.59(15)$
	ENS 2004 [3]	$-0.64(15)$
	Innsbruck [24]	$-0.73^{+12}_{-0.09}$
	Duke [25]	$-0.49(4)$
	Rice [26]	$-0.54(5)$
Experimental result on ^{40}K extrapolation to T=0	JILA [27]	$-0.54^{+0.05}_{-0.12}$
Theoretical predictions at $T = 0$	BCS theory [7, 8, 9]	-0.41
	Astrakharchik *et al.* [28]	$-0.58(1)$
	Carlson *et al.* [29, 30]	$-0.58(1)$
	Perali *et al.* [31]	-0.545
	Padé approximation [23, 32]	-0.67
	Steel [33]	-0.56
	Haussmann *et al.* [34]	-0.64
Theoretical predictions at $T = T_c$	Bulgac *et al.* [35]	-0.55
	Burovski *et al.* [36]	$-0.507(14)$

TABLE I. – *List of the recent experimental measurements and theoretical predictions of the universal scaling parameter β.*

for 0.5 ms in the presence of the magnetic field. After 0.5 ms of additional expansion at $B = 0$, the atoms are detected by absorption imaging. Fig. 5a and Fig. 5b show the measured value of the ellipticity as a function of the magnetic field for two different samples, which are at different temperatures. Together with the experimental results we have plotted the expected anisotropy from superfluid hydrodynamics [18]. For this, we have extracted from the quantum Monte Carlo simulation of ref. [28] the value of the polytropic exponent γ, defined as $\gamma = \frac{n}{\mu}\frac{\partial \mu}{\partial n}$.

The first series of measurements is done in a trap with frequencies $\omega_x = 2\pi \times 1.39$ kHz, $\omega_y = 2\pi \times 3.09$ kHz, $\omega_z = 2\pi \times 3.38$ kHz and trap depth $\sim 1.8\, T_F$. The measured ellipticity (Fig. 5a) is in good agreement with the hydrodynamic prediction on the BEC side, at resonance and on the BCS side until $1/k_F^0 a = -0.15$. It then decreases monotonically to 1.1 at $1/k_F^0 a = -0.5$.

For the second series of experiments we prepare a colder sample in a trap with frequencies $\omega_x = 2\pi \times 1.24$ kHz, $\omega_y = 2\pi \times 2.76$ kHz, $\omega_z = 2\pi \times 3.03$ kHz and trap depth $\sim 1.6\, T_F$. In this case the behavior of the anisotropy is very different (Fig. 5b). We observe a plateau until $1/k_F^0 a = -0.33$, in good agreement with the hydrodynamic prediction, and at this critical magnetic field there is a sharp decrease of η to a value close to 1.2. This sharp transition seems analogous to the sudden increase of the damping of the breathing mode observed in Innsbruck [37].

In a third experiment, we measure the ellipticity at unitarity as a function of trap depth (hence of the gas temperature). Below a critical trapping laser intensity, the ellipticity jumps from a low value (1.1) to the hydrodynamic prediction 1.45.

In all cases, the decrease of the anisotropy indicates a breakdown of superfluid hydrodynamics in the weakly attractive part of the phase diagram or at higher temperature. A first possibility would be that the gas crosses the critical temperature in the trap. However, we know from the MIT experiment [38] that pair breaking can occur during the expansion. During the time of flight, both the density and k_F decrease. On the BEC side of resonance, the binding energy of the molecules ($-\hbar^2/ma^2$) does not depend on the density and the pairs are very robust. By contrast, on the BCS side of resonance the generalized Cooper pairs become fragile as the gap decreases with $1/k_F a$ and they can be broken during the expansion. Our experiments use the ellipticity of the cloud as a probe and are complementary to the MIT approach, where the breakdown of superfluidity was characterized by the disappearance of vortices during the expansion of the gas. We are planning additional experiments in order to investigate wether the breakdown of superfluidity occurs in the trap or during the expansion.

6. – Conclusion

The results presented here constitute a first step in the understanding of the free flight properties of strongly correlated fermionic systems. In future work, we will investigate more thoroughly the pair breaking mechanism taking place during the expansion in the BCS part of the phase diagram. We point out the need for a dynamic model of the

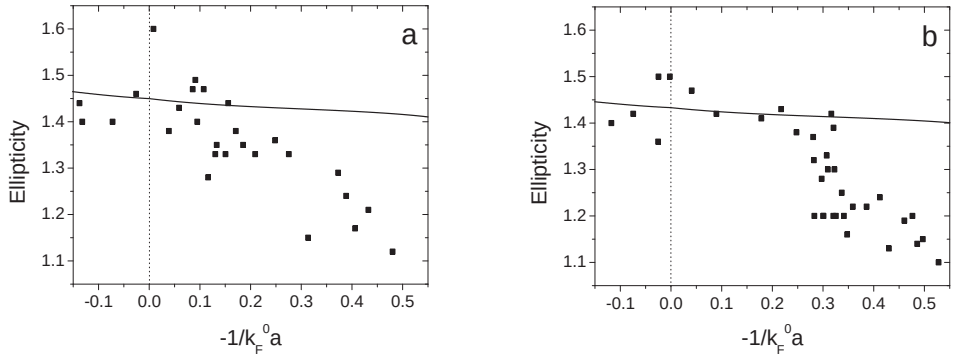

Fig. 5. – Ellipticity of the gas after expansion from a trap of depth $\sim 1.8\,T_F$(a) and from a trap of depth $\sim 1.6\,T_F$ (b). Solid lines: hydrodynamic predictions.

expanding gas at finite temperature.

7. – Acknowledgments

We gratefully acknowledge support by the IFRAF institute and the ACI Nanosciences 2004 NR 2019. We thank the ENS ultracold atoms group, S. Stringari, R. Combescot, D. Petrov and G. Shlyapnikov for stimulating discussions. Laboratoire Kastler Brossel is a research unit No. 8552 of CNRS, ENS, and Université Paris 6.

REFERENCES

[1] S. Jochim, M. Bartenstein, A. Altmeyer, G. Hendl, S. Riedl, C. Chin, J. Hecker Denschlag, and R. Grimm, *Science*, **302** (2003) 2101.
[2] M. Greiner, C. A. Regal, and D. S. Jin, *Nature*, **426** (2003) 537.
[3] T. Bourdel, L. Khaykovich, J. Cubizolles, J. Zhang, F. Chevy, M. Teichmann, L. Tarruell, S. J. J. M. F. Kokkelmans, and C. Salomon, *Phys. Rev. Lett.*, **93** (2004) 050401.
[4] M. W. Zwierlein, C. A. Stan, C. H. Schunck, S. M. F. Raupach, S. Gupta, Z. Hadzibabic, and W. Ketterle, *Phys. Rev. Lett.*, **91** (2003) 250401.
[5] J. Kinast, S. L. Hemmer, M. E. Gehm, A. Turlapov, and J. E. Thomas, *Phys. Rev. Lett.*, **92** (2004) 150402.
[6] G. B. Partridge, K. E. Strecker, R. I. Kamar, M. W. Jack, and R. G. Hulet, *Phys. Rev. Lett.*, **95** (2005) 020404.
[7] D. M. Eagles, *Phys. Rev.*, **186** (1969) 456.
[8] A. J. Leggett, in Modern Trends in the Theory of Condensed Matter, Lecture Notes in Physics Vol. 115, edited by A. Pekalski and R. Przystawa, (Springer-Verlag, Berlin) 1980, p. 13.
[9] P. Nozières and S. Schmitt-Rink, *J. Low Temp. Phys.*, **59** (1985) 195.
[10] E. Shuryak, *Prog. Part. Nucl. Phys.*, **53** (2004) 273.

[11] M. H. Anderson, J. R. Ensher, M. R. Matthews, C. E. Wieman and E. A. Cornell, *Science*, **269** (1995) 198.
[12] K. B. Davis, M.-O. Mewes, M. R. Andrews, N. J. van Druten, D. S. Durfee, D. M. Kurn and W. Ketterle, *Phys. Rev. Lett.*, **75** (1995) 3969.
[13] M. Greiner, O. Mandel, T. Esslinger, T. W. Hänsch, and I. Bloch, *Nature*, **415** (2002) 39.
[14] M. Köhl, H. Moritz, T. Stöferle, K. Günter, and T. Esslinger, *Phys. Rev. Lett.*, **94** (2005) 080403.
[15] C. A. Regal, M. Greiner, S. Giorgini, M. Holland, and D. S. Jin, *Phys. Rev. Lett.*, **95** (2005) 250404.
[16] T. Bourdel, J. Cubizolles, L. Khaykovich, K. M. F. Magalhães, S. J. J. M. F. Kokkelmans, G. V. Shlyapnikov, and C. Salomon, *Phys. Rev. Lett.*, **91** (2003) 020402.
[17] L. Viverit, S. Giorgini, L. Pitaevskii, and S. Stringari, *Phys. Rev. A*, **69** (2004) 013607.
[18] C. Menotti, P. Pedri, and S. Stringari, *Phys. Rev. Lett.*, **89** (2002) 250402.
[19] M. Zwierlein, PhD. Thesis, MIT (2006), p.107.
[20] J. Chwedeńczuk, K. Góral, T. Köhler, and P. Julienne, *Phys. Rev. Lett.*, **93** (2004) 260403.
[21] G. E. Astrakharchik, J. Boronat, J. Casulleras, and S. Giorgini, *Phys. Rev Lett.*, **95** (2005) 230405
[22] Q. Chen, C. A. Regal, D. S. Jin and K. Levin, *Phys. Rev. A*, **74** (2006) 011601.
[23] H. Heiselberg, *Phys. Rev. A*, **63** (2001) 043606
[24] M. Bartenstein, A. Altmeyer, S. Riedl, S. Jochim, C. Chin, J. H. Denschlag, and R. Grimm, *Phys. Rev. Lett.*, **92** (2004) 120401; revised value M. Bartenstein, PhD. Thesis, Universität Innsbruck, (2005), p.100.
[25] J. Kinast, A. Turlapov, J. Thomas, Q. Chen, J. Stajic, and K. Levin, *Science*, **307** (2005) 1296.
[26] G. B. Partridge, W. Li, R. I. Kamar, Y. Liao, and R. G. Hulet, *Science*, **311** (2005) 503.
[27] J. T. Stewart, J. T. Gaebler, C. A. Regal, and D. S. Jin, *Phys. Rev. Lett.*, **97** (2006) 220406.
[28] G. E. Astrakharchik, J. Boronat, J. Casulleras, and S. Giorgini, *Phys. Rev. Lett.*, **93** (2004) 200404.
[29] J. Carlson, S.-Y. Chang, V. R. Pandharipande, and K. E. Schmidt, *Phys. Rev. Lett.*, **91** (2003) 050401.
[30] J. Carlson and S. Reddy, *Phys. Rev. Lett.*, **95** (2005) 060401.
[31] A. Perali, P. Pieri, and G. C. Strinati, *Phys. Rev. Lett.*, **93** (2004) 100404.
[32] G. A. Baker, Jr., *Phys. Rev. C*, **60** (1999) 054311.
[33] J. V. Steele, e-print nucl-th/0010066.
[34] R. Haussmann, W. Rantner, S. Cerrito, and W. Zwerger, e-print cond-mat/0608282.
[35] A. Bulgac, J. E. Drut, and P. Magierski, *Phys. Rev. Lett.*, **96** (2006) 090404.
[36] E. Burovski, N. Prokof'ev, B. Svistunov, and M. Troyer, *Phys. Rev. Lett.*, **96** (2006) 160402.
[37] M. Bartenstein, A. Altmeyer, S. Riedl, S. Jochim, C. Chin, J. Hecker Denschlag, and R. Grimm, *Phys. Rev. Lett.*, **92** (2004) 203201.
[38] C. H. Schunck, M. W. Zwierlein, A. Schirotzek, and W. Ketterle, e-print cond-mat/0607298.

Appendix B

Bibliography

[1] H. Vogel, *Gerthsen Physik*, Springer, Berlin, 1999.

[2] R. P. Feynman, R. B. Leighton, and M. Sands, *The Feynman Lecturse on Physics*, Addison-Wesley, Reading, Mass., 1964.

[3] E. L. Raab, M. Prentiss, A. Cable, S. Chu, and D. E. Pritchard, *Trapping of Neutral Sodium Atoms with Radiation Pressure*, Phys. Rev. Lett. **59** (1987), 2631.

[4] D. G. Fried, T. C. Killian, L. Willmann, D. Landhuis, S. C. Moss, D. Kleppner, and T. J. Greytak, *Bose-Einstein Condensation of Atomic Hydrogen*, Phys. Rev. Lett. **81** (1998), 3811.

[5] M. H. Anderson, J. R. Ensher, M. R. Matthews, C. E. Wieman, and E. A. Cornell, *Observation of Bose-Einstein Condensation in a Dilute Atomic Vapor*, Science **269** (1995), 198.

[6] K. B. Davis, M.-O. Mewes, M. R. Andrews, N. J. van Druten, D. S. Durfee, D. M. Kurn, and W. Ketterle, *Bose-Einstein Condensation in a Gas of Sodium Atoms*, Phys. Rev. Lett. **75** (1995), 3969.

[7] R. C. Hwa and X.-N. Wang (eds.), *Quark-Gluon Plasma 3*, World Scientific, Singapore, 2004.

[8] F. London, *Superfluidity*, Wiley, New York, 1950.

[9] J. Bardeen, L. N. Cooper, and J. R. Schrieefer, *Theory of Superconductivity*, Phys. Rev. **108** (1957), 1175.

[10] M. Holland, S. J. J. M. F. Kokkelmans, M. L. Chiofalo, and R. Walser, *Resonance Superfluidity in a Quantum Degenerate Fermi Gas*, Phys. Rev. Lett. **87** (2001), 120406.

[11] R. F. Bishop, K. A. Gemoth, N. R. Walet, and Y. Xian (eds.), *Proceedings of the 10th International Conference on Recent Progress in Many-body Theories*, World Scientific, Singapore, 2000.

[12] H. Heiselberg, *Fermi systems with long scattering lengths*, Phys. Rev. A **63** (2001), 043606.

[13] B. DeMarco and D. S. Jin, *Onset of Fermi Degeneracy in a Trapped Atomic Gas*, Science **285** (1999), 1703.

[14] A. G. Truscott, K. E. Strecker, W. I. McAlexander, G. B. Partridge, and R. G. Hulet, *Observation of Fermi Pressure in a Gas of Trapped Atoms*, Science **291** (2001), 2570.

[15] F. Schreck, L. Khaykovich, K. L. Corwin, G. Ferrari, T. Bourdel, J. Cubizolles, and C. Salomon, *Quasipure Bose-Einstein Condensate Immersed in a Fermi Sea*, Phys. Rev. Lett. **87** (2001), 080403.

[16] Z. Hadzibabic, C. A. Stan, K. Dieckmann, S. Gupta, M. W. Zwierlein, A. Görlitz, and W. Ketterle, *Two-Species Mixture of Quantum Degenerate Bose and Fermi Gases*, Phys. Rev. Lett. **88** (2001), 160401.

[17] G. Roati, F. Riboli, G. Modugno, and M. Inguscio, *Fermi-Bose Quantum Degenerate ^{40}K-^{87}Rb Mixture with Attractive Interaction*, Phys. Rev. Lett. **89** (2002), 150403.

[18] T. Loftus, C. A. Regal, C. Ticknor, J. L. Bohn, and D. S. Jin, *Resonant Control of Elastic Collisions in an Optically Trapped Fermi Gas of Atoms*, Phys. Rev. Lett. **88** (2002), 173201.

[19] K. M. O'Hara, S. L. Hemmer, S. R. Granade, M. E. Gehm, J. E. Thomas, V. Venturi, E. Tiesinga, and C. J. Williams, *Measurement of the zero crossing in a Feshbach resonance of fermionic ^6Li*, Phys. Rev. A. **66** (2002), 041401.

[20] C. A. Regal, C. Ticknor, J. L. Bohn, and D. S. Jin, *Creation of ultracold molecules from a Fermi gas of atoms*, Nature **424** (2003), 47.

[21] J. Cubizolles, T. Bourdel, S. J. J. M. F. Kokkelmans, G. V. Shlyapnikov, and C. Salomon, *Production of Long-Lived Ultracold Li_2 Molecules from a Fermi Gas*, Phys. Rev. Lett. **91** (2003), 240401.

[22] D. S. Petrov, C. Salomon, and G. V. Shlyapikov, *Weakly bound dimers of Fermionic atoms*, Phys. Rev. Lett. **93** (2004), 090404.

[23] S. Jochim, M. Bartenstein, A. Altmeyer, G. Hendl, S. Riedl, C. Chin, J. Hecker Denschlag, and R. Grimm, *Bose-Einstein Condensation of Molecules*, Science **302** (2003), 2101.

[24] M. Greiner, C. A. Regal, and D. S. Jin, *Emergence of a molecular Bose-Einstein condensate from a Fermi gas*, Nature **426** (2003), 537–540.

[25] M. W. Zwierlein, C. A. Stan, C. H. Schunck, S. M. F. Raupach, A. J. Kerman, and W. Ketterle, *Observation of Bose-Einstein Condensation of Molecules*, Phys. Rev. Lett. **91** (2003), 250401.

[26] C. A. Regal, M. Greiner, and D. S. Jin, *Observation of Resonance Condensation of Fermionic Atom Pairs*, Phys. Rev. Lett. **92** (2004), 040403.

[27] Q. Chen, C. A. Regal, M. Greiner, D. S. Jin, and K. Levin, *Understanding the superfluid phase diagram in trapped Fermi gases*, Phys. Rev. A **73** (2006), 041601(R).

[28] C. Chin, M. Bartenstein, A. Altmeyer, S. Riedl, S. Jochim, J. Hecker Denschlag, and R. Grimm, *Observation of the Pairing Gap in a Strongly Interacting Fermi Gas*, Science **305** (2004), 5687.

[29] M. Bartenstein, A. Altmeyer, S. Riedl, S. Jochim, C. Chin, J. Hecker Denschlag, and R. Grimm, *Collective Excitations of a Degenerate Gas at the BEC-BCS Crossover*, Phys. Rev. Lett. **92** (2004), 203201.

[30] A. Altmeyer, S. Riedl, C. Kohstall, M. Wright, R. Geursen, M. Bartenstein, C. Chin, J. Hecker Denschlag, and R. Grimm, *Precision Measurements of Collective Oscillations in the BEC-BCS Crossover*, Phys. Rev. Lett. **98** (2007), 040401.

[31] J. Kinast, A. Turlapov, J. E. Thomas, Q. Chen, J. Stajic, and K. Levin, *Heat Capacity of a Strongly-Interacting Fermi Gas*, Science **307** (2005), 1296-1299.

[32] M. W. Zwierlein, A. Schirotzek, C. H. Schunck, and W. Ketterle, *Fermionic Superfluidity with Imbalanced Spin Populations*, Science **311** (2006), 492.

[33] C. A. Regal, C. Ticknor, J. L. Bohn, and D. S. Jin, *Tuning p-Wave Interactions in an Ultracold Fermi Gas of Atoms*, Phys. Rev. Lett. **90** (2003), 053201.

[34] C. H. Schunck, M. W. Zwierlein, C. A. Stan, S. M. F. Raupach, W. Ketterle, A. Simoni, E. Tiesinga, C. J. Williams, and P. S. Julienne, *Feshbach Resonances in Fermionic Lithium-6*, Phys. Rev. A **71** (2005), 045601.

[35] D. M. Lee, *The extraordinary phases of liquid ^{3}He*, Rev. Mod. Phys. **69** (1997), 645.

[36] M. Schellekens, R. Hoppeler, A. Perrin, J. Viana Gomes, D. Boiron, A. Aspect, and C. I. Westbrook, *Hanbury Brown Twiss Effect for Ultracold Quantum Gases*, Science **310** (2005), 648.

[37] T. Jeltes, J. M. McNamara, W. Hogervorst, W. Vassen, V. Krachmalnicoff, M. Schellekens, A. Perrin, H. Chang, D. Boiron, A. Aspect, and C. I. Westbrook, *Hanbury Brown Twiss effect for bosons versus fermions* (2006), available at `arXiv:cond-mat/0612278`.

[38] F. Schreck, *Mixtures of ultracold gases: fermi sea and bose-einstein condensate of Lithium isotopes*, Ph.D. Thesis, Université Paris VI, 2002.

[39] G. Ferrari, *Piégeage simultané des isotopes fermionique et bosonique du lithium, étude théorique de la relaxation collisionelle dans un gaz de Fermi dégénéré*, Université Paris 6, 2000.

[40] C. J. Pethick and H. Smith, *Bose-Einstein Condensation in Dilute Gases*, Cambridge, 2002.

[41] L. Pitaevskii and S. Stringari, *Bose-Einstein Condensation*, Clarendon, Oxford, 2003.

[42] S. Bose, *Plancks Gesetz und Lichtquantenhypothese*, Z. Phys. **26** (1924), 178.

[43] Л. Д. Ландау and Е. М. Лифжиц, *Квантовая механика (нерелятивистская теория)*, Nauka, Moscow, 1974 (russian); german transl. in *Quantenmechanik*, Lehrbuch der theoretischen Physik, vol. III, Akademie, Berlin, 1979.

[44] J. J. Sakurai, *Modern quantum mechanics*, Addison-Wesley, 1994.

[45] H. Bethe and R. Peierls, *Quantum Theory of the Diplon*, Proc. Roy. Soc. London A **148** (1935), 146.

[46] H. A. Bethe, *Theory of the Effective Range in Nuclear Scattering*, Phys. Rev. **76** (1949), 38.

[47] S. Simonucci, P. Pieri, and G. C. Strinati, *Broad vs. narrow Fano-Feshbach resonances in the BCS-BEC crossover with trapped Fermi atoms*, Europhys. Lett. **69** (2005), 713-718.

[48] K. E. Strecker, G. B. Partridge, and R. G. Hulet, *Conversion of an Atomic Fermi Gas to a Long-Lived Molecular Bose Gas*, Phys. Rev. Lett. **91** (2003), 080406.

[49] K. Huang and C. N. Yang, *Quantum-Mechanical Many-Body Problem with Hard-Sphere Interation*, Phys. Rev. **105** (1957), 767.

[50] Y. Castin, *Basic theory tools for degenerate Fermi gases*, Proceedings of the 2006 Enrico Fermi Summer School on "Ultracold Fermi gases", Varenna, Italy, 2007, available at `arXiv:cond-mat/0612613`.

[51] D. D. Konowalow, R. M. Regan, and M. E. Rosenkrantz, *The "most likely" potential energy curve for the lowest* $^3\Sigma_u^+$ *state of* Li_2, J. Chem. Phys. **81** (1984), 4534.

[52] D. D. Konowalow and M. L. Olson, *The electronic structure and spectra of the* $X^1\Sigma_g^+$ *and* $A^1\Sigma_u^+$ *states of* Li_2, J. Chem. Phys. **71** (1979), 450.

[53] H. Feshbach, *Unified Theory of Nuclear Reactions*, Ann. Phys. (N. Y.) **5** (1958), 357.

[54] U. Fano, *Effects of Configuration Interaction on Intensities and Phase Shifts*, Phys. Rev. **124** (1961), 1866.

[55] C. Chin, *A simple model of Feshbach molecules* (2005), available at `arXiv:cond-mat/0506313v2`.

[56] J. T. M. Walraven, *Elements of Quantum Gases: Thermodynamic and Collisional Properties of Trapped Atomic Gases*, 2006, unpublished., available at `http://staff.science.uva.nl/~walraven/walraven/Publications_files/LesHouches2006.pdf`

[57] B. Marcelis, E. G. M. van Kempen, B. J. Verhaar, and S. J. J. M. F. Kokkelmans, *Feshbach resonances with large background scattering length: Interplay with open-channel resonances*, Phys. Rev. A **70** (2004), 012701.

[58] M. Bartenstein, A. Altmeyer, S. Riedl, R. Geursen, S. Jochim, C. Chin, J. Hecker Denschlag, and R. Grimm, *Precise Determination of* ^{6}*Li Cold Collision Parameters by Radio-Frequency Spectroscopy on Weakly Bound Molecules*, Phys. Rev. Lett. **94** (2005), 103201.

[59] D. M. Eagles, *Effective Masses in Zr-Doped Superconducting Ceramic* $SrTiO_3$, Phys. Rev. **178**, 668.

[60] A. J. Legget, *Cooper Pairing in Spin-Polarized Fermi Systems*, J. Phys. (Paris) C **41** (1980), 7.

[61] C. A. R. Sá de Melo, M. Randeria, and J. R. Engelbrecht, *Crossover from BCS to Bose Superconductivity: Transition Temperature and Time-Dependent Ginzburg-Landau Theory*, Phys. Rev. Lett. **71** (1993), 3202.

[62] P. Nozières and S. Schmitt-Rink, *Bose condensation in an attractive fermion gas: From weak to strong coupling superconductivity*, J. Low Temp. Phys. **59** (1985), 195.

[63] K. Tanaka and F. Marsiglio, *Even-odd and super-even effects in the attractive Hubbard model*, Phys. Rev. B. **60** (1999), 3508.

[64] G. Bruun, Y. Castin, R. Dum, and K. Burnett, *BCS theory for trapped ultracold fermions*, Euro. Phys. J. D **7** (2004), 433.

[65] T. Bourdel, *Gaz de Fermi en interaction forte : Du condensat de molécules aux paires de Cooper*, Ph.D. Thesis, Université Paris 6, 2004.

[66] M. Tinkham, *Introduction to Superconductivity*, Dover, Mineola, N.Y., 1996.

[67] P. A. Lee, N. Nagaosa, and X.-G. Wen, *Doping a Mott insulator: Physics of high-temperature superconductivity*, Rev. Mod. Phys. **78** (2006), 17.

[68] Q. Chen, J. Stajic, S. Tan, and K. Levin, *BCS–BEC crossover: From high temperature superconductors to ultracold superfluids*, Phys. Rep. **412** (2005), 1.

[69] A. Perali, P. Pieri, L. Pisani, and G. C. Strinati, *BCS-BEC crossover at finite temperature for superfluid trapped Fermi atoms*, Phys. Rev. Lett. **92** (2004), 220404.

[70] G. E. Astrakharchik, J. Boronat, J. Casulleras, and S. Giorgini, *Momentum distribution and condensate fraction of a Fermi gas in the BCS-BEC crossover*, Phys. Rev. Lett. **95** (2005), 230405.

[71] J. Cubizolles, *Fermions et Bosons Dégénérés au Voisinage d'une Résonance de Feshbach : Production de Molécules et Solitons d'Ondes de Matière*, Ph.D. Thesis, Université Paris 6, 2004.

[72] M. Bartenstein, A. Altmeyer, S. Riedl, S. Jochim, C. Chin, J. Hecker Denschlag, and R. Grimm, *Crossover from a molecular Bose-Einstein condensate to a degenerate Fermi gas*, Phys. Rev. Lett. **92** (2004), 120401.

[73] M. Bartenstein, *From Molecules to Cooper Pairs: Experiments in the BEC-BCS Crossover*, Ph.D. Thesis, Leopold-Franzens-Universität Innsbruck, 2005.

[74] G. B. Partridge, W. Li, R. I. Kamar, Y.-a. Liao, and R. G. Hulet, *Pairing and Phase Separation in a Polarized Fermi Gas*, Science **311** (2006), 503.

[75] J. T. Stewart, J. P. Gaebler, C. A. Regal, and D. S. Jin, *The potential energy of a ^{40}K Fermi gas in the BCS-BEC crossover*, Phys. Rev. Lett. **97** (2006), 220406.

[76] J. Carlson, S.-Y. Chang, V. R. Pandharipande, and K. E. Schmidt, *Superfluid Fermi Gases with Large Scattering Length*, Phys. Rev. Lett. **91** (2003), 050401.

[77] J. Carlson and S. Reddy, *Asymmetric Two-Component Fermion Systems in Strong Coupling*, Phys. Rev. Lett. **95** (2005), 060401.

[78] A. Perali, P. Pieri, and G. C. Strinati, *Quantitative Comparison between Theoretical Predictions and Experimental Results for the BCS-BEC Crossover*, Phys. Rev. Lett. **93** (2004), 100404.

[79] G. E. Astrakharchik, J. Bornat, J. Casulleras, and S. Giorgini, *Equation of state of a Fermi gas in the BEC-BCS crossover: a quantum Monte Carlo study*, Phys. Rev. Lett. **93** (2004), 200404.

[80] J. H. Moore, C. C. Davis, M. A. Coplan, and S. C. Greer, *Building scientific apparatus*, Perseus, Cambridge Mass., 2003.

[81] D. E. Pritchard, *Cooling Neutral Atoms in a Magnetic Trap for Precision Spectroscopy*, Phys. Rev. Lett. **51** (1983), 1336.

[82] M. Greiner, I. Bloch, T. Hänsch, and T. Esslinger, *Magnetic transport of trapped cold atoms over a large distance*, Phys. Rev. A **63** (2001), 031401.

[83] A. Alberti, *Contributions to new generation ultra-cold Lithium experiments*, Tesi di Laurea, Università di Pisa, 2006.

[84] T. A. Savard, K. M. O'Hara, and J. E. Thomas, *Laser-noise-induced heating in far-off resonance optical traps*, Phys. Rev. A **56** (1997), R1095.

[85] S. R. Granade, M. E. Gehm, K. M. O'Hara, and J. E. Thomas, *All-Optical Production of a Degenerate Fermi Gas*, Phys. Rev. Lett. **88** (2002), 120405.

[86] S. Jochim, M. Bartenstein, G. Hendl, J. Hecker Denschlag, R. Grimm, A. Mosk, and M. Weidemüller, *Magnetic field control of elastic scattering in a cold gas of Fermionic lithium atoms*, Phys. Rev. Lett. **89** (2002), 273202.

[87] J. Goldwin, S. Inouye, M. L. Olsen, B. Newman, B. D. DePaola, and D. S. Jin, *Measurement of the interaction strength in a Bose-Fermi mixture with ^{87}Rb and ^{40}K*, Phys. Rev. A. **70** (2004), 021601(R).

[88] C. Silber, S. Günther, C. Marzok, B. Deh, P. W. Courteille, and C. Zimmermann, *Quantum-Degenerate Mixture of Fermionic Lithium and Bosonic Rubidium Gases*, Phys. Rev. Lett. **95** (2005), 170408.

[89] W. H. Wing, *On neutral particle trapping in quasistatic electromagnetic fields*, Prog. Quant. Elec. **8** (1984), 181.

[90] O. Zobay and B. M. Garraway, *Two-Dimensional Atom Trapping in Field-Induced Adiabatic Potentials*, Phys. Rev. Lett. **86** (2001), 1195.

[91] Y. Colombe, E. Knyazchyan, O. Morizot, B. Mercier, V. Lorent, and H. Perrin, *Ultracold atoms confined in rf-induced two-dimensional trapping potentials*, Europhys. Lett. **67** (2004), 594.

[92] J. D. Hunter, *Matplotlib: A 2D Graphics Environment*, Comp. Sci. Eng. **9** (2007), 90.

[93] T. E. Oliphant, *Python for Scientific Computing*, Comp. Sci. Eng. **9** (2007), 10.

[94] M. Galassi, J. Davies, J. Theiler, B. Gough, G. Jungman, M. Booth, and F. Rossi, *GNU Scientific Library Reference Manual*, Revised Second Edition (v1.8), Network Theory, Bristol, 2006.

[95] V. Magni, G. Cerullo, and S. de Silvestri, *High-accuracy fast Hankel transform for optical beam propagation*, J. Opt. Soc. Am. A **9** (1992), 2031.

[96] L. Viverit, S. Giorgini, L. P. Pitaevskii, and S. Stringari, *Momentum distribution of a trapped Fermi gas with large scattering length*, Phys. Rev. A **69** (2004), 013607.

[97] M. L. Chiofalo, S. Giorgini, and M. Holland, *Released Momentum Distribution of a Fermi Gas in the BCS-BEC Crossover*, Phys. Rev. Lett. **97** (2006), 070404.

[98] M. Marini, F. Pistolesi, and G. C. Strinati, *Evolution from BCS superconductivity to Bose condensation: analytic results for the crossover in three dimenstions*, Eur. Phys. J. B **1** (1998), 151–159.

[99] C. A. Regal, M. Greiner, S. Giorgini, M. Holland, and D. S. Jin, *Momentum Distribution of a Fermi Gas of Atoms in the BCS-BEC Crossover*, Phys. Rev. Lett. **95** (2005), 250404.

[100] Q. Chen, C. A. Regal, D. S. Jin, and K. Levin, *Finite Temperature Momentum Distribution of a Trapped Fermi Gas*, Phys. Rev. A **74** (2006), 011601(R).

[101] L. D. Landau, *Zur Theorie der Energieübertragung II*, Physik. Z. Sowjet. **2** (1932), 46.

[102] C. Zener, *Non-Adiabatic Crossing of Energy Levels*, Proc. Roy. Soc. London A **137** (1932), 696.

[103] K. Góral, T. Köhler, S. A. Gardiner, E. Tiesinga, and P. S. Julienne, *Adiabatic association of ultracold molecules via magnetic field tunable interactions*, J. Phys. B. **37** (2004), 3457.

[104] M. Zwierlein, *High-Temperature Superfluidity in an Ultracold Fermi Gas*, Ph.D. Thesis, Massachussets Institute of Technology, 2006.

[105] Y. Castin and R. Dum, *Bose-Einstein Condensates in Time Dependent Traps*, Phys. Rev. Lett. **77** (1996), 5315.

[106] M. E. Gehm, S. L. Hemmer, K. M. O'Hara, and J. E. Thomas, *Unitarity-Limited Elastic Collision Rate in a Harmonically-Trapped Fermi Gas*, Phys. Rev. A **68** (2003), 011603.

[107] K. M. O'Hara, S. L. Hemmer, M. E. Gehm, S. R. Granade, and J. E. Thomas, *Observation of a Strongly Interacting Degenerate Fermi Gas of Atoms*, Science **298** (2002), 2179.

[108] C. Menotti, P. Pedri, and S. Stringari, *Expansion of an Interacting Fermi Gas*, Phys. Rev. Lett. **89** (2002), 250402.

[109] B. Jackson, P. Pedri, and S. Stringari, *Collisions and expansion of an ultracold dilute Fermi gas*, Europhys. Lett. **67** (2004), 524.

[110] J. Kinast, S. L. Hemmer, M. E. Gehm, A. Turlapov, and J. E. Thomas, *Evidence for Superfluidity in a Resonantly Interacting Fermi Gas*, Phys. Rev. Lett. **92** (2004), 150402.

[111] H. Hu, A. Minguzzi, X.-J. Liu, and M. P. Tosi, *Collective modes and ballistic expansion of a Fermi gas in the BCS-BEC crossover*, Phys. Rev. Lett. **93** (2004), 190403.

[112] N. Manini and L. Salasnich, *Bulk and collective properties of a dilute Fermi gas in the BCS-BEC crossover*, Phys. Rev. A **71** (2005), 033625.

[113] S. Stringari, *Dynamics and superfluidity of an ultracold Fermi gas*, Proceedings of the 2006 Enrico Fermi Summer School on "Ultracold Fermi gases", Varenna, Italy, 2007, available at `arXiv:cond-mat/0702526`.

[114] Y. Castin, *Exact scaling transform for a unitary quantum gas in a time dependent harmonic potential*, Compt. Rend. Phys. **2004** (2004), 407.

[115] C. Lobo and S. D. Gensemer, *A proposal for measuring correlation functions in interacting gases*, available at arXiv:cond-mat/0702313.

[116] G. Diana, N. Manini, and L. Salasnich, *Expansion of a Fermi cloud in the BCS-BEC crossover*, Phys. Rev. A. **73** (2006), 065601.

[117] A. Altmeyer, S. Riedl, M. J. Wright, C. Kohstall, J. Hecker Denschlag, and R. Grimm, *Dynamics of a strongly interacting Fermi gas: the radial quadrupole mode*, available at arXiv:0704.3366v1.

[118] H. L. Bethlem, G. Berden, and G. Meijer, *Decelerating Neutral Dipolar Molecules*, Phys. Rev. Lett. **83** (1999), 1558.

[119] C. M. Dion, C. Drag, O. Dulieu, B. Laburthe Tolra, F. Masnou-Seeuws, and P. Pillet, *Resonant Coupling in the Formation of Ultracold Ground State Molecules via Photoassociation*, Phys. Rev. Lett. **86** (2000), 2253.

[120] T. Lahaye, T. Koch, B. Fröhlich, M. Fattori, J. Metz, A. Griesmaier, S. Giovanazzi, and T. Pfau, *A quantum ferrofluid* (2007), available at arXiv:0706.1670.

[121] J. J. Hudson, B. E. Sauer, M. R. Tarbutt, and E. A. Hinds, *Measurement of the Electron Electric Dipole Moment Using YbF Molecules*, Phys. Rev. Lett. **89** (2002), 023003.

[122] E. G. M. v. Kempen, B. Marcelis, and S. J. J. M. F. Kokkelmans, *Formation of fermionic molecules via interisotope Feshbach resonances*, Phys. Rev. A **70** (2004), 050701(R).

[123] C. A. Stan, M. W. Zwierlein, C. H. Schunck, S. M. F. Raupach, and W. Ketterle, *Observation of Feshbach resonances between two different atomic species*, Phys. Rev. Lett. **93** (2004), 143001.

[124] S. Inouye, J. Goldwin, M. L. Olsen, C. Ticknor, J. L. Bohn, and D. S. Jin, *Observation of Heteronuclear Feshbach Resonances in a Bose-Fermi Mixture*, Phys. Rev. Lett. **93** (2004), 183201.

[125] S. Ospelkaus, C. Ospelkaus, L. Humbert, K. Sengstock, and K. Bongs, *Tuning of heteronuclear interactions in a quantum-degenerate Fermi-Bose mixture*, Phys. Rev. Lett. **97** (2006), 120403.

[126] C. Ospelkaus, S. Ospelkaus, L. Humbert, P. Ernst, K. Sengstock, and K. Bongs, *Ultracold heteronuclear molecules in a 3D optical lattice*, Phys. Rev. Lett. **97** (2006), 120402.

[127] K. Günter, T. Stöferle, H. Moritz, M. Köhl, and T. Esslinger, *Bose-Fermi Mixtures in a Three-dimensional Optical Lattice*, Phys. Rev. Lett. **96** (2006), 180402.

[128] S. B. Papp and C. E. Wieman, *Observation of Heteronuclear Feshbach Molecules from a ^{85}Rb - ^{87}Rb gas*, Phys. Rev. Lett. **97** (2006), 180404.

[129] M. E. Gehm, *Preparation of an Optically-Trapped Degenerate Fermi Gas of ^{6}Li: Finding the Route to Degeneracy*, Duke University, 2003.

[130] G. E. Astrakharchik, R. Combescot, X. Leyronas, and S. Stringari, *Equation of State and Collective Frequencies of a Trapped Fermi Gas Along the BEC-Unitarity Crossover*, Phys. Rev. Lett. **95** (2005), 030404.

[131] S. Stringari, *Collective Excitations of a Trapped Bose-Condensed Gas*, Phys. Rev. Lett. **77** (1996), 2360.

[132] R. Combescot and X. Leyronas, *Axial collective excitations of a degenerate Fermi gas in the BEC to unitarity crossover*, Europhys. Lett. **68** (2004), 762.

[133] T. N. De Silva and E. J. Mueller, *Surface Tension in Unitary Fermi Gases with Population Imbalance*, Phys. Rev. Lett. **97** (2006), 070402.

[134] G. B. Partridge, W. Li, Y. A. Liao, R. G. Hulet, M. Haque, and H. T. C. Stooe, *Deformation of a Trapped Fermi Gas with Unequal Spin Populations*, Phys. Rev. A **74** (2006), 011602(R).

[135] Y. Shin, M. W. Zwierlein, C. H. Schunck, A. Schirotzek, and W. Ketterle, *Observation of Phase Separation in a Strongly-Interacting Imbalanced Fermi Gas*, Phys. Rev. Lett. **97** (2006), 030401.

[136] K. B. Gubbels, M. W. J. Romans, and H. T. C. Stooe, Phys. Rev. Lett. **97** (2006), 210402.

[137] A. M. Clogston, *Upper limit for the critical field in hard superconductors*, Phys. Rev. Lett. **9** (1962), 266.

[138] G. Sarma, *On the influence of a uniform exchange field action on the spins of the conduction electrons in a superconductor*, J. Phys. Chem. Solids **24** (1963), 1029.

[139] K. Machida, T. Mizushima, and M. Ichioka, Phys. Rev. Lett. **97** (2006), 120407.

[140] R. Combescot, *Introduction to FFLO phases and collective mode in the BEC-BCS crossover*, Proceedings of the 2006 Enrico Fermi Summer School on "Ultracold Fermi gases", Varenna, Italy, 2007, available at `arXiv:cond-mat/0702399`.

[141] P. Fulde and R. A. Ferrell, *Superconductivity in a Strong Spin-Exchange Field*, Phys. Rev. **135** (1964), A550.

[142] A. I. Larkin and Yu. N. Ovchinnikov, *Nonuniform state of superconductors*, Zh. Eksperim. i Teor. Fiz. **47** (1964), 1136.

[143] R. Combescot, A. Recati, C. Lobo, and F. Chevy, *Normal state of highly polarized Fermi gases: simple many-body approaches* (2007), available at `arXiv:cond-mat/0702313`.

[144] C. H. Schunck, Y. Shin, A. Schirotzek, M. W. Zwierlein, and W. Ketterle, *Pairing of Strongly Interacting Fermions without Superfluidity* (2007), available at `arXiv:cond-mat/0702066v2`.

[145] Y. Shin, C. H. Schunck, A. Schirotzek, and W. Ketterle, *Tomographic RF Spectroscopy of a Trapped Fermi Gas at Unitarity* (2007), available at `arXiv:0705.3858v1`.

[146] K. Günther, T. Stöferle, H. Moritz, M. Köhl, and T. Esslinger, *p-Wave Interactions in Low-Dimensional Fermionic Gases*, Phys. Rev. Lett. **95** (2005), 230401.

[147] J. P. Gaebler, J. T. Stewart, J. L. Bohn, and D. S. Jin, *p-wave Feshbach molecules*, available at `arXiv:cond-mat/0703087`.

[148] K. W. Madison, F. Chevy, W. Wohlleben, and J. Dalibard, *Vortex Formation in a Stirred Bose-Einstein Condensate*, Phys. Rev. Lett. **84** (2000), 806.

[149] M. W. Zwierlein, J. R. Abo-Shaeer, A. Schirotzek, C. H. Schunck, and W. Ketterle, *Vortices and Superfluidity in a Strongly Interacting Fermi Gas*, Nature **435** (2005), 1047.

[150] M. Greiner, C. A. Regal, J. T. Stewart, and D. S. Jin, Phys. Rev. Lett. **94** (2005), 110401.

[151] I. Bloch, *Ultracold quantum gases in optical lattices*, Nature Physics **1** (2005), 23.

[152] J. Hubbard, *Electron correlations in narrow energy bands*, Proc. Roy. Soc. London A **276** (1963), 238.

[153] H. Tasaki, *The Hubbard Model: Introduction and Selected Rigorous Results*, J. Phys. Cond. Mat. **10** (1998), 4353.

[154] D. Jaksch, C. Bruder, J. I. Cirac, C. W. Gardiner, and P. Zoller, *Cold Bosonic Atoms in Optical Lattices*, Phys. Rev. Lett. **81** (1998), 3108.

[155] M. Greiner, O. Mandel, T. Esslinger, T. W. Hänsch, and I. Bloch, *Quantum phase transition from a superfluid to a Mott insulator in a gas of ultracold atoms*, Nature **415** (2002), 39.

[156] H. Ott, E. de Mirandes, F. Ferlaino, G. Roati, G. Modugno, and M. Inguscio, *Collisionally Induced Transport in Periodic Potentials*, Phys. Rev. Lett. **92** (2004), 160601.

[157] J. K. Chin, D. E. Miller, Y. Liu, C. Stan, W. Setiawan, C. Sanner, K. Xu, and W. Ketterle, Nature **443** (2006), 961.

Résumé

Nous utilisons un gaz fermionique de lithium-6 en tant que système modèle pour étudier l'effet de la superfluidité. Les deux cas limites de la superfluidité sont la formation d'un condensat de Bose-Einstein (BEC) et la supraconductivité, décrite par la théorie de Bardeen, Cooper et Schrieffer (BCS). Dans un gaz de lithium-6 on peut explorer toute la transition entre ces deux limites, la *transition BEC-BCS*, grâce à une résonance de Feshbach.

Nous étudions le comportement de la distribution d'impulsions du gaz dans la zone de cette transition et la comparons avec des modèles théoriques. L'expansion hydrodynamique, caractéristique d'un gaz superfluide, est aussi étudiée. Nous observons un changement brusque de la forme du gaz en expansion à proximité de la transition vers la phase superfluide. Nous avons aussi localisé des résonances de Feshbach hétéronucléaires entre ^{6}Li et ^{7}Li.

Au cours d'une reconstruction du montage vers une expérience de deuxième génération, un nouveau système laser, basé sur des diodes laser à haute puissance, a été developpé. Des améliorations dans notre enceinte à vide, y compris une reconstruction complète du ralentisseur Zeeman, ont augmenté le flux d'atomes, permettant de diminuer le temps de répétition de l'expérience. La géometrie des pièges magnétiques a été modifiée afin d'augmenter le nombre d'atomes piégés.

Mots clés : transition BEC-BCS, superfluidité fermionique, résonance de Feshbach, résonance hétéronucléaire

Summary

We use a fermionic gas of Lithium-6 as a model system to study superfluidity. The limiting cases of superfludity are Bose-Einstein condensation (BEC) and superconductivity, described by the theory by Bardeen, Cooper and Schrieffer (BCS). In Lithium-6 gases, we can explore the whole range between the two cases, known as the BEC-BCS crossover, using a Feshbach resonance.

We study the change of the momentum distribution of the gas in this crossover and compare to theoretical models. We also investigate the hydrodynamic expansion, characteristic for a superfluid gas. We observe a sudden change of the ellipticity of the gas close to the transition to the superfluid phase. Moreover, we localized heteronuclear Feshbach resonances between ^{6}Li and ^{7}Li.

We are currently constructing a second generation of the experimental setup. An new laser system, based on high power laser diodes, was developped. Changes in the vacuum chamber, including a complete reconstruction of the Zeeman slower, have increased the atomic flux, allowing us to increase the repetition rate of our experiment. Modifications of the geometry of the magnetic traps lead to a higher number of trapped atoms.

Keywords: BEC-BCS crossover, fermionic superfluidity, Feshbach resonance, heteronuclear resonance